Basic Mathematics for Physically Correct Mechanical Properties from Indentations

Gerd Kaupp

B P International

Basic Mathematics for Physically Correct Mechanical Properties from Indentations

Basic Mathematics for Physically Correct Mechanical Properties from Indentations

India ■ United Kingdom

Author(s)

Dr. Gerd Kaupp

Carl von Ossietzky University of Oldenburg, Germany.
E-mail: gerd.kaupp@uni-oldenburg.de;

FIRST EDITION 2022

ISBN 978-93-5547-921-1 (Print)
ISBN 978-93-5547-922-8 (eBook)
DOI: 10.9734/bpi/mono/978-93-5547-921-1

Contents

PREFACE

This open-access E-Book collects all of the 16 open-access publications with the author's challenges of false treatments of indentation data in the literature in an up scaled form with cross linking to the more recent results and some replacements of older formulas. Not all of them could be developed in one publication at a time. It depicts the advancements from 2016 to 2022 on the basis of now mathematically dedu results with closed and universal formulas for all types of solid materials. The enforcing ISO 14577 techniques can still not detect the more than common phase-transitions under mechanical stress with formation of dangerous polymorph interfaces. Their now very easy detection (actually since 2004) helps to avoid dangerous failures by cracks in airliners, bridges, buildings, polymers, commodities, etc. This affords only the physically correct calculation of the materials' mechanical properties without relying on data-treatments, fittings, iterations, and simulations with not repeatable extremely complicated assumptions for concurring with false historical equations.

This will help the scientist, teacher, anonymous reviewer, editor, technician, journalist, and certification agent for more easily finding out how urgent is it to strengthen the falsification of the still not revised ISO-14577- ASTM enforcing standards. ISO-ASTM, industry and academic publications must stop with accepting violation of the energy law. And mechanical intelligence must be freed from faked tabulated mechanical properties, always requiring reliable re-determinations. This is particularly important for one-point technical indentation results that characterise unknown polymorphs depending on the applied very high forces.

Indentations with cones, pyramids, and spheres are described on the basis of sacrosanct calculation rules for mathematically founded closed universal formulas for the dept sensing loading curves. These can locate data-fittings in published loading curves, handle peculiarities like initial surface effects, pop-ins, gradients, pile-ups and of course phase-transition onset and transformation energies. The errors from the ISO-ASTM 14577 standardisations are extremely large and further increased by their false attribution of "equivalent" cone angles to the pyramids for decreasing computer times in simulations. We replace the wrong exponent 2 on depth h versus normal force F_N instead of correctly 3/2 for cones and pyramids, and deduce the variable R/h containing correction factor for spheres. We define the physical indentation hardness and the physical indentation modulus instead of iterated ISO-H and ISO-"Young's" modulus E_r. Spherical indentations are compared with anvil pressurizations.

The very precisely calculated applications cover all kinds of materials technology, solid-state chemistry, mineralogy, biology, earth crust geology. Actually, all applicants have to be aware of a multitude of not general and extremely complicated multiple simulation schemes and fitting formulas, but that requirement is now removed thanks undeniable calculation rules. And there arise liability problems against uneducated students and in the case of catastrophic failures of technical materials (crashes of airliners, bridges,

buildings, earth quakes, commodities, etc). Not criticised is ISO 14577 valuable high-level standardization for correct experimentation. But properly revised indentation analyses remain a very important fast characterization technique for all kinds of solid materials. Depth-sensing indentations become even more important by this E-Book, despite the deplorable present situation by unappreciated physical correctness.

Gerd Kaupp

Print ISBN: 978-93-5547-921-1, eBook ISBN: 978-93-5547-922-8

Basic Mathematics for Physically Correct Mechanical Properties from Indentations

Gerd Kaupp [a*]

DOI: 10.9734/bpi/mono/978-93-5547-921-1/CH0

ABSTRACT

This book dealt with basic mathematics for physically correct mechanical properties from indentations. The iteration-free physical description of pyramidal indentations with closed mathematical equations is comprehensively described and extended for creating new insights in this important field of research and applications. The book also stated the force vs depth loading curves of conical, pyramidal, wedged and for spherical indentations on a strict mathematical basis by explicit use of the indenter geometries rather than on still world-wide used iterated "contact depths" with elastic theory and violation of the energy law. The book also specified physical deduction of the loading curves for spherical and flat punch indentations, in particular as the parabola assumption for not self-similar spherical impressions appears impossible. This book contains various materials suitable for students, researchers and academicians.

Keywords: *Depth-sensing indentations with conical, pyramidal, spherical, and flat indenters; pop-in repair; pile-up reasons; basic algebra and trigonometry with calculation rules; challenge of false ISO 14577-ASTM standards with ISO-H, ISO-E_r, HV, etc and energy law violation; undue data-treatment, fitting, iteration, and simulation; correct loading curve formulas; H/E ratio challenge; false historical concepts and false Johnson formula; physical hardness=penetration resistance k (mN/μm$^{3/2}$); physical indentation modulus $E_{r\text{-}phys}$ without iteration; force direction and side-area; pyramids' non-equivalence with pseudo cones; phase-transition onset and transition energy detection; catastrophic crack nucleation at (multiple) polymorph intersections; long-range cracks formation; applications in crystallography for crystal structures; failure of technical materials including airliners turbines, bridges, superalloys, etc; earth sub-mantle crust exploration and earth quakes; comparison with anvil pressurizations; detailed interpretations in solid-state chemistry,*

[a] *Carl Von Ossietzky University of Oldenburg, Germany.*
**Corresponding author: E-mail: gerd.kaupp@uni-oldenburg.de;*

plastics, biology, and medicine; chances for updates for reliable mechanical intelligence, requiring warning and case-wise new indentation.

Chapter 1
Print ISBN: 978-93-5547-921-1, eBook ISBN: 978-93-5547-922-8

The Physical Foundation of $F_{\mathrm{N}} = kh^{5/2}$ for Conical/Pyramidal Indentation Loading Curves: Scientific Explanation

DOI: 10.9734/bpi/mono/978-93-5547-921-1/CH1

ABSTRACT

On the basis of fundamental mathematics, it has been possible to physically deduce the $F_{\mathrm{N}} = kh^{3/2}$ relation for conical/pyramidal indentation loading curves (where F_{N} is normal force, k penetration resistance, and h penetration depth) for conical/pyramidal indentation loading curves. It has been achieved on the basis of elementary mathematics. The displacement of material, which frequently partially plasticizes as a result of such pressure, is coupled with the productions of volume and pressure by the indentation process. As the pressure/plasticizing depends on the indenter volume, it follows that $F_{\mathrm{N}} = {F_{\mathrm{Np}}}^{1/3} \cdot {F_{\mathrm{NV}}}^{5/3}$, where the in dex p stands for pressure/plasticizing and V for indentation volume. F_{Np} does not contribute to the penetration, only F_{NV}. The exponent $2/3$ on F_{NV} shows t hat
while F_{N} is experimentally applied; only $F_{\mathrm{N}}^{2/3}$ is responsible for the penetration depth h. Thus, $F_{\mathrm{N}} = kh^{3/2}$ is deduced and the physical reason is the loss of $F_N^{1/3}$ for the depth. Unfortunately, when the Love/Sneddon deductions of an exponent 2 on *h* were accepted and applied, this was not taken into account in instruction, textbooks, or the earlier deduction of a number of common mechanical parameters. The author mentions and cites several unexpected experimental verifications and applications of the correct exponent$^{3/2}$.

Keywords: Force-depth relation; nanoindentation loading curves; penetration resistance; physical deduction, pressure and plasticizing.

1.1 INTRODUCTION

Both Love and Sneddon, who mathematically solved the "Boussinesq's issue" in 1939 and 1965 respectively, predicted that the normal force (F_{N}) would be proportional to the square of the depth *h* for conical and, hence, pyramidal indentations. This is still utilised for the derivation of numerous mechanical parameters that are still in use and has received widespread acceptance in papers and authoritative textbooks. Numerous finite element simulations that employ quadratic displacement elements, such as those by Wang et al. [1] and Soare et al. [2], have also used Exponent 2. Such simulations are often claimed to concur with published loading curves. However, more precise analysis reveals since 2004 that the experimental exponent is $3/2$ instead. Simulated and

experimental curves do not even correspond when published in the same paper. Only the analysis using the correct exponent can show, how to distinguish initial surface effects and phase changes under the load if these occur [3,4]. The linear correlation coefficient for the slope k (from F_N Vs. $h^{3/2}$) continues to always prove $r > 0.999$ or for less noisy measurements $\mathrm{r} > 0.9999$ [5,6], and the cited more recent publications up to 2014). It was, therefore, possible to introduce the concept of penetration resistance (k) for the safe comparison of materials' properties and compatibilities [6,7], the energetic of indentations with the important finding that 80% of F_N is used for the indentation work and 20% for all the other force-induced energetic events [7]. Temperature dependent indentations even allow for the calculation of the activation energy of phase changes from nothing else than from indentation loading curves [7,8]. What's still missing was the physical reason for the experimentally verified successful exponent $3/2$ on h, and this has been rightfully asked for by new-comers and experts in the field. Thus, the appreciation of the new exponent against textbooks (except [9]) requires the deduction of the Title formula. We report now on an unexpectedly short deduction of the physical reason that was not thought upon till now.

1.2 EXPERIMENTAL BACKGROUND

The instrumental indentation experiment uses in most cases a diamond indenter that is continuously pressed with normal force (F_N) onto a level surface until the continuously recorded depth h is reached. By doing so, the volume V of the indenter is intruded and it shifts material towards the bulk while producing pressure to it. Depending on the materials' properties, such pressure p may persist (fully elastic) or it is partly released by some sort of plasticizing and migration with all of the known long-range effects. This scheme is principally equivalent with all of the different loading types normal to level surfaces and has been experimentally verified for all mechanisms of plasticizing [10,11]. Kaupp and Naimi-Jamal, 2013). Such retained pressure is, of course, used in unloading curves for the calculation of the elastic modulus, which does, however, not apply to the present topic. With this in mind, we can start the deduction of the exponent $3/2$.

1.3 RESULTS AND DISCUSSION

The indentation couples two processes that must be differentiated because the applied force must serve both of them. The production of volume is attributed to the fraction ${F_\mathrm{Nv}}^\mathrm{m}$ for indentation. The production of pressure + loss of pressure (loss by plasticizing via pressure) to the displaced material is attributed to the fraction ${F_\mathrm{Np}}^\mathrm{n}$ for pressure. As the multiplication of both factors must give the product F_N, these fractional forces must have the exponents m and $\mathrm{n} < 1$, so that we obtain Equation (1.1).

$$F_\mathrm{N} = {F_\mathrm{Nv}}^\mathrm{m} \cdot {F_\mathrm{Np}}^\mathrm{n} \tag{1.1}$$

For the determination of the exponents m and n, we use the total pressure that could be reached at the depth h for absence of plasticizing. It is ($p + loss$ of p) and we call it p_{total}. Equation (1.2) is evident, and the mathematical expression for the cone volume is $V_{\mathrm{cone.}}$.

$$p_{\mathrm{total}} = KV; V_{\mathrm{cone}} = \pi(\tan\alpha)^2 h^3/3 \tag{1.2}$$

Equation (1.2) reveals that p_{total} and, thus, also F_{Np} are proportional to h^3 of the immersed cone. Formula (1.3) is, thus, obtained for cones and for pyramids, which occurs with the same proportionality.

$$p_{\mathrm{total}} \propto h^3 \text{and thus also } F_{\mathrm{Np}} \propto h^3 \tag{1.3}$$

Formula (1.3) reveals the $F_{\mathrm{Np}}^{1/3}$ proportionality to the depth h, but $F_{\mathrm{Np}}^{1/3}$ does not contribute to the depth. Nevertheless, when $\mathrm{n} = 1/3, \mathrm{m}$ must be $2/3$ according to Equation (1.1), and this gives Equation (1.4).

$$F_{\mathrm{N}} = {F_{\mathrm{NV}}}^{2/3} \cdot {F_{\mathrm{Np}}}^{1/3} \tag{1.4}$$

The exponent $2/3$ on ${F_{\mathrm{NV}}}^{2/3}$ in Equation (1.4) reveals that while the instrumental indentation applies F_{N}, only the fraction ${F_{\mathrm{NV}}}^{2/3}$ is responsible for the penetration and its depth h. This is expressed with the searched-for Equation (1.5), where we do no longer need the index V.

$$F_{\mathrm{N}}^{2/3} \propto h \text{ or } F_{\mathrm{N}} = kh^{3/2} \tag{1.5}$$

The unavoidable pressure/plasticizing factor ${F_{\mathrm{Np}}}^{1/3}$ is lost for the depth. This is the physical reason for the exponent $3/2$ on h instead of recently assumed 2 for cones and pyramids.

1.4 CONCLUSIONS

The straightforward physical deduction of the exponent $3/2$ on h with elementary mathematics for indentation loading curves of cones and pyramids reveals a clear-cut physical reason. It will certainly strengthen the appreciation of exactly quantitative instrumental nano-, micro-, and macro-indentations with conical or pyramidal indenters. When required, the respective penetration resistance constant $k\left(\mathrm{N/m^{3/2}}\right)$ can be easily parameterized (see Equation 1.2). An example would be when a penetration resistance k shall be compared with different indenter half-angles α. But when the exponent on h of loading curves is used for hardness H, modulus E, or further parameter calculations, the correct exponent $3/2$ should be used (but not 2 as for example at Oliver, [12], and many others). Also the numerous recent plasticity parameters for biological materials in a tutorial of Oyen and Cook [13] were deduced with the unsupported exponent 2

on h, and require urgent correction. Only the correct exponent $3/2$ allows for more advanced important applications that revealed and will reveal unexpected materials' qualities. Some of these are named in the Introduction, others can be found in the cited papers of the present author. Reliable mechanical qualities on the sound physical basis are most important for the proper adjustment of technical and medicinal composites and joints, for safety reasons. This is particularly important in the pressure range for phase changes, the onset of which can only be detected in the loading curves by analysis with the correct exponent $3/2$ on h. It is hoped that all of that will now be acknowledged in teaching, textbooks, and used for technical applications.

ACKNOWLEDGEMENTS

The author sincerely thanks all the physicists and mathematicians, whom he had asked for help with a (then presumed highly complicated) mathematical solution, for their interest and engagement. Furthermore, the author thanks the organizers of the Nanobrücken 2015 and ICM12 conferences in Potsdam, Germany (April 23, 2015) and Karlsruhe, Germany (May 11,2015), respectively, for the possibility to lecture on this deduction of exponent $3/2$.

COMPETING INTERESTS

Author has declared that no competing interests exist.

REFERENCES

1. Wang TH, Fang TH, Lin YC. 2008. Finite-element analysis of the mechanical behavior of $\mathrm{Au/Cu}$ and $\mathrm{Cu/Au}$ multilayers on silicon substrate under nanoindentation. Appl Phys A 90: 457-463.
2. Soare S, Bull SJ, Oila A, et al. 2005. Obtaining mechanical parameters for metallization stress sensor design using nanoindentation. Z Metallkd 96:1262-1266.
3. Kaupp G, Naimi-Jamal MR. 2004. Nanoscratching on surfaces: the relationships between lateral force, normal force and normal displacement. Z Metallkd 95:297-305.
4. Kaupp G, Naimi-Jamal MR. 2013. Penetration resistance and penetrability in pyramidal (nano) indentations. Scanning 35:88-111
5. Naimi-Jamal MR, Kaupp G. 2005. Quantitative evaluation of nanoindents: do we need more reliable mechanical parameters for the characterization of materials? Z Metallkd 96:1226-1236.
6. Kaupp G, Naimi-Jamal MR. 2010. The exponent $3/2$ at pyramidal nanoindentations. Scanning 32:265-281.
7. Kaupp G. 2013. Penetration resistance: a new approach to the energetics of indentations. Scanning 35:392-401.
8. Kaupp G. 2014. Activation energy of low-load NaCl transition from nanoindentation loading curves. Scanning 36:582-589.

9. Kaupp G. 2006. Atomic force microscopy, scanning nearfield optical microscopy and nanoscratching. Berlin: Springer. Erratum: ISBN 978-3-540-28405-5.
10. Kaupp G. The Loading Curve of Spherical Indentions Is Not a Parabola and Flat Punch Is Linear. Advances in Materials Physics and Chemistry. 2019 Aug 30;9(08):141.
11. Kaupp G. 2011. Reactive milling with metals for environmentally benign sustainable production. Cryst Eng Comm 13:3108-3121.
12. Oliver WC. 2001. Alternative techniques for analyzing instrumented indentation data. J Mater Res 16:3202-3206.
13. Oyen ML, Cook RF. 2009. A practical guide for analysis of nanoindentation data. J Mech Behav Biomed Mater 2:396-407.

DISCLAIMER
This chapter is an extended version of the article published by the same author(s) in the following journal.
SCANNING, 1(3): 255-265, 2015.

Chapter 2
Print ISBN: 978-93-5547-921-1, eBook ISBN: 978-93-5547-922-8

Significant Effects of the Exponent 3/2 for Pyramidal and Conical Indentations: New Meanings of Physical Hardness and Modulus

DOI: 10.9734/bpi/mono/978-93-5547-921-1/CH2

ABSTRACT

The now physically founded exponent $3/2$ that governs the relation of normal force to depth$^{3/2}$ in conical/pyramidal indentation is a physically founded $(F_{\mathrm{N}} = kh^{3/2})$. Strictly linear plots obtain non-iterated penetration resistance $k(\mathrm{mN}/\mu\mathrm{m}^{3/2})$ as slope, initial effects (including tip rounding), adhesion energy, and phase transitions with their transformation energy and activation energy. The Sneddon hypothesis fails because it uses the incorrect exponent 2, just like ABAQUS or ANSYS finite element simulations. This is because they ignore long-range effects from shearing. Polynomial fits and "best or variable exponent" iterations for curve fittings, which eliminate all distinctive information from the loading curve, are prior unjustified attempts to explain the absence of exponent 2. Also the ISO 14577 unloading hardness H_{iso} and reduced elastic modulus $E_{\mathrm{r-ISO}}$ lack physical reality. They are redefined to physical dimensions as new indentation parameters H_{phys} and $E_{\mathrm{r-phys}}$. For the first time, only based on loading curves, the physically sound indentation hardness H_{phys} is determined. Additionally, all Sneddon's exponent 2 dependent mechanical indentation parameters are illogical. They need to be redefined in terms of new dimensions. In a recent NIST lesson, this also applies to the visco-elastic-plastic parameters. The current ISO standards lead to a physics conundrum. However, there is a risk involved in applying the incorrect mechanical parameters to physics, and this risk is unstable.

Keywords: Adhesion energy; composites compatibility; first energy law violation; hardness and modulus definition; indentation exponent; physical consequences; penetration resistance; material's failure risk; undue iso-standards; undue tutorial.

ABBREVIATIONS

AFM : Atomic Force Microscopy
CFG : Common Fine Grain
FE : Finite Element

ISO : International Standardization Organization
JKR : Johnson, Kendall, and Roberts technique
NIST : National Institute of Standardization and Technology
PEEK : Polyetheretherketone
PMMA : Polymethylmethacrylate
POM : Polyoxymethylene
UFG : Ultra-fine Grain

2.1 INTRODUCTION

According to ISO 14577, diamond Berkovich indenters continue to be the main standard for instrumental nano-, micro-, and macro-indentations. These standards are based on contradictory mathematical inferences made by Love [1] and Sneddon [2], who claimed proportionality of the applied normal force F_{N} (they called it P) and h^2 for the loading curves (h denotes penetration depth) for all different types of (pseudo)conical indenters (the pseudo cone concept is no longer valid; see chapter 16). The belief that this exists is widely held in publications and textbooks, however experimental loading curves do not support this. Finite element (FE) simulations continue to converge with exponent 2 on h despite the numerous iterative "excuses" for this discrepancy that have been put forth. The published experimental loading curves analyse with exponent 3/2, refuting claims that they would replicate experimental loading curves [3,4]. In that situation ISO 14577 concentrated on the iterative analysis of the unloading curve with freely iterated exponent on h (between 1 and 3) for gaining values of indentation hardness H_{ISO} and reduced elastic modulus $E_{\mathrm{r-ISO}}$. Such iterations are with respect to standard materials and projected area A_{hc}. Analyses (rather than fitting) of F_{N} versus $h^{3/2}$ plots of published loading curves in the literature (and of own ones) starting from 2000 by the present author [5] validated the exponent $3/2$ by linear regression with excellent correlation coefficients of at least $r > 0.999$ and in less noisy cases $\mathrm{r} > 0.9999$ for the materials penetration resistance $k\left(\mathrm{mN}/\mu\mathrm{m}^{3/2}\right)$. Nevertheless, this met with severe difficulties from anonymous referees for being supported and published, as these claimed to consistently find "exponent 2" on h. But analysis for exponent 2 or $3/2$ is a matter of some minutes with Excel®, provided correct experimentation. Liability facts and unexpected applications with precise calculation were hardly appreciated. Only the correct analysis (Eq. 2.1) with excellent linear regression reveals surface effects (including tip rounding), influence of tip angle and radius on k, gradients, mechanical pretreatment, alternating layers, elbows, nanopores, phase transitions under load, transition energies, activation energies, and correct adhesion energies, all by simple mathematics without iterations (Eq. 2.1) [4,6-9].

$$F_{\mathrm{N}} = kh^{3/2} \tag{2.1}$$

The constant $k\left(\mathrm{mN}/\mu\mathrm{m}^{3/2}\right)$ is the penetration resistance, a materials property that is obtained with the highest precision in the (nano) indentation experiment, rather than multi-iterated hardness, reduced modulus, etc. After the recent physical foundation of the exponent $3/2$, giving the explanation why it must be

so, by considering both the simultaneous volume-formation and the thereby created total pressure with elementary mathematics [10], the physical law (2.1) is additionally enforced beyond any doubt and cannot be denied any more. Some updates in the bioarea are available elsewhere and may find attention of the readers [11-13]. We must herewith point out the necessity of using this new state of the art for removal of the dilemma between ISO 14577 and physics (for undue NIST tutorial from 2009) for all mechanical parameters that rely on h^2. They must be re-defined, and all the corresponding mechanical data require correction. Also the critics of three different working groups on the exponent $3/2$ on h [14] (before its physical deduction) deserves retraction: the self-similarity of conical/pyramidal indenters is by no means a "straightforward proof" for the unsupported exponent 2 on h, but it violates the basic energy conservation principle.

2.2 MATERIALS AND METHODS

A fully calibrated Hysitron Inc. TriboScope® Nanomechanical Test Instrument with a two-dimensional transducer and leveling device in load control mode was used for the author's nanoindentations after due calibration, including instrument compliance. The radii of the cube corner $(55\ \mathrm{nm})$ and Berkovich $(110\ \mathrm{nm})$ diamond indenters were directly measured by AFM in tapping mode. Three-dimensional microscopic inspection of the indenter tips secured smooth side faces of the diamonds for at least $2\mu\mathrm{m}$ from the (not resolved) apex. The samples were glued to magnetically hold plates and leveled at slopes of $\pm 1°$ in x and y directions under AFM control with disabled plainfit, and loading times were $10-30\ s$ for $400-500$ or 3000 data pairs [4]. The whole data set of the loading curve was used for analysis, using Excel®. Most analyses were however with published loading curves from the literature, as rapid sketches with pencil, paper, and calculator (10-20 data pairs), but for linear regressions always by digitization to give 50-70 almost uniformly arranged data pairs using the Plot Digitizer 2.5.1 program (www.Softpedia.com), unless complete original data sets could be obtained from the scientists. The precise kink positions were obtained by equating the linear branches before and after the phase change, and precise axis cuts from the regression lines. It was tried to cover all different materials types, all different indentation modes, equipments, response mechanisms, depth ranges, penetration resistance sizes, from numerous authors from all around the globe. Only the experimental curves are relevant, not the simulated ones.

2.3 RESULTS AND DISCUSSION

Information loss by finite element simulations, beliefs, polynomial fittings, and exponent iterations

Finite element simulations of loading curves (ABAQUS or ANSYS, etc.) consistently converge with the exponent 2 on h (e.g. [3]). There is thus never match with experimental results. However, there are claims that microindentations would require "exponent 2". For example, Oliver and Pharr [15] depicted in 1992 deep non-discussed Berkovich microindentation loading curves

of soda lime glass, sapphire, fused quartz, and α-quartz (001) up to $120\mathrm{mN}$ load, for obtaining unloading curves for hardness and elastic modulus iterations. But the former were not focal for that paper on unloading curves. All of these "loading curves" analyze with the impossible F_N versus h^2 relation, but experimental curves from various authors (including WC Oliver) go with $h^{3/2}$ (including those with phase change kink), as for example analyzed in $[4{,}16]$. I apologize for having believed in their validity in $2005/6$ [17]. There is, however, no exponential differences between nano- and micro- or macro-indentations (as long as these proceed properly with smooth tips and without cracks). All of these loading curves obey Eq. (2.1) $[4{,}6{,}8]$. It is thus not clear why the loading curves in [15] analyze with the (now disproved) Love/Sneddon exponent. Importantly, only the correct exponent could reveal the phase change of the standard fused quartz for H and E_r iterations at about $2.5\mathrm{mN}$ load [4,16].

The polynomial fitting $(F_N = c_0h^2 + c_1h + c_2)$ for the total loading curve [18] has been widely applauded. But it provides no information about initial effects, gradients, or phase transformations at all, and polynomial fittings are unreliable in view of linear regressions. Furthermore, iterated parameters c_0 and c_1 are often used to calculate exceedingly large "effective tip radii"(disproved in Chapter 16) up to $3.3\mu\mathrm{m}$ (for example for a Vickers with $68°$ semi-angle Θ that is close to the one of Berkovich at $65.3°$), depending on the yield-strength/modulus ratio [18]. However, blunt Berkovich tip radii range from 150 to $300\ \mathrm{nm}$. Such uncredible polynomial fitting parameters, are being used as an excuse for not obtaining the believed exponent 2 at the expense of linear regression with the physical exponent $3/2$. Importantly, properly executed experimental loading curves are required for exponential analyses. This implies indenters with flat side-faces, vertical (not tilted) indenting onto homogeneous materials with plain surfaces that must not be influenced by nearby impressions, or too close sample edges or sample borderlines, in order to avoid strange results with spurious too large exponents up to > 1.5 or even > 2. Unfortunately, leveling equipment for skew surfaces (with AFM precision check) often lack in commercial nanoindentation instruments. Nevertheless, measurements with blunt Berkovich $(R \approx 300\ \mathrm{nm})$ giving unusually long initial effects were tried to "discredit" the exponent $3/2$ with the F_N versus $h^{3/2}$ plot of fused quartz in Fig. 2.1 [19]. However, this plot confuses the 3 initial-effect points with the not considered straight line through the points # 4-17 at the actual kink position where the steeper second linear branch starts. Rather, the authors absurdly intersect a line through points $\#\ 1-3$ with the extrapolated second straight line from point17 onwards. Such intersection is far away from the plot. The false claim is then made that "Kaupp" would also have intersected with initial effect points at his analyses of the same material in $[4{,}16{,}17{,}20]$. However, Kaupp has always excluded initial effects at his regressions, and he provided obvious reasons for their occurrence. The actual kink (k_1 and k_2 lines) is at about $3.4\mathrm{mN}$ and $195\ \mathrm{nm}$. This is not too far away from the values for the known sharp Berkovich indents (2-2.5 mN and 120-160 nm) $[4{,}16{,}17{,}20]$ at very minor initial effects. The experimental data printed curves of [16] are therefore supporting but not at all "discrediting" the exponent of Eq. (1), if considering the unusually extended initial effect range (axis cut of the k_1 line at about $-1.2\mathrm{mN}$; not drawn in [13]) at this indentation. Nevertheless, the

authors in [13] deny their obvious support of $h^{3/2}$. Rather they undertook exponent fittings with $\mathrm{F} = \mathrm{kh}^{\mathrm{n}}$ (not italicized for distinction from physical k values) for varying depths onto fused quartz for proposing varying depth/exponent and depth $/\mathrm{k}$ relations. They refrain from indicating the dimensions of the so obtained variable proportionality constants. The published data sequence for different final depths onto fused quartz is as follows [19] (only the dimensions are now added): Up to $40\ \mathrm{nm}$ depth, $\mathrm{n} = 1.5, \mathrm{k} = 0.99411\ \mathrm{mN/nm}^{1.5}$; upto $60\ \mathrm{nm}, \mathrm{n} = 1.64533, \mathrm{k} = 0.61897\mathrm{mN/nm}^{1.64533}$; upto $80\ \mathrm{nm}, \mathrm{n} = 1.75285, \mathrm{k} = 0.41377\mathrm{mN/nm}^{1.75285}$; upto $300\ \mathrm{nm}, \mathrm{n} = 1.82723, \mathrm{k} = 3.00003\mathrm{E} - 4\mathrm{mN/nm}^{1.82723}$ for the overall curve [19]. It does not help to compare with FE simulations including further parameters. All of that is physically unsound and totally meaningless, but obviously not recognized by the authors, referees, and editors [19]. Clearly, one was not willing to recognize specific properties of materials under loading stress and strangely strived for concurring with the disproved Sneddon theory. The exponent on h is with mathematical precision $3/2$ and the dimension of k is (force/length$^{3/2}$) [10]. Minimal deviations are experimental errors. Initial effects (including tip rounding contribution) are quite common, and phase transitions upon indentation loads prior to macroscopic cracking are frequent. These are important properties!

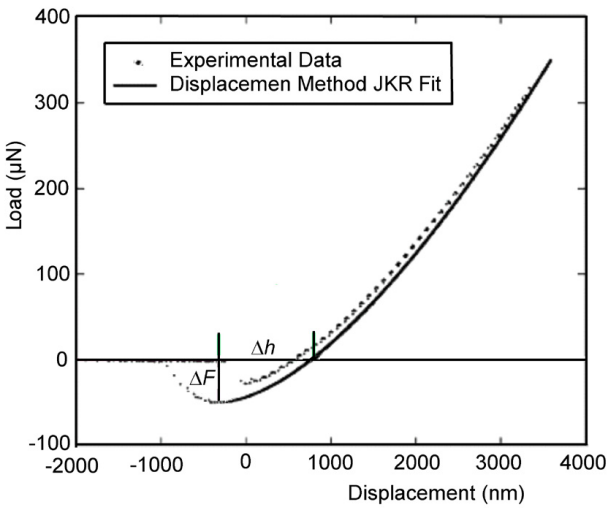

Fig. 2.1. Load (dotted) and JKR fitted unloading curve (full) on PDMS from a spherical indentation with radius of $192\mu\mathrm{m}; \Delta F = 48.73\mu\mathrm{N}; \Delta h = 1.0603\mu\mathrm{m}$ [6] (cf Chapters 9 and 13)

Different iteration induced flaws, provides the JKR (Johnson, Kendall, and Roberts) treatment of adhesion forces, even though these iterations start with the Hertzian exponent $3/2$ for spherical tips or rounded AFM cantilevers. However, based on the penetration resistance k the $+166\%$ error of the JKR-adhesion work is easily revealed both from indentations and AFM force curves. This has first been described in [6] and is another important application of Eq. (2.1). Both

curves (loading and iterated unloading) in Fig. 2.1 strictly follow Eq. 1 as well. Thus the full gained adhesion work (determined as pulloff work) is calculated by the triangle area, as described by ΔF and Δh, of the unloading curve giving the absolute value for $W_{\mathrm{pulloff}} = 0.5\ \Delta F \Delta h = 25.8342 \mu\mathrm{N}/\mu\mathrm{m}$. The published JKR treatment reported the $\Delta\gamma$ -value (that is called a basic JKR-formula) as $\Delta\gamma =$ "$2F_{\mathrm{adhesion}}(h)/3\pi R(h)$ ", where $R = 192\mu\mathrm{m}$ is "the radius of curvature of the tip, and the reported $\Delta\gamma$ is $0.05389\mu\mathrm{N}/\mu\mathrm{m}$, which is dimensionally a force constant, but it can also be interpreted as work over area by extension of the formula, as indicated by the bracketed h. By division of the absolute W_{pullof} value from our not iterating ENERGY technique [6] by the calotte surface of the spherical tip $(2\pi Rh)$ one obtains $W_{\mathrm{adh}}/$ area $= 0.5\ F_{\mathrm{adhesion}}\ h/2\pi R\ \ h = 0.02020\mu\mathrm{N}/\mu\mathrm{m}$, now with the same dimension for comparison with the JKR $\Delta\gamma$. We immediately see from the quoted $\Delta\gamma$ formula that JKR divides 4 times the work over 1.5 times the area, instead of ENERGY technique's correct work/area. The mathematically exact error of JKR calculates therefore from the wrong numerals $2/3$ in its "basic formula" instead of $0.5/2$. The ratio $2/3$ over $05/2$ is $8/3 = 2.6667$. This corresponds to a JKR error for $\Delta\gamma$ of $(8-3)100/3 = +166\%$ that is nicely confirmed by the numerical data: $0.05389/0.02020 = 2.66716$. This huge JKR error is particularly detrimental, as it also occurs (with the same 166% error) in AFM force-measurements (a typical example is presented in [6]) and that these $\Delta\gamma$-values are used for the "determination" of reduced elastic modulus values according to the JKR formula $E = 9\pi R^2 \Delta\gamma / 2\mathrm{a}^3$ that are thousand-fold "determined", used, and tabulated, particularly with soft medical/biological samples. There must be correction of all the tabulated elastic moduli from JKR-adhesion work.

Particularly strange are suggestions to deny the universal exponent $3/2$ on h, and the unexpected practical applications of Eq. (2.1), but to base the exponential analysis on FE simulations [14]. The authors from the three research groups do not separate out the initial surface effects and deny often occurring phase transformations, obviously because the search for them is impossible with FE simulations. It is unscientific to use fitted data or FE-simulated curves that converge to h^2, and to recalculate these for $\mathrm{h}^{3/2}$ with the aim to discredit the experimental (now physically founded [10]) exponent $3/2$, because such treatment inevitably gives bent curves. Such a "treated" curve was used for drawing tangents at the start and the end in Fig. 2.2 of [14] that intersect far away from the plot, for designing a false discrediting term called "Double $P - h^{3/2}$ fit after Kaupp et al." [14]. However, Kaupp et al. do not fit treated data but are analyzing experimental loading curves according to the physically deduced universal Eq. (2.1) [10], Chapter 1 to uncover individual properties (e.g. phase change yes or no) that are wiped out by data fittings or simulations as in [14,19]. It is unclear, where the data of [14] in opposition to physics [10] and to the published ones came from, and who did the calculations for fused quartz up to $300\mathrm{mN}$ load on what assumptions. The polynomial or FE correlations (Table 2.1) [14] are not helpful (for example phase changes are unavoidable for the partially crystallized POM and PEEK thermoplastics or compacted Al). Fig. 2 in [14] report either very different exponents (1.6 to 2.15 between 200 and $1300\ \mathrm{nm}$ depth) in

different loading ranges, or a "constant exponent 2 " for the linear P versus h^2 plot, respectively: a very severe discrepancy! And the above reference [19] is invoked with its unintentional support of Eq. (2.1) and the phase transition of fused quartz. Furthermore, earlier experimental loading curves of the author K Durst et al. [4] (e.g. spruce or UFG and CFG Fe), as analyzed in Fig. 2.2, precisely follow Eq. (2.1) with sharp kinks at $0.53, 0.87, 27.5$, and $40.9\mathrm{mN}$ load.

Penetration resistance reveals phase transformations

When within the loading range of the linear plot a sudden sharp kink discontinuity occurs, this is the onset of a phase change under load (numerous images for fused quartz and all types of materials [4,16,17,20]. This is one of the reasons for errors that have not been addressed with H_{ISO} and $E_{\mathrm{r-Iso}}$ determinations. Only properly analyzed loading curves (Eq. 2.1) detect or exclude (Table 2.1) and plots in [4] phase changes of all kinds (not only structural transitions), but neither exponent fittings nor present FE simulations can do so. Phase changes occur with many materials already in the nanoindentation range. Only rarely and exceptionally were phase transitions concluded from "elbows" in unloading curves, but then without any transition-onset information. A widely studied example, also with more advanced techniques, is silicon (Chapter 8). Original material is characterized by the penetration resistance k_1 before the kink in linearized loading curves. After the kink the k_2-value is obtained for transformed material in a matrix of the original one [4]. It provides an important bargain when both k_1 and $k_2\left(\mathrm{mN}/\mu\mathrm{m}^{3/2}\right)$ are known: The transition energy [6], and temperature dependent also the activation energy of the transition are revealed [7]. When the onset of phase changes is not uncovered, there is often a risk that such transition-onset has occurred before the applied load. Clearly, not detected phase changes bear a high risk for materials' failure upon aging under load and heat stress, when the mechanical load at the given temperature surpasses the transformation onset, for example with alloys, or ceramics, and other composites. Such failure upon impact can grow-up to disasters. Already that urges the correction of the corresponding ISO-standards as soon as possible.

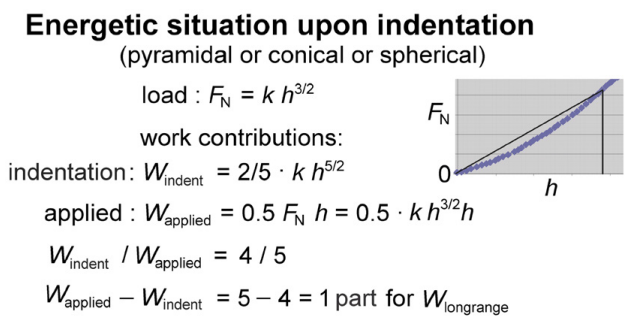

Fig. 2.2. Deduction of the long-range work energy upon pyramidal/conical indentations

Hardness and modulus

ISO 14577 uses the unloading curve for iteratively obtaining the hardness H_{ISO} with respect to standard materials (mostly fused quartz, or Al) with freely iterated exponent $(\mathrm{m}: 1-3)$. These iterations converge with respect to the standard material of "known" mechanical properties. However, the standard materials have in most cases different surface effects, and both undergo widely ignored phase transitions after their onset discontinuity (fused quartz in the nano-, aluminum in the microindentation region) [4,16].

The main objection of referees against Eq. (2.1) was the definition of the universal hardness (Martens hardness) as normal force over projected area $A_{\mathrm{proj}} = \pi h^2 \tan\alpha^2 (\alpha = 70.2996^\circ \text{ of Berkovich})$ (Eq. 2.2) with unit $\mathrm{mN}/\mu\mathrm{m}^2 = \mathrm{GPa}$. This covers the volume of ani nverted pyramid or (real) cone) $A_{\mathrm{proj}}\ h_{\max}$. But Eq. (2.2) is undue, as it implies the false " $F_{\mathrm{N}} \propto h^{2"}$ as in Eq. (2.3). But we write here the complete definition of $H_{\text{universal}}$ with incorrect eqn. (3) to open a chance for perhaps correcting the frequent publications that use it (cf eqn (6) that relies on (1)).

$$H_{\mathrm{universal}} = F_{\mathrm{Nmax}}/A_{\mathrm{proj}} \tag{2.2}$$

$F_{\mathrm{Nmax}} = \pi\ R^2 H_{\mathrm{universal}}$ and $R/h = \tan\alpha$ would give "$F_{\mathrm{Nmax}} = \pi h^2$ $\tan\alpha^2 H_{\mathrm{universal}}$ (2.3)

ISO uses normal force over contact area A_{hc} (effective $\pi\mathrm{R}^2$) as opposed to the cone area $(2\pi\mathrm{R}^2/\tan\alpha)$. Thus the covered volume is meant as the tube $A_{\mathrm{hc}}h_{\max}$ or $A_{\mathrm{hc}}h_{\mathrm{c}}$. But physics [6] beats definitions. The "contact height" h_{c} is defined with reference to the standard at peak load Eq. (4), where $\varepsilon = 0.75$ is an accepted but also debated dimensionless geometric factor, and S is unloading stiffness $(\mathrm{mN}/\mu\mathrm{m})$, the unloading slope at peak load. The iterative determination of H_{ISO} fits to the generally unrelated fused quartz that experiences some sink-in $(h_{\mathrm{s}} = h_{\max} - h_{\mathrm{c}}$, depending on the indenter) for A_{hc} at peak load. The iteration requires $F_{\mathrm{N}} = B(h_{\max} - h_{\mathrm{f}})^{\mathrm{m}}$ where B, h_{final} and exponent m (between 1 and 3) are freely iterated for the fitting down to 20% or eventually 50% of F_{Nmax} which is also troublesome indeed [17,20]. S at peak load is then obtained by differentiation $\left[S = B\ \mathrm{m}(h_{\max} - h_{\mathrm{f}})^{(\mathrm{m}-1)}\right]$ to obtain h_c, for the calculation of $A_{\mathrm{hc}} = 3^{3/2} h_{\mathrm{c}}^2 \tan^2\theta = 24.56 h_{\mathrm{c}}^2$ as a first guess for Berkovich $(\theta = 65.3^\circ)$ indentations. H_{ISO} is then iterated according to Eq. (2.5). Thus, H_{ISO} (Eq.2.5) also implies an $F_{\mathrm{N}} \propto h_{\mathrm{c}}^2$ relation, which is against physics as is Eq. (2.3), both violating the physically founded Eq. (2.1) [10] that is also valid for F_{Nmax} of course. Furthermore, any sink-in or pile-up is part of the energy requiring long-range effects.

$$h_{\mathrm{c}} = h_{\max} - \varepsilon F_{\mathrm{Nmax}}/S \tag{2.4}$$

$H_{\mathrm{ISO}} = F_{\mathrm{Nmax}}/A_{\mathrm{hc}} = F_{\mathrm{Nmax}}/\left(24.5 h_{\mathrm{c}}^2 + C_1 h_{\mathrm{c}} + C_2 h_{\mathrm{c}}^{1/2} + C_3 h_{\mathrm{c}}^{1/4} + \cdots + C_8 h_{\mathrm{c}}^{1/128}\right)[\mathrm{mN}/$ μm2 (2.5)

Rather strange trials to "save" h^2 and thus A_{hc} for the hardness iterations are still invoking the trivial "self-similarity" of conical or pyramidal indenters for claiming " $A_{\mathrm{c}} \propto h^2$ " and " $H = P/A_{\mathrm{c}}$ " (*P* stands for F_{N}) [14]. Such assertion is surprising since it is amply known and discussed, that the shear-force from the cone or pyramid produces far-reaching phenomena to the sides and below the defined tube volume (these include sink-in or pile-up, plastic deformation, elastic stress, rosettes, shear-bands, and so on) [6]. Such long-range processes convert or store energy that is lost for the impression. The denial of such loss inexcusably violates the basic first energy law (applied work = produced work/energy): Equation (1) and simple algebra deduce that precisely 20% of the applied work (for all materials) is used for the sum of long-range effects and lost for the indentation depth [6-10]. The energy loss for the penetration as deduced in [6], is summarized in the basic Fig. 2.2. The experimental loading curve follows $F_{\mathrm{N}} = kh^{3/2}$ (Eq. 2.1) in all cases, also the spherical ones and the indentation work is obtained by integration to give $W_{\mathrm{indent}} = 0.4kh^{5/2}$. This compares with the linearly applied work (area of the triangle up to the chosen depth h), which amounts to $W_{\mathrm{applied}} = 0.5F_{\mathrm{N}}, h = 0.5kh^{5/2}$ by substitution of F_{N} . It is thus arithmetically clear, that precisely 20% of the applied work is lost for the indentation work due to the sum of long-range work contributions [6]. This is therefore valid for all materials and mechanisms (e.g. elastic and plastic deformations, material's migrations, sink-in, pile-up, viscous flow) for all pyramidal/conical properly executed indentations, when detectable initial surface effects (that also contain tip rounding effects) are corrected for. In the case of sharply detected (kink in the plot of Eq. 2.1) phase change onset (endo- or exo-thermic), a second energetic term that includes the transition energy is calculated accordingly [6]. Both W_{indent} and $W_{\mathrm{longrange}}$ require their part from the normally applied force F_{N}, mathematically at an always constant ratio [6]. Thus, Eq. (2.2) (universal hardness) and (2.5) (ISO-hardness) violate not only the physically founded indentation law (1) but both hardness definitions also violate the first energy law, because they do not take into account that part of F_{Nmax} that is lost for 20% of the work. They have been doing so for half a century.

2.

In order to stay within the energy law it is not necessary to care for a definition of ensuing "lengths" for the long-range work. The change of the ISO 14577 hardness H_{ISO} has to occur in such a way that the $F_{\mathrm{N}} \propto h^{3/2}$ relation (Eq. 2.1) and thus the first energy law are not violated. The same is necessary for $H_{\mathrm{universal}}$. The dimensionable redefinition of $H_{\mathrm{universal}}$ or the previous ISO-hardness, is thus by multiplication of F_{Nmax} / $A_{\mathrm{projected}}$ (or $F_{\mathrm{Nmax}}/A_{\mathrm{hc}}$) with $h_{\mathrm{max}}^{1/2}$ (Eq.2.6). But iteration-free is H_{phys} = k (the penetration resistance). Since sink-in and pile-up effects do not influence the exponent [10], the H_{phys}-values (that do not longer depend on a standard) do not require A_{he}, and the universal $F_{\mathrm{N}} \propto h^{3/2}$ relation and the first energy law are obeyed by taking into account the long-range losses (long-range energy that requires part of the applied force) (Eq. (2.7). The dimension of physical indentation hardness H_{phys} has thus the units $\mathrm{mN}/\mu\mathrm{m}^{3/2} = \mathrm{GPa}\mu\mathrm{m}^{1/2}$, the same as the dimension of penetration resistance k in Eq. (2.1). By considering the first energy law [6] we obtain (2.7) with (2.1) and have therefore

both a precise and simple way to obtain the physical indentation hardness H_{phys} (2.6), and also directly from conical or pyramidal indenters' loading curves the indentation work W_{indent} Eq. (2.7). It follows from Eq. (2.1) (that is also valid for F_{Nmax}) that only the loading curve is

$$H_{\mathrm{phys}} = F_{\mathrm{N}}/h^{3/2} \tag{2.6}$$

$$W_{\mathrm{indent}} = 0.8\ W_{\mathrm{applied}} \tag{2.7}$$

required for H_{phys}. Eq. 2.(6) with the dimension of the penetration resistance k, opens an easy and simple way to obtain the physically deduced hardness $H_{\mathrm{phys}}(\mathrm{mN}/\mu\mathrm{m}^{3/2})$ *and* $W\mathrm{indent}\ (\mathrm{mN\mu m})$,without iterations, only from the loading curve with the unbeatable penetration resistance k_1 (before the kink) by linear regression. The tip rounding initial effect is not part of the linear regression of the penetration resistance (but it plays a role for adjustments between different pyramids/cones [4,21]). For the first time, this new technique controls the final load below any phase transition onset. The precise technique makes obsolete the iterative determination of a "contact area", and undue experiments (e.g. tilted, too tight with others, etc.) are easily detected. Unfortunately, conversions of previous $\mathrm{H_{ISO}}$ into H_{phys} values are not easy due to the various iterations within the ISO-treatment, but H_{univeral} does not have iterations due to totally different standard. The h_{max} values would however require the loading curves or original data. The correction of indentation $H_{\mathrm{universal}}(\mathrm{GPa})$ into $H_{\mathrm{phys}}(\mathrm{GPa}\mu\mathrm{m}^{1/2})$ works by

a) isolaton of h_{max}^2 : $H_{universal}\,\pi\tan^2/F_{\mathrm{Nmax}} = 1/h_{\mathrm{max}}^2(\mathrm{mN}/\mu\mathrm{m}^2$; non physical); H_{ISO}known, F_{Nmax} must be known;
b) calculation for $h_{\mathrm{max}}^{3/2}$: $H_{\mathrm{phys}}\pi\tan\alpha^2/F_{\mathrm{Nmax}} = 1/h_{\mathrm{max}}^{3/2}(\mathrm{mN}/\mu\mathrm{m}^{3/2}$; physical); H_{phys} can be calculated, when F_{Nmax} is known.

The results are exemplified in Table 2.1 from a paper [3] that published both experimental loading curve and finite element simulation loading curves far below of a phase change onset. One remarks considerable differences between H_{ISO} (from unloading curve with excessive iterations of aluminum on silicon for fitting with the ISO standard). Importantly, it is easiest to correct finite element H-values, because the unphysical exponent 2 cancels out by the correction with $h_{\mathrm{max}}{}^{1/2}$ and H_{phys} and simulated $\mathrm{H_{corr}}$ are so quite similar. However such good correspondence is only possible when absence of phase change onset is experimentally secured at $\mathrm{h_{max}}$, which finite element simulation cannot predict or exclude. The necessary k and k' values must still be determined from loading curves (Eq.2.1 or analogous for simulated k' with different dimension).

Similar to H_{ISO}, the definition of the modulus $E_{\mathrm{r-ISO}}$ contains A_{hc}, which does not comply with the long-range effects at peak load, is against physics. A quantitative connection to the penetration resistance k of the loading curve is however lost, because the unloading slope is needed for $S(\mathrm{mN}/\mu\mathrm{m})$. Also here, peak load must be below any kink load in the linearized loading curve (Eq. 2.1), in order to study

the pristine material. It follows for both reasons that $E_{\mathrm{r-ISO}}$ values of indentations are not appropriate, because they also violate physics by neglecting the energy consuming shearing effects.

The correction of indentation $E_{\mathrm{r\text{-}ISO}}$ (GPa) into $E_{\mathrm{r-phys}}\left(\mathrm{GPa}\ \mu\mathrm{m}^{1/4}\right)$ works by

(a) isolation of $h_{\max}^2$: when $E_{\mathrm{r-ISO}}$ is known; $h_{\max}$ and reliable S before phase change onset must also be known;

(b) calculation for $h_{\max}^{3/2}$: $E_{\mathrm{r-phys}}$ can be calculated, when $h_{\max}$ and reliable S are known.

The application of non-physical H_{ISO} and non-physical $E_{\mathrm{r-ISO}}$, as well as from these derived further mechanical parameters in theoretical and practical mechanics, bears high risks for materials' performance and must be stopped. Tabulated materials' properties must become reliable for artificial intelligence AI and for centuries. Therefore, the most precise and undeniable penetration resistance k, H_{phys}, and $E_{\mathrm{r-phys}}$ should be urgently used for the characterization of materials and the compatibility of different materials, including solder etc. [8,9].

Undue tutorial parameters

All "Sneddon theory"-derived mechanical indentation parameters rely directly or indirectly on the presumed incorrect " $F_{\mathrm{N}} \propto h^{2"}$ relation. This is exemplary demonstrated with some of the incorrect parameters that ensue. For example, NIST authors [22] published a tutorial in 2009 , as based on their earlier publication [23], with the erroneous deduction of six "viscous-elastic-plastic mechanical parameters". The authors used their loading-rate dependent Berkovich indentations onto PMMA and claimed that all of their published curves [22,23] would obey the Sneddon exponent 2 on h. But NIST could have easily found out that their loading curves of PMMA with a sharp Berkovich indenter fantastically support the universal F_{N} versus $h^{3/2}$ plots (Eq. (1)) with excellent straight lines for all of their loading rates from zero to their very deep penetrations (down to maximal depth of $6.5\mu\mathrm{m}$), within less than $10\ \mathrm{min}$, and with excellent linear regression. So NIST missed the validity of exponent $3/2$ instead of 2 . Rather, starting with the non-supported equations " $F_{\mathrm{Np}} = \alpha_1 H h_{\mathrm{p}}^{2"}$ and " $F_{\mathrm{Ne}} = \alpha_2 E_{\mathrm{r}} h_{\mathrm{e}}^{2"}$ (sub-p for plastic, sub-e for elastic) and after various steps (with inclusion of a "quadratic viscous element") they defined thus six incorrect mechanical parameters:

"$\mathrm{y} = (\alpha_1 H/\alpha_2 E_{\mathrm{r}})^{1/2"}$ as "indentation plastic yield resistance",
" $d = 3\tau/2t_{\mathrm{r}}$ " as "indentation viscous flow resistance" (with t_{r} as rise time), and the double logarithmic plot of y versus d was termed "indentation behavior map",
"1/*e* = 1 + 1/*y* + 1/*d*" (with *e* as "elastic fraction"),
"$H = F_{\mathrm{Nmax}}\, y^2/h_{\mathrm{max}}^2\ \alpha_1\ e^{2"}$, and "$E_{\mathrm{r}} = F_{\mathrm{Nmax}}/h_{\mathrm{max}}^2\ \alpha_2\ e^{2"}$.

There is no experimental or physical basis for that and these papers from NIST (a prominent ISO member) require urgent retraction (after the successful physical deduction of Eq. (2.1) [10]). It is to be expected that a tutorial from representatives of the US-agency, which is responsive for standardizations with close to legal character, will be largely understood as a "state-of-the-art". But it is against physics. Therefore, an enormous risk has been arisen with this "tutorial" that has already been widely taught and used to produce and tabulate wrong data, with the potential of doing harm primarily to biology and medicine, but also to all further research on (nano) mechanics.

Furthermore, all the other textbook mechanical indentation parameters that directly or indirectly rely on h^2 require re-deduction, by starting with the physically correct exponent $3/2$, and it has always to be considered that their dimensions will unavoidably change. The indentation experiment is now a quantitative technique on the basis of the new physics with the penetration resistance k, the inverse of which has been called penetrability [4]. The easily obtained penetration resistance, detects phase transition onset and conversion energy as well as activation energy, etc. and it provides detection of physically correct indentation hardness H with correct dimension, all from the loading curves without iterations or simulations.

Table 2.1. Comparison of an experimental unloading curve H_{ISO} of Al on Si with loading curve H_{phys} and ANSYS finite element simulated corrected or uncorrected H-values from [3]

Technique	h_{max}^{n}	*k* or k'[(a)]	Basis	Hardness only from the loading curve (not H_{ISO})
Experimental with $h_{max}^{1/2}$ factor	$h_{max}^{3/2}$	k = 7.4425 (mN/μm$^{3/2}$)	$F_N = kh^{3/2}$	$H_{phys} = k/\pi\tan\alpha^2$ = 0.30373 (mN/μm$^{3/2}$)independent on F_N and h_{max} (before phase change)
Experimental no correction	$h_{max}^{3/2}$	k = 7.4425 (mN/μm$^{3/2}$)	$F_N = kh^2$ wrongly	H_{ISO} = 0.761; $H_{univ} = k/\pi\tan\alpha^2$ = 0.60745 (mN/μm^2) $k + h_{max}^{1/2}$ are needed for correction (value + dimension)
Finite element no correction	h_{max}^{2}	k' = 4.7433 (mN/μm^2)	$F_N = k'h^2$	$H_{uncorr} = k'/\pi\tan\alpha^2$ = 0.60167 (mN/μm^2) false dimension, multiply with $h_{max}^{1/2}$ when available
Finite element with $h_{max}^{1/2}$ factor	h_{max}^{2}	k' = 4.7433 (mN/μm^2)	$F_N = k'h^2$	$H_{corr} = k'h_{max}^{1/2}/\pi\tan\alpha^2$ = 0.30083 (mN/μm$^{3/2}$) (k' with dimension mN/μm^2, must be determined)

(a) simulated parameters are not italicized; these entries rely on the bona-fide believe in the pseudo-cones for pyramids and would falsely assume that these values were obtained from real cones with their alpha half angles, cf Chapter 16

2.4 CONCLUSION

The recent physical foundation of the universal exponent $3/2$ on pyramidal/conical indentations enforces appreciation of the abundant empiric results, and that has important consequences. Thus, the ISO 14577 indentation hardness H_{ISO}, the reduced elastic modulus $E_{\mathrm{r-1SO'}}$ and the there from deduced

mechanical parameters must be urgently corrected in dimension and value, to provide the physically sound $H_{\mathrm{phys}}, E_{r-\mathrm{phys}}$, and there from deduced parameters. Their perhaps odd appearing dimensions are the peculiarity of indentations with pyramids and cones, applying both normal force and lateral force at the same time. The present ISO definitions rely on a wrongly proposed [1,2] "$\mathrm{F} \propto \mathrm{h}^{2}$" relation and thus also on the undue reference to "projected area $\mathrm{A_{hc}}$ ". Its application does not consider the far-reaching shear-force effects outside the $A_{hc}h$ object and is thus violating the basic first energy law. Physically sound hardness is now for the first time obtained from the loading curves without iterations or simulations by only using simple algebra, and H_{phys} is now a genuine physical parameter. Also all other mechanical parameters for pyramidal and conical indentation that rely directly or indirectly on disproved " h^{2}" from the loading curves require redefinition and re-determination by using $h^{3/2}$ instead of " h^{2}" . The almost universally published wrong mechanical parameters from indentations and AFM force curves constitute high risks that are often adopted and defended, subject to change. The large errors caused by the wrong exponent are exponential dependent, not proportional. Any non-appreciation of the physical exponent is at risk for the stability of incorrectly-calculated composite materials and solders, as for example implanted endo-prostheses (mechanical adjustments to the actual bones of the composite, "bone cements", alloys, composite ceramics, coatings, and inlays, adhesion energies etc.), or composed materials of daily life (for example longevity of turbines, cars, airplanes, medical implants, etc.). Wrong parameters against physics (values and dimensions) must be adjusted to avoid cracking and failure, when materials are under mechanical and thermal stress. It is the penetration resistance $k(\mathrm{mN}/\ \mu\mathrm{m}^{3/2}\ )$ of the components that must closely be adjusted to coincide for the applied force and temperature ranges. Of particular importance are the now easily recognized phase changes under load as detected by the onset of sharp kink discontinuities in the F_N versus $h^{3/2}$ plots that must always be considered. Different components have their transitions at different pressure and different temperature onsets. Thus, their now also available transformation- and activation-energies require the capabilities of the penetration resistance $k\left(\mathrm{mN}/\mu\mathrm{m}^{3/2}\right)$. This should help in adjusting the components of mechanical and thermal stressed super alloys with their grains and domains that must be optimized, etc.

Textbooks must be rewritten, new dimensions of mechanical indentation parameters accepted. This is a tremendous task, because all mechanical parameter's dimensions become different. For spherical indentations $h^{3/2}$ is long iteratively used, but please do not use JKR technique with 166% error. Thus, both the Hertzian-type $\left(h^{3/2}\right)$ and Sneddon-type (h^{2}) analyses that are offered to choose from at some instrumental AFM-software require correction or cancellation of $\mathrm{H_{ISO}}$, $\mathrm{E_{r-ISO}}$, $\mathrm{E_r}$, and all mechanical parameters that are derived from $\mathrm{false}\, h^{2}$ exhibit huge systematic errors after very complicated data treatments with iterations, simulations, and approximations. Fortunately, the now available physics detects iterative data-fittings and allows for precise algebraic data evaluation. Nobody in the field can reasonably continue proceeding against basic physics. The numerous unexpected possibilities with quantitative

indentation loading (or AFM force-curves' scanning) must be pursued on the available easy and precise algebra. Further unexpected applications are expected by the measurement of penetration resistance, $H_{\mathrm{phys}}, E_{\mathrm{rphys}}, W_{\mathrm{adh}}$, and mechanical phase transformation onsets with energies of transformation and energies of activation.

ISO and its member NIST cannot abruptly but only considerately change their standards, because all academic and industrial players are trained with their non-physical formulas and thinking from the hard to repeat or realize high mathematics of [1-2] that did not consider the first energy law. Therefore, ISO/NIST should now release a caveat relating to their ISO 14577 standards, telling that new physical results (with proper citation of open access work [10]) is being processed for unexpected revision, as a first step. This would create relieve from dilemma of ISO against physics and exempt security engineers in industry and administration who are bound to ISO standards from the dilemma concerning liability questions when using either physical state of the art or non-physical standards. Worldwide ISO and ASTM are slow in making the urgent change of their ISO 14577 standards. The clear wording is required to speed this process for a smooth non-chaotic change to physical standards for the sake of every days' security.

COMPETING INTERESTS

Author has declared that no competing interests exist.

REFERENCES

1. Love AEH (1939) Boussinesq's problem for a rigid cone. Q J Math (Oxford) 10: 161-175.
2. Sneddon IN (1965) The relation between load and penetration in the axisymmetric Boussinesq problem for a punch of arbitrary profile. Int J Eng Sci 3: 47-57.
3. Soare S, Bull SJ, Oila A, O'Neill AG, Wright NG, et al. (2005) Obtaining mechanical parameters for metallization stress sensor design using nanoindentation. Int J Mater Res 96: 1262-1266.
4. Kaupp G, Naimi-Jamal MR (2013) Penetration resistance and penetrability in pyramidal (nano) indentations. Scanning 35: 88-111.
5. Kaupp G (2003) Nanoscratching on crystal surfaces. Proceedings of the 4th European Symposium on Nanomechanical Testing, Hückelhoven, Germany.
6. Kaupp G (2013) Penetration resistance: A new approach to the energetics of indentations. Scanning 35: 392-402.
7. Kaupp G (2014) Activation energy of the low-load NaCl transition from nanoindentation loading curves. Scanning 36: 582-589.
8. Kaupp G (2016) Consequences of the physical foundation of the exponent 3/2 in pyramidal/conical (nano) indentations for the mechanical parameters and for daily life. 5th World Congress on Materials Science & Engineering, Alicante, Spain.

9. Kaupp G (2016) Nanotechnology to solve dilemma between ISO and physics.
10. Kaupp G (2015) The physical foundation of $F_N = k\ h^{3/2}$ for conical/pyramidal indentation loading curves. Scanning 38: 177−179.
11. Sokolov I. Contact Problem in Indentation Measurements of Soft, Biological and Bioinspired Materials. InContact Problems for Soft, Biological and Bioinspired Materials 2022 (pp. 31-49). Springer, Cham.
12. Xu B, Chen X, Yue Z. Indentation Fatigue Mechanics. In Handbook of Nonlocal Continuum Mechanics for Materials and Structures 2019 (pp. 401-431). Springer, Cham.
13. Chen X. Computational Modeling of Indentation. In Handbook of Nanoindentation with biological applications 2019 Apr 1 (pp. 153-183). Jenny Stanford Publishing.
14. Merle B, Maier V, Durst K (2014) Experimental and theoretical confirmation of the scaling exponent 2 in pyramidal load displacement data for depth sensing indentation. Scanning 36: 526-529.
15. Oliver WC, Pharr GM (1992) An improved technique for determining hardness and elastic modulus using load and displacement sensing indentation experiments. J Mater Res 7: 1564-1583.
16. Kaupp G, Naimi-Jamal MR (2010) The exponent 3/2 at pyramidal nanoindentations. Scanning 32: 265-281.
17. Kaupp G (2006) Atomic force microscopy, scanning nearfield optical microscopy and nanoscratching − application to rough and natural surfaces. Springer, Berlin.
18. Cheng YT, Cheng CM (1998) Further analysis of indentation loading curves: Effects of tip rounding on mechanical property measurements. J Mater Res 13: 1059-1064.
19. Troyon M, Abbes F, Garcia Guzman JA (2012) Is the exponent 3/2 justified in analysis of loading curve of pyramidal nanoindentation? Scanning 34: 410-417.
20. Naimi-Jamal MR, Kaupp G (2005) Quantitative evaluation of nanoindents: Do we need more reliable mechanical parameters for the characterization of materials? Int J Mater Res 96: 1226-1236.
21. Kaupp G, Naimi-Jamal MR (2011) Nutshells' mechanical response: from nanoindentation and structure to bionics models. J Mater Chem 21: 8389-8400.
22. Oyen ML, Cook RF (2009) A practical guide for analysis of nanoindentation data. J Mech Behav Biomed Mater 2009: 396-407.
23. Cook RF, Oyen ML (2007) Nanoindentation behavior and mechanical properties measurement of polymeric materials. Int J Mater Res 98: 370-378.

DISCLAIMER
This chapter is an extended version of the article published by the same author(s) in the following journal.
Journal of Material Sciences & Engineering, 5:6, 2016.

Chapter 3
Print ISBN: 978-93-5547-921-1, eBook ISBN: 978-93-5547-922-8

ISO Violates the First Energy Law and Denies Physical Dimensions Based on Standard 14577 for Mechanics

DOI: 10.9734/bpi/mono/978-93-5547-921-1/CH3

ABSTRACT

The physically founded $F_{\mathrm{N}} = kh^{3/2}$ relation is the foundation of the quantitative conical/pyramidal depth-sensing indentation, without fittings, iterations, or simulations. The linear plot with excellent regression's constant *k* (penetration resistance, $\mathrm{mN}/\mu\mathrm{m}^{3/2}$) eliminates early surface effects, indicates significant phase transition onsets, conversion and activation energies, and reveals severe errors. These possibilities are absent from the failing Sneddon theory of ISO, which also ignores shear-force work and breaks the first energy law from almost fifty years. The denied but strictly quantified loss of energy (20% for physical $h^{3/2}$; 33.33% at believed h^2) violates the first energy law and disregards the loss of energy for the penetration. The correction factors $h^{1/2}$ and 0.8 are applied via joint maximal force to the FE-simulated ISO hardness, and ISO modulus that unduly rely on h^2, to give approximately the physically founded values with their correct dimensions. H_{phys} is directly obtained from the loading curve regression using previously corrected *k*-values. Previous incomplete corrections are rectified. Discussions of the new dimensions and daily risk responsibilities resulting from the ISO versus physics conundrum take into account the influence that hardness and modulus have on all mechanical characteristics in relation to technology, biology, medicine, and everyday life.

Keywords: Correction of ISO hardness and modulus; energy law violations; failure risks; false materials parameters; false ISO-standards; indentation exponent; new hardness and modulus definitions; penetration resistance; physical consequences; physical hardness from loading curve.

3.1 INTRODUCTION

The energy conservation law is the most fundamental natural and technical rule that cannot be ignored and must always be properly followed. No organisation may deny its authenticity because it is something that all worlds depend on. However, despite the exhaustively complex mathematical calculations of Sneddon and Love [1,2], ISO and its US affiliate NIST continue to violate ISO norm 14577. These writers, however, plainly overlooked the shear-force work

that occurs when a stiff indenter is compelled to penetrate vertically into a solid. It must be very obvious that the rigid indenter's pressure (and/or plastic deformation) against the solid substance it has displaced requires work. Nevertheless, the whole applied force and thus the whole applied energy is still falsely considered to be only acting in vertical direction of the impact. Unfortunately, there was no protest from physics. Rather the work of Oliver and Pharr [3] on the indentation of cones or pyramids was highly acclaimed and adapted by ISO/NIST for ISO 14577. It thus became undisclosed that their assumed relation between force and depth is incorrect and that the hardness and elastic modulus determinations violate the first principle of energy conservation. Such disregard has still been retained till now, even though the unphysical exponent 2 on the depth h had been experimentally demonstrated to be replaced by $3/2$ from the present author since 2000 with convincing evidence.

In 1939 and 1965 two mathematicians solved the long standing Boussinesq problem using very complicated mathematics and came (with different constant) to the same exponent 2 on the depth h in relation to the normally applied force in conical indentation when the indenter remains stiff (Fig. 3.1). The Sneddon/Love exponent $[1,2]$ has also been used for partly plastic response (it is a consequence of pressure!) by Oliver and Pharr in 1992 [3], the ISO standard 14577, and finite element (FE) simulations (e.g. ANSYS or ABACUS software), even though the shear force of the conical (also unduely effective cone of pyramids, see Chapters 15 and 16) indenter to the environment did apparently not find any concern in physics. Some updates in this area are available elsewhere and may find attention of the readers [4-6]. Rather numerous fitting procedures were put forward over the years for the excuse, that the exponent 2 on h could not be found experimentally but only with FE-simulations converging to such exponent. Thus, these historical mathematical deductions (Fig. 3.1) cannot be correct. It did apparently not help that the energetics of the conical indentation was for the first time quantitatively clarified in a publication from 2013 [7] because the experimental exponent on h was consistently found as $3/2$ instead of 2 [8]. The thoughtful convincing physical foundation of exponent $3/2$ in Equation (1) that followed prepublished since 2015 [9] requires only first grade mathematics.

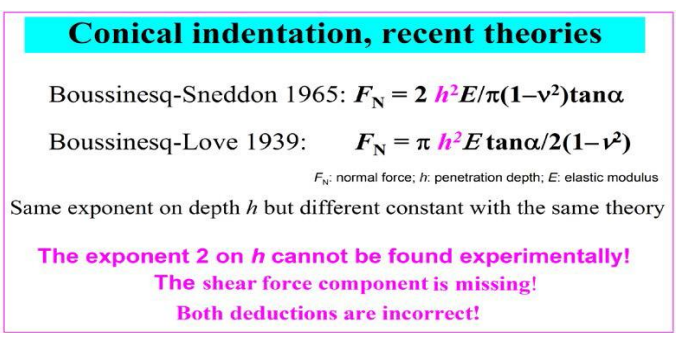

Fig. 3.1. Previous highest grade mathematic deductions of load-displacement indentation curves with cones and pyramids

3.2 MATERIALS AND METHODS

The author's nanoindentations used a fully calibrated Hysitron Inc. TriboScope $^{(R)}$ Nanomechanical Test Instrument with a twodimensional transducer and leveling device in force control mode after due calibration, including instrument compliance. The samples were glued to magnetically hold plates and leveled at slopes of $\pm 1°$ in x and y directions under AFM control with disabled plain-fit, and loading times were $10 - 30\ s$ for $400 - 500$ or 3000 data pairs [8,10]. The radii of the cube corner $(55\ \mathrm{nm})$ and Berkovich $(110\ \mathrm{nm})$ diamond indenters were directly measured by AFM in tapping mode. Three-dimensional microscopic inspection of the indenter tips secured smooth side faces of the diamonds for at least $2\mu\mathrm{m}$ from the (not resolved) apex. The whole data set of the loading curve was used for analysis, using $Excel^{(R)}$. Most analyses were however with published loading curves from the literature, as rapid sketches with pencil, paper, and calculator (10 – 20 data pairs), but for linear regressions always by digitization to give 50 –70 almost uniformly arranged data pairs using the Plot Digitizer 2.5.1 program (www.Softpedia.com), unless complete original data sets could be obtained from the scientists with $400 - 500$ or 3000 data points. They were handled with $Excel^{(R)}$. The distinction of experimental and simulated loading curves succeeded by performing the "Kaupp-plot" (3.1) revealing $F_N \propto h^{3/2}$ (experimental), surface effects and most important phase changes' onset [11]. The necessary force correction to comply with the energy law is made with the physical k-value (the slope). Only FE-simulated or iterated curves gave linear unphysical $\mathrm{F_V} \propto \mathrm{h^2}$ plots. The linear regressions were calculated with $Excel^{(R)}$. In the case of phase changes the kink positions were precisely calculated by equating the regression lines before and after the kink. Initial surface effects were, of course, exempt from the linear regressions. Previous penetration resistance values k was corrected for complying with the energy/force / depth loss in Fig. 3.2. A 10-figures pocket-calculator was used for the physical calculations, but the final results are reasonably rounded. It was tried to cover all different materials types, all different indentation modes, equipments, response mechanisms, depth ranges, penetration resistance sizes, from numerous authors from all around the globe, in order to show their universal obeying to basic mathematics.

3.3 RESULTS

The mathematical clarification of the energetics upon (pseudo)conical indentation

We proceed analogous to the deduction in Kaupp [7]. In force controlled indentations the total force F_N is linearly applied. This can provisionally be imaged together with an assumed normal parabola (with exponent 2) as is used by ISO etc. in a force versus depth diagram, as obtained by a FE-calculation from the literature (Fig. 3.3). Such normal parabola has the Formula (2). The work of the simulated indentation (W_indent) gives (3) by integration. The applied work (W_applied) is the area of the triangle under the applied work $(0 - F_\mathrm{Nmax})$ in (4). Substitution of F_Nmax from (2) into (4) gives (5). The ratio (W_applied /

$W_{\text{indent}})_{\text{simul}} = 0.5/1/3 = 3:2$. That means: only $2/3(66.67\%)$ of the applied work (and thus also force) would be left for the indent and $1/3(33.33\%)$ would be for the sum of the reversible pressure and the mostly or completely irreversible plastic deformation energies to the environment. Clearly the disregard of $1/3$ from F_{N} when using the false h^2 for the calculation of e.g. ISO hardness H_{ISO} and ISO modulus $E_{\text{r-ISO}}$, or universal hardness $(H_{\text{univ}} = F_{\text{N}}/A_{\text{proj}}$, where A_{proj} is projected indenter area, also called Martens hardness), is an obvious and severe violation of the basic energy conservation law. The long-known long-range effects and the elastic deformation would require here $1/3$ of the applied energy that would be lost for the penetration depth with ISO, FE-simulation and universal hardness. But a correction for the false exponent is also required.

$$F_{\text{N-phys}} = kh^{3/2} \tag{3.1}$$

$F_{\text{N-simul}}$ = "const h^{2}" “(3.2)”

$$W_{\text{simul-indent}} = 1/3\text{const}h^3 \tag{3.3}$$

$$\text{W}_{\text{applied}} = 0.5F_{\text{N-max}}h_{\text{max}} \tag{3.4}$$

$$\text{W}_{\text{simul-applied}} = 0.5\text{const}'h_{\text{max}}^3 \tag{3.5}$$

Material	Indenter	h_{max}	k μN nm$^{-3/2}$	r	Reference for original data
PMMA (122 s)	Berkovich	1.6 μm	0.0739	0.9999	Lu 2010
PMMA (33 s)	Berkovich	4.7 μm	0.2626	0.9991	Cook and Oyen 2007
PMMA (28 min)	Berkovich	6.5 μm	0.1554	0.9998	Cook and Oyen 2007
PMMA (33 min)	Berkovich	6.9 μm	0.1418	0.9999	Cook and Oyen 2007
it-PP (10 s)	Cube Corner	433 nm	0.0102	0.9997	Naimi-Jamal and Kaupp 2008
it-PP (10 s)	Berkovich	300 nm	0.0274	0.9997	Tranchida 2010
Polystyrene (1 s)	stiff Si-lever	553 nm	0.9738	0.9997	Kaupp and Naimi-Jamal 2010
Human Bone	Berkovich	500 nm	0.3394	0.9999	Weber et al. 2005
Lobster shell	Cube Corner	270 nm	0.0259	0.9993	Kaupp and Naimi-Jamal 2010
Pistachio	Cube Corner	420 nm	0.0360	0.9998	(Kaupp and
Macadamia	Cube Corner	300 nm	0.0389	0.9995	Naimi-Jamal 2011)
Cherry Stone	Berkovich	400 nm	0.0936	0.9995	Kaupp and Naimi-Jamal 2010
Copper (001)	Berkovich	200 nm	0.3043	0.9999	Shibutani and Tsuru 2007
γ-TiAl	Cube Corner	360 nm	0.2818	0.9996	Zambaldi et al. (2011)
InAs	Berkovich	200 nm	1.0666	0.9999	Le Bourhis and Patriarche 2005
Aluminum (exp.)	Berkovich	250 nm	0.1887	0.9994	Soare et al. 2005
Aluminum	Berkovich	1.2 μm	0.2233	0.9999	Naimi-Jamal and Kaupp 2004
ZnO	Berkovich	200 nm	1.3100	0.9997	Fang and Kang 2008
MgO	Berkovich	530 nm	4.1625	0.9999	Tromas et al. 1999
PDMS	Sphere(192μm)	3.5μm	0.001262	0.9999	Ebenstein et al. 2006
PDMS(1:10)	Cone (90°)	556μm	0.000878	0.9981	Lim, Chaudhri 2004

Fig. 3.2. Slightly supplemented table from Reference [10] with corrected penetration resistance $k(1)$ (factor 0.8), with unchanged correlation coefficients of various materials, indenters, methods, and authors for the whole length, all without phase transition up to h_{max}; in view of more recent results all of these *k* values should be multiplied with 1.25

In order to clarify the unlikely objection that the applied force would be parabolic, we plot here in Fig. 3.4 both applied force and depth side by side against the time as these develop. It is, of course seen that these develop simultaneously with total F_{N} linearly but depth h parabolic. We can thus safely calculate the total applied work from the triangle as in Fig. 3.3 (or Fig. 3.5). Different ways of normal force applications (force controlled, displacement controlled, continuou stiffness, squared progression of the load increments) cannot decrease this applied work. Furthermore, the analysis of strongly creeping loadings (e.g. PMMA data in Fig. 3.2) also gives the unfitted h^{32} parabolas (Fig. 3.1) with excellent correlation [8] excluding chances to improve the ISO- or FE-indentation efficiency. The formerly forgotten and not considered decreased energy for the indentation and thus also for the actual indentation load part is a striking violation of the first energy law. Only the fraction of the full applied work depends on the exponent on h.

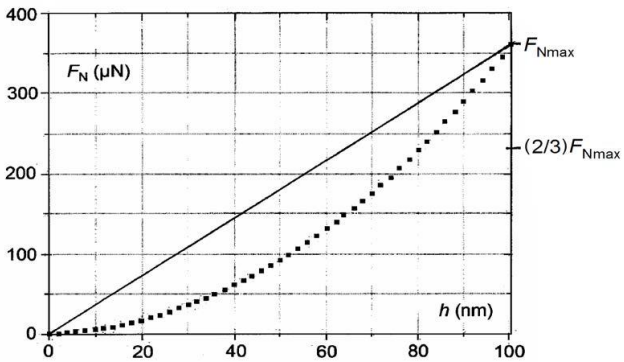

Fig. 3.3. FE-simulated force displacement curve for $500\ \mathrm{nm}$ thick gold assuming h^2 with an ideal Berkovich and our comparison with the linearly applied total work (straight line from zero to F_{Nmax} [7]); the force-corrected parabola would end at the (2/3) F_{Nmax} point; evidently a large part of the applied work would be lost for the indentation; the dotted simulated force curve would precisely follow h^2; the simulated data points were taken from Reference [11] (their Fig. 3b)

But unfortunately, we have to respond against continuing strange attacks on the quantitative treatment of conical or pyramidal indentations without any approximations, simulations or fittings despite the publications [7,8]. The probably last denial of the well-established experimental evidence of the exponent $3/2$ on h [12] repeat the offence of Troyon (advocating depth dependent broken exponents such as 1.64533 or 1.75285 on h without discussing the incredibly changing dimensions) [13], which is combined with the violation of the first energy law (not considering [7]). Furthermore, Merle [12] trie to invoke the undisputed self-similarity of cones and pyramids as theoretical argument. But Merle [12] incorrectly claims that this should be in favor of exponent 2. Self-similarity can by no means decide between the exponents in question. The exponent $3/2$ is physically founded [9], and all data relying on the

false exponent 2 require correction with the dimensional factor $h^{1/2}$. Furthermore, these unduly opposing authors tried to discredit the successful Kaupp-plot (F_{N} versus $h^{3/2}$) by calling it "Kaupp's double $P - h^{3/2}$ fit" [12] (P means force, the same as F_{N} here), even though the "Kaupp-plot" does not fit at all. They pretend that the kink (phase transformation) in the fused quartz example would have been claimed by intersecting an initial surface effect extrapolation line with the second linear branch, instead of equating the first and second linear branches (more of it in the Discussion). Kaupp has always been identifying surface effects and removing them from the regression.

Experimental and physical basis of pyramidal and conical instrumental indentation

The violation of the basic energy law is connected with the use of unphysical exponent 2 on h with implied assumption that the one third loss of the applied energy ∝ force (Fig. 3.3) would not count for the peak load in the hardness H and modulus E_{r} calculations that use F_{Nmax} for the start of the unloading curve. The connection is quite simple and direct with the definition of universal hardness for indentations $H_{\mathrm{universal}} = F_{\mathrm{Nmax}}/A_{\mathrm{proj}}$ (where A_{proj} is the projected area of the indenter). This has been worked out in Kaupp [9] and Chapter 1 with the formula sequence (3.6) leading to a disproved unphysical ISO $F_{\mathrm{N}} \propto h^2$ relation:

$$F_{\mathrm{Nmax}} = \pi R^2 H_{\mathrm{cone}} \text{ and } R/h \text{ and } \tan\alpha \text{ give } F_{\mathrm{Nmax}} = \pi h_{\mathrm{max}}^{\ 2} \tan\alpha H_{\mathrm{cone}} \qquad (3.6)$$

The ISO $F_{\mathrm{N}} \propto h_{\mathrm{c}}^2$ relation is also obtained for the ISO-hardness $H_{\mathrm{ISO}} = F_{\mathrm{Nmax}}/A_{hc}$, where the so-called contact height h_{c} must be adjusted to a standard material in a complicated procedure, including two multiparameter iteration steps [10]. Clearly there are three undisputable flaws against physics with these hardness determinations: 1. the violation of the basic energy law, 2. the use of unphysical exponent and 3. the non-considering of the often-occurring phase transformations under load before the chosen peak load is reached, which can only be detected with the Kaupp-plot of (3.1). The energy law correction will be discussed in the next Section after presenting further support. The dimensional correction will be exemplified in the Sections dealing with the correction of hardness and modulus into physical values.

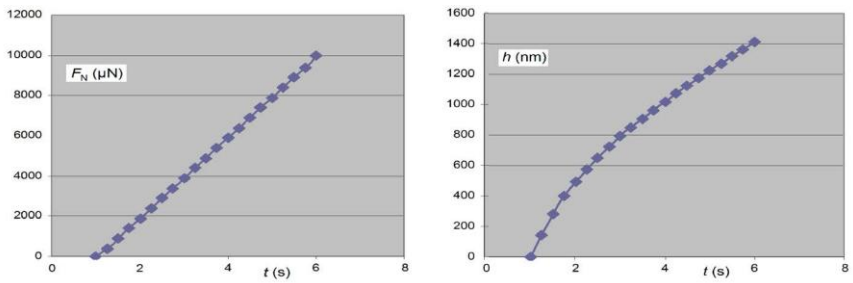

Fig. 3.4. Plots of applied normal force F_N and depth h against time in a typical load-controlled NaCl indentation showing linearity of the applied force and non-linearity of depth

The convincing physical foundation of exponent $3/2$ in the force depth relation (3.1) [9] (pre-published in 2015) leaves no doubt whatsoever with respect to the present author's analysis of his own and published loading curves from others who wrongly trusted and used the Sneddon/ISO/Oliver-Pharr exponent 2. All details of the loading curves can only be detected when the correct exponent $3/2$ on h is used for the analysis. The details are lost with unphysical plots and more so with data fitting, iterations, or present FE-simulations. Conversely, the physically founded linear F_{N} versus $h^{3/2}$ Kaupp-plots, as first introduced in lectures since 2000 , correct for initial surface effects, reveal phase transformation if they occur within the chosen force range. Furthermore, they detect alternating layers, gradients, pores, defective tips, tilted impressions, and edge interface or too close-by impressions. For example, fused quartz Berkovich indents exhibit the well-known amorphous to amorphous phase transformation [14,15] at about 2.50 or $2.25\mathrm{mN}$ applied work and 113 or $107\ \mathrm{nm}$ depth (analyzed loading curve of Triboscope or CSIRO-UMIS manual, respectively) [14]. This is indicated by a sharp kink in the Kaupp-plot, as it occurs in the chosen loading range $[8{,}14{,}16]$.

The force F_{N} is linearly applied in force controlled experimental indentations. This can again be imaged together with the exponent $3/2$ parabola, which is physically founded [9] and experimentally found (Fig. 3.2) $[8{,}14]$) and (1). Similar to Equations (3.2)-(3.5) deducing $W_{\mathrm{applied}}/W_{\mathrm{indent}}$ for the wrongly assumed ISO exponent 2 on h, the energetic deduction for the physical exponent $3/2$ on h is given by the formulas (3.7)-(3.9). The physical ratio is thus $W_{\mathrm{applied}}/W_{\mathrm{indent}} = 5{:}\,4$. The difference $5-4=1$ is for the shear force component exerting pressure and plasticization on the adjacent material. That means: precisely 80% of the applied work and (as $\propto F$) also applied force F_{N} is left for the penetration. Thus, 20% is for exerting the sum of pressure and plastic deformation energies to the solid environment. This is considerably less loss for the indentation than if the assumed unphysical exponent 2 would apply (33.33%, see above). The new knowledge is expressively supported with Fig. 3.5 that shows the difference in relation to the Fig. 3.3 for the false exponent.

$$F_{\mathrm{N}} = kh^{3/2}$$

$$W_{\mathrm{indent}} = 0.4\mathrm{const}h^{5/2} \tag{3.7}$$

$$W_{\mathrm{applied}} = 0.5F_{\mathrm{Nmax}}h_{\mathrm{max}} \tag{3.8}$$

$$W_{\mathrm{applied}} = 0.5\mathrm{const}\,h_{\mathrm{max}}^{5/2} \tag{3.9}$$

We have now $W_{\mathrm{indent}} = 0.8W_{\mathrm{applied}}$. The basic energy law is thus no longer violated when the applied force F_{N} (and thus also k) is corrected with the factor 0.8. Furthermore the definition of all physical parameters that are related to the indentation force must also not violate the first energy law and require the factor 0.8, provided the exponent correction (2 giving $3/2$) has also be performed. Importantly, the now deduced universal 5/4/1 ratio (applied/indent/long-range

work) for pyramids and cones is valid for all uniform materials, be they elastic, plastic, migrating, viscous, sinking in, piling up, and flowing. Particular cases are surface effects, gradients, tilted or too tight or edge indentations, pores, micro-voids, cracks, defective tips' effects, and most important kink indicating phase transformation onset. It is valid for all differently angled smooth pyramids or cones with mathematical precision. Any deviations are experimental errors. Surface effects include water layers, gradients, oxides, hydroxides, surface compaction, tip rounding (sometimes compensating other surface effects), and the like. They do not belong to the bulk material and must therefore be eliminated from regressions.

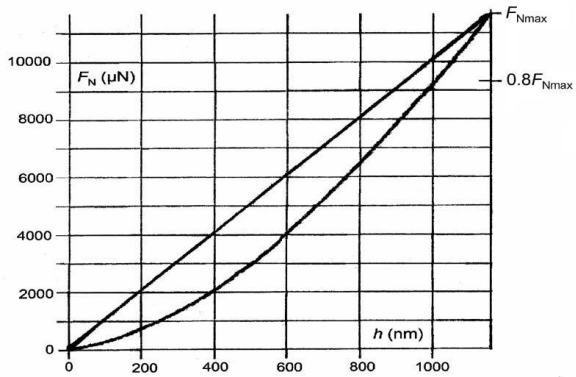

Fig. 3.5. Experimental force displacement curve of aluminum (following the physical exponent $3/2$ on the depth h [9]) and the comparison with the linearly applied force line, showing the loss of force (and energy) for the indentation depth; the measurement was with a Hysitron Nanoindenter $^{(R)}$; the force-corrected parabola would end at the $0.8F_{Nmax}$ point

Implementation of the first energy law in instrumented indentation

The energetics of the instrumented depth sensing indentation with pyramids or cones has first been published in 2013 [7] for the $F_N = k\ h^{3/2}$ relation. 20% of the applied work is lost for the indentation with mathematical precision due to the shear-force elastic and plastic work, including sink-in or pile-up. This is universal for all different shapes and materials.

As deduced above, the applied force F_N with the directly proportional otherwise physically correct published parameters (including H_{phys} in [10]) must be corrected with the factor 0.8 (5/4 ratio, 80%) (similarly for E_{r-phys} see below). Thus, Fig. 3.2 (all with correct exponent $3/2$) corrects now the data from the originals in Kaupp [8,10]. Considering the now advanced knowledge, this includes all the phase-transformation conversion energies W_{conv} (both correction with the factor 5/4). Not affected are the activation energies and the phase-transformation onsets at characteristic depth, because of cancellation. Also, most

of the other mechanical parameters from indentations in the literature including ISO-hardness (that does not account for pressure loss) and ISO-modulus are affected. The new knowledge that requires a further specification also for the hardness and modulus definitions requires separate treatment in the next Section below, because these require also the above mentioned dimensional correction.

The tip influence on the k-values (Fig. 3.2) and their conversion between different tips has been demonstrated and can be normalized [16]. Creep depends on force and temperature. It is a materials property but does not change the exponent on h of the loading curve, only the penetration resistance k. Loading times should thus not exceed $30\ s$ to avoid such influence. Independent creep measurements and corrections must only be performed for most precise rankings of materials. But it is usually much less severe than with the viscoelastic PMMA (strongly diverging from different authors) and certainly for the PDMS values of Fig. 3.2. Indentation times are in fact generally very fast (10-30 s) and Fig. 3.2. Indentation times are in fact generally very fast $(10-30\ \mathrm{s})$ and creep is mostly slow even at high temperatures, so that a rating along the k-values is a good choice already without creep corrections. Creep is mostly not corrected for or published, while thermal drift can be easily corrected for. Creep has however great importance for long-term pressure under heat and for the properties of viscoelastic materials with time dependent behavior. Importantly, the exponent on h remains $3/2$ also at indentations of organic crystals with lattice guided anisotropic migrations [16,17].

Basic energy law and dimensional corrections of indentation hardness

A quantitative foundation of conical or pyramidal nanoindentation results as for hardness (and modulus) has to obey the first energy law. All world suffers from such violation that requires correction. The $F_N = kh^{3/2}$ relation (3.1) corrects the fact that only 80% of F_N is used for the indentation with the k-value in accordance with the energy law. The correction of $H_{phys} = k / h^{3/2}$ (mN/µm$^{3/2}$) (as taken from the correct loading curve, where the factor 0.8 is included in the k-values (as only the penetration is involved), is exhaustive and complies with the first energy law. The physical indentation hardness has unavoidably the dimension $(\mu\mathrm{N/nm^{3/2}})$ or $(\mathrm{mN}/\mu\mathrm{m}^{3/2})$. The loading curve provides the easiest, most precise, most rapid and cheap way to obtain the correct physical hardness H_{phys}. Importantly, the physical hardness H_{phys} is thus independent of projected area, F_{Nmax}, and standard material. Only depth, actual material, and indenter geometry are essential. It avoids all iterations or fittings or approximations but is experimentally obtained by linear regression and it becomes a genuine physical $H_{phys} = k/h^{3/2}$ quantity for the first time. It is also not falsified by undetected phase transformations, because these would show-up in the linear regression. A sharp kink before F_{Nmax} must be absent! The applications of H_{phys} should be very welcome. It is nothing else than a normalized penetration resistance. For example, the physical hardness values can be directly obtained from the examples in Fig. 3.2 by using the corresponding indenters (Berkovich is ISO-standard).

The odd appearing dimension $\mathrm{mN}/\mu\mathrm{m}^{3/2}$ (also $\mathrm{GPa}\mu\mathrm{m}^{1/2}$) of the physical indentation hardness, which does only resemble to a pressure is unavoidable, due to the mathematically fixed shear force component of indentations that cannot be avoided. Nevertheless, indentation remains a very useful particularly precise technique.

Universal hardness, ISO hardness, and FE-simulated hardness would require multiplication with $h_{\mathrm{max}}^{1/2}$ for dimensional correction and the force correction becomes 0.8 (Fig. 3.5). However, such corrections of the ISO hardness can only be approximate, because the h and thus A_{hc} iterations with respect to a standard material cannot be reverted. Force induced phase-transformations must always be excluded with a Kaupp-plot that at the same time obtains the physical hardness more safely and directly.

The equations (3.10) and (3.11) show how easy it is to approximately calculate H_{phys} from published H_{univ} or $\mathrm{H_{simul}}$ values, provided the h_{max} values for F_{Nmax} are available, and when phase changes are excluded before F_{Nmax} is reached. The corrections are multiplications with $h_{\mathrm{max}}^{1/2}$ for the correct exponent $3/2$ and factor 0.8 for the force loss. However, these formulas were deduced with the bona fide used false pseudo cone angle for pyramids, see Chapters 15 and 16. They are however valid for real cones with their half opening angles.

$$H_{\mathrm{univ}} = F_{\mathrm{Nmax}}/\pi\tan\alpha^2{h_{\mathrm{max}}}^2 \tag{3.10}$$

$$H_{\mathrm{univ-corr}} = H_{\mathrm{phys}} = 0.8h_{\mathrm{max}}^{1/2}F_{\mathrm{Nmax}}/\pi\tan\alpha^2h_{\mathrm{max}}^2 \tag{3.11}$$

This is exemplified in Table 3.1 with a numerical example from a published indentation onto aluminum, where H_{ISO} and both the FEsimulated $\mathrm{H_{simul}}$ (ANSYS software) with exponent 2 on h and the experimental Berkovich loading curves are published (falsely claimed exponent 2 but according to the Kaupp-plot determined with exponent $3/2$ on h) [18]. Any universal hardness (H_{univ}) treatment would be the same as the one for $\mathrm{H_{simul}}$ The published loading curve was also provisionally analyzed as $\mathrm{F_V vs\, h^2}$ plot but only used for numerical achievement of the conversions.

Entry 1 in Table 3.1 gives the H_{phys} from the analyzed loading curve (3.11), which is certainly the most reliable value. It does not rely on F_{Nmax} h_{max}, any h_{c} or A_{hc} and it secures the absence of a phase change up to the maximal force. And it compares with H_{ISO} and the hardness values that derive from $\mathrm{H_{simul}}$ with various stages of correction.

Entry 2 shows that H_{ISO} exhibits a far too high value and an unphysical dimension. The energy correction for leaving exponent 2, removing only the energy law violation, decreases the value insufficiently, still with the unphysical dimension $\mathrm{mN}/\mu\mathrm{m}^2$. A value for h_{max} is not available for a final correction. When exceptionally a guess was tried that it might be in a $0.25\mu\mathrm{m}$ region one would guess a further decrease that would look like 0.239 with the changed dimension

$\mathrm{mN}/\ \mu\mathrm{m}^{3/2}$. This would be in the region of H_{phys} although with all reservation because it is only a free guess only indicating the direction. This show the difficulties for the conversion when $h_{\max}$ for the used F_{Nmax} is not reported. It is thus much easier to apply the Kaupp-plot to the loading curve (3.1). We renounce of including the uncorrected simulated value $(0.6016\mathrm{mN}/\mu\mathrm{m}^2)$.

Entry 3 gives only the exponent correction of $\mathrm{FEH}_{\mathrm{simul}}$ (ANSYS software) that was probably obtained by using Young's modulus E (either known or iterated) input, with converging criterion to exponent 2 on h.

Entry 4 gives only the energy correction with a rather high value. Table 3.1 show that neither the exponent correction for exponent 2 alone nor the energy correction (Fig. 3.3) alone (removing energy law violation) is sufficient.

Entry 5, finally with both exponent correction and then smaller energy correction factor for $\mathrm{h}^{3/2}$ (Fig. 3.5) provides $\mathrm{H}_{\mathrm{simul-phys}}$, with surprisingly good match (2%) with H_{phys}. The surprisingly close coincidence of H_{phys} and $\mathrm{H}_{\mathrm{simul-phys}}$ supports the numerical correctness of the non-fitting (!) straightforward deduction and it also reminds the unbeatable precision of the Kaupp-plot's linear regression (Fig. 3.2). The close correspondence with $\mathrm{H}_{\mathrm{simul-phys}}$ in this case should however be tested for generality, because this single example could be fortuitous when considering the parameterizations and iteration procedures at FE simulations.

Importantly, the striking dilemma of ISO with physics persists with the false dimension of too large H_{ISO} and unphysical dimension. All of the values and dimensions of the mechanical parameters that depend on it are severely wrong, also those that depend on wrong ISO elastic modulus E_{r} (see Chapters 4 and 5). Clearly, Table 3.1 and Equations (3.10) with (3.11) show preliminary corrections of H_{univ}, probably $\mathrm{H}_{\mathrm{simul}}$ and with reservation H_{ISO}, provided the $h_{\max}$ values are known. However, despite the straightforward corrections none of them can handle the very often occurring and so important phase transformations under load (here they were experimentally excluded with Kaupp-plot).

Table 3.1. Comparison and correction of unloading H_{ISO} and FE-simulated $\mathrm{H}_{\mathrm{simul}}$ loading curves of Al on Si[18] with the physical H_{phys}, which is in accordance with the energy law

Number	Technique	$h_{\max}{}^{\mathrm{n}}$	k or $\mathrm{h}_{\max}^{(\mathrm{a})}$	Hardness calculations and corrections
1	Experimental linear regression	$h_{\max}^{3/2}$	$k = 5.9540(\mathrm{mN}/\mu\mathrm{m}3/2$ (energy corrected)[(b)]	$H_{phys=}k/\pi\tan^2 = 0.24295(\mathrm{mN}/\mu\mathrm{m}^{3/2})$ independent on F_{N} and $h_{\max}$ (no phase trans.)
2	Experimental with $2/3$ factor	$\mathrm{h}_{\max}^2$	$-\cdot$	$H_{\mathrm{H}_{Iso}}\ 0.716(\mathrm{GPa}) \times 2/3 = 0.477(\mathrm{mN}/\mu\mathrm{m}^2$) (unphysical dimension) $h_{\max}$ not known
3	FE-simul. $h_{\max}{}^{1/2}$ no energy corr.	$\mathrm{h}_{\max}^2$	$\mathrm{h}_{\max} = 251.984\ \mathrm{nm}\mathrm{H}_{\text{simul-corr1}}$ (as H_{univ}) $= \mathrm{F}_{\mathrm{Nmax}}/$	$\pi\tan^2\ \mathrm{h}_{\max}^{3/2} = 0.2977(\mathrm{mN}/\mu\mathrm{m}^{3/2})$

Number	Technique	$h_{max}{}^{n}$	k or $h_{max}^{(a)}$	Hardness calculations and corrections
				(energy law violation!)
4	FE-simul. 2/3; no exponent corr.	h_{max}^2	$h_{max} = 251.984$ nm	$H_{simul\text{-}corr\ 2} = 2\ F_{Nmax}/3\pi tana^2\ \ h_{max}3/2 = 0.4011$ $(mN/\mu m^2)$ (wrong exponent)
5	FE-simul, 0.8, and $h_{max}{}^{1/2}$	h_{max}^2	$h_{max} = 251.984$ nm	$H_{simul\text{-}phys} = 0.8\ F_{Nmax}/\pi tana^2\ \ h_{max}{}^{3/2} = 0.2382(mN/\mu m^{3/2})$

Note: $^{(a)}$ Simulated parameters are not italicized; $^{(b)}$ correction factor 0.8; the alpha-values are biased pseudo-cone angles, see Chapter 16. That means, the false pseudo-cones were bona-fide used, even though the cited results were obtained with Berkovich and no longer the physical values

3.4 DISCUSSION

The extremely complicated mathematical deductions of Sneddon/ Love ([1,2]; Fig. 3.1) for the conical or pyramidal indentations did not consider the energetics of the process, as illustrated with the Figs. 3.3 and 3.5. And there was no protest from physicists. Almost all involved people followed Sneddon [1], Oliver Pharr [3], and ISO 14577 all with violating the first energy law for more than half a century. The general acceptance for half a century of the implied claim that pressure formation and plasticization could be workless achieved is hard to understand. It is apparently the result of hype upon the publication [3] that unfortunately was believed by ISO/NIST. The simple equations as derived starting in 2000 ([17] and before in lectures, and in refused manuscripts) and the point-by-point unraveling of the field until now against strong impediments did not help. The newcomers had to obey ISO 14577 and many very complex rules, and they used the software of the instrument suppliers that had to trust in the ISO/NIST-standards. By doing so they forgot to think on the physical foundations. Thus, the basic formulas (3.3)-(3.5) and (3.7)-(3.9) that essentially rely on the experimentally (since 2000) (Fig. 3.2) and physically founded (since 2015) Equation (3.1) [9] found much refusal, various excuses for no experimentally finding exponent 2 with data-fittings, multi-parameter iterations, and simulations. The actions against the elementary algebraic treatment without any fitting/iterating/simulating were undue repetitive offenses. Rather acknowledgement had to be expected because everything became much easier and quantitative on a sound physical basis with simple closed mathematical formulas, proving the universal validity.

Apparently, nobody else (not even textbook or tutorial writers) asked themselves why all of the applied normal force with cones or pyramids is claimed to be used for the indentation depth, even though the loading curve proceeds not linearly but parabolic. The obvious answer is that well-known long range effects and pressure formation to the environmental solid material require energy that is lost for the indentation depth. When this energy/force/loss was quantified and finally (after difficulties with anonymous Reviewers) published in 2013 [7] with the universal loss of $1/5$ for the physical (3.1) and $1/3$ for unphysical (3.2) equations, there was discussion about the validity for comparing applied work and indentation work. But these proceed at the same time to the same endpoint F_{max}. Surprised about the ease of the mathematical deduction and the strict and

universal result requiring difficult necessary changes, there were objections and much open discussion in plenary lectures from the audience with the guess that all of the linearly applied force might instead go along the parabolic curve during the experiment. This prevented the opponents from recognizing that the first energy law was evidently violated. The linearity of the applied force is however also evident, simply from the additional applied force F_{N} versus time plot in Fig. 3.4.

The undue opposition against straight forward physics and algebra is surprising even after it was very clear with Kaupp [7] that the ISO system violates the first energy law (the present author could not dare to verbally express the energy law violation at that time). The offenses have been continuing. For example, the opposing manuscript [12] was received at Scanning on May 27, 2014, whereas the clarifying manuscript [7] was received at Scanning on October 4, 2012 and published on February 25, 2013. The content of Kaupp [7] had thus to be taken up again in Kaupp [10] with more details, because the authors, reviewers, and editors of Merle [12] continued violating the basic energy law. And the Merle [12] continued arguing against the most precise Kaupp-plot that actually was the basis for the quantification of the violation. The opponents tried with iterated own loading curves of fused quartz. But when doing it correctly, even the invoked curve in Troyon [13] would roughly reproduce the well-known transformation onset, despite its using a blunt tip that gave an unusually long initial effect. And Merle [12] tries again with a false intersection at its microindentation "Kaupp-plot" (up to $300\mathrm{mN}$ and $1600\,\mathrm{nm}$) where the region with all of the nanoindentation details is almost totally obscured in a short unstructured part of it. The false intersection with a remote line far away from the plot is useless. But it is used for falsely criticizing the Kaupp-plots that never used or use such faulty tricks. When properly looking at this linear plot in Reference [12] with a ruler, one recognizes an intersection of two straight lines at about $175\mathrm{mN}$ and $1225\,\mathrm{nm}$, which the authors do neither trace nor recognize. Four possibilities exist for this kink very close to the plot: either a new highload phase transition of fused quartz occurred, or a smoothness defect of the tip was present at this depth, or a remote crack at such deep impression was formed, or the impression was too close to an edge/ interface/impression. Furthermore, these authors claim and draw a straight single line for their unphysical so called "P- h^2 fit with 0.999 fit quality". However, despite their claimed "three-nines fit", their depicted unphysical "P- h^2 fit" gives two roughly linear branches, intersecting in the region of $60-70\mathrm{mN}$ force (that is far away from surface effects). This deviation from the claim is easily "overlooked" without a ruler in a wide pencil stroke representation at totally false depth-square scaling (better seen when more precisely drawn, the first part steeper and cutting at small angle). This shall only be a necessary contradiction to the false claim of linearity for a "P- h^2 fit" trying to discredit our simple algebraic treatment on a sound physical foundation. Fitted or FE curves, converging with h^2, must not be used for denying thoughtful and repeatable physically founded [9] and experimental Equation (3.1). Only untreated experimental loading curves are able to detect surface effects, the important phase changes, conversion energies, etc., when using the physically founded exponent on h.

A problem might arise when fitted, iterated or FE-simulated curves and experimental loading curves might be mixed up in publications. However, when experimental force data are plotted with or fitted to the non-physical h^2, the deviations from a straight line might appear minor for example as in Merle [12]. Also a minor endothermic phase change slightly levels the unphysical $F_N - h^2$ trial-plot with respect to the stronger curved appearance without phase change $[8,14]$. Such leveling behavior of the test material fused quartz might have strengthened the belief in h^2, but it reflects the inability to find phase transformation with the physically wrong exponent 2 on h. All of the important details of nanoindentation are lost with h^2. But the kink at $F_\mathrm{N} \approx 2.4\mathrm{mN}$ (Berkovich) and initial surface effects of the fused quartz standard are easily seen by sharp kinks with the precise Kaupp-plot (3.1) in nanoindentations, notwithstanding the cases of later or further phase changes in microindentations (e.g. NaCl in $[8,14]$). But there is no excuse for using the unphysical exponent and thus denial of the phase transitions if these occur, combined with the violation of the first energy law.

The readers of Kaupp [7] and the attendants of the present author's lectures on numerous worldwide conferences were repeatedly urged to think about the unexpected and surprisingly easy deduced energetic facts (3.2)-(3.6) and (3.7)-(3.9) but the expected response of the scientific establishment is still missing. It appeared unlikely that all of the scientific Celebrities and their successors including textbook authors, ISO/NIST, and numerous anonymous referees have, consciously or not, been violating the first energy law for more than 50 years. Hesitation to use only the normal force left for the indentation depth was thus advisable, before any non-apparent compensation effect for saving the energy law was excluded in the desperate situation. Publications of the truth should stay as close as possible with the current indentation theory unless all objections are removed. Clearly, the believers in exponent 2 on h could for themselves have easily performed the deductions as in Equations (3.1)-(3.5) and could have tried to change their minds because of this inexcusable energy law violation. But they did not try to take into account the always occurring energy loss. Based on their believed exponent 2 on h it would have amounted to $1/3$ (33.33%) of F_N, due to the work and force proportionality, as shown above with the trial Equations (3.2)-(3.5). And they would have found that the violation is also programmed and used in FE-simulations. They refused till now to accept the undeniable wealth of the Kaupp-plot and the physical deduction for the correct exponent $3/2$ on h [9] that finally proves energy/force loss of $1/5(20\%)$ according to Equations (3.7)-(3.9), as only the physical exponent is correct. Since ISO/NIST have been reluctant to change their minds, or to announce reconsideration with an alert, there was the urgent preliminary publication in Kaupp [10] for expressively naming the incredible claim of workless pressure formation and plasticization as "violation of the basic first energy law". This is now completed with valid transformation formulas for obtaining the physical values and the necessary conditions for that from unphysical publications. Furthermore, the most easy and precise H_phys deter-mination by linear regression of the loading curve (3.1) (hitherto strongly refuted Kaupp plot) with energy-based correction is now again strongly advocated for.

3.5 CONCLUSIONS

The still not settled dilemma between ISO and physics with respect to ISO 14577 (not even an alert has been filed yet) is unbearable due to its enormous risks for science and daily life's safety. It appears unbelievable and even desperate that the first energy law was drastically violated for more than 50 years and none of the physicists protested against such habit. Everything is easily deduced with first grade algebra, avoiding fittings, iterations, simulations, and approximations, making everything much easier. Hardness is now obtainable by linear regression, no longer by iterations, fittings, approximations, and simulations that are not ready for a controlling assessment. The physical indentation hardness $H_{\mathrm{phys}}\left(\mathrm{mN}/\mu\mathrm{m}^{3/2}\right)$ is now for the first time a genuine physical quantity, obeying Equation (3.1) and the first energy law. The same is true for the indentation modulus $E_{\text{r-phys}}$ (d1.25 F_{N}/dh) /A. We note: in the original published paper was bona fide for $E_{\text{r-phys}}$ the false biased angle α for the pseudo-cone used, but see Chapters 15,16. The complete, more precise deduction than in Chapter 5 reveals also the simple conversion from $E_{\mathrm{r-ISO}}$. Only the quantitative indentation on the physical basis reveals numerous otherwise impossible applications. Examples are phase change [7,8,19], conversion energies [7,19] and activation energies [19] of materials, all on the basis of the so-called Kaupp-plot [7,9] that also checks for correctly performed indentations and provides extrapolation facility up to recognized phase change qualities under pressure. Furthermore, it reveals a large number of special materials' properties and indentation errors that are named above. But it is still being heavily suppressed by the ignoring establishment, including ISO and some anonymous Reviewers with incredible unqualified wording instead of acknowledging this wealth.

The liability with unphysical calculated materials' properties is totally unclear at the present dilemma between ISO and physics, because all safety engineers are falsely trained. That means, the issue counts for every day's safety unless ISO files at least an urgent alert. Everybody knows how many materials fail shortly after the warranty period, certainly not purposeful but often with falsely calculated materials. Even worse, falsely calculated components like poorly adjusted medicinal implants or larger scale composites can produce disasters. There is good reason why passenger traffic airplanes require frequent safety checks and complete replacement of all parts within 2 years. For example, h goes with $F_{\mathrm{N}}^{2/3}$ not with $F_{\mathrm{N}}^{1/2}$[8] with all implications for fatigue, and wear, to name a few.

Despite the highly comprehensive results of this paper and numerous worldwide lectures on conferences the ISO versus physics dilemma still remains. The physical indentation H_{phys} and $E_{\mathrm{r-phs}}$ dimensions that only resemble pressures is perhaps difficult to understand at first glance. But it is real and the reasons have been discussed. Importantly this does not detract from indentation as a very precise and reproducible technique, when properly executed, checked, and algebraic evaluated, that means without fittings, iterations, and simulations. Rather the unavoidable dimensional changes have an enormous bearing for science and practice. The not fitted and not iterated physical quantities must be

used to redefine the numerous further mechanical parameters that were deduced from unphysical H_{ISO} or $E_{\mathrm{r-ISO}}$. Further studies are necessary and further important insights are to be expected when the violation of the first and most basic energy law will be removed also for the deduced parameters. This should help for a better understanding and open new horizons. Also textbooks must be rewritten for the sake of physics, compatible materials sciences, and new insights. Since there was the violation of the first energy law, the new results will prove to be more compatible with all related techniques that do not violate physical laws, which is very desirable. The quantitative indentation at the now physical basis has the indispensable advantages of being precise, and in accord with basic principles. This is promising and cannot be denied. The further advancement on the physical basis is a very urgent task that must be pursued, hopefully soon also with ISO/NIST against all of the incredible resistance, because violating the first energy law is an inexcusable fault.

COMPETING INTERESTS

Author has declared that no competing interests exist.

REFERENCES

1. Sneddon IN (1965) The relation between load and penetration in the axisymmetric Boussinesq problem for a punch of arbitrary profile. Int J Engn Sci 3: 47-57.
2. Love AEH (1939) Boussinesq's problem for a rigid cone. Q J Math (Oxford) 10: 161-175.
3. Oliver WC, Pharr GM (1992) An improved technique for determining hardness and elastic modulus using load and displacement sensing indentation experiments. J Mater Res 7: 1564-1583.
4. Ou H, Yi H, Qaiser Z, Ur Rehman T, Johnson S. A structural optimization framework to design compliant constant force mechanisms with large energy storage. Journal of Mechanisms and Robotics. 2022 Jun 21;15(2):021008.
5. Skalka P, Kotoul M. Determination of Mechanical and Fracture Properties of Silicon Single Crystal from Indentation Experiments and Finite Element Modelling. Materials. 2021 Nov 14;14(22):6864.
6. Feuillet R, Marcum D, Alauzet F. A closed advancing-layer method for generating curved boundary layer mesh. InAIAA Aviation 2019 Forum 2019 (p. 3675).
7. Kaupp G (2013) Penetration resistance: a new approach to the energetics of indentations. Scanning 35: 392-401.
8. Kaupp G (2013) Penetration resistance and penetrability in pyramidal (nano) indentations. Scanning 35: 88-111.
9. Kaupp G (2016) The physical foundation of $F_N = k\ h^{3/2}$ for conical/pyramidal indentation loading curves. Scanning 38: 177-179.
10. Kaupp G (2016) Important consequences of the exponent 3/2 for pyramidal/ conical indentations-new definitions of physical hardness and modulus. J Mater Sci & Engineering 5: 285-291.

11. Wang TH, Fang TH, Lin YC (2008) Finite-element analysis of the mechanical behavior of Au/Cu and Cu/Au multilayers on silicon substrate under nanoindentation. Phys Appl A 90: 457-463.
12. Merle E, Maier V, Durst K (2014) Experimental and theoretical confirmation of the scaling exponent 2 in pyramidal load displacement data for depth sensing indentation. Scanning 36: 526-529.
13. Troyon M, Abbes F, Garcia Guzman JA (2012) Is the exponent 3/2 justified in analysis of loading curve of pyramidal nanoindentations? Scanning 34: 410-417.
14. Kaupp G, Naimi-Jamal MR (2010) The exponent 3/2 at pyramidal nanoindentations. Scanning 32: 265-281.
15. Trachenko K, Dove M (2003) Intermediate state in pressurized silica glass: reversibility window analogue. Phys Rev B 67:212203/1-212203/3.
16. Kaupp G (2006) Atomic force microscopy, scanning nearfield optical microscopy and nanoscratching - application to rough and natural surfaces. Springer, Berlin.
17. Kaupp G, Schmeyers J, Hangen UD (2002) Anisotropic molecular movements in organic crystals by mechanical stress. J Phys Org Chem 15: 307-313.
18. Soare S, Bull SJ, Oila A, O'Neill AG, Wright NG, et al. (2005) Obtaining mechanical parameters for metallization stress sensor design using nanoindentation. Int J Mater Res 96: 1262-1266.
19. Kaupp G (2014) Activation energy of the low-load NaCl transition from nanoindentation loading curves. Scanning 36: 582-589.

DISCLAIMER
This chapter is an extended version of the article published by the same author(s) in the following journal.
Journal of Material Sciences & Engineering, 6: 2, 2017.

Chapter 4
Print ISBN: 978-93-5547-921-1, eBook ISBN: 978-93-5547-922-8

Industrial High-load One-point Hardness and Depth Sensing Modulus

DOI: 10.9734/bpi/mono/978-93-5547-921-1/CH4

ABSTRACT

The depth-sensing nano, micro, and macro instrumental hardness technique, which provides several additional mechanical parameters when using the proper force/depth curves exponent 3/2 on the depth of the loading curves, is compared to the physics of industrial single-point force indentation hardness measurements (Vickers, Knoop, Brinell, Rockwell, Shore, Leeb, and others). The equipment software usually calculates and displays most of the different types of macro hardness but not of the pristine material in favor of polymorphs due to mostly several consecutive phase transitions, to be only found by depth sensing indentations. The ISO or ASTM standards do also not take into account the temperature dependent activation energy and phase change onset with phase-transition energy, which is vital information for applications of all sorts of solids. Only the latter reveal these, when not using the disproved exponent 2 on the depth h for the analysis. Furthermore, the high-load one-point approaches miss the inevitable stronger and more varied subsequent phase-transformations, leading to inaccurate interpretations of the properties of pristine materials. Examples are provided for the conversion of iterated ISO-hardness and finite element simulated hardness to physical hardness. The one-point procedures are still crucial for industry, but to ensure the accuracy of their conclusions, physical hardness and phase transition onset sequence detection must be added. That requires depth-sensing indentations and correct loading curve analysis. Multidirectional indentation moduli mix of (mostly) anisotropic materials without high-force depth-sensing equipment produce only faked Young's moduli. For Young's moduli one needs tension, compression, or ultrasound techniques. Only these give reliable Young's moduli for the multitude of mechanical parameters derived from them. Also, the iterated ISO indentation moduli must no longer be used for there-from calculated faked mechanical parameters.

Keywords: Brinell hardness; elastic modulus; force-depth curves; Hook's law; ISO and ASTM standards; macroindentation; physical hardness and modulus; rockwell hardness; ultrasound; vickers hardness, young's modulus.

4.1 INTRODUCTION

Although instrumented macro-indentation is also an option up to 80 N, the current depth-sensing indentation hardness and modulus determination is

obtained by nano- and occasionally micro-indentation (nN to µN and mN). Vickers (HV), Knoop (HK), Brinell (HB), Rockwell (HR), Shore, rebound LH (Leeb), or other specific macro-hardness tests are still the focus of industrial non-depth sensing techniques. Although they have subsets for particular types of materials, these measure the impression diagonal, or diameters, or final depths under predetermined conditions. One subset of HV is the UCI technique (ultrasonic contact impedance, requiring elastic modulus E_{eff}) measuring vibration damping of a swinging stick with a Vickers diamond at the end, as inserted at a predefined load. All these single-point high-force techniques require 1:1-calibration with test plates of closely related materials of "known" hardness, also for canceling out not specified tip end radii. Several hand-hold devices exist, which is practical in the steel industry. Handhold equipment includes UCI, Leeb, Rockwell clamp, Brinell clamp, Brinell Poldi hammer, etc. All of these techniques use rather empirical definition and ISO (International Standard Organization) or the now compelling ASTM (American Society for Testing and Materials) standards. Between HV, HK (low load range), HB, HRB, and HRC exist approximate conversion equations. This indicates relationships between them. The equipment software usually calculates and displays most of the different types of macro hardness. However, conversion between them is often not precise enough for construction purposes, notwithstanding the sometimes large experimental uncertainties, due notwithstanding the sometimes large experimental uncertainties, due to often low reproducibility between different user sites. And there is serious non-compliance with basic physics.

The comparison with depth-sensing instrumented indentation according to ISO 14577 where three major flaws occur in the universal, ISO, and finite element (FE) simulated hardness, is difficult. The instrumented depth-sensing could recently be corrected for providing the physical hardness, eqn. (4.1) (where k is the slope) of the14577 [1-3]. The energy law is not violated because the *k*-value refers only to the penetration.

$$H_{\mathrm{phys}} = k = F_{\mathrm{N}}/h^{3/2}\ (\mathrm{mN/\mu m^{3/2}}) \tag{4.1}$$

$$F_{\mathrm{N}} = k\, h^{3/2} \tag{4.2}$$

Corresponding violations of physical laws have not yet been considered in the single-point-load techniques, but these must equally exist. This bears an important risk for the mechanics quality of industrial goods. A prevailing source of uncertainty is the non-considered phase transformation of materials that change the material's hardness and other mechanical properties, under the very large local pressure. It is well-known [1,3] that phase changes occur already at nanoindentation and lower micro-indentation. They must therefore be even more common in the macro range. Furthermore, the possibilities for detection of hidden horizontal cracks (except when these occur upon unloading) are not evident. All of the industrial indentation techniques also penetrate vertically onto flat surfaces, but now with a defined holding time at the predetermined force. Creep is assumed to be negligible. Some of these macro-techniques (HV, HK,

HB) measure diagonals or diameters of the impressions that is left at the surface, others (HR, Shore) the indentation depth. But final depths can also be calculated from the indenter geometries in the former cases. The physical flaws as detected in the instrumented depth-sensing should be the same in all macro-hardness tests. Clearly, the depth relates to the diagonal or diameter left at the surface. So there is no principal difference to more precise depth sensing, except that the applied forces are usually very much higher. Very detailed and constantly refined ISO and ASTM standards are available. A comparison between these and the depth-sensing techniques is thus in urgent order, by applying the physical news from the nano- and micro-indentations [3]. The readers may be interested in certain updates in this topic that are available elsewhere [4-6].

Similar difficulties with elastic moduli concern only the depth sensing unloading. The same dimensional energetic and phase change violations of ISO standards can be hardly corrected. However, it turns out, there is not the claimed correspondence of ISO or physical indentation moduli with Hook's Young's moduli, so that $\mathrm{E_{ISO}}$ should no longer be iterated (Oliver-Pharr method), falsely called "Young's" modulus, and used. Even E_{phys} is only a counterpart of H_{phys} the physical hardness. It will however be suggested to use bulk moduli instead.

4.2 MATERIALS AND METHODS

The nanoindentations onto a polished optical disc $2\ \mathrm{mm}$ thick NaCl single crystal (purchased from Alpha Aesar GmbH Co KG, Karlsruhe, Germany) were performed at a Triboindenter $^{(\mathrm{R})}$ with AFM of Hysitron Inc, Minneapolis, USA, with proper calibration at 23, 100,300, and $400°\mathrm{C}$ (average of eight measurements). The author's nanoindentations used a fully calibrated Hysitron Inc. Triboscope $\mathrm{e}^{(\mathrm{R})}$ instrument with AFM in force-controlled mode also with a Berkovich diamond $(R = 110\ \mathrm{nm})$. The cited literature data have been carefully searched and interpreted in view of the generally deduced physical laws, in accordance with validated experimental data. Phase changes under load are detected by kink-type discontinuity [7] in so-called "Kaupp-plots" according to eqn. (4.2) [1-3,7,8]. The precise intersection point is obtained by equating the regression lines before and after the onset of the phase change. The regression coefficients are calculated with all 400-500 ottr 3000 original data point pairs using $Excel^{(\mathrm{R})}$, but excluding those from initial surface effects. Digitizing 50-70 almost uniformly arranged data pairs were obtained from published loading curves with the aid of the Plot Digitizer 2.5.1 program (www.Softpedia. com). The distinction of experimental from FE-simulated loading curves succeeded with the "Kaupp-plot". The use of *k* tells that we comply with the energy law.

4.3 RESULTS

Dilemma between ISO Standards and Physics

The comparison of depth-sensing instrumented ISO-hardness with non-depth-sensing single point high-load techniques reveals undeniable physical

similarities. The industrially used macro indentation techniques are governed by the same physical laws as depth-sensing nano to macro indentations. Unfortunately, present ISO standards are at variance with the corresponding physical laws [1-3] and the possible corrections of previously published indentation data require a detailed discussion here. The physical requirements for singlepoint load indentations reveal equally from the precisely determined facts of the better controlled depth-sensing continuous indentations, including the macro-indentation ones.

Table 4.1 compares the depth-sensing hardness values of H_{phys} H_{ISO}, and $H_{\mathrm{simulated}}$, to demonstrate the importance of correct depth-sensing evaluation. It is also shown how the latter two can be corrected, provided that the loading curves were published as for example in ref. [9]. This is a practical application for the conversions of FE-simulated or ISO hardness values (energy law violations and incorrect exponents) into physical hardness.

Entry 1 shows the correct value H_{phys} according to the Kaupp-plot with linear regression from the experimental loading curve in ref. [9].

Entry 2 deals with the published iterated H_{ISO} value that enormously differs in value and dimension. The difference is still very large when the energetic law violation is removed (based on the falsely believed "h^2" the energy or force loss for the indention calculates to 33.33% energy law violation) (cf. refs. $[1,2]$). This is incomplete correction. It is not clear, which F_{N}/h pair was used in the H_{ISO} iteration. Complete correction would also suffer from the exhaustive iterations that cannot be reverted.

Entry 3 deals with the FE-simulated hardness without the necessary corrections: again, a large deviation in value and dimension from H_{phys}.

Entry 4 demonstrates only the dimensional correction, as $h_{\mathrm{max}}{}^2$ The use of *k* tells that $h_{\mathrm{max}}{}^2$ was used instead of $h_{\mathrm{max}}{}^{3/2}$ for the relation with F_{max}, but it is clearly not sufficient.

Entry 5 similarly reveals that only the removal of the energy law violation (for believed h^2 only $2/3$ of $\mathrm{F_N}$ is available) is not sufficient.

Entry 6 shows that only both corrections $\left(\mathrm{h}^{1/2}\right.$ and thereafter $0.8)$ give a good value. But it has to be checked if all FE-simulations with different iterations will give equally good correspondence with the correct experimental H_{phys} value. All of the corrections in Table 4.1 are equally valid for the one-point non-depth-sensing macro techniques. However, there is another very important flaw: phase changes under load. Their occurrence and onset load can only be detected by depthsensing indentation and Kaupp-plot.

As hardness is for the first time a physical quantity, there is no possibility to change the physical hardness dimension. The inherent dimension has its

meaning for all applications of the k-value (force/depth$^{3/2}$, mN/µm$^{3/2}$) that cannot be dismissed. These include depth-force relation (mar, wear, tribology), physical deduction with elementary mathematic, adhesion work, pull-off curves, safe ratings of materials, correlation coefficients with > 3 nines or less noisy with > 4 nines, quantitative far-reaching energy, phase transition onset, indentation work, compatibilities, transformation energies, activation energies, creep, size effects, maximal load for reasonable unloading curves, initial surface effects, high sensitivity by linear unloading curves, initial surface effects, high sensitivity by linear regression, tip normalization, tip rounding effects, materials gradients, inhomogeneous materials, geodes, crystal defects, edge interface, too close impressions, grain boundaries, cracks, alternating, improvement of FE-simulations, avoidance of polynomial iterations or varying broken exponents, correct visco-elastic-plastic parameters, nanopores, micro-voids, alternating layers, blunted tip effects, correction of false mechanical parameters that rely on h^2, elementary mathematics instead of iterative fitting, avoiding violation of the basic energy law with factor 0.8, failure risks with false mechanical parameters, tilted impressions, faulty standards with phase change, all types of solid materials and plasticization types [1-3, 7,8,11], quantitative sound mathematical basis, universal validity, distinction of FE-simulated from experimental loading curves, no denial of phase changes, and daily risk with unphysical mechanic parameters [3].

Macroscopic depth-sensing, hardness and phase transitions

Depth-sensing nanoindentation extends up to $10\,\mathrm{mN}$ load, microindentations up to 1 N, mostly with Berkovich indenter. Extensions to macro- indentations have been achieved with Vickers up to 80 N for soda-lime glass [10], but rarely repeated. Eqn. (2) has been experimentally secured and physically deduced. It secures (see Figs. 4.1, 4.2, and Chapter 6 for the phase-transitions upon depth-sensing) the Kaupp plots for all of the force ranges [2,8]. The dilemma of physics and ISO 14577, still believing in " h^2", is clearly evident from Fig. 4.1. It indicates exclusion of h^2 and phase transitions of soda-lime-glass, sapphire, and sodium chloride in the macro-indentation range (the nano-ranges are "hidden" at these macro-indentation ranges). The kink-type discontinuities (the phase transition onsets) are at 15.37,10.43, and 2.469 N load, respectively.

The most important advantage of macro-depth-sensing is the detection of secondary phase transitions at very large forces. In the case of NaCl, the also endothermic fcc to bcc transition at $4.233\,\mathrm{mN}$[11] is hidden at that scale. The same is true for a transition onset of sapphire at $26.5\,\mathrm{mN}$ load and for soda-lime-glass at $4.81\,\mathrm{mN}$ [8]. The other macroindentation techniques have the disadvantage that they cannot detect phase transition onsets: they practically always measure the hardness from (often secondarily) phase transformed materials, as embedded in the original material. They do not characterize the pristine materials! Clearly, one needs nano, micro and macro depth-sensing indentation in addition to the technical ones, for judging the materials mechanics. Most of the time, materials are not under such very high pressure. Also, the

primary transition onset is important for material's mechanics (e.g. failure or fatigue).

Table 4.1. Comparison and correction of H_{phys}, H_{ISO}, and FE-simulated H_{simul} loading curves of Al [9] including the corrections in accordance with the exponential and energy laws; extended table from ref. [3]

Entry	Technique	$h_{max}{}^{n}$	k or $h_{max}F_{max}^{(a)}$	Hardness calculations and corrections
1	Experimental curve linear regression	$h_{max}^{3/2}$	k = 5.9540 mN/μm$^{3/2}$ (energy-corrected)[b]	$H_{phys} = k/\pi \tan\alpha^2$ = 0.24295(mN/μm$^{3/2}$) [(c)]; independent on F_N and h_{max} (no phase trans.)
2	Iterated H_{Iso} with $2/3$ factor	$h_{max}{}^{2}$	--	$H_{ISO} = 0.716(\mathrm{GPa}) \times (2/3) \approx 0.477(\mathrm{mN}/\mu\mathrm{m}^2)$ (still unphysical dimension, h_{max} unknown)
3	FE-simulated not corrected	$h_{max}{}^{2}$	$h_{max} = 0.250\mu\mathrm{m}$ $F_{max}^{max} = 0.912\mathrm{mN}$	H_{simul} (as H_{univ}) = $0.6016(\mathrm{mN}/\mu\mathrm{m}^2)$
4	FE-simul. $h_{max}^{1/2}$ no energetic corr.	$h_{max}{}^{2}$	$h_{max} = 0.250\mu\mathrm{m}$ $F_{max}^{max} = 0.912\mathrm{mN}$	H_{simul} (as H_{univ}) = $F_{Nmax}/\pi\tan\alpha^2 h_{max}{}^{3/2}$ = $0.2977(\mathrm{mN}/\mu\mathrm{m}^{3/2})$ (still energy law violation!)
5	FE-simul. 2/3; no exponent corr.	$h_{max}{}^{2}$	$h_{max} = 0.250\mu\mathrm{m}$	$H_{simul\text{-}corr2} = 2 \times 0.6016/3 = 0.4011(\mathrm{mN}/\mu\mathrm{m}^2)$ (wrong exponent)
6	FE-simul. $h_{max}^{1/2}$ and energetic corr.	$h_{max}{}^{2}$	$h_{max} = 0.250\mu\mathrm{m}$ $F_{max}^{max} = 0.912\mathrm{mN}$	$H_{simul\text{-}phys} = 0.8 \times 0{,}2977 = 0.2382(\mathrm{mN}/\mu\mathrm{m}^{3/2})$

(a) simulated parameters are not italicized; (b)energy correction factor 0.8*; (c) this value has been calculated with the false pseudo-cone formula (see Chapter 16)*

The comparison of hardness measurements of sodium chloride is particularly revealing, because (as in the case of sapphire and soda-lime-glass) consecutive phase transitions are involved. The literature knows Vickers microhardness data from the list for NaCl properties of the MaTecK-Material-Technologie and Kristalle GmbH collection (Jülich, Germany), reporting 0.20 GPa. Probably, this is the same value as cited [10], but F_{max}/h_{max} is not known. $H_{ISO} = 0.252\mathrm{GPa}$ $(\pm 2\%)$ was recently measured at $F_{max} = 10\mathrm{mN}$, but that is uncorrected after its fcc-bcc phase transition (from the loading data for ref. [11]). After energy and exponent correction before the phase transition onset this gives with $k = 7.2786$ the H_{phys} value of $0.2970\ \mathrm{mN}/\mu\mathrm{m}^{3/2}\left(\mathrm{GPa}\mu\mathrm{m}^{1/2}\right)$ (not violating the energy law etc.), as calculated with eqn. (4.1) [3]. H_{phys} is only obtained by linear regression of original data pairs without any of the iterations for $\mathrm{H_{ISO}}$. The nanoindentation up to $10\mathrm{mN}$ load (sharp Berkovich, $1.17\mu\mathrm{m}$ depth at $10\mathrm{mN}$ force) creates the halite to cesium chloride type phase transition (fcc to bcc) with onset at $0.697\ \mu\mathrm{m}$ and $4.233\mathrm{mN}$ load. It requires $+0.04418\mu\mathrm{J}/\mu\mathrm{N}$ phase transition work [11]. Ref. [11] reports also the activation energy $(23$ to $400^{\circ}\mathrm{C})$ of this first transition. The

preferred hydrostatic transition pressure is known as 26.8GPa [12]. The calculated second phase transition (bcc to layered CrB-type NaCl space group Cmcm) is hydrostatically expected at 322GPa, metallic from $584\text{GPa}[13]$. Most probably, the second transition corresponds with the kink in the Kaupp-plot at $2.49\ \text{N}$ load and $21.1\mu\text{m}$ depth [11] according to the loading curve of ref. [10]. The transition work is $+3.647\mu\text{J}/\mu\text{N}$, which is very large when compared to $+0.04418$ for fcc to bcc of NaCl, or for example $+0.007066$ for SrTiO_3, or $-0.01126\mu\text{J}/\mu\text{N}$ for $\alpha-\text{SiO}_2[11]$. The discontinuity at $21.31\mu\text{m}$ depth of a sharp Vickers is a candidate for the predicted Cmcm phase of NaCl.

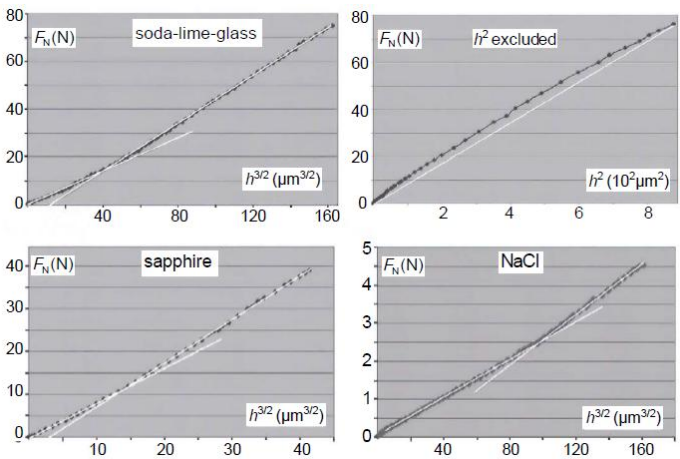

Fig. 4.1. Kaupp-plot (F_N versus $h^{3/2}$) of published depth-sensing macro-indentations [8] showing kink-point intersections (phase transformation onsets) and linearity up to 80 N load; an "h^2 relation" as believed in ref. [10] is excluded; the data have been extracted from ref. [10]; the correlation coefficients for all six regression lines are r>0.999

Vickers hardness test and other one-point-load macrohardness tests

The load for HV varies in three ranges from $0.1\ \text{N}$ up to $1500\ \text{N}$ (HBW10/3000 even with $30000\ \text{N}$; the W indicates tungsten-carbide); the normal range is $40-980\ \text{N}$ (HV4 - HV98). The Vickers hardness test is most similar to the pyramidal instrumental depth-sensing, as the Vickers indenter can be used in both techniques. One indents to the chosen load, holds for 10-15 s (now $14\ \text{s}$), unloads, and calculates HV from the average of the diagonals d of the impression. The standard is given by eqn. (4.3), where F_N is in kpf (kilopond force, it is a very old standard) and d the diagonal length in mm of the residual impression. Then, after conversion to N/mm^2 units one reports (mHVn), where m is the hardness value and n the vertical load F_N in kpf.

$$\text{HV} = 1.86F_\text{N}/d^2 \tag{4.3}$$

The first flaw deals with the dimensional error. Since the depth h is geometrically related with HV's impression diagonal d according to eqn. (4.4), the d^2 relates again with h^2 rather than with $h^{3/2}$. This gives again a faulty inherent " $\mathrm{F_N} \propto \mathrm{h}^{2}$" relation (instead of the physically deduced eqn. (4.2)), as in the instrumented depth-sensing force-depth curve [2,3].

$$h = d/(2\sqrt{2}\ \tan\ 68) = d/7.006 \tag{4.4}$$

Next to the dimensional violation there is the second flaw: violation of the basic energy law. The applied load is not only used for the indentation depth but with 20% force and thus energy loss (physically correct $h^{3/2}$): the sum of stress formation and plasticization, including sink-in or pile-up, requires energy (if correction of h^2 to $h^{3/2}$ is not performed, the energy loss would be 33%) [1,3]. Long-range features, often with pile-up around the square impressions, have long been seen. Their universally quantitative occurrence in addition to been seen. Their universally quantitative occurrence in addition to the created stress ($W_{\mathrm{longrange}}$) derives from the physically deduced ratio of the different work contributions in eqn. (4.5) [1]. Clearly, the nonconsideration of pressurizing and plasticization work is violation of the most basic energy law! The same is true with HB, HR, Shore, rebound, and the techniques that use spherical impression instead of pyramidal/ conical ones, because these must also obey the physical relation of eqn. (4.2) ($h^{3/2}$ instead of h^2) as quantitatively deduced for depth-sensing indentation. Also the UCI-Vickers hardness values, using ultrasound frequency, suffer from the same flaws.

$$W_{\mathrm{applied}}/W_{\mathrm{indent}}/W_{\mathrm{longrange}} = 5/4/1 \tag{4.5}$$

The third flaw is even more severe than in depth-sensing indentation, because the forces/works and depths are much larger (compare the NaCl, sapphire, and soda-lime-glass cases in Fig. 4.1. Inevitably, there must be several endothermic or exothermic phase changes following each other, not to speak of hidden horizontal cracks that can also occur upon pressure release at the unloading. Furthermore, one-point measurements (rather than linear regression of loading curves with Kaupp-plot) bare the risk of uncontrolled errors. This fact makes it difficult to judge the reliability of HV etc. measurements that could be approximately corrected for energy law and dimension (requiring depth with tip rounding correction), but not with respect to force dependent phase transformations under pressure, the detection of which require analyzed force/depth curves with the physically founded exponent $3/2$ on the depth (eqn.4.2) [2,8].

The interpretation difficulties are demonstrated for HV measurements with the test material 316L stainless steel. The general claim is that HV values must not depend on the load. A publication of 2016 gives a value of $281.6\mathrm{HV}0.1(\ \mathrm{N/mm^2})$ at $0.981\ \mathrm{N}$ load [14]. The rounding of the Vickers pyramid is not given (its influence is eliminated by comparison with test-plates impressions), but we calculate for ideal Vickers a depth of $3.66\mu\mathrm{m}$. Another publication of 2016 reports

$280\text{HV3}(\text{N/mm}^2)$ at $29.43\,\text{N}$ load [15] at a calculated depth of $20.12\mu\text{m}$. Important questions are: why is the value for the much deeper and 30 times higher force smaller by $1.6\,\text{MPa}$? Could it be experimental error (this is calibration at a test material!), or was the tip rounding too different, or are there undetected cracks, or are consecutive phase transitions at the 30 times higher force exothermic? Such considerations are missing, but the 208HV3 value was also converted into 217HB; 95 HRBmax, and 89 HRB. Numerous calibration tables exist and equipment software often displays such converted results as well. The most important of the conversion formulas that interconnect the various techniques are listed in Table 4.2. Such conversions are termed "approximate" (conversion norm: $\pm 3.5\%$ of HV), but their use indicates their correlation. That means: all of the single-point macro-indentations exhibit the same flaws with respect to physics, notwithstanding the apparent technical problems. Clearly, size effects due to phase changes are assumed to stay within the large error allowance, and the end radii of the Vickers and Knoop pyramids are not taken particular care of. Apparently, Table 4.2 is only valid for the same force, and these techniques are by no means universal, but they need for every material a separate test sample with "known" HV that must have been agreed upon. The phase change events are not considered and neither can they be detected by the $1:1$ calibration, even though the forces vary from 0.1 to $150\,\text{kpf}$. Conversely, depth-sensing is universally applicable to all solid materials but requires knowledge of the tip rounding that should be small enough, so that its influence can be treated and corrected for as initial effect. ISO uses iterative relation to a standard like fused quartz or aluminum. However, the physically founded depth-sensing obtains absolute hardness values without test samples [2,3], and it detects phase transitions directly as in Fig. 4.1 and [8].

Table 4.2. Some conversion formulas for one-point-load hardness values

HV to HB	$HV \approx 1.05\text{HB}$
HVtoHK	HV ≈ HK(low load region)
HB to HV	HB ≈ 0.95HV
HRB to HB	$\text{HRB} \approx 176 - 1165/\text{HB}^{1/2}$
HRC to HV	$\text{HRC} \approx 116 - 1500/\text{HV}^{1/2}$

These considerations clearly indicate the close relation of the empirical single-point load macro-techniques that use either surface (HV, HK, HB) or depth measurements (HR, Shore, etc.) to the instrumental nano- and micro- and macro-indentations. Thus the same flaws, as in the ISO standards or FE-simulations, as based on the Oliver-Pharr technique, are involved: first the violation of the basic energy law, second the wrong dimensional error (violation of the Equation 4.2), and third the non-consideration of phase transformations that cannot be detected during the load and hold periods. The high load capabilities of depth sensing should be extended above $80\,\text{N}$. Clearly, depth-sensing measurements should always be separately available for every material's charge in addition to the fast HV, HR, etc. measurements for rapid and on-site production control, in order to avoid risks from unrespected phase change

onsets giving polymorphs with different mechanical properties. And the study of crack onsets is important.

Tension, compression and speed of ultrasound for Young's modulus E

Elastic moduli cannot be obtained by one-point-load hardness tests, but ISO iterates it with depth-sensing unloading. The transformation of $E_{\mathrm{r-ISO}}$ into false "Young's" E_{ISO} from exhaustively iterated unloading curves is achieved with eqn. (4.6), where both the Poisson's ratio and modulus of the material and the indenter (diamond) occur. This gives values with unchanged dimension but still burdened with the violating of physical laws by the three major physical flaws (dimensional, energetics, unclear solid phase). ISO calls such E values from unloading curves "Young's" moduli.

There may however be severe objections against equating indentation moduli E_{ISO} with Hook's Young's moduli. This holds also for the indentation $E_{\mathrm{r-phys}}$ (Chapter 5) and with eqn. (4.6) E_{phys} (the pendant to H_{phys}) [3] with different dimension $\left(\mathrm{GPa}\ \mu\mathrm{m}^{1/2}\right)$ [10].

$$1/E_{\mathrm{r}} = (1-\nu^2)/E + \left(1-\nu_{\mathrm{i}}^2\right)/E_{\mathrm{i}} \tag{4.6}$$

It does not help that the UCI-Vickers hardness test uses ultrasound response, which requires an effective elastic modulus E_{eff} from calibration tables for consideration of the E-module. UCI is not a technique for modulus measurement. The reason for eqn. (4.7) is the universal eqns. (4.2) and (4.5) for indentations, which means long-range work for pressurizing and plasticization consumes 20% of the applied work, and thus force, in case of correct dimension according to eqn. (4.2) (or 33% as long as the false exponent 2 on h would be applied). But the use of E_{phys} requires some efforts with the calculation of the initial slope of the unloading curve using the original data, rather than a ruler to the recorded curve.

$$E_{\text{r-phys}} = (\mathrm{d}1.25F/\mathrm{d}h)/A \tag{4.7}$$

In the absence of original data, it can appear impossible to graphically approach the initial slope $\Delta F_{\mathrm{max}}/\Delta h_{\mathrm{max}}$ that is the iteration result by Oliver-Pharr. It claimed E_{ISO} value of $73\mathrm{GPa}$ (Berkovich, $\mathrm{R} = 50\ \mathrm{nm}$) from ref. [9] up to $215.8\ \mathrm{nm}$ followed by creep up to 266 nm depth. Actually, ISO iterates A (projected contact area) with an unrelated standard for final height $h_{\mathrm{f}} = h_{\mathrm{max}} - 2F_{\mathrm{max}}/S$ for A and fits 80% or 50% of the exponential unloading curve iteratively with $F_{\mathrm{N}} = A(h_{\mathrm{max}} - h_{\mathrm{final}})^{\mathrm{m}}$, where A, h_{final}, and exponent m (between 1 and 3) are the free parameters. Stiffness S at peak load is then obtained by the differentiation $\mathrm{d}F_{\mathrm{N}}/\mathrm{d}h = S = A\ \mathrm{m}(h_{\mathrm{max}} - h_{\mathrm{final}})^{(\mathrm{m}-1)}$ for obtaining the maximal slope. This circumvents the slope detection. $E_{\mathrm{r-SO}}$ is then calculated as $\pi^{1/2}S/2A_{\mathrm{hc}}^{1/2}$ and the result is called "Young's modulus" after application of eqn. (4.6). This is objectionable ISO standard.

The principal problem with such definition of an indentation modulus is the anisotropy of most materials that cannot be tackled by indentation, irrespective of the possible physical corrections eqn. (4.7). For example, it is known from the fact that different faces of a crystal give different *E*r-ISO moduli depending on the different predominance of the crystal faces towards the tip (e.g. $\alpha - \mathrm{SiO_2}$ varies $E_{\mathrm{r-1SO}}$ between 105.0 and $133.6\mathrm{GPa}$ onto 5 different faces) [16]. The skew indenter surfaces collect in fact a mixture of some sort of different elastic moduli from all of the different directions around the tip and there are also shear-moduli involved upon the unloading. This is far away from unidirectional Young's modulus, depending on Hook's law eqns. (4.8) and (4.9). Thus, E_{ISO} is incompatible with Hook's law, and indentation- E_{phys} can also not be made compatible. Any similarities of E_{ISO} values with Young's moduli are thus fortuitous. They derive from the iterative fitting to the unidirectional Hook's value of a standard. They are therefore fortuitous, because of both the multi-directionality and because of the striking physical errors of E_{ISO}. They do not have the same meaning, as might be suggested by the unfortunate common wording. Fortunately, an extensive amount of well-studied Hook's Young's moduli for all independent directions of preferably cubic and other high symmetry crystals are tabulated and do not need repetition by indentation. The complexity of the 6x6-matrix treatment of Young's moduli, leading by some matrix symmetry to generally 21 independent elastic constants that are further reduced by crystal-symmetry to 9,7,6 and in the cubic case 3 independent moduli has been amply described (for example in ref. [17]). So, it is suggested to call E_{phys} eqns. (4.6) and (4.7) "indentation modulus" and check, whether the three-dimensional bulk modulus, as obtainable from hydrostatic pressurizing, is an equa or superior parameter for characterizing the elastic properties of micro or macro materials.

It is essential now to briefly repeat the Hook's technique for obtaining Young's moduli E, where the shear modulus detection is excluded. The clearest experimental determinations of E are by tension compression eqn. (4.8) or ultrasound speed eqn. (4.9). The uniaxial tension or compression gives the simple elongation/depression Hook's law eqn. (4.8), as long as these are fully reversible. Transversal thinning/ thickening is always mentioned, but transversal work can apparently be neglected. L is length, p is the generated pressure (force per area), E Young's modulus.

$$\Delta L/L = p/E \tag{4.8}$$

Eqn. (4.9) recalls the ultrasound speed technique in long rods with diameters smaller than the ultrasound-wavelength, excluding shearwaves, where frictional loss may be small or ineffective. It is used for the longitudinal speed v_{s} in such rods, where E is Young's modulus and ρ is density. These and more complicated Hook's techniques are generally accepted textbook physics.

$$v_{\mathrm{s}} = \mathrm{E}^{1/2}/\rho^{1/2} \tag{4.9}$$

For practical reasons we regret that the Hook's law techniques require much larger test samples with highly specialized geometric shape. They are therefore

more difficult to perform and less versatile than would be indentations, that appear however inappropriate for E. The present situation is at best exemplified with the simplest case, cubic isotropic aluminium.

We have to distinguish tabulated Young's modulus ($E = 69\mathrm{GPa}$), shear modulus ($G = 25.5\mathrm{GPa}$) and bulk modulus at hydrostatic compression ($K = 76\mathrm{GPa}$). This compares to claimed invalid $E_{\mathrm{ISO}} = 73$ GPa [9] that must be decreased to $10.7\mathrm{GPa}$ by making the physical corrections. Clearly, nothing from the unloading is fitting with the reliable Hook's values. There is no hope left that indent- $E_{\mathrm{phys}}(\mathrm{mN}/\,\mu\mathrm{m}^{3/2})$ values could be converted into Hook- $E_{\mathrm{phys}}(\mathrm{mN}/\mu\mathrm{m}^2)$ values (for example by division with ${h_{\max}}^{1/2}$), because they would have totally different meaning. Again, it does not help that $\mathrm{E_{ISO}}$ is iteratively fitted with respect to a unidirectional Hooks's Youngs modulus of a test material.

The consequences for the recent use of physically unsound E_{ISO} values are detrimental, when their use for mechanical parameters is considered. The particular importance of an indentation modulus is evident from numerous applications. The listing 1 through 12 indicates various examples.

1. All elastic properties
2. Input for FE-simulations
3. Stress-strain response
4. Film hardness and film adhesive strength
5. Strain hardening
6. Creep calculation
7. Material fatigue, fatigue strength
8. Adhesion calculation (DMT or JKR)
9. Viscoelasticity studies
10. Sliding friction coefficient
11. Contact area at dynamic testing in continuous stiffness mode
12. Fracture toughness

At present it appears only possible to calculate Young's modulus E of new materials for certain directions and test the quality of such calculations with as close as possible materials, for which the Hook's values are known, or to rely on indentation- E_{phys} or on bulk modulus K by hydrostatic pressure experiments for the consideration of reliable elastic materials properties.

Reasons for obeying physical laws

It is very clear that mechanical properties must not violate basic physics, be it in academia, industry, medicine, or daily life. That does not mean that purely empiric methods like the Mohs hardness scale (who scratches whom) are also useful. However unphysical parameters must not violate physics. And one must not try to make physical correlations with unphysical parameters. For example, Mohs says steel cuts leather. However, there is also mechanochemistry that explains why barbers can sharpen their blades with leather [18]. Clearly, also the

size of the components and the chemical composition of the solids play an important role (here polymers are tribomaterials) [18]. Brittleness, ductility, lubrication are further qualities apart from hardness and elasticity, that have their meaning in particular applications. Hardness and elastic moduli should be physical rather than empirical due to countless technical constructions where different materials must work together and alloys or composites must be compatible rather than fail upon short use. Materials are often used under low pressure where they are not phase-transformed. And different materials have their phase change onsets at varied pressures. This provides severe risks when they are perhaps only compatible under very high pressure as high pressure polymorphs, but not at lower or ambient pressure where they are at rest. Everyone knows that virtually all purchased goods with granted guarantee periods fail (shortly) after that period, or airliners must have very short control and replacement terms of all parts, because they must not fail. Only physically sound parameters of hardness and modulus with all of the numerous other mechanical parameters that depend on them should be used, instead of violating basic physical laws with H_{ISO} and E_{ISO}. The dilemma of ISO-standards against physics is a thread for daily life, because falsely calculated materials bear enormous risks for lifetime and failure. Some examples are composite materials (also solders) that may not properly fit together, or exploding turbines, or breaking windmill blades, or micro-cracks in airplanes and huge pressure vessels of power plants, or breaking medicinal bone implants due to incompatibility, etc.

4.4 CONCLUSION

The comparison of single-point load macro-indentations with physical and mathematical precisely handled depth-sensing nano, micro, and macro indentations reveals three major flaws of the former that can be and have been removed for the latter [3]. All depends on the physically deduced exponential law $F_{\mathrm{N}} \propto h^{3/2}$, instead of the believed h^2 from Sneddon, Oliver-Pharr, and ISO standards [3]. The same flaws (violation of the basic energy law, dimensional error against physics and disregard of phase changes under load) are also inherent in present ISO and ASTM standards that still do not apply basic physics from the depth-sensing techniques. Since the one-point force techniques are much more rapid and comfortable in industry, these purely empiric techniques with standardized calibration necessities at test plates and tables for different material types are now only acceptable, when the materials in question have also been studied on the genuine physical basis with force/depth curves, as described here and in ref. [3]. Depthsensing ISO-standards are subject to urgent changes for complying with physics. Most serious in view of failure risks are the present disregard of phase transition (phase change) onsets, and size depending very large differences between faulty H_{ISO} and the much more precise H_{phys} values with different dimensions. Similarly, indentation elastic modulus E_{ISO} (falsely called "Young's modulus") fails: it suffers from the same physical flaws and has no relation to unidirectional Hook's law. The unloading skew pyramid or cone surfaces collect a mixture of multidirectional elastic moduli and shear moduli. Therefore, indentation-moduli have a totally different meaning than Hook's Young's modulus. They cannot be given the same name, and the term E_{ISO} is

also worthless due to three physical flaws, and to questionable iterating fitting techniques as initiated by Oliver-Pharr and taken up by ISO. The incredible claim that ISO would deal with unidirectional Young's modulus has to be rejected. It is not at all available for indentation unloading. E_{ISO} and deductions there from are unphysical and their use must be discontinued. The use of indentation- E_{phys} or bulk moduli K should be used in situations where the one or the other appears more appropriate or better both for the mechanical characterization of materials. Phase changes under pressure must be controlled as detected from the mathematical analysis of instrumented loading curves, so that the rapid single point high-load indentations can find the appropriate interpretation.

ACKNOWLEDGEMENT

We thank Dr. U. Hangen Aachen, Germany from Hysitron Inc for the indentions onto NaCl with a Triboindenter®.

COMPETING INTERESTS

Author has declared that no competing interests exist.

REFERENCES

1. Kaupp G (2013) Penetration Resistance: a new approach to the energetics of indentations. Scanning 35: 392-401.
2. Kaupp G (2016) The physical foundation of $F_N = k\ h^{3/2}$ for conical/pyramidal indentation loading curves. Scanning 38: 177-179.
3. Kaupp G (2017) The ISO standard 14577 for mechanics violates the first energy law and denies physical dimensions. J Mater Sci Eng 6: 321-328.
4. Ghanbari SS, Mahmoudi AH. An improvement in data interpretation to estimate residual stresses and mechanical properties using instrumented indentation: A comparison between machine learning and Kriging model. Engineering Applications of Artificial Intelligence. 2022 Sep 1;114:105186.
5. Schiavi A, Origlia C, Germak A, Prato A, Genta G. Indentation modulus, indentation work and creep of metals and alloys at the macro-scale Level: Experimental insights into the use of a primary Vickers hardness standard machine. Materials. 2021 May 28;14(11):2912.
6. Campbell JE, Zhang H, Burley M, Gee M, Fry AT, Dean J, Clyne TW. A Critical Appraisal of the Instrumented Indentation Technique and Profilometry-Based Inverse Finite Element Method Indentation Plastometry for Obtaining Stress–Strain Curves. Advanced Engineering Materials. 2021 May;23(5):2001496.
7. Kaupp G, Naimi-Jamal MR (2010) The exponent 3/2 at pyramidal nanoindentations. Scanning 32: 265-281.
8. Kaupp G, Naimi-Jamal MR (2013) Penetration resistance and penetrability in pyramidal (nano) indentations. Scanning 35: 88-111.

9. Soare S, Bull SJ, Oila A, O'Neill AG, Wright NG, et al. (2005) Obtaining mechanical parameters for metallization stress sensor design using nanoindentation. Int J Mater Res 96: 1262-1266.
10. Thurn J, Morris DJ, Cook RF (2002) Depth-sensing indentation at macroscopic dimensions. J Mater Res 17:2679-2690.
11. Kaupp G (2014) Activation energy of the low-load NaCl transition from nanoindentation loading curves. Scanning 36: 582-589
12. Li X, Jeanloz R (1987) Measurement of the B1-B2 transition pressure in NaCl at high temperatures. Phys Rev B 36: 474-479.
13. Chen X, Ma Y (2012) High pressure structures and metallization of sodium chloride. Europhys Lett 100: 25005-1 - 25005-4.
14. Wang D, Song C, Yang Y, Bai Y (2016) Investigation of crystal growth mechanism during selective laser melting and mechanical property characterization of 316 L stainless steel parts. Mater Design 100: 291-299.
15. Maestracci R, Sova A, Jeandin M, Malhaire JM, Movchan I, et al. (2016) Deposition of composite coatings by cold spray using stainless steel 316 L, copper and tribaloy T-700 powder mixtures. Surface and Coatings Technol 287: 1-8.
16. Naimi-Jamal MR, Kaupp G (2005) Quantitative evaluation of nanoindents: do we need more reliable mechanical parameters for the characterization of materials? Int J Mater Res 11: 1226-1236.
17. Bower AF (2012) Mechanics of solids, Chapter 3. Electronic Text and Taylor & Francis, ISBN 9781439802472- CAT#K10131.
18. Kaupp G (2009) Mechanochemistry: the varied applications of mechanical bond-breaking. Cryst Eng Comm 11: 388-403.

DISCLAIMER
This chapter is an extended version of the article published by the same author(s) in the following journal.
Journal of Material Sciences & Engineering, 6:3, 2017.

Chapter 5
Print ISBN: 978-93-5547-921-1, eBook ISBN: 978-93-5547-922-8

Highlighting the Dilemma between Physics and ISO Elastic Indentation Modulus

DOI: 10.9734/bpi/mono/978-93-5547-921-1/CH5

ABSTRACT

This chapter questions the ISO standard 14577, which calculates the elastic indentation modulus by breaking the first energy law and ignoring easily detectable phase change onsets and initial surface effects under load. It is necessary to cancel and stop the double iteration for incorrectly fitting the indentation modulus to a standard with up to 11 free parameters. The iterative evaluation of the elastic modulus $E_{r-\mathrm{ISO}}$ can by far not be reproduced by iteration-free direct calculation of E_r, when using the underlying formulas for S, h_c, A_{hc}, and ε. For cubic aluminium the errors amount to a factor of 3.5 or 3.1, respectively. Every interpretation of indentation moduli as single unidirectional "Young's moduli" is false. They contain shear moduli and are mixes in all directions. Even in this straightforward but already anisotropic instance, the three separate packing diagrams of body-centered cubic α-iron provide as an example of the combination of three independent Young's moduli (and hence also three shear moduli). More linear moduli ensue in lower symmetry crystals as exemplified with α-quartz. The first physical indentation modulus is deduced by removal of the physical errors of $E_{\mathrm{r-ISO}}$, or after indenter compliance correction E_{ISO}. Only $E_{\mathrm{r-phys}}$ does no longer violate the energy law. The conflict between physics and ISO is especially harmful because E_{iso} is utilised to calculate several mechanical characteristics that are frequently used. Due to serious violations of the fundamental energy law and other physical rules that govern daily life, these spread the inaccuracies into failure risks of incorrectly estimated materials. There are issues that need to be resolved quickly by new ISO standards. The first recommendations for using E_{phys}, and ultimately measured bulk modulus *K* are made. This needs to be evaluated and discussed right now.

Keywords: Bulk modulus; compressibility; data correction; errors of elastic moduli; falsely calculated materials; falsified iterations; HookRUS-technique; indentation modulus; ISO-standard; Mechanical parameters; physical modulus; shear modulus; young' s modulus.

5.1 INTRODUCTION

The availability of physically accurate mechanical parameters was made possible by the ISO-standard 14577 for indentation hardness (H_{ISO}) and so-called Young's

modulus (E_{ISO}) [1-3]. This suggested a return to the first energy conservation law—the elimination of dimensional errors—after a half-century. In addition, any surface effects or phase transition onsets that might occur under a mechanical load are now disclosed by depth sensing (unlike with single load techniques like Vickers, Brinell, Rockwell, etc. hardness), and these can be avoided by applying a lower force [1-3]. Iterations and approximations are now easily avoided at the expense of linear regression analyses. Indentation hardness H_{phys} was deduced as physical quantity for the first time and ISO modulus definition was provisionally improved. Materials can now be physically correct described and numerous unexpected applications ensue by use of simple closed formulas. But there remains further trouble with ISO-modulus E_{ISO} [2,4]. It is falsely called "Young's modulus" but a unique indentation modulus E_r as compared to unidirectional Young's modulus E, shear modulus G and bulk modulus K. And the physical modulus $E_{\text{r-phys}}$ = (d1.25F_N/dh)/A is shown in Chapter 4. Only this one is the unfitted indentation modulus. It is therefore timely to unravel the misleading situation with $E_{r-\mathrm{ISO}}$ and $E_{\mathrm{r-phys}}$. The readers may remark in certain updates of this topic [5-7] that such considerations are still badly missing in these papers.

5.2 MATERIALS AND METHODS

The nano-indentations used a fully calibrated Hysitron Inc. Triboscope (R) instrument with AFM leveling in force-controlled mode with a Berkovich indenter ($R = 110\ \mathrm{nm}$) at the exclusion of phase change below $F_{\max}$ and validity check with the "Kaupp-plot" F_N versus $h^{3/2}$ [2,8] throughout, also for correction of initial surface effects. Stiffness values S are calculated by linear regression of the upper unloading data points, as long as these decrease linearly. Crystal packing was imaged by use of the program Schakal 99 from Egbert Keller, University of Freiburg i.Br., Germany. The cited literature data have been checked and interpreted in view of the mathematically deduced new general physical laws with closed simple formulas in accordance with validated experimental data, excluding all forms of iterations or approximations. Phase changes under load were detected by kink-type discontinuity in linear regressions. The precise intersection point was obtained by equating the regression lines before and after the onset of the phase change. The necessary energy law correction by virtue of the physically deduced $F_N \propto h^{3/2}$ law is $0.8\,[3]$ (the energy law violation correction of ISO would be $2/3$, as long as the unphysical exponent 2 on the depth h would still be continued).

5.3 RESULTS AND DISCUSSION

Flaws of the ISO indentation modulus

The reduced ISO indentation moduli values are defined as $E_{\mathrm{r-\ ISO}} = S\pi^{1/2}/2A_{\mathrm{hc}}^{1/2}$ and iteratively obtained against a standard. These are therefore no absolute but relative quantities. The corresponding definition of absolute E_{r} is then $S\pi^{1/2}/$

$2A_{\text{projected}}{}^{1/2}$. At first, ISO iterates the unloading curve according to $F_N = B(h_{\max} - h_{\text{final}})^{\text{m}}$ with the three independent parameters B, h_{final} and exponent m for obtaining the maximal slope with $\mathrm{d}F_{\text{N}}/\mathrm{d}h = S = B\ \text{m}(h_{\max} - h_{\text{final}})^{(\text{m}-1)}$. E_{r-ISO} is then calculated as $S\pi^{1/2}/2A_{hc}^{1/2}$ and from there E_{ISO} with $1/E_{\text{r}} = (1-\nu^2)/E + (1-\nu_{\text{i}}^2)/E_{\text{i}}$, where i denotes the values of diamond. It follows a further iteration of A_{hc} with eight parameters C_{n} (also sign change option allowed): $A_{hc} = \pi E_{\text{r}}^{-2}(C - C_{\text{f}})^{-\,2}/4 = \left(24.5{h_{\text{c}}}^2 + C_1 h_{\text{c}} + C_2 h_{\text{c}}^{1/2} + C_3 h_{\text{c}}^{1/4} + \cdots + C_8 h_{\text{c}}^{1/128}\right)$ for fit to the Young's modulus of a standard. This result is then falsely called "Young's modulus" [9] in ISO-14577. This iterative procedure with eleven free parameters does however not obtain a physical quantity [2]. It is per se troublesome.

Even more serious problems occur with the convergence prescription of the iteration. While the direct calculation of A_{hc} is possible with $S = \mathrm{d}F_{\max}/\mathrm{d}h$ and the deduced formulas $(11,12,17)$ of [9], this path was not followed by ISO, but they standardize the described iterative procedures by fitting against a standard. The diversion between the two paths is enormous. By using the direct path we follow the defined underlying basis of [9] and obtain for the unloading curve of, for example, cubic aluminium [10] with uncorrected $S = \mathrm{d}F_{\text{Nmax}}/\mathrm{d}h = 902 \cdot 10^3/35.79\text{nN/nm}$, and $\varepsilon = 0.72$ the value $h_{\text{c}} = h_{\max} - \varepsilon F_{\text{N-max}}/S = 190.03\ \text{nm}$ and the value of $E_{\text{r}-ISO-\text{Ahc}-\text{direct}} = 23.74\text{nN/nm}^2$. When the direct calculation with A_{hc} is changed for $A_{\text{projected}}$, we obtain the absolute $E_{\text{r}-\text{direct}} = 20.9\text{nN/nm}^2$. The respective error factors 3.1 and 3.5 when compared with $E_{\text{riso}-\text{iterated}} = 73\text{GPa}$ [10] are enormous! They falsify convincingly these ISO iteration standards not only for this example. Such discrepancy similarly happens with other materials but it can be less drastically. The described iteration procedures for $E_{\text{r.ISo}}$ cannot describe the claimed above definition of $E_{\text{r}-1\text{so}}$. This demonstrates enormous data-treatment by false iterative fitting to unrelated Young's modulus.

Clearly, the "Young's modulus" claim of ISO is faulty from the beginning. It cannot describe a response to a unique linear elastic stress. Indentation moduli are face-dependent multiple mixtures of linear and shear moduli around the skew conical, pyramidal, spherical, and further indenters. Furthermore, it violates the energy law because F_{N} creates not only work for volume but also 20% of its value work for pressure generation and long-range modifications. This surprising generality has been easily deduced $[1,2,3,11]$. Finally, ISO does not detect and avoid any phase transition onset that might occur at $< F_{\max}[1-3]$, which must be done by checking for sharp kink in the linear Kaupp plot $[1-2,8]$ of the loading curve.

The physical indentation modulus

With the generally required aim for minimal change of existing hypotheses we start with the formal relation between unloading stiffness $(\mathrm{d}F_{\text{N}-\max}/\mathrm{d}h = S;\ \text{but now}$ experimental) and elastic modulus (E_{r}) in the form of $E_{\text{r}} = \pi^{1/2}S/2A^{1/2}$ as above, which appears to have been successful in several

Russian papers of the 1970s and 1980s, as cited [9]. The $\pi^{1/2}/2\ A^{1/2}$ factor is obviously derived from elastic contact theory arguments. The $A^{1/2}$ reflects one-dimensionality. It was adopted by [9] and ISO with the complication that it had been termed as root of contact area $A_{\mathrm{hc}}^{1/2}$ (see preceding paragraph). F_{max} for S must now be corrected with factor 1.25, because one must also include the 20% pressure part that is lost for the depth. We deduce so the physical hardness. As pyramids and cones have different areas A we prefer now the general equation 5.1 for the physical indentation modulus.

$$E_{\text{r-phys}} = (\mathrm{d}1.25F_{\mathrm{max}}/\mathrm{d}h)/A \tag{5.1}$$

The physical formula avoids energy law violation, and initial surface effects. But the maximal force must be below the phase-transition onset force for obtaining the impression modulus of the pristine material. All what's needed is the simple mathematic correction after linear regression of the loading curve before the kink. $E_{\mathrm{r-phys}}$ also avoids multi-parameter iteration fitting to a standard's Young's modulus. We obtain the absolute elasticity modulus of $E_{\mathrm{r}-phys} = 16.73\mathrm{nN/nm^2}$ for aluminium. That is very different from the obsolete iterated ISOmodulus (73 GPa) published [10].

Comparison of indentation with Young's moduli

We must now stress the principal difference of indentation moduli $E_{r-\mathrm{phys}}$ and unidirectional Young's moduli. Valid Young's modul detections require Hook's law, for example by unidirectional reversible tension ($\Delta L/L = p/E; p$ is pressure), or ultrasound speed in long rod $\left(v_s = E^{1/2}/\rho^{1/2}; \rho\right.$ is density). In more complicated cases resonance ultrasound spectroscopy (RUS) is used. Correct linear Young's moduli are unique in different directions, excluding shear-moduli. The 6 by 6 matrix of Young's moduli gives by cancellation 21 of them. This decreases further by crystal symmetry to $9{,}7{,}6$, or in the cubic case 3 independent moduli, as is generally communicated. Conversely, indentation moduli are multiple mixtures of linear and shear moduli around the skew conical, pyramidal or spherical and further indenter from all sides. They are face-dependent due to their different weight at different positions. As there seems to be some uncertainty about isotropy of cubic crystals that have been termed as "very isotropic" for the case of metals [9] and also by ISO, we demonstrate here cubic anisotropy. Fig. 5.1 exemplifies the different packing of bcc α-iron along [100], [110], and [111]. These directions exhibit marked different packing properties and thus also three independent linear moduli in these directions, according to the complete matrix analysis. This is a basic model for all types of cubic crystals as for example fcc aluminium or sodium chloride, etc. Furthermore, also three independent shear moduli ensue upon indentation into cubic crystals. The situation becomes more complicated in all other crystal systems with more elastic constants. Importantly, Fig. 5.1 indicates that the common relations between Young's, shear, bulk modulus, and Poisson's ratio cannot be applied to any crystalline materials, due to their anisotropy. However, that has been frequently carried out.

A more complex system is exemplified with trigonal-trapezoidal α-quartz (P3,21 or enantiomer P3,21) that mixes 6 independent Young's moduli upon indentation, according to the matrix analysis each with additional shear moduli. The dilemma is evident from Fig. 5.2. The various reported moduli values are reported by Crystan Ltd [12] and the linear moduli were determined by NIST with the elaborate RUS technique [13]. Only the -18 value is still judged "troublesome". Also the tensional moduli E for two directions and the shear modulus G from bending shearing of the main axis and the hydrostatic bulk modulus K [12] are also included. These values are compared with the obsolete phase-transformed iterated ISO indentation E_{ISO} (no surface designation and no original data available [9]), the for that purpose still useful though obsolete phase-transformed iterated $\mathrm{E_{r-ISO}}$ moduli on 5 different faces of α-quartz from 2005 [14], and the formula for the physical indentation modulus [2].

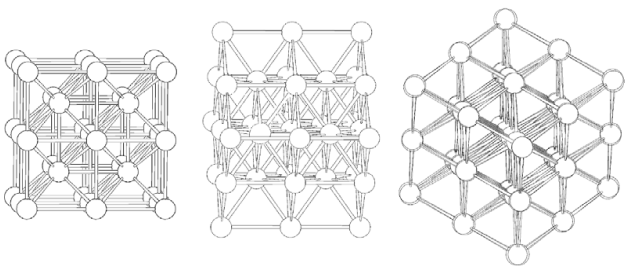

Fig. 5.1. The packing variation at the bcc α-iron (Im-3m; a $= 2.8665$Å) along the frontal [100], [110], and [111] directions, from left to right, respectively, showing the variable packing differences in these directions

Elastic moduli of α-quartz (trigonal, from Crystran)

6 independent Young's moduli: 106; 87; 58; -18; 13; 7 GPa (Hook, RUS)

Parallel to main axis:	E = 97.2 GPa	(Hook)
Perpendicular to main axis:	E = 76.5 GPa	(Hook)
Shear modulus:	G = 31.14 GPa	(Hook, bending, shearing)
Bulk modulus:	K = 36.4 GPa	(hydrostatic: –V (dp/dV)

Compared with Oliver-Pharr: E_{ISO}= 124 GPa (1992; uncorrected with the 3 flaws)

$E_{\mathrm{r\text{-}ISO}}$ onto 5 different faces of α-quartz (trigonal) varies within 20%: 133.6 (01-11), 119.7 (01-10), 109.4 (1-100), 109.0 (10-10), 105.0 GPa (10-11); (Indent)

$E_{\mathrm{r\text{-}phys}} = 0.8\ (\Delta F/\Delta h)\ /2h_{max} \tan\alpha$ nN/nm^2 (Indent)

What shall be used for mechanical parameters as deduced from indention modulus?

Fig. 5.2. Comparison of various elastic moduli of α-quartz; this $E_{\mathrm{r\text{-}phys}}$ formula is false and obsolete; cf Sections 15 and 16

The largest variations are in the Hook RUS Young's moduli series. The main axis tensile values are closest to the highest RUS values. All of these and the shear and bulk moduli are much smaller and unrelated to the much higher obsolete indentation modulus of Oliver-Pharr who initiated the ISO iterative modulus determinations with the false claim that these be "Young's moduli" [9]. Similarly, our five old ISO indentation modulus values on five different faces [14] are much too high at the obsolete ISO iteration level, due to the faulty iterations and phase transition. Unlike the strong variation in the RUS series, they vary within 20% (the largest at the direction with the thinnest channels) indicating at least the incompatibility and the surface dependence. However, these experimental values [14] are now obsolete. Valid E_{phys} indentation moduli appear most promising for the correction of the further mechanical parameters that derive from indentation (Fig. 5.3). They can not be identical with bulk moduli K. But K-values from compressibility measurements are much more difficult to obtain and their use with respect to indentation data would have to be carefully discussed. But this might perhaps also appear promising, because K includes all types of elasticity. Again, any relation of indentation moduli to Young's moduli is excluded and must not be tried.

Problems with elastic modulus E_{ISO} are detrimental because of its use in various widespread applications

All elastic properties of solid materials including viscoelastics

Elasticity index H/E

Input for FE-simulations

Stress-strain responce $\sigma = K(Y/E)^x$ and $K = Y(E/Y)^x$

Film adhesive strength $\sigma_f = E_s t_s^2/(1-\nu_s)\, 6 t_f (1/R - 1/R_0)$

Adhesion calculation (DMT and JKR) $F_N = 4E_r a^2/3R - 4\pi R\Delta\gamma$ and $a^3 = 9\pi R^2\gamma/E_r$, resp.

Creep, **viscoelasticity, rheology, Kelvin-Voight model use *mostly* K and G**

Material fatigue, fatigue strength **e.g. const** $(E/H)^n P/c^{3/2}$

Fracture toughness $K_c = 1.073 x_v (a/l)^{1/2} (E/H)^{2/3} P/c^{3/2}$

Sliding friction coefficient $\mu_s \propto \pi(3/4E_r)^{2/3} TR^{2/3}/F_N^{1/3}$

Contact area at dynamic testing in continuous stiffness mode $A = (dP/dh)^2 \pi/4E_r$

Film hardness $H_{eff} = H_s + (H_f - H_s) \exp(-Y_f E_s / Y_s E_f (h/t)^2$

Fig. 5.3. Some applications of elastic modulus as deduced for mechanical properties

Modulus-containing mechanical parameters

Fig. 5.2 indicates that the choice of an elastic modulus for the characterizing of further mechanical properties is not yet clear when most easily obtained indentation results are involved. The present problems are detrimental because of the numerous deduced parameters. The widespread use of the iterated so called "Young's modulus" indentation moduli E_{ISO} must be stopped. Fig. 5.3 collects the still most frequently applied uses of false-designated obsolete iterated E_{ISO} with its numerous described flaws. This is a detrimental situation with high general risk, as these values are unphysical. Any The unsuitable choice

for elasticity deduced mechanical parameters is detrimental. dilemma of ISO-standard 14577 with physics has to be replaced as soon as possible for the sake of correct science and even more importantly for every day's security; because most of the mechanical parameters in Fig. 5.3 are ill-calculated against basic physics and falsified iteration. The perhaps first ray of hope for a change is perhaps the use of the bulk (volume) modulus K in the rheological Kelvin-Voight model [15,16]. It should be noted in this respect that the parameters containing the H/E fraction change their dimension with E_{rphys} or with K. This might pose difficulties with their meanings. With the other mechanical parameters of Fig. 5.3 only their size will strongly change. The iterated ISO-moduli are obsolete and the non-iterated ISO moduli are still burdened with the physical flaws. But energetic and phase integrity flaws of the latter can be solved for reaching E_{phys}. The present situation is still involved. Detailed discussion and much work must resolve these most important questions.

5.4 CONCLUSION

The situation of elastic modulus from depth sensing indentations requires complete revision. The physical flaws of E_{ISO} are energy law violation, not caring for exclusion of phase change onsets, and not correcting for initial surface effects under load. Another very severe flaw derives from falsifying iterations with up to 11 free parameters (free sign change option) by obviously converging to Hook-law Young's modulus of standard materials by misinterpretation of the meaning. However, the indentation experiment is not at all unidirectional but contains linear and shear contributions from all sides of the skew indenters. This behavior also violates against the underlying definition of the ISO modulus and must be urgently discontinued. The false iteration becomes evident for example from cubic aluminium with $E_{\mathrm{r-ISO-Ahc-iterative}} = 73\mathrm{GPa}$ and iterative-free $E_{\mathrm{r-ISO-Ahc-direct}} = 23.74\mathrm{nN/nm^2}$, or $E_{\mathrm{r-absolute-direct-Aprojected}} = 20.9\mathrm{nN/nm^2}$ (all with the physical faults). Thus, only the newly defined absolute E_{phys} of $16.73\mathrm{nN/nm^2}$ or the corrected stiffness contain all elastic effects around the tip impression. Indentation moduli are thus not related to Young's moduli. Fortunately, $E_{\mathrm{r-phys}}$ or S_{phys} do not contain any of the physical and iterational flaws of $E_{\mathrm{r-ISO(-Ahc)}}$. There remains the question whether $E_{\mathrm{r-phys}}$ can be rapidly and broadly applied for the elasticity derived parameters of Fig. 5.3, Alternatives might be S_{phys} or compressively measured bulk modulus K. Such decision may depend on theoretical or practical arguments. Corresponding series of data pairs from both fields for comparison are missing and should be made available for evaluation.

E_{ISO} variations should no longer be used for Fig. 5.3 parameters and the like. Why shouldn't we stay with physics? Who is liable upon failure of ill-calculated materials, and what about the judge and the victims? ISO standardization procedures are slow:

1. We need new ISO standards and new textbooks for indentations!
2. We must be enabled to rely on material's properties and save health, time, and money!

3. Everything must become easier with simple mathematics without data-fittings and/or iterations!
4. We must no longer violate the first energy law and other basic physical laws!
5. We must honestly teach on basic physics!
6. We must remove previous errors!
7. We must make daily life safer in the future!
8. It is dangerous to fight against experimental evidence and convincing physical deductions based on elementary mathematics!
9. Life becomes safer, and brighter with admission of the physical truth.

COMPETING INTERESTS

Author has declared that no competing interests exist.

REFERENCES

1. Kaupp G (2016) The physical foundation of $F_N = k\,h^{3/2}$ for conical/pyramidal indentation loading curves. Scanning 38: 177-179.
2. Kaupp G (2017) Challenge of industrial high-load one-point hardness and of depth sensing modulus. J Mater Sci Eng 6: 348-355
3. Kaupp G (2017) The ISO standard 14577 for mechanics violates the first energy law and denies physical dimensions. J Mater Sci Eng 6: 321-328.
4. Kaupp G (2016) Important consequences of the exponent 3/2 for pyramidal/ conical indentations - new definitions of physical hardness and modulus. Mater Sci & Eng 5: 285-291.
5. Zhao S, Zhang J, Li Y, Liu H, Wang B, Zhao M. An indentation method for determining the film thickness, Young's modulus, and hardness of bilayer materials. Journal of Physics D: Applied Physics. 2022 Apr 21;55(27):274002.
6. Guo Y, Li J, Zhang Y, Feng S, Sun H. High-entropy R2O3-Y2O3-TiO2-ZrO2-Al2O3 glasses with ultrahigh hardness, Young's modulus, and indentation fracture toughness. Iscience. 2021 Jul 23;24(7):102735.
7. Phani PS, Oliver WC. A critical assessment of the effect of indentation spacing on the measurement of hardness and modulus using instrumented indentation testing. Materials & Design. 2019 Feb 15;164:107563.
8. Kaupp G, Naimi-Jamal MR (2010) The exponent 3/2 at pyramidal nanoindentations. Scanning 32: 265-281.
9. Oliver WC, Pharr GM (1992) An improved technique for determining hardness and elastic modulus using load and displacement sensing indentation experiments. J Mater Res 7: 1564-1583.
10. Soare S, Bull SJ, Oila A, O'Neill AG, Wright NG, et al. (2005) Obtaining mechanical parameters for metallization stress sensor design using nanoindentation. Int J Mater Res 96: 1262-1266.
11. Kaupp G (2013) Penetration resistance: a new approach to the energetics of indentations. Scanning 35: 392-401.
12. https://issuu.com/crystran/docs/handbook

13. Heyliger P, Ledbetter H, Kim S (2003) Elastic constants of natural quartz. J Acoust Soc Am 114: 644-650.
14. Naimi-Jamal MR, Kaupp G (2005) Quantitative evaluation of nanoindents: do we need more reliable mechanical parameters for the characterization o materials? Int J Mater Res 11: 1226-1236.
15. Metzger TG (2016) Das Rheologie Handbuch (5thedn), Vincentz Network GmbH&Co.KG, Hannover, Germany
16. Cheng L, Scriven LE, Gerberich WW (1998) Viscoelastic analysis of micro- and nanoindentation. Mat Res Symp Proc 522: 193-198.

DISCLAIMER
This chapter is an extended version of the article published by the same author(s) in the following journal.
Journal of Material Sciences & Engineering, 6:6, 2017.

Chapter 6
Print ISBN: 978-93-5547-921-1, eBook ISBN: 978-93-5547-922-8

Investigation on Six Polymorphs of Sodium Chloride upon Depth-Sensing Macroindentation with Unusual Long-Range Cracks Requiring 30 N Load

DOI: 10.9734/bpi/mono/978-93-5547-921-1/CH6

ABSTRACT

A sodium chloride single crystal is depth-sensing indented with a Vickers indenter at a Zwick/Roell ZHV Zwicky Z2.5 macro region instrument, together with Stephanie Rösner from Zwick GmbH & Co KG, Ulm, Germany. In order to experimentally secure the onsets of both known and unknown phase-transitions and to locate them with direct linear regression analyses while eliminating iterations. Normal forces up to 50 N load and 120 μm depth are applied. Four sharp phase-transition onsets could thus be identified experimentally, uncovering four new NaCl polymorphs in addition to the long-known fcc and bcc polymorphs. It is unclear how they relate to the three theoretically anticipated higher pressure crystal forms in Reference. The projected metallic character is not clear because the author did not see any colour development or metallic reflection up to 50 N loads. At the indenter tip, there is no cracking of any kind, but at the 30 N ranges, there was a new sort of long-range cracking, and its highly resolved microscopy revealed two-step nucleation at a polymorphs' interface exit. Unloading observed with an inverted 3D microscope that a macroscopic crack had developed along the created interface direction and exited apon slightly higher force, far apart at the crystal edge. Seven powers of ten are covered by the calculated phase-transition energies. These data cast doubt on the accuracy of non-depth-sensing ISO/ASTM Standards for industrial Vickers, Brinell, and Rockwell hardness parameters because they cannot account for multiple phase-changes that are ineluctable under very high loads, do not define pristine as opposed to phase-transformed industrial materials (including super-alloys), and fail to recognise the allowable pressure stress for delaying phase changes, etc. Depth sensing is necessary due to the possibility of failure from crack nucleation at polymorph interfaces. A quick way to identify phase changes is the analysis of the sharp unsteadiness in the $F_N = k\ h^{3/2}$ plots, as shown by previously reported loading curves. The mathematically required 5/4 ratio of applied work over indentation work is then easily determined (Chapter 2).

Keywords: 3D-Microscope; 3D impression shape; 5 consecutive phase-changes; consequences for vickers hardness; far distance crack nucleation; far-distance effects; favorable model; high pressure depthsensing

indentation; indentation work; kaupp-plot; linear regression; metallization problem; new cracking behavior; physical hardness; physical modulus; sodium chloride.

6.1 INTRODUCTION

One of the most researched sodium chloride features is its mechanical Properties. Additionally, it has been calculated that the phase-transition above the well-known B1 (Halite, fcc, Fm3m) to B2 (bcc, Pm3m) of sodium chloride into more energetic ionic polymorphs with predicted metallic character ("above 584GPa via indirect band-gap closure") could occur. These structures include Cmcm, Imm, and Pbcm at increasing pressure ranges and formation enthalpies [1]. Experimental evidence is still lacking, though. From a published experimental Vickers indentation diagram of NaCl, just one higher energy phase-transition (to yield #3 in the explanation that follows) had been taken out [2]. The linearization is the physically deduced "Kaupp-plot" (so scolded by skeptic iteration experts) $\left(F_{\mathrm{N}} = kh^{3/2}\right)$, as calculated from the experimental F_{N} versus h loading plot [2]. It had revealed a kink discontinuity at $2.5\ \mathrm{N}$, which was attributed to the #3 polymorph (perhaps CrB type?) under pressure [3], provided repeatability of the work [4]. Thus, the repetition experiment was necessary, because the paper of [4] contains several inconsistencies: multi-parameter iterations using ISO-$14577h$ from $E_{\mathrm{r-ISO}} = 50\mathrm{GPa}$ iteration, followed by a second order polynomial with $\alpha_{\mathrm{eff}} = 70.4°$and " $R_{\mathrm{eff}}3.3\mu\mathrm{m}$ " for a "sharp" Vickers indenter were used for the construction of an unphysical " F_{N} versus h^2 relation", or pileup was mentioned but it is not discernable in the provided images, or the figure refers to in situ values for NaCl up to post-indentation values up to $45\ \mathrm{N}$ (!) with error bars as "calculated from $P-h$ data" [4]. Apparently, this tried to substantiate an (unphysical) " F_{N} versus h^2 relation", whereas the maximal load was only $4.6\ \mathrm{N}$. That is more than puzzling! Phase-changes were not considered [4]. All of that requires an experimental check for reproduction, in order to secure the result of our physical analysis that found a sharp kink at $2.5\ \mathrm{N}$ by a phase-change. Furthermore, it was to be checked whether further increased load would allow the detection of further polymorphs with metallization of sodium chloride by local color change with a metallic reflection $[2,5]$. Also, the reproduction with the elucidation of any cracking appeared necessary. The thermal conductivity of the fcc NaCl at $298\ \mathrm{K}$ is $4.6\ \mathrm{W/mK}$ [6]. Also the thermal expansion (44 10^{-6}/K) of the fcc [6] and bcc phase at are rather low [9]. This is relatively high for a non-metal so that we do not expect significant temperature increase during the endothermic phase-transitions upon the indentation. The effects of NaCl on cements have been studied in [7]. A recent compression (not indentation) study [8] of a chloride-anion from trimethylammonium chloride containing polymerized hydrogel sample provided a stress-strain curve for real Young's modulus (deformed length/original length) and numerous further mechanical properties. But a compression test is not indentation. The activation energy of the fcc to bcc transition (from RT to $400°\mathrm{C}$) is $0.001716\mu\mathrm{J}/\mu\mathrm{N}$ [3]. The physical hardness H_{phys} is the normalized energy-corrected indentation resistance k for conical/ pyramidal indenters [2]. That is general for Vickers indenter with $H_{\mathrm{phys}} =$

$0.0325745k$, where k is the penetration resistance (the slope of the so-called Kaupp-plot) from $F_N = kh^{3/2}$ (Fig. 6.1).

6.2 MATERIALS AND METHODS

A drilled $40.323.06.3\ \mathrm{mm}^3$ two sides polished sodium chloride mono-crystal window plate from Alpha Aesar Thermo Fischer GmbH, Kandel, Germany was used for the indentations at (for technical reasons) $2.5 - 3.5\ \mathrm{mm}$ distance from the sides. 3 at least $5\ \mathrm{mm}$ distant in-dentations at $5\ \mathrm{N}$ loads were averaged. One indentation each was performed displaced at opposing sides for 20 and $50\ \mathrm{N}$ loads. The kinks have been calculated from the linear branches' trend lines with > 0.999 correlation coefficients. The displacement-controlled measurements used a depth sensing Zwick/Roell ZHV Zwicky Z2.5 macro region instrument according to ISO 14577 with compliance of $0.0046985\ \mu\mathrm{m/N}$ at $1\mu\mathrm{m/s}$ load and unload rates, and unloads after $30\ s$ hold periods, in the open air by the sample in the ambient atmosphere. The calibrated Vickers indenter (E 27781, MPA Stuttgart, Germany (DIN EN ISO 6507-2) withstood "the functional requirements within the allowed limits". A 3D digital optical microscope Keyence VHX 100 with a lens providing the $500\mathrm{X}$ to $5000\mathrm{X}$ enlargement range was used with a CCD-camera at almost uniform coaxial vertical (surjective) illumination through an optical fiber in the open air. The separate $25\mathrm{X}$ lens was not adapted to the 3D-facility. The light of a halogen lamp was coaxially reflected back by the sample in ambient atmosphere through a half mirror along the illumination axis into an optical fiber, sending the signals for digital imaging. Equidistant focal images at either 1 or $5\mu\mathrm{m}$ distance were taken under automatic position correction. The Keyence software composed these to 3D-images or projections therefrom. As the indentations and microscopy were performed in ambient atmosphere, control images were performed after 10 months storage in a closed box in the air with the silica drying grain of Alpha Aesar, to check the stability of the features.

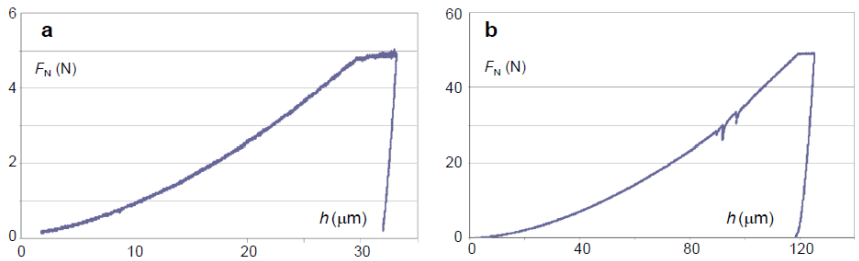

Fig. 6.1. Indentation force-depth curves on NaCl (a) up to 5 N and (b) up to 50 N with a minor depression at 28.5 N and main depressions at 29.8 and 34.0 N loads that are also seen in the linearized F_N versus $h^{3/2}$ plot (Fig. 6.2). They indicate the formation of very distant cracks

The data analysis for indentations with pyramidal or conical indenters used the physically founded "Kaupp-plot" (normal force versus depth$^{3/2}$ relation; (6.1)

(Fig. 6.2), the energy law-corrected universal indentation hardness H_{phys} [10], and also the energy corrected indentation modulus $E_{\mathrm{r-phys}}$ all without any free-parameter iterations or polynomials or curve fittings [2,10,11]. Everything started with the penetration resistance values k (the slope of the so called Kaupp-plot) before and after the sharp kink onsets at the intersections of the calculated regression lines. Sectional integrations with respect to phase-changes obtained indentation work W_{indent}, applied work W_{applied} and by energy balance the phase-transition energy $W_{\mathrm{transition}}$. Only these known physically deduced eqns. (6.1-6.7) were used for the calculations [2,3,10,12-14]. Correction for any axis-cut is necessary. The linear regression lines are calculated with $Excel^{(\mathrm{R})}$ in their regions. The correlation coefficient was always $r > 0.999$. The linear red regression lines in Fig. 6.2 are hand-drawn along the plot branches for visualization. The unloading stiffness S, as obtained from the slope at maximal force of the loading force F_{max}, is obtained from the regression of the first linear points (with 100 to 500, mostly 200 points) of the original unloading data. The factor 0.8 is necessary for complying with the energy law, because the depth and volume have been created only with $0.8F_{\mathrm{N}}$ [5,11]. The use of eqn. (6.3) for $E_{\mathrm{r\text{-}phys}}$ is reformulated for pyramids that are no longer pseudo-cones (Chapter 16, see there), with respect to incorrect, when excluding false pseudo-cone and correctly using the experimental stiffness S at peak load of the unloading curve. Eqns. (6.5 and 6.7) are the physical deductions for the applied energy, for obtaining the energetic balance as phase-transition energy [5]. Due to the exponents and differences, the calculations used up to 9 numerals after the decimal point with a pocket calculator, followed by reasonable rounding at the end results.

$$F_{\mathrm{N}} = k\,h^{3/2} + F_{\mathrm{a}} \tag{6.1}$$

$$H_{\mathrm{phys}} = k = F_{\mathrm{N}} / h^{3/2}\ [\mathrm{mN/\mu m^{3/2}}] \tag{6.2}$$

$$E_{\mathrm{r\text{-}phys}} = (\mathrm{d}1.25F_{\mathrm{N}}/\mathrm{d}h)\,/A\ [\mathrm{mN/\mu m^{2}}] \tag{6.3}$$

$$W_{\mathrm{indent}} = 0.4k\left(h^{5/2} - h_{\mathrm{kink}}^{5/2}\right) + Fa(h - h_{\mathrm{kink}}) \tag{6.4}$$

$$W_{\mathrm{applied}} = 1.25W_{\mathrm{indent}} \tag{6.5}$$

$$W_{\mathrm{transition}} = \mathrm{full}W_{\mathrm{applied}} - \Sigma\left(W_{\mathrm{applied}}\right)_{\mathrm{n}} \tag{6.6}$$

$$\mathrm{full}W_{\mathrm{applied}} = 0.5F_{\mathrm{N-max}}h_{\mathrm{max}} \tag{6.7}$$

All eqns. (6.2-6.7) derive from the principal eqn. (6.1), where h is the penetration depth. The linear Kaupp-plot according to eqn. (6.1) reveals all initial surface effects by axis cut F_{a} for correction, and all exothermic or endothermic phase transition onsets as kinks between linear branches if these occur at the chosen load-ranges (Fig. 6.2).

The eqns. (6.1-6.7) are not reproducing the long history of conical indentations. The first trial was the Boussinesq's problem of 1885 that found two different mathematical solutions in 1939 and 1965, but both with an exponent 2 on h instead of $3/2$ as in eqn. (6.1). The result from reference [15] was taken up from Oliver-Pharr and this became the basis for ISO 14577 with annual refinements and extensions, but still keeping with the exponent 2, [15-17], which is however at variance with experimental loading parabolas. All of these did not appreciate that the normal force is not only used for creating a volume but also for creating pressure to the environment of such volume. Due to the thus wrong exponent 2 on h, polynomial iterations are required for fitting the load/depth parabolas, be there phase changes or none of them at the chosen loading ranges. Only most finite element simulations are made to converge with h^2, but these fail [14]. Unfortunately, the software of instrument builders must apparently obey to the false ISO standards with the Oliver-Pharr multi-parameter iterations for the measurement of $\mathrm{H_{ISO}}$ and $\mathrm{E_{r-ISO}}$. As long as eqn. (6.1) was only empirically secured by the exponent analysis of loading curves there was a strange objection against eqn. (6.1) with the absurd construction of the transformation kink from a line between two points of a poor very blunt indenter measurement with the second linear branch, instead of between the also there depicted extended first and second linear branches [18]. They advocated the fitting of the whole loading curve instead, without separating out their considerable initial effect, by using broken exponents (e.g., exponent 1.75285 or 1.82723) for different parts of the loading parabola and thus acknowledging the very odd dimensions of such parabola constants. This failure encouraged another defaming publication in 2014 with an equally undue trial to degrade the physically correct "Kaupp plot" as "Kaupp-fitting" [19]. But the "Kaupp-plot" using eqn. (6.1) excludes all data-treatment, and it is therefore totally different from these author's iterative polynomial data fitting procedures. They tried with a strange so-called "Theoretical Confirmation of the exponent 2 on h ", which is far away from any scientific deduction, by including the result in their "deduction" of their "theoretical confirmation", and they did not consider the excellent opposing curves [14]. It is unscientific to use a definition of hardness $\mathrm{H_{ISO}}$ that includes the (false) exponent 2 on h (the hardness is the constant in the force-depth relation!) in connection with an also defined projected contact area $\mathrm{A} \propto \mathrm{h}^2$, for reaching $\mathrm{H} = \mathrm{P}/\mathrm{A}$ giving $\mathrm{P} \propto \mathrm{h}^2$ as already defined in the definitions. The capital error in these definitions is their energy law violation, by not considering the energy for the pressure generation (a parabola with the false exponent 2 would require 33% of the applied indentation energy that cannot be obtained from nothing [5,10]. With other words: the coupling of volume formation with pressure formation is again totally disregarded [19]. Both factors require work that comes from the normal force P we call it F_{N}[5,10].

These invalid allegations have been overcome by the physical deductions of the energetic situation in 2013 and of the exponent $3/2$ as published in 2016[2] (See also Chapter 11). The scientifically valid deduction of the exponent on h of the force-depth loading curve starts with normal force $F_{\mathrm{N}} = kh^{\mathrm{x}}$. Reference [2,5] rightfully combines the components of the normally applied force F_{N} with $F_{\mathrm{N}} = {F_{\mathrm{Nv}}}^{m}{F_{\mathrm{Nv}}}^{\mathrm{n}}$ (p for pressure, v for volume). The total pressure (+ loss

of p by plasticization, etc) is $p \propto V_{\mathrm{cone}}$ [2]. With the volume $V_{\mathrm{cone}} = \pi(\frac{\tan\alpha)^2 h^3}{3}$ it follows p_{total} and thus also $F^m \propto h^3$ that is lost for the penetration. With $h = {F_{Np}}^{1/3}$ one obtains the exponent $\mathrm{m} = 1/3$ for ${F_{\mathrm{Np}}}^{\mathrm{m}}$, and thus also the exponent $\mathrm{n} = 2/3$ for ${F_{\mathrm{Np}}}^{\mathrm{n}}$. Therefore (after conversion), $F_{\mathrm{Np}} = k'h^3$, which had to be deduced. It is Therefore (after conversion), $F_{\mathrm{Nv}} = kh^{3/2}$, which had to be deduced. It is a universal physical law with mathematical precision [2,10,11]. The here printed eqn. (6.4) contains also the obvious extensions for the case of phase change. The linearly applied work is $W_{\mathrm{applied}} = 0.5F_{\mathrm{Nmax}}h_{\mathrm{max}}$ from where it follows with the indentation work $W_{\mathrm{indent}} = 0.4kh^{5/2}$ and eqn. (6.1) that $W_{\mathrm{applied}} = 1.25W_{\mathrm{indent}}$ in eqn. (6.5). Thus, eqn. (6.1) mathematically quantifies 20% of the lost work (a property of every parabola with exponent $3/2$) and thus also the lost normal force of F_{N} for the indentation [5,10]. Transition energies from phase changes (new phases have different k values) are the energy balance as in eqn. (6.6). Eqn. (6.7) describes the linear normal force application, eqns, (6.3) and (6.5) are deduced [5,11].

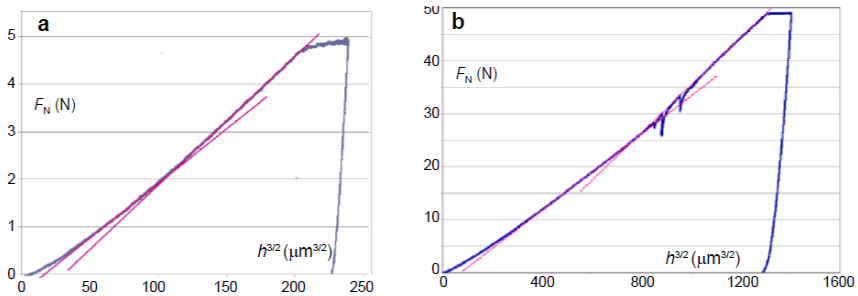

Fig. 6.2. Linearized loading curves (Kaupp-plots) (F_N versus $h^{3/2}$) at (a) 5 N and (b) 50 N load, showing in red the linear branches that intersect at the phase-transition points: (a) at 2.487 N, (b) at 24.428 N

6.3 RESULTS

Hardness, modulus, and polymorphs

The ISO standard 14577 for pyramidal indentations violates the first energy law and denies physical dimensions. The analysis of loading curves ((F_{N} versus h) (Fig. 6.1) according to the Kaupp-plot ($F_{\mathrm{N}} = kh^{3/2}$). (Fig. 6.2) recognizes phase-change onsets by sharp kink unsteadiness only in the linearized loading curves with the correct exponent 3/2 on h [3,10]. The physical hardness is obtained without complications from the penetration resistance k (the slope of the so called Kaupp-plot) eqn. (6.2) and the reduced modulus directly from stiffness S and h according to eqn. (6.3) (without one with 3 and one with up to 8 freeparameter iterations of ISO) [11]. Different polymorphs must have different

hardness and elasticity [11]. The H_{phys} values in Table 6.1 vary by a factor of 5.939, the indentation moduli by a factor 2.246. However, the meaning of the latter must be considered with care, as multiply phase transitioned polymorphs are unloaded, the reversion rates of which are unknown. There is no modulus value for the halite (fcc) and for #5 in Table 6.1, as unloading curves within their load ranges for the present conditions are lacking. But such values cannot be easily judged and present conditions are lacking. But such values cannot be easily judged due to the expected strong enhancement of elastic moduli at increasing pressure (the tabulated Young's modulus of $50\mathrm{GPa}$ for fcc NaCl cannot be compared) [20]. The physically deduced $E_{\mathrm{r-phys}}(3)$ definition both are not Young's moduli. They are "indentation moduli". Young's moduli are strictly unidirectional [11]. This restricts the general value of indentation moduli, even though they belong to the most cited and used values from indentations. Nevertheless, the $E_{\mathrm{r-phys}}$ sizes are listed.

Table 6.1 shows the k-values (penetration resistances) and transition onsets with the H_{phys}-values. The values of k and thus H_{phys} increase by a factor of 5.939 and indicate four phase-changes though at very different normal force ranges from $10\mathrm{mN}$ to $50\ \mathrm{N}$. Their discussion must take into account that the polymorphs exist between their kink pressures, which are often disregarded.

The pristine materials' values have to be taken at loads before the first phase-change kink that has to be detected with eqn. (6.1) and Kaupp-plot. For example, the Figs. 6.1a and $6.1\ \mathrm{b}$ with F_{N} versus h do not recognize phase-transition onsets. These are only revealed by the Kaupp-plots in Fig. 6.2 according to eqn. (6.1), as exemplified for the 5 and $50\ \mathrm{N}$ impressions, The kinks are clearly seen there, but the ranges of fcc to bcc are almost hidden at the $5\ \mathrm{N}$ ranges and require the corresponding plots at much lower force that are not displayed here (Table 6.1).

The validity of the NaCl loading curve of [4] could be confirmed. Its residual impression diameter (ca $225\mu\mathrm{m}$ at $4.3\ \mathrm{N}$) compares favorably with the present one ($243.73\mu\mathrm{m}$ after $5.0\ \mathrm{N}$ load). Also the second transition onsets at $21.096\mu\mathrm{m}$ and $2.5\ \mathrm{N}$, as calculated from the loading curve data [4] and published [3,5] comply excellent with the $20.8076\ \mu\mathrm{m}$ and $2.487 \pm 0{,}05\ \mathrm{N}$ values in Tables 6.1 and 6.2 . This confirms the first experimental proof of a third NaCl polymorph at high pressure since 2013. The fcc to bcc transition of NaCl of [2] is also present in Fig. 6.2a, but not precisely accessible at the scale of $5\ \mathrm{N}$. Figs. $6.1\ \mathrm{b}$ and $6.2\ \mathrm{b}$ demonstrate the situation with the $50\ \mathrm{N}$ indents. The depressions in the $30\ \mathrm{N}$ regions locate the cracking onsets. These cracks are not radial or horizontal at the indenter but far-away long-range and they do not disturb the linear branch as depicted with the upper thin red line (the depression points are of course not part of the regression). Interestingly, the second through fifth phase-changes from the 5 , 20 , and $50\ \mathrm{N}$ impressions did not exhibit a color change or metallic reflection d own to $0.120\ \mathrm{mm}$ (Tables 6.1 and 6.2), as should be expected for metals, but electric conductance measurements during indentation of NaCl are additionally planned.

Phase-transition work

Table 6.1 also contains the indentation works (6.4) for their stability ranges (for #6 only up to $50\ \mathrm{N}$) of the various polymorphs and the normalized values that strongly increase with the loads. As integrations are not allowed over unsteadiness such as e.g., kinks, these W_{indent} (Table 6.1) were obtained by integration eqn. (6.4) from zero to first kink, then kinks to next kinks, and finally last kink to the chosen end. The variation of the indentation works is very large (> 7 powers of 10, and normalized by a factor of 872). While the fcc (Fm3m) and bcc (Pm3m) polymorphs are well documented, only quantum chemical calculations predict higher pressure polymorphs with space groups Cmcm, Imma, and Pbcm [1]. Further possibilities for the sixth polymorph are perhaps the not predicted Pnma, twinning, or amorphous phase. There is yet no means for selecting and inserting another polymorph into the theoretical sequence of 3 polymorphs with increasing enthalpy.

The quantitative physical indentation allows for the determination of phase-transition energies, using the non-iterative elementary closed eqns. (6.5-6.7). The energy balance is calculated using W_{indent} kink by kink from Table 6.1 that is multiplied with $5/4$ for obtaining the applied work $W_{\mathrm{applied}}(6.5)$ and then the phase-transition work $W_{\mathrm{transition}}$ (6.6) that is subtracted from the full applied work for all sections from zero to the kink value in $F_{\mathrm{N}} - h$ [5]. Finally the whole transformation energy up to $50\ \mathrm{N}$ is obtained by summing up all sectional W_{applied} contributions. The values and sums are listed in Table 6.2. For example the full W_{applied} up to $50\ \mathrm{N}$ is the area of the triangle of zero to h_{max} of the $F_{\mathrm{N}} - h$ curve $(119.235\mu\mathrm{m})$, up to the final load (50N), and hypotenuse from zero to $F_{\mathrm{max}}\ (50\ \mathrm{N})$. Fig. 6.1 b when extrapolated to $50.00\ \mathrm{N}$ gives $2980.88\ \mathrm{N}\mu\mathrm{m}$ for full W_{applied} The sum of all sectional W_{applied} values is $2708.6913\ \mathrm{N}\mu\mathrm{m}$ (Table 6.2). The subtraction from full $W_{\mathrm{applied}}(2980.88\ \mathrm{N}\mu\mathrm{m})$ gives the full transformation energy from zero to $50.00\ \mathrm{N}$ as $272.189\ \mathrm{N}\mu\mathrm{m}$. This is remarkably 9.13% of the indenter work: the indenter has to provide that work for the 5 endothermic phase-transitions to occur up to $50.00\ \mathrm{N}$ load.

The energy treatment provides variations up to 3.61×10^7 (W_{applied}), 5.05×10^7 (full W_{applied}), and 2.63×10^7 fold ($W_{\mathrm{transition}}$) of the different works (the capping of the #6 value at $50.00\ \mathrm{N}$ load is arbitrary, not related to a physical event). All of these 4 phase-changes of NaCl are endothermic. The contributions of the normalized transition work $(\mathrm{N}\mu\mathrm{m}$ per $\mu\mathrm{m})$ are also strongly increasing with the load by a factor of 4.15×10^4 (Table 6.2). We deal here with the polymorphs that actually exist at the indenter interface for a characteristic load-range, in addition to the displaced phase-changes regions that, of course, continue to be shifted, more and more away from the tip interface with formation of their respective interfaces that may or may not be commensurate. Here we have no cracks around the tip but only very distant macro-cracks at very high load (Figs. 6.3-6.6). This certainly complicates the meaning of the indentation moduli from the unloading curves, when the highly energetic polymorphs revert to the stable halite (fcc).

Table 6.1. Mechanical data of depth sensing Vickers indentations onto an optical NaCl window plate, including the physical indentation work

The NaCl transition onsets	*k*-values (mN/μm$^{3/2}$) and F_a (N)	$F_{N\ kink}$ (N)	$H_{phys}=0.8\ k/(\pi\ tg\ \alpha^2)$ (mN/μm$^{3/2}$)[e)]	$E_{r\text{-}phys}=0.8\ S/(2\ h_{max}\ tg\ \alpha)$ (mN/μm^2)[e)]	$W_{indent}=0.4\ k\ (h_2^{5/2}-h_1^{5/2})+F_a(h_2-h_1)$ (Nμm)	Normalized W_{indent}(Nμm/N)
fcc to kink[a)]	4.1014; 0. 000067	0.000618	0.2408	n.a.b)	0.000038908	0.06296
fcc to bcc[a)]	6.6796; 0.0005632	0.003397	0.2724	32.245	0.00076675	0.2759
bcc to #3[c)]	28.2; 0.0222	2.4870 d)	0.7427	21.617	21.9236	8.6668
#3 to #4	33.8; −0.6964	9.1186	1.101	17.698	136.1690	20.533
#4 to #5	35.6; −1.0890	24.4284	1.160	n.a.b)	604.6890	39.5121
#5 up to 50N	43.9;	up to 50	1.430	14.356	1404.5208	54.925
(part of #6)	−8.3251					

a) Indented with Berkovich [3];
b) Not available; a first principle calculation predicts bulk moduli of $27.117 GPa$ for fcc-NaCl and $27.934 GPa$ for bcc $NaCl$ at zero pressure [20];
c) This polymorph was assumed to be the bcc $NaCl$ [2] but already corrected [4];
d)This reproduces the $2.5\ N$ value at $21.1 \mu m$ depth [2] as had been extracted from the published loading curve of [4]. e)These values had been calculated with the now disproved pseudo-cone formulas (see Chapter 16)

Table 6.2. The arithmetically obtained applied and transition energies of the various NaCl polymorphs upon depth sensing nano to macro indentation with the Vickers indenter

NaCl transi-tion onsets	h_{kink} (μm)	$W_{applied}$ (Nμm)	$\Sigma W_{applied}$ (Nμm)	Full $W_{applied}$ (Nμm)	$W_{transition}$ (6) (Nμm)	Normalized $W_{transition}$ (Nμm per μm)
fcc to kinka)	0.1909	$4.8639 \cdot 10^{-5}$	$4.8639 \cdot 10^{-5}$	$5.8988 \cdot 10^{-5}$	$1.0349 \cdot 10^{-5}$	$5.4212 \cdot 10^{-5}$
fcc to bcca)	0.69784	$95.8437 \cdot 10^{-5}$	$1.007076 \cdot 10^{-3}$	$1.4790 \cdot 10^{-3}$	$0.471924 \cdot 10^{-3}$	$0.6763 \cdot 10^{-3}$
bcc to #3	20.80762	26.95876	26.959767	27.018690	0.058923	$2.8318 \cdot 10^{-3}$
#3 to #4	45.01300	170.21126	197.17103	205.22778	8.05675	0.1790
#4 to #5	82.89834	755.86927	953.04030	1012.29245	59.25215	0.7148
#5 up to 50N (capped #6)	120.8539	1755.6510	2708.6913	2980.88	272.189	2.2522

a) Indented with Berkovich [3]

Inverted shape of the residual impressions

Impressions are better imaged in the inverted pyramidal form and as sharp projection of their 3D-images for better looks at their height and surfaces. This helps to qualify the surface appearances (Fig. 6.3). The side faces are mostly smooth, but there is always some material on the impression faces, small at the lower load and larger at the higher and highest loads. The edges and apices are always rough and thus clear indications of reverting NaCl polymorphs. Particularly the $20\ \mathrm{N}$ (cubic to brick-like) and $50\ \mathrm{N}$ inverted impressions (less so also at $5\ \mathrm{N}$) reveal crystallization at the apex (actually depth) and at the edges. This confirms the obvious corresponding polymorph reversions. The regular structures that cover the edges are also seen in the 2D-projections and these differ from each other, due to the varying number of reverting polymorphs. Upon 10 months storage, the features along the rims completed their crystallization giving linearly aligned cubes each with $7\mu\mathrm{m}$ side lengths; most of them almost perfect to both sides in the horizontal direction of Fig. 6.3c. The depth of the $50\ \mathrm{N}$ impression stays at measured $110\mu\mathrm{m}$; most of the side faces remain smooth. The white areas augmented 4 to 5-fold, but their maximal height of $6\mu\mathrm{m}$ towards the indentation surface was not superseded (these are, of course, depressions at the inverted Fig. 6.3). This augmentation upon long storage excludes their being surface defects of the indenter. The darker areas remained less than $1\mu\mathrm{m}$ high giving more straylight than the white ones. Moisture influence is thus very unlikely, as that would have influenced the extremely small $(< 1\mu\mathrm{m})$ crack lines in Fig. 6.6a, below.

On-site studies with highly focused X-ray diffraction would appear promising for verification of the theoretically predicted structures and for the elucidation of the sixth polymer's structure.

Cracking behavior

The lack of any radial or lateral cracks at the indenter tip interfaces up to $50\ \mathrm{N}$ load and $120\mu\mathrm{m}$ depth is surprising in view of the multiple phase-changes. It is not only due to a high ductility, but also to an apparently reasonable compatibility between the adjacent polymorphs, as these are formed. This is already seen from the fact that the bcc NaCl volume undergoes a considerable decrease from 27.6 to $17.6\ \mathrm{A}^3$ at $300\ \mathrm{K}$, when the pressure in an anvil cell is increased from 30.6 to $180\mathrm{GPa}$ [21]. Furthermore, the experimental $\mathrm{fcc} \rightarrow \mathrm{bcc}$ volume drop of 5.7% [22], and the small predicted volume drops from first-principle calculated polymorphs of $5.03\%(\mathrm{fcc} \rightarrow \mathrm{bcc})$, $1.19\%, 0.92\%$, and 0.33% [1], are also judged helpful for avoiding cracks. Fig. 6.4 proves the absence of radial cracks with highest precision by $500\mathrm{X}$ and $5000\mathrm{X}$ lens 3D-microscopy. This excludes calculation of common fracture toughness values. Also lateral cracks were not seen on careful visual inspection of the fully transparent sample. Importantly, the absence of cracks from the corners is still retained after 10 months storage ($50\ \mathrm{N}$ impression with $5000\mathrm{X}$ lens).

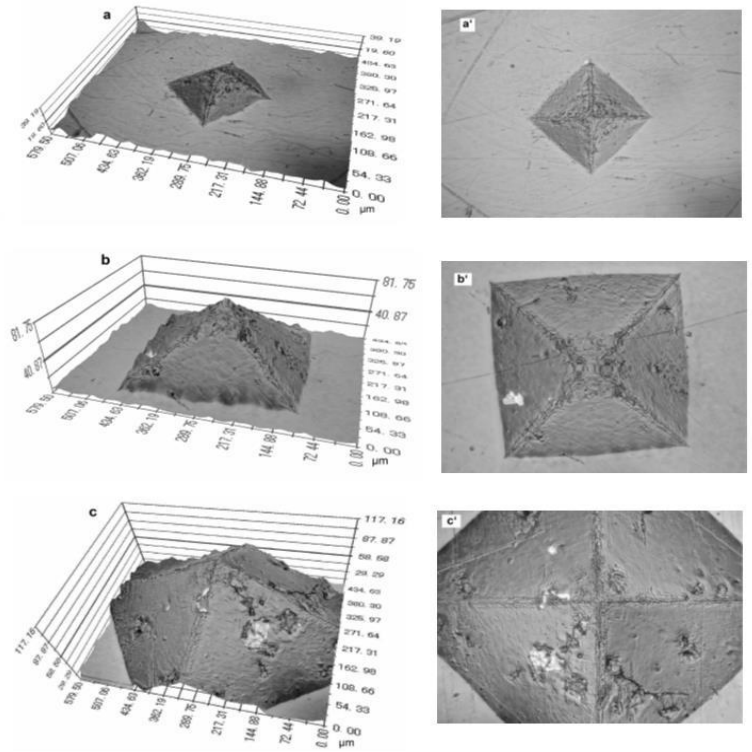

Fig. 6.3. 3D-microscopic images of inverted residual impressions, and their projections (a,a') 5 N, $h_{\max}31\mu$m; (b,b') 20 N, $h_{\max}$ 78μm; (c, c′) 50 N, $h_{\max}115\mu$m

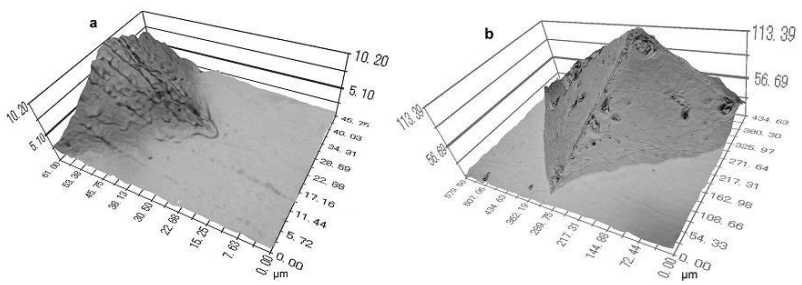

Fig. 6.4. 3D-microscopic inverted corner images of indented NaCl with the apices capped of (a) residual 20 N impression (5000X lens; 14 x 1-μm focal distance images composed), (b) 50 N impression (500X lens; 28 x 5-μm focal distance images composed), showing the distinct end at the corners, excluding any radial cracking

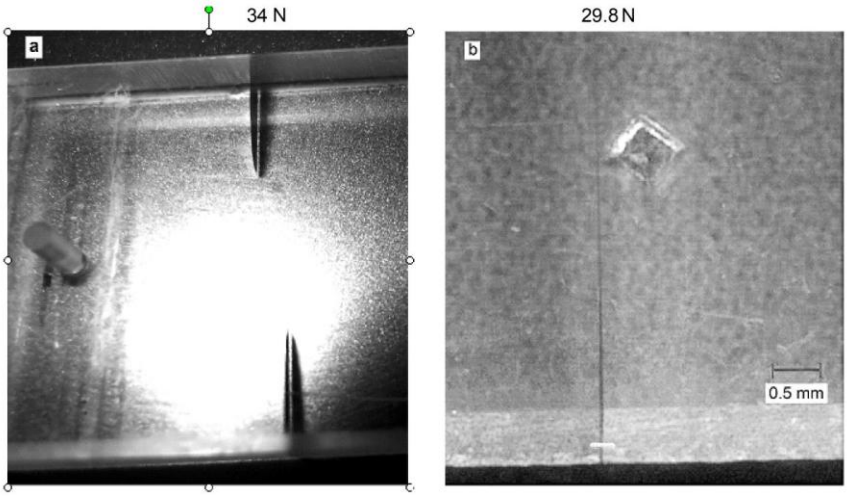

Fig. 6.5. (a) Flash photo on (-100) of NaCl at 29,8 and 34 N at the 50 N indentation, showing both cracks enhanced by the shadows; (b) microscopic 2D-image with $25X$ lens on (-100), showing both the base of the impression on (100) shining through from underneath and the crack on (-100); unfortunately the actual stop of the crack after $2/3$ of the front face could not be shown by the 2D-microscope with vertical illumination in reflection mode. The crack ends at the white bar that was added

Only two large cracks formed at short sequence in the 30 N regions, far away from the indenter corner, but only at the opposite side of the 6.3 mm thick sample. They happened when the depressions of Fig. 6.1 b occurred. The exclusive formations of 5.8 and 6.9 mm long cracks on (-100) of sodium chloride along the (00-1) cleavage planes (with respect to (100) for the indentation) at the extreme loads of 29.8 and 34.0 N when reaching 92.94 and 97.31μm indentation depth (Fig. 6.1b) are unusually far away from the actual impression. Fig. 6.5a shows a flash-light photo of the (-100) surface (opposite to the impression side). These cracks are enhanced by the so generated shadows. The top one ends at half of the outer sample depth, the bottom one at about $2/3$ of the sample depth of 6.3 mm. The distance between the crack planes is 1.89 mm.

The 2D-microscopic image with a 25X lens (Fig. 6.5b) shows the 50N indent from the backside (coming up) with its basal diameter of 0.815 mm. For technical reasons the stop of the crack at $2/3$ of the front face (a white bar has been included) cannot be shown by the 2D microscope with vertical illumination at reflection mode in Fig. 6.5b. The distance of the indent to the sample edge is 3.32 mm. The distance from indent's center to the (00−1) planes of the cracks is 0.18 mm and 2.07 mm, the distances to the start of these cracks on their surfaces are 6.15 and 13.31 mm, respectively. The cracks reach a maximal width of 11.2

and 7μm towards their exits, where their depths are 3.15 and 4.2 mm down with end-widths at the 1μm range. The very far distances of the cracks from the indentation and none of them at the indenter deserve a closer inspection (Fig. 6.6). As already mentioned in the Hardness, Modulus, and Polymorphs Section, the long-range crack formations are responsible for the depressions in the Fig. 6.1 b. The miniscule depression at 28.5 N preceding the first more important one at 29.8 N provides an important clue for the nucleation event. Clearly, there must have been a primary cracking trial and that is seen in Fig. 6.6a with the 6.15 mm distant nucleation that appeared first. It shows the interrupted nucleation (position 2) that grew from a very narrow tail along a (00−1) plane, apparently starting at an about $20°$ inclined interface of polymorphs, reaching 1.64um width, but shortly thereafter ceasing, again along (00−1). Shortly thereafter it resumed, formed a grain that still seemed to have some problems for proceeding, but it was finally successful (position 1 in Fig. 6.6a), without interruption till the exit. It rapidly reached 4μm width, narrowed to 1 to 1.5μm after 150μm and again after 280μm (both for about 30μm length), and more or less continuously assumed 4 to finally 11.2μm width till the exit. All of that strictly keeps with the (00−1) cleavage plane without any sidewise branching to the equally packed () cleavage plane (Fig. 6.6c). And all details of the nucleation (including the slight imperfections of the surface at 5000X enlargement) were precisely reproduced after 10 months storage of the sample. This confirms the cracking from an interface exit of different polymorphs, as pushed away from the indenter by increasing load, where it coincided with a $(00-1)$ cleavage plane. It proceeded along with it by using part of the flatly upcoming (about $20°$) interphase.

Apparently, the first macroscopic cracking produced enough stress for triggering the common but still highly hindered nucleation at the 13.31 mm distance from the indent around a thus formed grain, as shown in Fig. 6.6b. This second crack continues from there with 2μm width for 1 mm length where it interrupts 12 times giving parts with $0.6-2\mu$m width all along $(00-1)$. From there it resumes continuously first with $2-3$, then $4-5$, and 5-7 μm width till its exit at 6.9 mm length, again strictly along the (00-1) plane. This must not have been happening along an interface of polymorphs at so far distance from the indent. This more distant crack is thus taller than the closer one. The 12 interruptions after 1 mm length indicate again the difficulties for such cracking of the optical NaCl single crystal material. Fig. 6.6 d again shows the smooth run without side branching.

6.4 DISCUSSION

Indentation hardness and modulus

The depth-sensing indentation answers from the transparent NaCl model are particularly reliable, because there were no distortions by cracking emanations from the indenter up to 50 N loads. The first physically defined linear regression hardness H_{phys} should gain increased application value at the expense of unclear indentation moduli E and their false equalization with Young's modulus by the

ISO standard 14577. Due to their different physical meaning any numerical resemblance between unidirectional Young's modulus and the ISO or physical indentation modulus is at best fortuitous [11]. The disregarded change by phase transitions and poor repeatability of unphysical E_{ISO} are particularly troublesome, as numerous mechanical properties are continuously deduced from E_{ISO}[11]. For example, they are used as finite element iteration input. Also, the still multi-directional indentation moduli $E_{\mathrm{r}-p\mathrm{hys}}$ values in Table 6.1 (bcc NaCl: $32.245\mathrm{mN}/\mu\mathrm{m}^2$) can not be compared with published experimental or first-principle calculations of for NaCl (fcc: 53.466, bcc: $75.615\mathrm{GPa}$), or experimental bulk moduli (fcc: 23.40 to $26.40\mathrm{GPa}$; $\mathrm{bcc}: 26.60\mathrm{GPa}$) [20,23,24]. The steep pressure dependences of unidirectional Young's moduli or bulk moduli (from constant hydrostatic pressure) are not comparable with the pressure changes at a retracting indenter. For example, the first-principle calculations predict for the transition pressure $(30\mathrm{GPa})E_{\mathrm{V}}$ V values of $300\mathrm{GPa}$ for fcc NaCl and $210\mathrm{GPa}$ for the bcc polymorph. The latter value is predicted to increase to $350\mathrm{GPa}$ at $70\mathrm{GPa}$ pressure. Also, the calculated bulk and shear moduli are predicted to steeply increase with applied pressure [20]. And there is also the temperature dependence with heated materials. To learn more about the elasticity behavior upon unloading, it might be useful to very carefully study the unloading rate dependences within every phase transition onset ranges. Reliable elastic moduli for materials at high pressures combined with high temperature are certainly required. The indentation modulus situation is very confusing indeed and one should always take into account, whether an elastic modulus types' use is for length- or volume-related properties. ISO and ASTM add most severely to this confusion with indentation moduli by not detecting or appreciating the phase-transition onsets (Table 6.1). This creates high risks for the widespread use of E_{ISO}, including thereof deduced and calculated other mechanical parameters (more than 10, from adhesion to toughness) [11]. These unacknowledged daily-life risks derive from formation of interfaces between polymorphs, facilitating crack nucleation. They must be discontinued and replaced by reliable physical techniques.

Indentation $E_{\mathrm{r}-\mathrm{phys}}$ moduli reliably characterize pristine materials only before the first phase transition onset, but they are also not Young's moduli. Unlike $E_{\mathrm{r}-\mathrm{phys}}$, the linear regression hardness H_{phys} (penetration resistance k, the slope of the so called Kaupp-plot) values from depth-sensing indentations (2) favorably govern the energetics (Tables 6.1 and 6.2), detect other important material's properties (e. g. surface effects, gradients, inter-layers, cracks, adhesion effects, phase transitions, exclusion of one-point invaluable measurements), and are most promising for further unprecedented applications.

Phase transition and unusual cracking

The sharp phase transition onset at the kink position - of with Kaupp-plot (6.1) analyzed loading curves - succeeds with on-site Raman spectroscopy, electron diffraction, X-ray, and electric conductance, or other physical techniques, both in hydrostatic and indentation experiments. Most studied are the phase-transitions

of NaCl and silicon with various methods that fit nicely together. This is already reviewed in reference [3]. After the unloading all energetic polymorphs must have reformed the halite structure, at the edges as cubes, and at some face sites probably as sub-micro crystallites. One should however check, whether these features would be amorphous or twinned NaCl instead. This might perhaps open up another technique for achievement of twinned NaCl (cf for references of NaCl twinning) [3]. Pressure induced cracking is generally facilitated by phase transitions. The transparent and phase-transforming NaCl is nevertheless crackresistant for depth-sensing macro indentation. This is favorable for the demonstration of the sequence of phase-transitions, yielding reliable results. It allows for characterizing the polymorphs energetically with respect to work of indentation within their loading range and thus for obtaining the transformation energies. These important data required correct physical data and appreciation of the physically correct closed eqns. (1-7). The arithmetic covers multiplications, integrations, summations, and subtractions. The detection of phase-transition energies by checking the energy that is lost for an endothermic case (to be provided by the indenter), or won for an exothermic case (to help the indenter), is a major advance in mechanical physics [5]. The obtained results show better than the also determined H and E values how strongly these vary from kink to kink. It turns out that values how strongly these vary from kink to kink. It turns out that the pressure and plasticity including phase transformations is being distributed over very long distances in macro-indentations. Clearly, every more energetic polymorph zone at the indenter shifts all earlier energetic zones with their lower energetic polymorphs more and more away. This adds a new interface after every new phase transition onset. Any one of these may facilitate nucleation of long-range cracks. On the other hand, phase transition with volume drop helps to prevent cracks originating directly from the indenter, as in this case. The unusual cracking behavior of NaCl deviates from the common radial, lateral, median, and combined types of strongly incommensurable polymorphs of brittle materials. The main reason for the non-cracking at the Vickers indenter within NaCl, up to 50 N loads appears to be the marked volume decrease under pressure. A volume decrease of 35% was reported for the first $fcc \rightarrow$ bcc transition at the hydrostatic transformation pressure of $29.1\,\mathrm{GPa}$ [25]. Fig. 6.6a clearly indicates that phase transitions under load and temperature stress have to be avoided in materials of technical use. Uncountable transformations and reversions in strained objects above and below the transformation force create a risk for crack nucleation by always forming polymorph interfaces. Thus, the transition onset must be determined via Kaupp-plot and defined as maximal allowance of the material in revised ISO/ ASTM Standards.

One-point industrial indentations

The most important flaw of ISO and ASTM standards is their nonconsideration of phase-changes that are of outstanding importance for the reliable characterization of the original material (before the load at phase-transition onset). The occurrence of sequential multi phase-changes with always higher energetic polymorphs is particularly troublesome for industrial one-point macro-indentions (HV, HK, HB, HR, shore, LH, and more specialized hardness values) at

very high loads [12]. The first phase-changes occur already in the μN and mN ranges, and unrevealed multiple phase-changes inevitably occur at the very high loads that falsify the mechanical descriptions and facilitate materials' failures. These problems must be urgently avoided for industrial products that are used under high pressure stress. The present work underlines it with the study of highly crack-resistant sodium chloride as a suitable very simple cubic model system, exhibiting four consecutive phase-changes (only two of them were already known) and an unusual type of cracking. 50 N (corresponding to HV5) is still low for the "common" Vickers hardness load range of 40-980 N (HV 4-98) and may extend up to 1500 N (HV 150). But also the lowest loading region of 0.1 N to 40 N (HV 0.01-HV 4) cannot avoid phase changes [12]. Only the depth-sensing macro-indentation and nanoindentations can reveal the phase-transition onsets (6.1). Theoretical calculations do not help, if they predict mechanical parameters that are far off the experimental results.

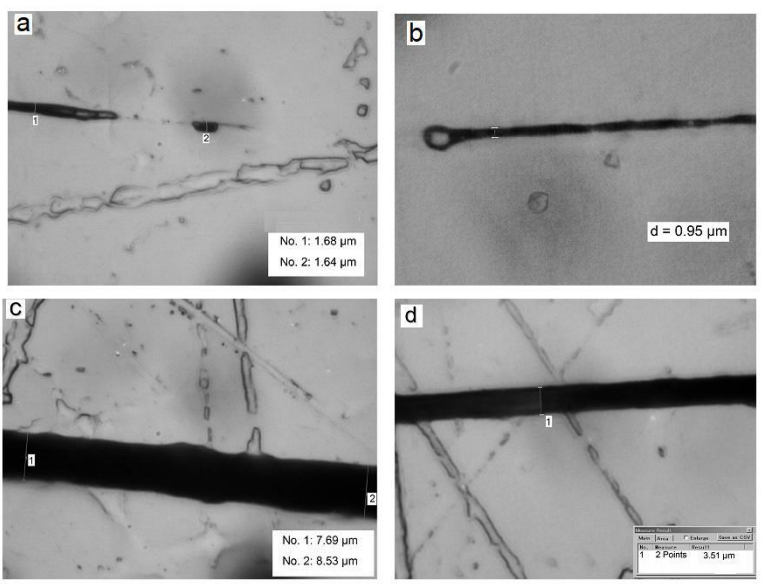

Fig. 6.6. Optical 3D-microscopic projection images (5000X lens) of the cracks' nucleation details on sodium chloride; the widths of the rectangles are $76 \times 55\mu$m; (a) the less distant from indention crack at 28.5 and 29.8 N load with an interruption, (b) the more distant from the indention crack as nucleated from a grain at 34.0 N load; (c) first crack (5000X lens) at 3.2 mm of its length; (d) second crack (5000X lens) at 1.7 mm of its length, also showing its smoothness

Long-range cracking nucleation

The complete absence of radial, median, half-disc, and horizontal cracks at the Vickers indenter up to 50 N force upon NaCl at the expense of 5.8 and 6.9 mm

long cracks along the (00-1) planes at large distance is unusual (Fig. 6.5). The cracks at the high loads of 29.8 and 34.0 N represent a new cracking type that is highly resolved by the 3D microscopy. The depressions in Fig. 6.1 b indicate the time of cracking, and that the first one had a two-step nucleation for the cracking,. Both cracks started 6.15 and 13.31 mm away from the residual 50 N indentation onto the 6.3 mm thick single crystal. The difficult nucleation of the less distant first crack, obviously at an interface between two different polymorphs under load, in Fig. 6.6 a starts with a very narrow ($<< 1\mu$m) scratch along $(00-1)$ providing 1.64μm width, but shortly thereafter it is reverting to such tiny scratch and resuming with a new trial that is finally successful strictly along $(00-1)$. No branching into $(0-10)$ or (-100) (Fig. 6.6a) occurs. The interfaces of the polymorphs occur about 20° inclined, and this concurs with the self-evident formation of phase transition interfaces. This happens away from the indenter further and further, as the load increases, and more so from the edge sides and apex of the indenter.

The more distant second crack has been announced by the final depression of the loading curve (Fig. 6.1b). It was evidently triggered by the first macro-crack and has a common non-interrupted nucleation from around a grain, as seen in Fig. 6.6b. It runs smoothly with 2μm width but experiences trouble after 1 mm length with 12 interruptions within 90μm of the length, but still strictly keeping with the once selected cleavage plane, and finally resuming uninterrupted with widths from $4-7\mu$m for a total of 6.9 mm. The value of highly resolving 3D-microscopy for such detailed knowledge is evident. The right/left bias in the present experiment is by chance (both are on the left side in Fig. 6.5). This may not be surprising for the second crack as triggered by the first one, but there are four corners of the Vickers and all orthogonal directions have identical cleavage planes in the cubic crystal lattice. The reasons may be some unavoidable miniscule deviation of perfectly normal indentation and the unavoidable wedge apex orientation of the four-sided Vickers pyramid. Disorder of this single crystal structure with extraordinary high crack-resistance appears a less probable choice than finding a coincidence of polymorphs' interface exit with cleavage plane. In so far, the orientation bias of the cracks will probably differ in future experiments.

Prospects for polymorphs' structure determination

The inverted 3D-images of the impressions and their 2D-projections retaining the depth sharpness yield important new information. Their surfaces are not completely flat but confirm the phase-changes into unstable polymorphs at the apices (deepest impression points) and particularly at the edges of the indentation with the reversions upon the unloading. These appear to partly crystallize into cubic halite features, which is best seen in Figs. 6.3 b and 6.3 b′ as brick-like or cubic objects. The by necessity fast reversions explain the different appearance of the ordered structures from the different polymorphs that only exist under load. The apparent crystallite formations are thus promising for onsite X-ray crystal structure determinations under load with sharply focused X-ray diffraction studies, which is an important task for the future.

The high energy transformations starting at $2.487, 9.1186$, and 24.4284 N (in addition to the 2 two known ones, giving a total of six polymorphs) are now found experimentally. But recent first-principle calculations predicted only three higher energy polymorphs with Cmcm, Imma, and Pbcm structures (describing only five polymorphs). The respective volume drops starting with the basic halite structure are predicted to $5.03\%, 1.19\%, 0.92\%$, and 0.33% [1]. We cannot locate the sixth experimentally found unstable polymorph that could be Pnma, twin, or amorphous. The missing color changes up to 50 N loads leave questions, whether ionic with metallic character of NaCl is in fact present in the pressurized predicted Cmcm, *I*mma, and Pbcm polymorphs [1]. Measurements of electric conductance upon similar depth sensing macro-indentation are our next task for clarifying these points.

6.5 CONCLUSIONS AND APPLICATIONS

Indentation is not only hardness and indentation modulus. The iteration-less physical treatment of indentations opens several new advents and improves the techniques' importance. The present work uses NaCl as favorable ductile standard material to reveal a sequence of polymorphs by depth-sensing macro-indentation at forces that would be used for Vickers hardness values of HV0.5,2, and 5. The NaCl single crystal profits from full transparency and surprising crackresistance. New mechanical parameters are revealed, such as physical hardness H_{phys} physical indentation modulus (avoiding iterations!) $E_{\mathrm{r-phys}}$ phase change onset data, indentation work W_{indent} and phase transition work W_{indent} for all transformation steps with normalized transition work, and unexpected remote crack-nucleation details. This includes measurements of activation energies of phase transitions from temperature dependent indentation loading curves for the NaCl fcc → bcc transition, as already published in 2014 [3]. All of that is only possible by using the physically founded universally valid closed eqns. (6.1-6.7), rather than iterations.

Six different NaCl polymorphs have been identified by their onset load and transition energies. In addition to fcc and bcc, first principle calculations predicted structures for three of them, proposing both ionic and metallic behavior [1], but we could not see color or metallic reflection up to 50 N load (final clarification of theoretically predicted NaCl metallization requires on-site electric conductance measurements that is planned). There remains the sixth polymorph to be energetically arranged. The surface shapes of the inverted residual impression images from 3D-microscopy furnish highly resolved images. These depict the reversion into halite (fcc) with clear sign of crystallization during the unloading at the (inverted) apex and tip edges. This makes on-site structure determinations with highly focused X-ray diffraction promising. The enormous crack-resistance of the single crystal NaCl withstands 50 N loads around the Vickers indenter without any trace of cracking at 5000 -fold magnification with 3D microscopy of the inverted residual impressions. Only very distant long-range cracks have been localized in the 30 N regions and analyzed with highly resolving 3D-microscopy. These did not obstruct the further data regression up to 50 N. The strongly

varying H_{phys}, $E_{\mathrm{r.}}$ phys, W_{indent} and $W_{\mathrm{transition}}$ values in the force ranges of the Tables 1 and 2 provide an idea about the huge errors of the not depth-sensing force macro-indentation techniques, according to ASTM Standards that do not acknowledge that pristine materials exist only up to the first phase-transition onset load. Severe errors are also occurring when phase transfer onsets are not determined or disregarded by the ISO Standard 14577 for nano- and micro-indentations. These prescribe the still common double multi-parameter iterations on the basis of wrong exponent on the indentation depth, disregard (1), and still violate the principal energy law. The determination of the correct exponent $3/2$ on h (6.1) from the loading data is a matter of < 1 minute when loading them to Excel and calculating the Kaupp-plot (eqn. (6.1) is finding any F_a correction term) [2]. When however innocent graphical integration of a loading curve deviates from the mathematical $5/4$ requirement of eqn. (6.5), this must not be used for questioning (6.5). On the contrary, such undue habit would be a new technique for the initial search of phase-transitions occurring under load, by avoiding data point's collection from published old loading curves for the Kaupp-plot. This can be demonstrated with an undue trial calculation: when the loading curve of Fig. $6.1\,\mathrm{b}$ (not regarding the depressions) would be graphically integrated despite the 4 phase-change unsteadiness kinks (part of them are shown in Fig. 6.2), and if such "result" would be compared with the applied work according to (6.5), the ratio "$W_{applied}$"/"W_{indent}" would come out as "1.3857" but not 1.250 and therefore confirm the actual phase changes. Clearly, the physically sound eqn. (6.5) must not be questioned by faulty integration over phase-change kinks' unsteadiness, but we can so rapidly obtain initial phase change information from innocently published previous loading curves for further studies. This work shows that only the now first physically defined nanoscale hardness H_{phys} is precisely obtained by linear regression at loads before phase-change offsets. Only that characterizes the pristine material up to permissible load stress for its risk-reduced application, often within nano-indentation, exceptionally at first within micro-indentation. The H_{phys} importance will therefore increase at the expense of unphysical H_ISO and troublesome E_{ISO} indentation modulus. Also the ASTM standards for one-point $\mathrm{HV, HK, HB}$, HR, Shore, LH, etc and hardness values are unphysical, as they do not consider the correct exponent $3/2$ on h, violate the energy law, and disregard the multiple phase changes (also occurring at the calibration plates). These fast techniques must rather be complemented by depth-sensing macro-indentations with hitherto scolded Kaupp-plot (eqn. (6.1)) analysis, and supplemented with nano-indentation. This detects the most important phase-change onsets. Polymorph interfaces facilitate the nucleation of cracks with severe failure risks. When the phase changes are irreversible (e.g., $\alpha - \mathrm{SiO_2}$ to amorphousness [5]) the material might immediately fail. In the reversible case, cracks might occur after numerous transformations back and forth. This will ask for different materials or for addition of particular mediation agents that increase the load for phase-change onsets. But this must be controlled with depth sensing physical indentation analysis. Also the alternation of minor reversible endothermic and exothermic phase changes might be helpful. For example, this could be shown up to $700°\mathrm{C}$ with the famous ODS super-alloy INCOLOY MA956® (but only up to $5\ \mathrm{mN}$) that exhibits alternating almost equally important endo- and exothermal

phase change onsets in the Kaupp-plot [26,27]. Conversely, the $Fe_{43}Cr_{16}Mo_{16}C_{15}\ B_{10}$ super-alloy gave a strong endothermic transition at $72.4\ mN$ und $0.495\ mm$ at RT (two linear branches, Berkovich, up to $260 mN$). Radial and horizontal cracks emanating from the impacting tip (these might also start upon the pressure release) must also be suppressed. Most high pressure polymorphs are unstable and additional thermal stress must also be considered with activation energy measurements of the phase-changes [3]. It is therefore highly relevant having exemplified the situation with a material exhibiting four phasechanges with a total of six energetically characterized polymorphs, not distorted by cracking up to $50\ N$ load. Only a new type of cracking (far away from the indenter on the opposite sample side) occurred in the 30 N load region (corresponding to HV 3). Such type of cracking might escape visual recognition in opaque materials. It is only indicated in the depth-sensing loading curve by small depressions as in Fig. $6.1\ b$. These are also indispensable diagnostic tools. Thus, industrial depth-sensing macro-indentations, as supplemented by nanoindentation, appear as urgent tools for the failure fighting management to avoid unnecessary risks of technical products; urgently requiring revised ISO/ASTM Standards. Failures of materials have undoubtedly physical reasons. Mechanical parameters must therefore correspond with physics!

ACKNOWLEDGEMENTS

We thank Dr. Ehrhard Reimann from Zwick GmbH & Co KG Ulm, Germany for providing access to the depth sensing Zwick/Roell ZHV Zwicky Z2.5 macro region instrument and Stephanie Rösner for her experienced running the instrument at the $NaCl$ macro-indentations according to the author's on-site wishes.

COMPETING INTERESTS

Author has declared that no competing interests exist.

REFERENCES

1. Chen X, Ma Y (2012) High-pressure structures and metallization of sodium chloride. EUROPHYS LETT 100: 26005-26008.
2. Kaupp G (2016) The physical foundation of $F_N = k\ h^{3/2}$ for conical/pyramidal indentation loading curves. Scanning 38: 177-179.
3. Kaupp G (2014) Activation energy of the low-load $NaCl$ transition from nano indentation loading curves. Scanning 36: 582-589.
4. Thurn J, Morris DJ, Cook RF (2002) Depth-sensing indentation at macroscopic dimensions. J Mater Res 17: 2679-2690.
5. Kaupp G (2013) Penetration Resistance: A new approach to the energetics of indentations. Scanning 35: 392-401.
6. Korth Kristalle Ltd. (2018) Itenholz-Kiel, Germany.

7. Chen S, Du Z, Zhang Z, Zhang H, Xia Z, Feng F. Effects of chloride on the early mechanical properties and microstructure of gangue-cemented paste backfill. Construction and Building Materials. 2020 Feb 28;235:117504.
8. Toleutay G, Su E, Kudaibergenov SE. Swelling and mechanical properties of quenched polyampholyte hydrogels based on 2-acrylamido-2-methyl-1-propanesulfonic acid sodium salt (AMPS) and (3-acrylamidopropyl) trimethylammonium chloride (APTAC). Вестник Карагандинского университета. Серия: Химия. 2019(4):35-43.
9. Fei Y, Ricolleau A, Mibe K, Shen G, Prakapenka V (2007) Toward an internally consistent pressure scale. Proc Natl Acad Sci 104: 9182-9186.
10. Kaupp G (2017) The ISO Standard 14577 for mechanics violates the first energy law and denies physical dimensions. J Mater Sci Engin 6: 321-328.
11. Kaupp G (2017) Dilemma between Physics and ISO elastic indentation modulus. J Mater Sci Engin 6: 402-405.
12. Kaupp G (2017) Challenge of industrial high-load one-point hardness and of depth sensing modulus. J Mater Sci Engin 6: 348-354.
13. Kaupp G, Naimi-Jamal MR (2013) Penetration resistance and penetrability in pyramidal nano indentations. Scanning 35: 88-111.
14. Kaupp G, Naimi-Jamal MR (2010) The exponent $3/2$ at pyramidal nanoindentations. Scanning 32: 265-281.
15. Sneddon IN (1965) The relation between load and penetration in the axisymmetric Boussinesq problem for a punch of arbitrary profile. Int J Engn Sci 3: 47-57.
16. Oliver WC, Pharr GM (1992) An improved technique for determining hardness and elastic modulus using load and displacement sensing indentation experiments. J Mater Res 7: 1584-1583.
17. ISO (International Organization for Standardization). ISO 14577. Available from the member of the particular country; for USA: American National Standards Institute, 25 West 43rd Street, Fourth Floor, US-New York, NY 10036-7417
18. Troyon M, Abbes F, Garcia Guzman JA (2012) Is the exponent $3/2$ justified in analysis of loading curve of pyramidal nanoindentations? Scanning 34: 410 417.
19. Merle B, Maier V, Durst K (2014) Experimental and theoretical confirmation of the scaling exponent 2 in pyramidal load displacement data for depth sensing indentation. Scanning 36: 526-529.
20. Lu C, Kuang XY, Zhu QS (2008) Characterization of the high-pressure structural transition and thermodynamic properties in sodium chloride: a computational investigation on the basis of the density functional theory. J Phys Chem B 112 : 1389-1395
21. Ono S (2010) The equation of state of B2-type NaCl. J Phys Conf Ser 215: 012196-012208.
22. Bassett WA, Takahashi T, Mao HK Weaver JS (1968) Pressure-induced phase transformation in NaCl. J Appl Phys 39: 319-325.
23. Birch F (1985) Finite strain isotherm and velocities for single-crystal and polycrystalline sodium chloride at high pressures and $300^{\circ}\mathrm{K}$. J Geophys Res 83: $1257 - 1268$.

24. Bukowinski MST, Aidun J (1985) First principles versus spherical ion models of the B1 and B2 phases of sodium chloride. J Geophys Res $90(B2): 1794 - 1800$
25. Piermarini GJ, Block S (1975) Ultrahigh pressure diamond-anvil cell and several semiconductor phase transition pressures in relation to the fixed-point pressure scale. Rev Sci Instrum 46: 973-979.
26. Kaupp G (2018) Basic physics disproves the obligatory ISO-14577 standards: a dilemma for all indentation mechanics. 2018, Oct. 4, Keynote at the 26th International Conference on Advanced Nanotechnology & 2nd Edition of International Conference on Materials Technology and Manufacturing Innovations.
October 04-05, 2018 Moscow, Russia
27. Kaupp G (2017) ISO violates the first energy law including hardness/elasticity standards from indentations: What can be done? July 31 2017 Chicago USA. Keynote at the International Conference on Nanotechnology and Nanoregulations

DISCLAIMER
This chapter is an extended version of the article published by the same author(s) in the following journal.
Journal of Material Sciences & Engineering, 7:4, 2018.

Chapter 7
Print ISBN: 978-93-5547-921-1, eBook ISBN: 978-93-5547-922-8

New Characterization of Solid Materials and Anisotropy: An Approach towards Phase-Transition Energies

DOI: 10.9734/bpi/mono/978-93-5547-921-1/CH7

ABSTRACT

The detection of phase transitions under load and their transition energy is made possible by non-iterative analysis of the indentation findings. On the basis of the empirically based normal force depth$^{3/2}$ relation, the closed algebraic equations have been derived. The precise transition onset position is obtained by linear regression of the $F_N = kh^{3/2}$ plot, where k is the penetration resistance, which also provides the axis cuts of both polymorphs of first order phase transitions. The phase changes can be endothermic or exothermic. They are normalized per µN or mN normal load. The validity of the loading curves, including those from calibration standards that display previously undiscovered phase-transitions and are thus unreliable, is checked using analyses of indentation loading curves with self-similar diamond indenters. The loading curves from instrument vendor handbooks are utilized to calculate the phase-transition energy for fused quartz. For the first time, the anisotropic behavior of phase transition energies is examined. A helpful test item is α-quartz. On the basis of the local crystal structure under and surrounding the inserting tip, the causes of the packing-dependent changes are explained.

Keywords: Instrumented Indentation, loading curve; phase transition onset and energy; iteration-less plot; physical exponent; present ISO standard; energy law violations; physical hardness; error detections.

7.1 INTRODUCTION

Analyses and accurate calibrations are needed for instrumented indentations. Since at least 1998, modern instruments have been quite reliable, and the most common standards, fused quartz, aluminium, and sapphire, are consistently accessible in good quality. However, there are issues with not taking into account phase transitions that occur at even moderately high stresses of conical or pyramidal indentations [1,2]. Even worse is the data-treatment in the highly regarded Oliver-Pharr method is treated with data according to the ISO14577 standard (of the International Organization for Standardization) [3]. As generally known, this is based on very complicated mathematical deductions that clearly forgot to take into account the sidewise forces and thus energies at conical or pyramidal penetrations. Their deduced normal force (F_N)-depth square (h^2)

proportionality [4,5] is therefore invalid. This standard cannot describe the experimental loading curves. Rather polynomial iterations are used, but these wipe out all surface effects, local gradients, elbows, and phase transitions under load. It was empirically found that the exponent 3/2 on h correctly describes the load parabola. This was first published in 2005 [6], with a review in 2006 [7], and later in [1] and [2]. Equation (7.1) provided excellent correlations and numerous unprecedented applications without fittings, or iterations. The validity of (7.1) was physically deduced in a clear-cut way. This was published electronically in 2015 and open access in 2016 [8]. The basic idea for the physical deduction of the exponent 3/2 on h (7.1) [8] is the undeniable fact that the entire pressure plus pressure work—and thus also the corresponding part of the normal force F_N goes with the indented volume of cones or pyramids, which is proportional to h^3. This deduction of the physically enforced Equation (7.1) can easily be repeated with simple arithmetic. Or graphically: the work that is lost for the penetration is the area between the parabola with exponent 3/2 and its secant that starts at zero. Furthermore, the applied work ($W_{applied}$) is the area under such secant of the parabola (down to the zero line). Furthermore, the indentation work (W_{indent}) covers the area below the parabola, and it can also be described by the area of the 0 - h_{max} - 0.8 F_N triangle [9]. It follows the 5/4 ratio of $W_{applied}/W_{indent}$ that was already mathematically deduced by integration of (7.1) in [10]. The k-values in Equation (7.1) are the validated penetration resistances. They are obtained by linear regression of the F_N versus $h^{3/2}$ plots with excellent correlation. This viable analytical tool is disdainfully known as “Kaupp fitting” in the literature. We must therefore call it now “Kaupp plot (7.1)” to underline that it must not be degraded to a fitting technique.

$$F_N = kh^{3/2} \tag{7.1}$$

The $W_{applied}/W_{indent}$ = 5/4 relation means that the loss of F_N for the penetration depth h is for exponent 3/2 always 20% with universal mathematical precision. This is totally independent of the material. For an assumed exponent 2 it would calculate to be 33.33% [9,10]. The non-consideration of such energy and thus also force losses is a violation of the first energy law in the ISO14577 standards and [3] ! Our energy correction for directly depth related mechanical parameters is the factor 0.8 (4/5 ratio), for keeping with the first energy law. This is, of course, already implied in the indentation work W_{indent} [10].

For example, motorized aviation with flying machines required new physical understanding of aerodynamics and also knowledge of materials’ properties [11]. To make the former usable for airliners and airplanes they had to become faster, lighter, more efficient, and safer. The local analyses with (nano)indentation at the unphysical and iterating H_{ISO} and $E_{r\text{-}ISO}$ level are unsuitable. They could therefore not prevent catastrophic failures (not only with airliners), which have been termed “failure by fatigue of materials”. The liability clearly requires that local test procedures identify phase-transitions on the physical mathematic basis. We again urge ISO-ASTM to use the undeniable strict mathematical analyses, as presented here and in our cited publications since 2005. Addition of suitable ductilizers must optimize the super-alloys, so that the first phase transition onset force will be considerably above the permitted maximal force on them (also “pop-

ins" must not occur upon load). Such analytical tests are required after the common long-term stretching, bending treatments, and after the repeated thermo-mechanical stress upon application with loading curves at the prescribed service intervals. The present technique is fast and easy for obtaining the onset information.

The penetration resistance k [$mN/\mu m^{3/2}$] is literately the physical hardness with respect to the used indenter geometry. For the general applications the (effective) cone angle dependency of the self similar indenters (see Chapter 16) is removed by the normalization as "penetration-resistance" hardness $H_{phys} = k = F_N/h^{3/2}$.

Conversely, the still generally accepted definitions of indentation hardness as $H = F_N/A_{projected}$ or $H_{ISO} = F_N/A_{contact}$ use the entire maximal loading force for the depth. This seemed to verify the physically false exponent 2. But the reasoning that the area of a cone "varies as the square of the depth of contact" [3] is misleading: such area ($\pi h^2 \tan\alpha^2$) variation is self evident, but the volume of the conical indenter varies with $\pi h^3 \tan\alpha^2/3$. Neither is the definition of indentation hardness according to ISO and [3] as "force (of a cone) over contact area" a "theoretical confirmation" of an "exponent 2" on h as claimed in [12]. This definition severely violates the first energy law! 33.33% (for an exponent 2) of applied energy cannot be made out of nothing, and force is related to energy! Unfortunately, the energy violation remained apparently undiscovered for all of these authors since 1939 [4], and even so after our paper in 2013 [10] that quantified the violation with basic algebra. As above: the area of the 0 - F_{Nmax} - h_{max} triangle minus the area under the loading parabola with an exponent 2 would amount to one third of the total applied work. Nevertheless, this violation of the first energy law was not allowed to be literally expressed in publications before 1997 [9,13]. ISO14577 and apparently most of the indentation world are urged to stop with tolerating the violations against basic physics.

A further advantage of the physical indentation resistance hardness $H_{phys} = k = F_N / h^{3/2}$ is its independence of the depth (self-similar indenter!). We can therefore for the first time choose from hardness with respect to the penetration act (0.8 k) or with respect to the full indentation resistance (uncorrected k). An important discussion on what should be used for what theoretical and practical use is now opened. The papers [9,13], and [14] chose the first version for theoretical reasons. This can however easily be changed for more practical reasons. The definition of indentation elastic moduli E_r from the unloading curve. But we need the full applied energy (for penetration and pressure) that is a factor 1.25 to the force responsible for the penetration. Indentation moduli are the still claimed "Young's moduli". But at best, they resemble the bulk moduli [13]. Clearly, all hardness and moduli determinations must be at loads before the phase-transition onset and it can no longer be avoided to detect it with the Kaupp plot (7.1).

These important developments facilitated the easy detection of phase transitions by indentation. Previously such detection was restricted to a kink in the unloading curve. There is one in the unloading curve of silicon (though without onset information), which had been amply discussed as a particular exception [3]. On-

site Raman spectroscopy, TEM, electrical resistance, electron diffraction, or micro-diffraction by synchrotron radiation revealed discontinuities and verified phase transition. We have a sharp kink upon Berkovich indentation onto silicon at the loading curve with onset information [1] [15]. Similar discontinuities in the Raman and current flow studies (see [15]) provided final support for our kink discontinuities as phase-transition onset. About 10 further examples using the more costly and highly specialized techniques are known. Correct indentation analysis obtains transitions right away with high frequency for all kinds of materials with transition onset and transition energy by simple indentation using Equation (7.1). Only the elucidation of the polymorph structures requires preferably onsite diffraction with highly focused synchrotron irradiation. Numerous confirmed phase transitions under hydrostatic pressure are long known, but these techniques are expensive and laborious without providing transition energies. Phase transition onset detections are indispensable for proper analyses of indentations.

A further application of Equation (7.1) with the penetration resistance k is the reliability control of published measurements on the strict physical basis [8]. All partial deviations are either particular physical properties of the material (e.g. surface effects, phase changes, gradients, etc.) or experimental errors (e.g. poor calibration of force linearity, non-vertical indents, mix-up events, etc.). Importantly, the unphysical “exponent 2 on h” claim for the loading parabola enforced several multi-parameter polynomial iterations that prevented data checks by wiping out all particular effects including the phase transitions. Only Equation (7.1) with its linear plots sorts out the special effects from published loading curves and detects deviations from unsuitable experimentation. These include too close indentations, false assignment of materials or polymorphs at large indents, integrations over phase transition onset discontinuities, false transition energy sign, and further flaws that are discussed below. These checks remove severe additional errors of published H and E_r next to all other systematic errors, even with calibration standards. Some further types for disclosed errors can be found in the corresponding Section below.

Further applications use phase transition energies at different temperatures for the determination of phase transition activation energies [15]. Also multiple consecutive phase transitions have been published [14], and the transition energies of $SrTiO_3$ on (011), α-quartz on (010), $InGaAs_2$ on (001) are already known [10]. Some updates in this area are available elsewhere and may find attention of the readers [16-18]. These report interesting structural investigations of geologically transformed minerals, or they correct questionable quartz structures, or they study the influence of different quartz crystal shapes to their piezoelectric performance. This underlines the importance of crystallography in the distinction of polymorphs. However, the surface dependent anisotropy of phase transition energies upon indentation awaited elucidation. Quartz is available in amorphous state and as hexagonal crystal and it has different crystallographic faces. It is a particularly valuable material for that purpose. We describe the first anisotropies at four prominent crystal faces of α-quartz.

7.2 MATERIALS AND METHODS

A fully calibrated Hysitron Inc. Triboscope® Nanomechanical Test Instrument with 2D transducer and leveling device, connected to a Nanoscope AFM was used for the own indentations. The apex radii of the cube corner (55 nm) and Berkovich (110 nm) diamond indenter were directly measured by AFM in tapping mode. The leveling to ±1° was in x and y direction. Loading times were 30 s up to 5000 µN final load. All our measurements were performed with the same cube corner. The original data with about 1500 points each of our loading curves for α-quartz (rock crystal) from [2], [6], and [7] were now used with more precise calculation (up to 10 significant figures) for the determination of the phase transition energies. Thus, rounding errors are minimized and Table 7.1 with many numbers characterize the specific data set as precisely as necessary. Loading data from the literature have been digitized with the Plot Digitizer 2.5.1 program (http://www.softpedia.com/). Electronic fittings or iterations whatsoever were never performed. The crystal structure data (P3(2)21, a 4.914, c 5.405) are from [19]. The crystal models were calculated using the Schakal 97 program [20].

A single well developed rock crystal with smooth surfaces and excellent colorless clarity was the α-quartz sample without twins at the surface. Its indexed major faces were horizontally leveled to slopes of ±1° in x and y direction under AFM control at disabled plane-fit. All F_N and h data pairs from the loading curves were loaded to Excel® (Microsoft; Redmond, USA, WA) for the calculation of the $h^{3/2}$ values and the linear branches of the regression lines provided the slopes (penetration resistances) k_1 and k_2, and the axis cuts $F_{1\text{-a}}$ and $F_{2\text{-a}}$. They were used with all of their figures for avoiding rounding errors. The linear regression coefficients R^2 were in all cases > 0.999 - 0.9999. The precise sharp intersection point (transition onset) was obtained by equalizing of the regression line equations and the so obtained h_{kink} and F_{Nkink} values were calculated by using Equation (2). All necessary terms are thus obtained, as h_{max} and F_{Nmax} are directly available.

$$F_{\mathrm{N}} = kh^{3/2} + F_{1\text{-a}} \tag{7.2}$$

$$W_{1\text{-applied}} = 0.5\, h_{kink}\,(F_{\text{N-kink}} + F_{1\text{-a}}) \tag{7.3}$$

$$W_{1\text{-indent}} = 0.8 W_{1\text{-applied}} \tag{7.4}$$

$$W_{2\text{-indent}} = 0.4k\left(h^{5/2} - h_{\mathrm{kink}}^{5/2}\right) + F_{2\text{-a}}\left(h - h_{\mathrm{kink}}\right) \tag{7.5}$$

$$\mathrm{full}\, W_{\mathrm{applied}} = 0.5 F_{\text{N-max}} h_{\mathrm{max}} \tag{7.6}$$

$$W_{\mathrm{transition}} = \mathrm{full}\, W_{\mathrm{applied}} - \Sigma\left(W_{\mathrm{applied}}\right) \tag{7.7}$$

Table 7.1. Physical parameters from the cube corner indentations onto four different surfaces of α-quartz (rock crystal) up to 5000 μN load

Entry	Surface (hkl)	k_1 (μN/nm$^{3/2}$)	k_2 (μN/nm$^{3/2}$)	h_{kink} (nm)	F_{Nkink} (μN nm)	$\Sigma W_{applied}/5000$ (μNnm/μN)	$W_{trans}/\mu N^{(a)}$ (μNnm/μN)
1	(011)	2.5443	1.8609	85.75601036	2097.594374	97.6134	−15.744
2	(010)	2.1574	1.7169	105.8103095	2237.798772	101.3803	−11.048
3	(1−10)	2.2037	1.6475	101.5669094	2264.183535	104.5936	−14.663
4	(101)	2.2147	1.6773	100.3591866	2241.625060	103.4883	−14.032

[(a)] *For practical reasons we do not use the factor 0.8 to the μN values for the normalizations from kink to the final force*

The used Equations (7.2)-(7.7) for the calculations contain all of the obvious corrections [14]. The meaning of the terms has already been explained. F_a corrects for axis cuts of the regression lines that are due to surface effects. Only $F_{1\text{-}a}$ is also influenced by the apical tip rounding radius (R), giving larger penetration resistance up to $h_{cone} = R\ (1\text{-}\sin\alpha)$. It varies with the surface properties (including water layers). These depend on ambient conditions, which exclude their tabulation. The $W_{1\text{-indent}}$ is calculated from $W_{1\text{-applied}}$ according to Equation (7.4). $W_{2\text{-indent}}$ must use integration and correction with $F_{2\text{-}a}$ as in Equation (7.5), and $W_{2\text{-applied}}$ is then obtained by multiplication with 1.25 in analogy to Equation (7.4). The balance of Equation (7.6) and Equation (7.7) gives the transition energy W_{trans} that was reasonable rounded in Table 7.1.

7.3 RESULTS AND DISCUSSION

7.3.1 Quartz, Aluminium, Tungsten, and Sapphire as Calibration Standards of ISO

Unfortunately, all indentations of the most cited publication of Oliver-Pharr in 1992 [3] with their iterated values of hardness H and reduced elastic modulus E_r (from there with Poisson's ratio elastic modulus E, which has been unduly called "Young's modulus" [13]). They became standards for instrument calibration and numerous further quantities of materials for iterations and finite element calculations. It appears therefore of primary importance to check the validity of these old though still used measurements that lacked the 1992 not available physical insights. The authors of [3] did not have universal Equation (7.1) and thus missed that their force linearity and so their instrument compliance were not well adjusted above 90 mN to120 mN load for their published curves as designated with aluminium (their Fig. 4), "quarts" on (001) (their Fig. 5), sapphire (their Fig. 7), and tungsten (their (Fig. 9). That is consistently revealed by strong positive deviations from linearity (without kink appearance) above about 90 mN in our Kaupp plots (7.1). Defective tip surface cannot be the reason, as these deviations occur at different depths h. There is only one exception in [3]: the Kaupp plot of their Fig. 7.6 for soda lime glass has the last branch staying linear up to 120 mN load. Nevertheless, the iterated standard values of hardness H and modulus E_r that use the maximal force are in error for all 5 examples: the faulty calibration adds to the unphysical h^2, the energy law violation, and the non-consideration of the phase transition onsets that occur before that load. Not the pristine material is tried to be characterized! These errors perpetuate in all further iterations that are made to converge to these values and the numerous qualities that are deduced from all of these values. They have at least influenced various reference table entries, not to speak of finite element calculations. Particularly troublesome are the errors in [3] for aluminium, which is often used as a standard for microindentation. Its phase change onset under Berkovich is known to be at 30 - 40 mN, which became first known in 2013 [2]. And there are further errors in [3]. The designation of their Fig. 8 in [3] with "fused quartz" is in error. It reveals three linear branches ($k_1 = 76.044$, $k_2 = 109.12$, and $k_3 = 123.3$ mN/μm$^{3/2}$, all with $R^2 > 0.999$) when plotted with Equation (7.1). This corresponds so perfectly with

the soda lime glass values from their Fig. 6 of [3] (k_1 = 77.909, k_2 = 105.28, and k_3 = 122.0 mN/μm$^{3/2}$) that the claimed "fused quartz" curve must in fact belong to the result from another soda lime glass indentation, despite the about 250 nm different maximal depths. Furthermore, their Fig. 5 in [3] of crystalline quartz on (001) is totally misinterpreted. The authors do not realize the situation from 0 to 5 mN loads that is not really discernible in the Kaupp plot (7.1) up to 120 mN. As expected for crystalline quartz it rightfully starts steeply and soon thereafter continues less steeply, apparently by producing amorphous quartz around the Berkovich with its then endothermic phase transition. The initial exothermic α-quartz transition [6] [7] can however not be analyzed in more detail at that loading range without a large number of original data points. But it is extremely troublesome to the reader of their Fig. 5 in [3], who became misguided about the mechanical properties of crystalline quartz until [6] and [7] had appeared. Clearly, the indentation of fused quartz up to 120 mN deserves new investigation. The exothermic α-quartz indentations ending at 5 mN are discussed in Table 7.1. Importantly, the properties of tungsten (k_1 = 95.57, k_2 = 114.50 mN/μm$^{3/2}$; kink ≈ 35.6 mN) and sapphire on (0001) (k_1 = 236.58 and k_2 = 264.68 mN/mm$^{3/2}$, kink ≈ 31.5 mN) (the better older curve up to 90 mN load of [21] was used) are poor calibration standards for the harder materials without consideration of their phase transitions. Further phase transitions are detected in macro-indentations for example sapphire transforms also at about 12 N load and 5.9 μm depth [2], and so does soda-lime glass at about 14 N at 11.7 μm when the loading curves with a Vickers indenter of [22] are analyzed with the Kaupp plot (7.1), and we mention here to the four consecutive phase transition onsets of NaCl at 0.003397, 2.487, 9.1186, and 24.4284 N loads [14]. Any non-consideration of phase transitions generates errors at hardness and modulus iterations, including other materials and finite element calculations as these values concern not detected polymorphs, but not the pristine material. We complain that apparently nobody else did check all these grave inconsistencies since 1992 and hope that the new physical insights and possibilities will be used, instead of violating basic physics.

7.3.2 Fused Quarts, Transition Energy

Fused quartz is the most used calibration standard for nanoindentations. We analyze therefore the corresponding Berkovich (with half angle θ of 65.3°) loading curves of prominent instrument provider Handbooks with respect to the Equations (7.1)-(7.7) and use of the new applications without any iteration. The first point is the detection of the long known amorphous to amorphous phase transition [23] under indentation [1], because hardness and modulus of pristine materials must be determined at loads before the first phase transition onset. The early onset of this endothermic transition ($k_2 > k_1$) has been denied on the basis of poor, or fitted, or too extended curves with low precision (e.g. [12], and many others), but a more detailed analysis with the Kaupp plot (7.1) reveals the transition as long as these are experimental [14] and so do the excellent loading curves from instrument builders as analyzed in [1]. However, the energetics of such transition is still unknown. The calculation is therefore performed by using the loading curves as published in the TriboScope manuals of Hysitron and of CISCO for UMIS. Both linearized loading curves give two linear branches that

correlate with $R^2 = 0.9999$, each upon regression with the Kaupp plot (7.1). Their penetration resistance values are for k_1 1.9654 and 1.9672 and those for k_2 are 2.4392 and 2.3936 μN/nm$^{3/2}$ for Hysitron and CISCO, respectively. This leads after surface-cut corrections to transition onset depths of 109.6476605 and 100.682078 nm at 2.348 and 2.117 mN. These differences reflect different measurement conditions. Most likely are different force calibrations or horizontal sample leveling devices that are not specified. It is therefore not surprising that the calculated normalized per μN transition energy values also differ: we calculate 6.206 and 3.563 μNnm/μN, respectively, for the endothermic transitions. These values are remarkably large when compared with the exothermic transitions that give the negative values of crystalline quartz (Table 7.1).

7.3.3 α-Quartz, Transition Energies at Different Faces

Unlike fused quartz, crystalline α-quartz in the form of rock crystal undergoes at first an exothermic phase transition upon sufficient indentation stress. The projected images of the studied surfaces are shown in Fig. 7.1. Anisotropic behavior for the transition energies upon cube-corner indentation is to be expected, as the crystal packing is different. In particular the penetration resistances k_1 and k_2 had already been shown to be anisotropic with different indentation works W_{indent} [2]. Table 7.1 with Miller indices (hkl) for simplicity (as the "i" in (hkil) is redundant) repeats less rounded k and kink values. The structure of the indented surface is important for the understanding of the varying W_{trans} values of Table 7.1. Channels will facilitate penetration the better these are vertically aligned. That is roughly reflected by the k_1, h_{kink}, and $W_{trans}/\mu N$ values (entries 1 and 2 are most different, 3 and 4 are in between), but not by k_2, F_{Nkink}, and $\Sigma W_{applied}/\mu N$. Clearly, there is also the force that acts normal to the surface of the cube corner with the opposite of its half angle $\theta = 35.26^\circ$. It is therefore important to also consider the location of channels exiting from the side faces at the indenter surface for the transition energies. We therefore construct such surfaces at 35° and assume that not all of their so seen shapes will be destructed while the cube corner penetrates. They are obtained by rotation of the crystal structure around the X axis by + and − 35° (rX ± 35° ≡≡ 180° ± 35°) and the same around an Y axis (as rY ± 35° ≡≡ 180° ± 35°). The resulting images are projected (Fig. 7.2 and Fig. 7.3) and visually analyzed. The differences on the determined circumventing skew faces prove large enough to be helpful for the understanding of the different results. It turns out that the highest amount of normalized exothermic energy $W_{trans} = -15.744$ μNnm/μN is produced by indentation upon the (011) surface (entry 1) of α-quartz with a cube corner indenter. The (011) packing exhibits not very favorable skew channels, as can be best seen in the center of the image where the view goes through 5 of the interlocked pyramidal layers (Fig. 7.1(a)). The normal indentation depth for the phase transition onset h_{kink} and F_{Nkink} are the least of all studied cases and the required work down to the transition onset force is lower than with the other surfaces. Furthermore, Fig. 7.2 shows four of the eight 35° skew side structures around the cube corner under (011). In that case only comparatively small channels are available all around the cube corner. Therefore, the exothermic phase-transition is produced

in a highly concentrated manner. This does not cost much displacement energy. It just detracts least from the transition energy, leaving more for it.

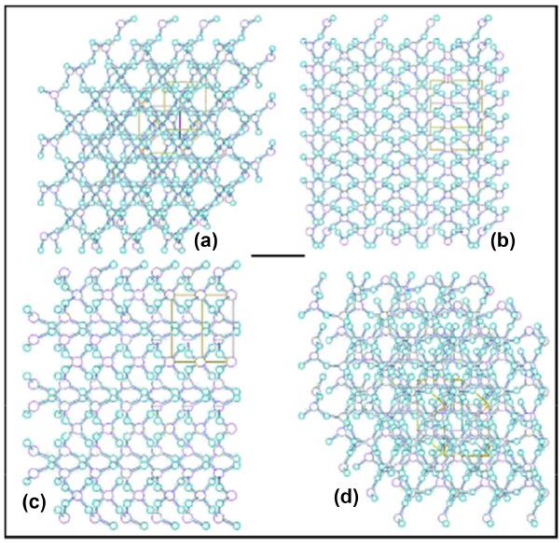

Fig. 7.1. Surface projections on α-quartz with four different tetrahedrons upon each other in the center areas; (a) (011); (b) 010); (c) (1−10); (d) (101); the bar corresponds to 5 Å length

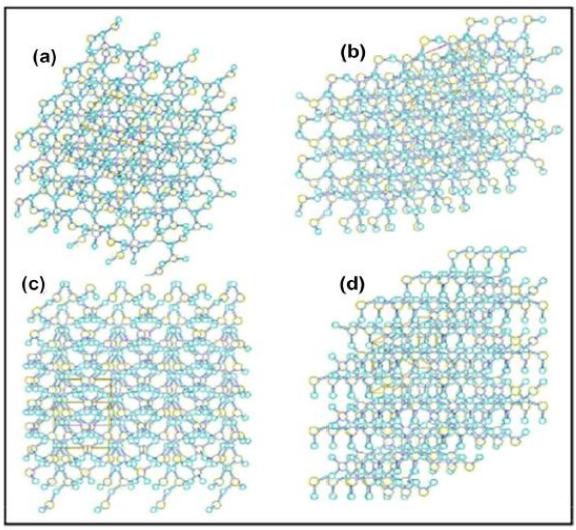

Fig. 7.2. α-Quartz 35˚ skew side faces under the (011) surface ; (a) rX 35˚; (b) rX −35˚; (c) rY 35˚; (d) rY −35˚

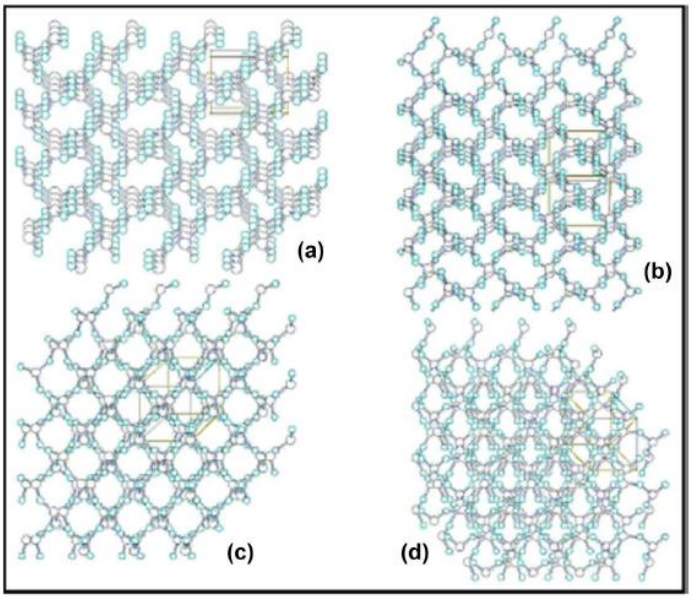

Fig. 7.3. α-Quartz 35˚ skew side faces under the (010) surface; (a) rX 35˚; (b) rX −35˚; (c) rY 35˚; (d) rY −35˚

Consistently, the least exothermic transition energy among the tested surfaces is produced under the (010) surface (entry 2) with −11.0485 μN nm / μN. It exhibits straight channels (Fig. 7.1(b)). The penetration down to the phase transition onset is deep and the required onset energy from F_{Nkink} is high (Table 7.1). The cube corner is surrounded by large 35˚ skew faces with almost orthogonal channels that are well shaped for the transport of materials (Fig. 7.3). Such materials transports cost energy, which detracts from the exothermic transition energy. This certainly helps to understand the reasons for the extremes under the (011) and (010) surfaces. Consistently, the normalized transition energies (under (1−10) and (101) indentations (entries 3 and 4) are between these extremes. They penetrate almost with the similar depth of entry 2 and their 35˚ skew side walls (not shown here) are less favorable under (011) and (010). Thus, their normalized W_{trans} values are almost equal and between the extremes (Table 7.1). Clearly, the complicated variations of the normalized anisotropic transition energies require the whole anisotropic 3D packing of the crystal. All qualities of Table 7.1 interact. This has to be taken into account for all crystals and other non-isotropic materials.

7.4 CONCLUSION

The universal Equations (7.1)-(7.7) are physically and mathematically deduced beyond any doubt for vertical indentations with self-similar indenters [8,10]. All

depend on the physical exponent 3/2 on h rather than on the assumed exponent 2 that requires iterations with violation of the first energy law. The now possible detections of phase transition onsets and phase transition energies are indispensable for the characterization of materials and proper analyses of indentations. They are of theoretical and practical importance. Their unprecedented anisotropy deserves consideration with further crystals, not uniform materials, and composites for a better understanding of their failures. Numerous further studies on those lines are therefore essential. We used the iteration-less physical analysis of common normal force-depth parabolas not only for data checks, but also for the detection of phase transitions under load. These include the most cited force-depth curves in [3]. Unfortunately these data of Oliver Pharr were taken as the basis for ISO14577, without knowing of their force calibration errors and the further errors in the absence of the physical data check possibilities from Equation (7.1). Their definition of H_{ISO} and $E_{r\text{-}ISO}$ does not consider phase transitions under load and they violate the first energy law. For example [24] fitted the incorrect data for aluminium and tungsten, and others continued with fitting of loading curves without considering initial effects, phase transitions, and other particularities. All of these errors with iterations since 1992 must be corrected with physically sound analyses. We tell here how the various and obvious errors of the iterative indentation treatments are avoided: the closed formulas (7.1)-(7.7) for the calculations are presented and used at characteristic examples. They rely on excellent linear correlations, contain the corrections for initial effects, and do not violate the first energy law. Unfortunately, there was no other protest against the first energy law violation for 70 years, even though the remaining pressure for elastic moduli and long-range plasticization were always known and discussed. Surprisingly enough, it was not asked from where the necessary force and energy might come from. We continue to urge ISO for changing its 14577 Standard, so that the very common phase transitions upon indentations do not longer stay undetected, etc. It is certainly good scientific practice to consider the physically enforced formulas (7.1)-(7.7). Their perhaps most important advances are the unprecedented applications of nano-, micro- and macro-indentations without violating the first energy law. We cannot live with [3] and ISO followers who still want to “produce” the pressure plus plasticization work from nothing. Only the iteration-free physical formulas are able to obtain reliable materials’ properties, including the phase transitions and their energies under load. That applies to crystalline, amorphous, and plastic materials under mechanical stress that must always be smaller than the phase transition stress for avoiding failure of materials in daily life, not to speak of liability problems. Clearly, first order phase transformations produce polymorph’s interfaces that increase the probability for cracking [14]. Reversibility of phase transitions upon pressure release is more likely for the endothermic transitions than for exothermic ones. It has already been shown that the activation energies of phase transitions can be obtained by temperature dependent indentations with their phase transitions [15]. So this appears particularly important for the choice of proper materials that are stressed by both load and temperature. That will be particularly important for the field of super alloys [10]. Such measurements are easily and cheaply available with presently existing instrumentation.

COMPETING INTERESTS

Author has declared that no competing interests exist.

REFERENCES

1. Kaupp, G. and Naimi-Jamal, M.R. (2010) The Exponent 3/2 at Pyramidal Nanoindentations. Scanning, 32, 265-281. https://doi.org/10.1002/sca.20206
2. Kaupp, G. and Naimi-Jamal, M.R. (2013) Penetration Resistance and Penetrability in Pyramidal (Nano)Indentations. Scanning, 35, 88-111. https://doi.org/10.1002/sca.21038
3. Oliver, W.C. and Pharr, G.M. (1992) An Improved Technique for Determining Hardness and Elastic Modulus Using Load and Displacement Sensing Indentation Experiments. Journal of Materials Research, 7, 1564-1583. https://doi.org/10.1557/JMR.1992.1564
4. Love, A.E.H. (1939) Boussinesq's Problem for a Rigid Cone. The Quarterly Journal of Mathematics (Oxford), 10, 161-175. https://doi.org/10.1093/qmath/os-10.1.161
5. Sneddon, I.N. (1965) The Relation between Load and Penetration in the Axisymmetric Boussinesq Problem for a Punch of Arbitrary Profile. International Journal of Engineering Science, 3, 47-57. https://doi.org/10.1016/0020-7225(65)90019-4
6. Naimi-Jamal, M.R. and Kaupp, G. (2005) Quantitative Evaluation of Nanoindents: Do We Need More Reliable Mechanical Parameters for the Characterization of Materials? International Journal of Materials Research, 11, 1226-1236.
7. Kaupp, G. (2006) Atomic Force Microscopy, Scanning Nearfield Optical Microscopy and Nanoscratching—Application to Rough and Natural Surfaces. Springer, Berlin-Heidelberg, New York.
8. Kaupp, G. (2016) The Physical Foundation of $F_N = k\ h^{3/2}$ for Conical/Pyramidal Indentation Loading Curves. Scanning, 38, 177-179. https://doi.org/10.1002/sca.21223
9. Kaupp, G. (2017) The ISO Standard 14577 for Mechanics Violates the First Energy Law and Denies Physical Dimensions. Journal of Materials Science and Engineering, 6, 321-328. https://doi.org/10.4172/2169-0022.1000321
10. Kaupp, G. (2013) Penetration Resistance: A New Approach to the Energetics of Indentations. Scanning, 35, 392-401.
11. Wright, W. (1906) Flying-Machine. US Patent No. 821393.
12. Merle, B., Maier, V. and Durst, K. (2014) Experimental and Theoretical Confirmation of the Scaling Exponent 2 in Pyramidal Load Displacement Data for Depth Sensing Indentation. Scanning, 36, 526-529. https://doi.org/10.1002/sca.21151
13. Kaupp, G. (2017) Challenge of Industrial High-Load One-Point Hardness and of Depth Sensing Modulus. Journal of Materials Science and Engineering, 6, 348-355.

14. Kaupp, G. (2018) Six Polymorphs of Sodium Chloride upon Depth-Sensing Scanning Macroindentation with Unusual Long-Range Cracks Requiring 30 N Load. Journal of Materials Science and Engineering, 7, 473-483.
https://doi.org/10.4172/2169-0022.1000473
15. Kaupp, G. (2014) Activation Energy of the Low-Load NaCl Transition from Nanoindentation Loading Curves. Scanning, 36, 582-589.
https://doi.org/10.1002/sca.21158
16. Otálora F, Mazurier A, Garcia-Ruiz JM, Van Kranendonk MJ, Kotopoulou E, El Albani A, Garrido CJ. A crystallographic study of crystalline casts and pseudomorphs from the 3.5 Ga Dresser Formation, Pilbara Craton (Australia). Journal of applied crystallography. 2018 Aug 1;51(4):1050-8.
17. Huang XR, Gog T, Kim J, Kasman E, Said AH, Casa DM, Wieczorek M, Hönnicke MG, Assoufid L. Correct interpretation of diffraction properties of quartz crystals for X-ray optics applications. Journal of Applied Crystallography. 2018 Feb 1;51(1):140-7.
18. Li Y, Wang G, Huang S, Sun X, Feng Z. Effect of Quartz Crystal Form on the Measurement Performance of Multi-dimensional Force Sensor. InIOP Conference Series: Materials Science and Engineering 2018 Sep 1 (Vol. 428, No. 1, p. 012008). IOP Publishing.
19. Smith, G.S. and Alexander, L.E. (1963) Refinement of the Atomic Parameters of α-Quartz. Acta Crystallographica, 16, 462-471.
https://doi.org/10.1107/S0365110X63001298
20. Keller, E. (1997) Schakal 97. Kristallographisches Institut der Universität Freiburg i. Br.
21. Page, T.F., Oliver, W.C. and McHargue, C.J. (1992) The Deformation Behavior of Ceramic Crystals Subjected to Very Low Load (Nanoindentations). Journal of Materials Research, 7, 450-473.
https://doi.org/10.1557/JMR.1992.0450
22. Thurn, J., Morris, D.J. and Cook, R.F. (2002) Depth-Sensing Indentation at Macroscopic Dimensions. Journal of Materials Research, 17, 2679-2690.
https://doi.org/10.1557/JMR.2002.0388
23. Trachenko, K. and Dove, M. (2003) Intermediate State in Pressurized Silica Glass: Reversibility Window Analogue. Physical Review B, 67, 212203/1-212203/3.
https://doi.org/10.1103/PhysRevB.67.212203
24. Cheng, Y.T. and Cheng, C.M. (1998) Further Analysis of Indentation Loading Curves: Effects of Tip rounding on Mechanical Property Measurements. Journal of Materials Research, 13, 1059-1064.
https://doi.org/10.1557/JMR.1998.0147

DISCLAIMER
This chapter is an extended version of the article published by the same author(s) in the following journal.
Advances in Materials Physics and Chemistry, 9, 57-70, 2019.

Chapter 8
Print ISBN: 978-93-5547-921-1, eBook ISBN: 978-93-5547-922-8

An Advance Study on Physical Nanoindentation: From Penetration Resistance to Phase-transition Energies

DOI: 10.9734/bpi/mono/978-93-5547-921-1/CH8

ABSTRACT

The ISO standard 14577 is contested due to its iterative processes, violation of the energy law, and incorrect relationships between the normal force (F_N) and impression depth (h). The solution of this dilemma is the use of *sacrosanct* simplest calculation rules for the loading parabola (now $F_N = kh^{3/2}$) giving straight lines for cones, pyramids and wedges. They provide the physical penetration resistance hardness k with dimension [$Nm^{-3/2}$] upon plotting and allow for non-iterative calculations with closed formulas, using simple undeniable calculation rules. The physically correct F_N versus $h^{3/2}$ plot is universally valid. It distinguishes between the most typical surface effects and makes gradients visible. Unmatched precision is provided, including reliability analyses of experimental data. A regression study of the F_N vs $h^{3/2}$ graphs demonstrates that the transition-energy coincides with the beginning of the kink-unsteadiness phase transition. All types of solid materials, including salts, silicon, organics, polymers, composites, and superalloys, are shown to exhibit this. The abrupt phase-transition onsets and transition energies offer unheard-of most crucial material properties that are essential for safety. As a result, ISO ASTM is requested to modify ISO 14577 in its entirety and to develop new standards for mechanically (and thermally) stressed materials. For instance, materials must only be admitted for maximal forces considerably below the first phase-transition commencement, and the consistency of the first phase-transition parameters must be controlled. These onset loads can now be calculated with ease. Even nevertheless, persistent arguments against the physical analysis of indentations are based on severely inadequate understanding of fundamental mathematics and mistakes. The properties of the current nonphysical materials are reviewed with regard to their effects on safety.

Keywords: Energy law violation; ISO-14577 challenge; calculation rules for indentations; phase-transition onset and energy; multiple transitions; safety problems.

8.1 INTRODUCTION

We have been working since the early 2000s to persuade the American division of ASTM (American Society for Testing Materials) and ISO (International

Organization for Standardization) to rectify their ISO 14577 standard. This standard requires the entire field of materials sciences to analyze (nano) indentation curves. Contrary to experiment, a conical or pyramidal indentation must not pierce a projected or iterated contact area with a violation of the first energy law. The diamond indentation rather creates the semi-angle dependent volume of the cone or the pyramid (but not with a pseudo cone angle) that is geometrically well known and available from all indentation compendia. A pyramid volume was also falsely calculated using an "effective cone angle," which is unfortunately frequently used in indentation compendia that must not be used any further. Therefore, the mathematic calculation is compelling for the loading parabola that relates the force with the depth$^{3/2}$. The physically and mathematically founded deduction of the parabola exponent 3/2 with the linear F_N versus $h^{3/2}$ plot is thus universally proved. It needs only the use of basic calculation rules that are sacrosanct to everybody. Any deviations from the exponent 3/2 of the loading parabola are thus experimental errors. Materials with gradients are no exceptions. They still require exponent 3/2 on *h*: tangents to the loading F_N versus $h^{3/2}$ plot (instead of straight lines in that case) provide the physical hardness (*k*-values) depth-dependent, which will also be valuable in these cases, as discussed in [1] for an ion implantation. The calculation rules are taught in public and private schools and cannot be argued against. Universal facts ensue throughout. Scientists, teachers, anonymous reviewers, editors, technicians, Certification Agencies, etc. must urgently stop with their believing in their errors of [2,3,4] and of ISO 14577. Their basic errors are the false exponent 2 on h and their violation of the first energy law. ISO etc. are still continuously exacting worldwide agreement. Actually, they think that the undisputed elastic and plastic deformations upon indentation can be created from nothing since 1939! Clearly, as the force-depth loading parabolas do not proceed with h^2, as erroneously proposed since 1939 by Love [2], 1965 Sneddon [3], 1992 Oliver-Pharr [4], ISO 14577, etc., their ISO-hardnesses and ISO moduli are multiply fitted and iterated but not calculated. Conversely, diverging empirical results were finally published since 2004 [5] and 2005 [6] after various preceding international lectures. The mathematically proved exponent 3/2 on h (Equation (8.1)) [7] that experimentally correlates excellently ($R^2 > 0.999$ - 0.9999) had the advantage to physicochemical correctly identify and remove the various surface effects (including tip rounding). Importantly, it also detected phase-transitions with their onset data. But strange resistance arose against the iteration-less calculations. And surprisingly, this did not change after the break-through, when elementary calculation rules quantified the universal fraction of applied energy that is responsible for the elastic plus plastic deformations with mathematical precision. We apply 20% of the applied work and use the proved exponent 3/2 on h. But 33.33% violation is still tolerated by using the false exponent 2. Only the proved calculation settles the violation of the energy law with the factor 0.8 (Equation (8.4)), but it is strictly connected to the exponent 3/2. This could again only be published after a large delay in 2013 [8]. It allows now a distinction between the applied work (by the instrument) and indentation work (the work for the vertical impression) when using the proved correct exponent (Equation (8.4)). The final universality of the exponent 3/2 was mathematically proved with the most important, particularly elegant and straightforward one-page physical deduction

[7]. It used only simple mathematical equations but could only appear with delay in 2016 [7]. These calculations proved the validity of the earlier amply verified empiric results and opened unprecedented new horizons with the first physical hardness that is the penetration resistance k [1]. Unfortunately, the undeniable calculation rules are still not widely appreciated, and the necessary standardization is certainly difficult for ISO ASTM for various non-scientific reasons, not to forget the liability. Some updates in this area are available elsewhere and may find attention of the readers [9-11]. Paper [9] deals with cyclic indentation of steel but still on the iterative ISO-14577 basis. [10] indents onto heterogenous areas of cements also still on the iterative ISO-14577 basis and applies statistical techniques. [11] uses the physical indentation analyses and is the Chapter 10 of this E-Book.

The author's very successful non-iterative plots (F_N against $h^{3/2}$, Equation (8.1)) were unduly scolded as "Kaupp-fitting" [12] and must therefore now be called "Kaupp-plot" for not being mixed up with any "fittings", and as nobody else used it before. Such physical and precise plotting of the regression lines (correlations of always >0.999 - 0.9999) of hundreds of materials after the competent elimination of initial surface effects detected numerous phase-transitions by kink discontinuities separating two linear branches with different penetration resistance slopes k_1 and k_2 (mN/μm$^{3/2}$) (physical hardness). This culminated in the determination of the first phase-transition energies [8] and, temperature dependent, phase-transition activation energies [13].

As the still exacting of false exponent 2 on h by ISO 14577 cannot reproduce experimental loading parabolas, people tried with "excuses" by exponent fittings, polynomial and least squares iterations. Hardness was defined as F_N over projected or iterated areas because the false exponent 2 on h was not removed [4,12]. Unbelievably, authors, anonymous reviewers, editors, ISO-ASTM, and Certification Agencies did not even try to think about getting out of their mess with their unbelievable violation against the energy law. The present author was therefore forced to point it out in a more drastically way [14]. The exponent 2 was also defended by the prescription to start the analysis of loading curves only above a "minimal force value of 30 mN load for all solids" [15]. That means, the nano-part of the indentation by analysis of the "power function" should not be considered at all in nanoindentations. Or it has been claimed and imaged with very short log-log plots (their Fig. 4 in [16]) that the exponent 2 on h would be "validated" at high F_N values. Such argumentation shows however little expertise in basic mathematics: all parabolas $F_N = k\ h^n$ loose more and more of their flexure at increasing F_N for all exponents n. However the k values of parabolas depend strongly on the exponent n and even worse, k is not a dimensionless constant, but its dimension is [N/m^n]. The requirement of equal dimension on both sides of every equation has been poorly disregarded. The same mathematical error is made with exponent fitting: for example [17] fits loading curves from zero (not removing the initial surface effect) to various indentation depths. He obtains thus very diverse broken exponents (e.g. n = 1.64533, or 1.75265, or 1.82723, etc. with respective "k-values" of 0.61897, 0.41377, and 3.0003×10^{-4}, but without dimensions. Why did the anonymous referees and editors of that paper not stop the print of such nonsense? The same paper [17]

tried to disprove the Kaupp-plot by totally falsely claiming that “Kaupp” would draw a line through three initial points of his initial surface effect (at a tip-rounding of 300 nm!) and cut it with the second linear branch extension in his imaged Kaupp-plot. But the cited “Kaupp” always eliminated and eliminates initial surface effects from regressions and he only considers the kink between the also in [17] clearly present first and second linear branches! Another unfair attack against the Kaupp-plot was by the above mentioned [12], senior author Durst: these authors claim that the Oliver-Pharr [4] and ISO 14577 definition of indentation hardness as force over area would “theoretically confirm” the exponent 2 on h and thus disprove the Kaupp-plot. How can a definition of an iterated (with a total of 11 free parameters in two steps) “hardness” be the basis of a physical deduction? This is more of a juggler trick but not reasonable or scientific. Again, why did anonymous reviewers and editors not reject such publication? Also, finite element calculations cannot “confirm” the exponent 2 on h because they converge to h^2, which of course cannot prove anything. Also, any claim that such FE-calculations would reproduce experimental results are incorrect, even if such claim was made with curves on different pages in the same publication (e.g. in [18]). Such a claim was easily disproved by curve analyses in [1].

Despite such, unfortunately, continuing fights against the iteration-free mathematical treatment on the clear-cut physical foundation and mathematical proof [7] with closed formulas, the correct analyses opened unprecedented new horizons to the indentation technique. One cannot longer exact to the whole world a violation of the energy law; and one cannot deny the mathematical quantification of the indentation energy that is universally responsible for the work of elastic pressure plus all different pressure-following plastic events [8]. At the same time one must universally remove the falsifying exponent 2 on h and use the proved $h^{3/2}$ for the loading parabola [7]. There is now for the first time a physically founded indentation hardness that is the penetration resistance *k* with dimension [$N/m^{3/2}$]. It is simply obtained as the slope of the first regression line (Equation (8.1) or Equation (8.2)) always with correlation coefficient >0.999 - 0.9999) of the Kaupp-plot before the first phase-transition onset. It provides also for the first time the checking of the experimental correctness of previous calibrating measurements [19]. We provide the easiest and fastest means for detecting hitherto unknown phase-transition onsets of materials and for the calculation of phase-transition energies. These are unprecedented and the subject of this paper. Phase-transition energies have also been calculated at different temperatures, which allows for the calculation of the activation energies of the phase-transitions [13]. All of that is obtained with closed formulas, never using iterations or fittings. Materials can now be qualified for their application limits with respect to mechanical and thermal stress, for avoiding catastrophic failures in practical use. Examples are materials for various turbine materials in airliners, cars, ships, mills, bridges, buildings, roads, etc, etc. Clearly, the sudden first type transformations form polymorph interfaces. These increase the probability for the nucleation of catastrophic failures [20,21,22]. Their failures are generally termed as “material’s fatigue”. But e.g. the mosaic structures of multi-component superalloys often changes upon continued stress and stress-relief. The required constancy of the advanced mechanical parameters can and must

now urgently be tested at proper time intervals by indentations with their physical analyses. We provide these in this paper from reliable data of salts, silicon, organics, polymers, composites, and superalloys. The results are compared in Tables 8.1-8.5, including face dependencies and multiple phase transitions. They are also discussed with respect to checking a posteriori the reasons for recent catastrophic failures to help to avoid them a priori for the future. Indentations of the materials are the technique of choice, but only on the basis of the calculation rules that disprove the unfortunately still common ISO-ASTM standards 14577.

8.2 MATERIALS AND METHODS

The own measurements were performed with a fully calibrated Hysitron Inc. Triboscope$^{(R)}$ Nanomechanical Test Instrument with 2D transducer and levelling device, connected to a Nanoscope AFM, using all of about 15,000 data pairs. The apex radii of the cube corner (55 nm) and Berkovich (110 nm) diamond indenter were directly measured by AFM in tapping mode. The levelling to ±1° was in x and y direction. Loading times were 30 s up to 10 mN load. Most initial data are from digitized published loading curves (Plot Digitizer 2.5.1 program; https://www.softpedia.com/) up to the microindentation regions with about 500 points. It was necessary for avoiding any bias suspicion that had sometimes been expressed by anonymous Reviewers. Fittings or iterations whatsoever were never performed. The crystal structure models were calculated using the Schakal 97 program [23]. The polished strontium titanate samples (100), (110), and (111) were from Aldrich Chemical Company. Grade 80 isotactic polypropylene was from Imam Khomeini Petroleum Co, Tehran, Iran.

The own or digitized data pairs of F_N and h were read into Excel$^{(R)}$ for the calculation and print of the Kaupp-plot and calculation of the regressions up to and from the at first roughly judged kink position after the cut-off of the initial surface effect points. This is exemplified in Fig. 8.1 for aragonite, purposely with a larger initial effect than usual. In that case, the surface effect is primarily due to hydrated surface twins. The precise kink position is then calculated by equating y_1 and y_2 that contain the slopes k and axis-cuts F_a (Equation (8.2)). The y denotes F_N and the x denote $h^{3/2}$, while the regression certainties are calculated as R^2. All transition energy values are normalized per force unit for the respective polymorph ranges.

We repeat here the evaluation formulas from [19] for convenience. These contain all necessary correction requirements that might be necessary and are self-evident based on the physically deduced Equation (8.1) [7]. The factor 0.8 in Equation (8.4) settles the energy law violation [8], but only for the correct exponent 3/2 on h (Equation (8.1)). The calculations of the phase-transition work were performed with 10 figures to avoid rounding errors. The tabulated values were then reasonably rounded. Equation (8.2) is used for interconversions between different units of the k-values (physical hardness) and for the values at the kink points or end points. This has been exemplified with the data in Fig. 8.1 that were converted into the units of Table 8.1.

$$F_N = k\, h^{3/2} \tag{8.1}$$

$$F_N = k\, h^{3/2} + F_{1\text{-a}} \tag{8.2}$$

$$W_{1\text{-applied}} = 0.5\, h_{kink}\, (F_{N\text{-kink}} + F_{1\text{-a}}) \tag{8.3}$$

$$W_{1\text{-indent}} = 0.8 W_{1\text{-applied}} \tag{8.4}$$

$$W_{2\text{-indent}} = 0.4k\left(h^{5/2} - h_{\text{kink}}{}^{5/2}\right) + F_{2\text{-a}}\left(h - h_{\text{kink}}\right) \tag{8.5}$$

$$\text{full}\, W_{\text{applied}} = 0.5 F_{\text{N-max}} h_{\text{max}} \tag{8.6}$$

$$W_{\text{transition}} = \text{full}\, W_{\text{applied}} - \sum\left(W_{\text{applied}}\right) \tag{8.7}$$

The slopes of the different linear branches (Fig.8.1) are the k-values (depth independent penetration resistance = physical hardness) with dimension [N/m$^{3/2}$] (but not N/m^2). They are obtained together with the axis cuts (F_a). The initial surface effect (water layer, surface treatments, roughness, possible zero-error, tip rounding, etc) has to be carefully separated from the desired bulk properties. Its detailed elucidation requires separate indentation but at much lower depths (here up to 100 µN load). Most metals and semiconductors have hydrated oxide/hydroxide (rarely nitride) layers, often despite surface hardening by polishing. All of these contribute to F_a and have to be corrected for (Equation (8.2), Equation (8.3) and Equation (8.5)), but their varying values are not bulk materials constants and are thus not tabulated.

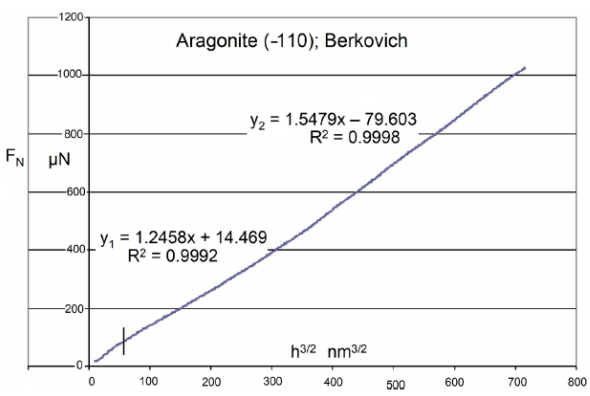

Fig. 8.1. Kaupp-plot (F_N versus $h^{3/2}$) analysis, as exemplified with a Berkovich indentation onto aragonite ($CaCO_3$; Table 8.1), showing the phase-transition kink unsteadiness onset by the kink and cut-off of the initial surface effects that include the tip rounding

Table 8.1. Penetration resistance and phase-transition energies of various types of materials (Berkovich), including organics

Material	k_1 and k_2 ($mN/\mu m^{3/2}$)	F_{Nmax} (mN)	F_{Nkink} (mN)	h_{kink} (μm)	$W_{transition}$/mN (mNμm/mN)	Literature for Data Origin
Aragonite $CaCO_3$ (-110)	89.396 48.962	1.0	0.4086	0.04644	0.002758	Kearney, Phys Rev Lett 2006, 96, 255505
Calcite $CaCO_3$ (100)[a)]	17.911 23.176	10.0	0.3655	0.08266	0.01599	Guillonneau, J Mater Res 2012, 27, 2551
Calcite $CaCO_3$ (100)[b)]	33.156 48.943	40.0[b)]	11.869	0.4940	0.10692	Presser, J Mater Sci 2010, 45, 2408
Sapphire Al_2O_3	236.05 267.08	90.0	34.326	0.2763	0.13453	Page, J Mater Res 1992 7 450
Zirconium dioxide ZrO_2	134.74 210.88	33.0	8.7514	0.1665	0.02828	Zeng, Acta Mater 2001, 49, 3539
Tungsten W	95.57 114.50	85.0	35.607	0.5525	0.070059	Oliver-Pharr, J Mater Res 1992, 7, 1584
$InGaAs_2$ (001)	36.272 32.477	2.7	1.2703	0.1070	−0.005380	Kaupp, Scanning 2013, 35, 392
Mica, Muscovite $KAl_2[(OH,F)_2/AlSi_3O_{10})]$	34.522 3.566	50.0	11.556	0.4434	0.01016	Hutchinson, Acta Metall Mater 40 295, 1992
$Ce(C_2O_4)_2(CO_2H)$ (001) "MOF"	52.848 64.907	20.0	8.0745	0.3102	0.06554	Tan, J Am Chem Soc 2009, 131, 14252
Pine latewood radial	0.1342 0.1705	1.8	0.5469	2.5625	0.23926	Brandt, Acta Biomater 2000, 6, 4345
Pine latewood axial	0.2098 0.3043	3.0	0.9631	2.7638	0.36510	ditto
Saccharin (011)[c)]	1.9543 2.3179	6.0	1.7108	0.9426	0.08293	Kira, Cryst Growth Design 2010, 10, 4650
Benzylidene-butyrolactone (010)[c)]	0.4807 0.5724	2.1	1.0634	1.6671	0.07893	Kaupp, Angew Chem 1996, 35, 2774

[Dea)] After initial twinning; [b)] second transition of calcite; [c)] cube corner indenter; the organic structures are in Fig.8.2

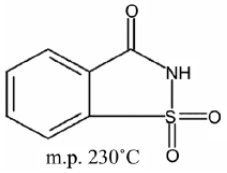

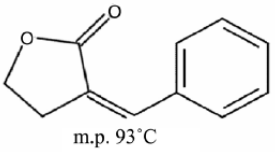

Fig. 8.2 Molecular structures of saccharin and benzylidene butyrolactone

8.3 RESULTS AND DISCUSSION

8.3.1 Various Types of Materials

Phase-transitions upon indentations cover all types of materials and the penetration resistances = physical hardnesses) of the two branches in their Kaupp-plots (they profit from the physical and mathematical proved Equations (8.1)-(8.7). Typical examples are collected in Table 8.1. All units are made equal by using Equation (8.2) with the corresponding units. It contains salts, oxides, metal, semiconductor, metal organic framework (MOF), polymer composite (wood), organic crystals, and the complicated mineral Mica. They cover nano- and micro-indentations, using Berkovich or for the organics cube corner indenters. The maximal forces are given to indicate the experimentally studied ranges. This does not exclude further phase-transitions at higher loads as has been shown with NaCl, where 4 phase-transitions (6 polymorphs) had been located [20]. Further polymorphs are even likely for calcite, where already two phase-transitions (4 polymorphs) are energetically analyzed in Table 8.1 (further examples are in Tables 8.3-5). The k-, F_N- and h_{kink}-values do not systematically relate to their unprecedented transition-works that are normalized per mN of their ranges. We did not transform the mNμm or μNnm units into Joules for easier transformation possibility into different units. These quantities relate to the chemistry of the materials and the transitions can be mostly endothermic but also exothermic. It is seen that the less stable aragonite has a lower endothermic $W_{transition}$ than the calcite polymorph. The second transition of calcite affords about 7 times more energy than its first one. Surprisingly, the $W_{transition}$ of the very hard sapphire is only 8.4 times higher (at 94 times higher transition onset) than the first one of calcite. Furthermore, $W_{transition}$ of sapphire is only 1.6 and1.7 times higher than the ones of the organic crystals in this Table 8.1. The latter are however extended molecules requiring energy consuming solid-state migrations into other polymorph structures, whereas the cooperative transformation of Al_2O_3 from its trigonal space group (R-3c) does not require considerable molecular migrations. The proportion of transition energies between Al_2O_3 (m.p. 2050˚C) and ZrO_2 (m.p. 2715˚C) (4.75 fold) is much higher than the one of physical hardnesses k (1.25 fold). This underlines the independence of transition energies from such qualities as hardness, or melting point, etc. The high pressure polymorphs of sapphire are probably either the orthorhombic (Pbcn) or the (Pbnm) polymorph of Al_2O_3, both with a volume decrease of 3.1% [24], even now at room temperature, because of the shearing upon pyramidal indentation.

Similarly, monoclinic ZrO_2 ($P2_1/c$) transforms probably into the denser monoclinic polymorph (still $P2_1/c$) or the orthorhombic polymorph with (Pbcm) structure, both with higher density. The hard metal tungsten (m.p. 3400˚C) has a lower hardness than the two oxides, but its transition energy is 2.5 times higher than the one of ZrO_2, which is quite remarkable.

Surprisingly, the semiconductor $InGaAs_2$ exhibits a significantly exothermic phase-transition, and mica (Muscovite) has a very low normalized endothermic transition energy, smaller than the two organics. Both of them experience very easy phase-transitions and they can only be detected by our iterative-free precise technique.

The metallorganic MOF, wood, and organics exhibit phase-transition energies that are not very different from the ones of the inorganics. The anisotropy of radial or circular pinewood is remarkable. Clearly, the non-iterative technique is very sensitive and avoids all of the strange recent techniques that are wiping out all of the important information from phase-transitions with incredible data treatments.

8.3.2 Bond-Breaking of Polymers

The phase-transitions of organic polymers under mechanical load are initial bond-breakings into radicals. This requires relatively high energy if these primary cleavage products are not stabilized by substituents. Therefore, their phase-transition onset must relate to the bond energies of the weakest chain bond. Further reactions of the so formed radical pairs are manifold, but overall there is hardening by cross-linking, which is well known for the technical treatments of polymers, e.g. upon extrusions, etc. Table 8.2 collects the data of some linear polymers upon Berkovich indentation. Most of these are highly amorphous and their hardnesses (k-values) are low. An exception is isotactic polypropylene it-PP with high crystallinity and much higher k-values. This is however not so important for the C-C bond strength. It is nicely seen in Table 8.2 that the phase change onset (chain breaking) relates to the strength of the carbon-carbon bonds. In the case of high density polyethylene (hd-PE) without chain substitution and isotactic polypropylene (it-PP) with slightly less efficient methyl-substituents, the strong unsubstituted C-C bonds exhibit similar bond energies and thus also similar phase-transition energies, much higher than those in Table 8.1. The details with kink forces and depths depend only slightly on further properties of the materials. Substitution of the polymer chains with phenyl groups as in polystyrene (PS, 1.04 g/cm^3) decreases the bond energy, due to stabilization of the radicals, and thus also the phase-transition energy is decreased. The methylester groups in the side chain of polymethylmethacrylate PMMA (1.19 g/cm^3) are 13 times more effective with decreasing the transition energy when compared with polystyrene PS. The h_{kink} of PMMA is 7.7 times lower even though the required onset force is 6.2 fold higher. But it appears that the elimination of methylformate (HCO_2CH_3) is energetically easier than the chain breakage. Polycarbonate Macrolon$^{(R)}$ (PC) contains no C-C breakage chain. But the ArO-C(O)OAr bond (Ar = aryl) is cleaved, starting the energetically favorable loss of CO_2. This is the largest

decrease of phase-transition energy of the polymers in Table 8.2: 145 fold decrease of $W_{transition}$ when compared with the C-C breakage of PE. The analyses of cross-linked polymer indentations promise further interesting insights.

8.3.3 Multiple Phase-Transitions

Table 8.1 contains already the double phase-transition of calcite and it is well-known that several phase-transitions can occur consecutively at higher and higher loads. This has been shown with the depth-sensing macroindentation of sodium chloride up to 50 N loads with a Vickers indenter when 4 phase-transitions were detected. The thus experimentally detected 6 polymorphs formed their polymorph interfaces under load with the facilitated production of seeds for catastrophic breakages [20]. Further examples have been found by analyses of published macroindentations [25]. For example, sapphire has its second phase-transition at 12.8 N and 5.82 µm depth (not included in Table 8.1) and soda-lime glass has the third transition at 14.0 N and 11.7 µm depth (not included in Table 8.3) [1]. Importantly, phase-transitions are, of course, not achievable by technical one-point Vickers, Brinell, Rockwell, etc. hardness measurements. Interestingly, already microindentations (mN to low N-ranges) are a rich but hitherto undetected field of consecutive phase-transitions. Table 8.3 shows it for the standard materials soda lime glass, aluminium, and silicon, the latter on two different faces (another example is calcite in Table 8.1). The h_{end} and $W_{applied}$/mN values indicate only the experimental range. The undoubtedly amorphous soda lime glass exhibits two endothermic phase-transitions at the microindentation range (sharp kinks with linear branches in the Kaupp-plot) and exists thus in 4 or together with the macroindentation 5 polymorphic forms, the structures of which are subject to further studies. We can only conclude from the absence of cracks or pop-ins that there are different degrees of density under load that increases the penetration resistance from state to state. The transition energies of the first two transitions of soda lime glass vary by a factor of roughly 4, which is quite remarkable. Aluminium requires about 12.1 and 60.4 mN load for its first and second phase-transition and its proper use as a calibration standard ends already below the values of the first one. Some onset-depths are still in a range of nanoindentations. Also the transition work for both transitions is similar to the one of much harder sapphire and smaller than the ones of pinewood (Table 8.1) and PE, PP, and PS (Table 8.2). This reflects the weak metallic bonds of aluminium that facilitate rearrangements in the crystal lattice.

The transitions of cubic silicon (Ed3m), exhibiting an exceptional pop-out of the unloading curve, found more theoretical interest. Several polymorphs (including an amorphous phase) were detected by electron diffraction, Raman spectroscopy, and electric conductance onset from the loading curve. The obtained values from the papers, as cited in [13], are similar to the ones found more easily directly from the Kaupp-plot of the loading curve in Table 8.3. Particularly helpful in that respect are the in-situ current flow onsets at about 5 mN of the metallic Si II [26], which agrees with the first kink discontinuity in our analysis. This electrical unsteadiness confirms again the first phase-transition

onset under the (001) face of silicon. We observe however 3 phase-transitions (5 polymorphs) from the physical Kaupp-plots (Table 8.3). And the data from the two different faces exhibit considerable differences. The first transition is hidden at the scales of 50 and 100 mN. It is thus helpful that also a nanoindentation was published in [27] for the (001) face. The variation of the 3 endothermic transition energies is by a factor of 28 for the (001) indention and there were no pop-ins but only “fine cracks emanating from the corners” at 50 mN load/displacement. It can be assumed that the boron-doping does not make much difference to the mechanical properties of silicon. We can, therefore, compare the (001) with the (100) phase. The five polymorphs of the silicon in the loading curve up to 50 mN load have been located for the first time together with the energetic information. The striking differences in the endothermic phase-transition energies at the different faces require a crystallographic understanding. This can be obtained by considering the crystal structure, similar to the procedure, as developed in [19]. Fig.8.3 compares the different surface structures. It shows the two probed surfaces of silicon. The channels under (001) are slightly smaller than the ones under (100). That explains the deeper onset penetration under (100), but it cannot explain the differences in the corresponding transition onset forces $F_{N\text{-}kink}$ and the phase-transition energies $W_{transition}$. We have thus to consider how the Berkovich indenter with its skew faces at the face angle (semi angle $\theta = 65.3^{\circ}$) interacts orthogonally with the interior of the crystal at the opposite angle, due to the penetrated Berkovich. The equally skew face structures around the Berkovich are calculated by rotations from the indented face by $rx \pm 65^{\circ}$ and $ry \pm 65^{\circ}$. This models 8 opposing skew faces because the corresponding rotations around 245° and 115° are mirrored or doubly mirrored. Fig. 8.4 and Fig. 8.5 image the striking differences. Fig.8.4 under (001) exhibits large channels for migrations that facilitate the phase changes. Clearly, that makes them less endothermic. Conversely, in the correspondingly calculated Fig.8.5, under (100) one observes 3 blocking (a, c, d) opposing faces and only one (b) with channels. Clearly, the migrational possibilities are more impeding under (100). The phase-transition and the endothermic result are thus considerably higher, as has to be expected.

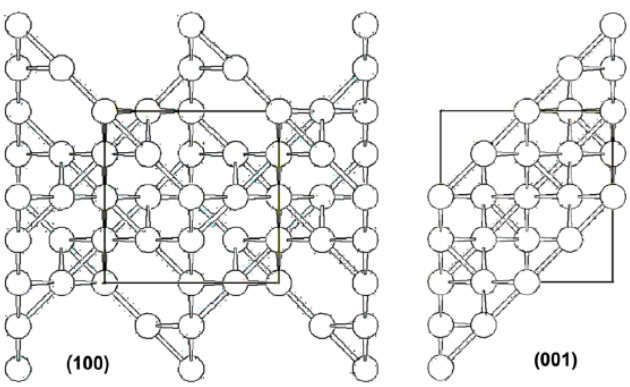

Fig. 8.3 View onto the two indented crystal surface structures of silicon

Table 8.2. Phase-transition onsets and energies of linear polymers upon indentation

Polymer	k_1 and k_2 $mN\mu m^{3/2}$	$F_{N\text{-}max}$ (mN)	$F_{N\text{-}kink}$ (mN)	h_{kink} (μm)	$W_{transition}$/mN mNμm/mN	Bond energy (kJ/mol[a)])	Literature of data origin
hd-PE	0.65776 1.08782	1.0	0.3247	0.6299	3.0159	363.2	This work
it-PP	11.030 14.001	3.0	1.8840	0.3064	3.1463	362.3	This work
PS--6C	0.02955 0.04303	0.450	0.1243	2.6202	0.5401	272.8	CSM Webinar 14.02.2010
PMMA	4.0252 4.9629	1.6	0.7758	0.3422	0.04116	n.a.[b)]	Brisccoe, Appl Phys 1998, 31, 2315
Cast PC	2.6385 3.3079	1.10	0.3779	0.2713	0.02083	Loss of CO_2	ditto

[a)]86th Handbook of Chemistry and Physics, CRC Press, 2006; [b)]not available, probably loss of the side group rather than chain breakage

Table 8.3 Multiple phase transitions of soda lime glass and silicon upon Berkovich indentation

Material	**k-value** $mNμm^{3/2}$	h_{kink} **(μm)**	$F_{N\text{-}kink}$ **(mN)**	$W_{transition}$ **mNμm/mN**	**Origin of Data**
Soda Lime Glass	77.909	0.4925	23.6782	0.1173	Oliver-Pharr 1992, J Mater Res 7, 1584
	105.28	0.7739	58.9005	0.4744	
	122.01	1.1173[a)]	up to 120 mN	0.6228[b)]	
Al (only the experimental)	9.7181	1.2105	12.1330	0.1418	K. Zeng, Acta Mater 2001, 49, 3539
	11.613	2.0997[a)]	up to 32 mN	1.2095[b)]	
Al (only data up to 90 mN)	12.036	3.1086	60.4343	0.2230	Oliver-Pharr 1992, J Mater Res 7, 1584
	13.377	3.8963[a)]	up to 90 mN	2.4958[b)]	
Si (001), B-doped, p-type	112.14[c)]	0.1501	6.5328	0.00687	T.F. Page, 1992, J Mater Res 7, 450
	121.75	0.2522	15.2899	0.02687	
	155.62	0.3309	25.2002	0.1942	
	160.62	0.4917[a)]	up to 50 mN	0.3014[b)]	
Si (100)	123.2	0.4077	29.1622	0.1545	S.V. Hainsworth 1996, J Mater Res 11, 1987
	145.44	0.7245	81.0015	0.4684	
	151.53	0.81968[a)]	up to 100 mN	0.5659[b)]	

[a)] h_{end} (μm); [b)] final $W_{applied}$/mN; [c)] k_2 = 124.80 from a separate measurement up to 11 mN after cut-off of the initial effect at 1 mN, including the hydrated oxide layer

Table 8.4. Face-dependent phase-transition onsets and transition energies of α-iron and strontiumtitanate

Material	**k_1 and k_2 $\mu N/nm^{3/2}$**	**Indenter**	**h_{kink} nm**	**$F_{N\text{-}kink}$ μN**	**$W_{transition}$ μNnm/μN**	**Data Origin**
Fe (100)	0.3590 0.2618	Cube Corner	103.0337	461.9156	−40.0372	Smith, Phys Rev B2003, 67 245405
Fe (110)	0.2332 0.1986	Cube Corner	109.0949	358.9707	−33.5112	ditto
$SrTiO_3$ (100)	3.0436 3.7145	Berkovich	69.7824	1738.2160	6.489	Kaupp, Scanning 2013, 35, 392
$SrTiO_3$ (110)	2.5217 3.3841	Berkovich	65.7308	1355.4438	7.020	ditto
$SrTiO_3$ (111)	2.7591 4.0878	Berkovich	102.8636	2860.4600	14. 821	ditto

Table 8.5 Unprecedented phase-transition qualities of γ-TiAl and various superalloys

Material	**max. F_N μN**	**k_1,k_2 and k_3 μN/nm$^{3/2}$**	**h_{kink}; h_{end} nm**	**$F_{N\text{-}kink}$ μN**	**$W_{transition}$ μNnm/μN**	**Data Origin**
γ-TiAl[a)]	3000	0.3213 0.4353	312.100	1787.7591	25.0885	Zambaldi 2010, Acta Mater 58, 3516
$Zr_{41}Ti_{14}Cu_{12.5}Ni_{10}Be_{22.5}$[a)] Vileroy105	500,000	0.90332 1.14282	2532.967	107,930.106	291.4861	Moser 2006, Phil Mag 86, 5715
$Fe_{43}Cr_{16}Mo_{16}C_{15}B_{10}$ (I)[b)]		7.21378 9.54375	505.499 1021.109	74,517.819	87.3435	Li, Intermetallics, 2007, 15, 706
$Fe_{43}Cr_{16}Mo_{16}C_{15}B_{10}$ (II)[c)]	300,000	11.64109	2532.967	176,653.607	176.2607	ditto
$Mg_{65}Cu_{25}Gd_{10}$[b)]	62,000	1.53921 1.93759	846.241	36,893.360	105.5932	ditto
$Cu_{60}Zr_{30}Ti_{10}$(I)[b)]		2.1803 2.6791	158.674 245.244	4056.1699	21.9236	Jiang, Mater Sci Eng, A2006, 430, 350
$Cu_{60}Zr_{30}Ti_{10}$(II)[c)]	18,000	2.8397	366.2825	8999.645	141.8416	ditto

[a)]Cube corner; it appears likely that there might have also been some Vanadium in that sample; [b)]Berkovich; [c)]Second transition

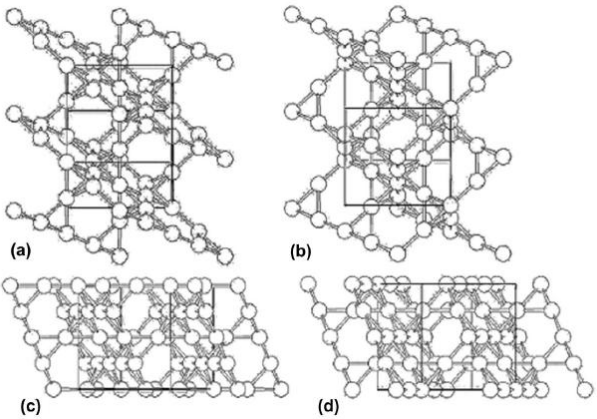

Fig. 8.4 Silicon skew faces as obtained by the rotations from (001); (a) rx = 65˚, (b) rx = −65˚, (c) ry = 65˚, (d) ry = −65˚

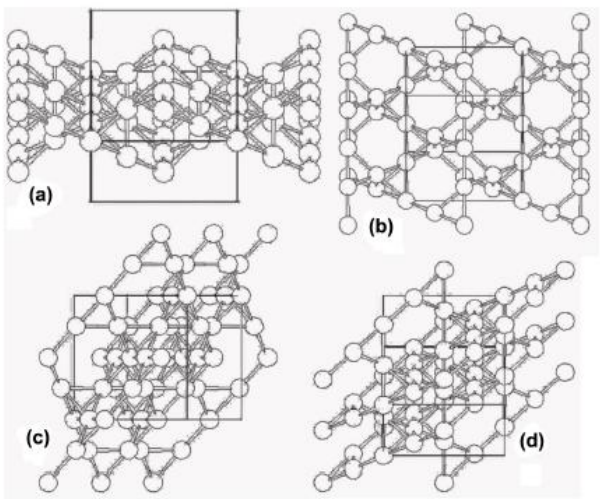

Fig. 8.5. Silicon skew faces as obtained by the rotations from (100); (a) rx = 65˚, (b) rx = −65˚, (c) ry = 65˚, (d) ry = −65˚

8.3.4 Further Face-Dependent Phase-Transitions

The multiple phase transitions of silicon (Berkovich) are also face specific and this is described in detail in Section 8.3.3, Table 8.3 and Figs. 8.3-8.5. Also, the anisotropic single exothermic phase-transition energies of α-quartz (cube corner)

on four different faces have already been analyzed for crystallographic reasons and reported in [19]. All crystalline materials must have different phase-transition energies under different faces. Further typical examples are with bcc α-iron (ferrite, Im3m) under two faces and with strontium titanate perovskite type (Pm−3m) under three faces (Table 8.4). These measurements require the high precision that is only available with the physical regression analysis without iterations or data fittings.

The crystal of α-iron on (100) and (110) exhibits different exothermic phase-transition values. For strontium titanate with three endothermic phase-transition energies, two of them have closer together values, but the lowest and largest values are far apart. This is again not consistently reflected by the different onset forces and onset depths (Table 8.4). The reasons are the different crystal packing, similar to the reasoning with silicon (Table 8.3) and α-quartz in [19]. The understanding of the exothermic phase-transition of α-iron rests again on the fact that the penetrating pyramid interacts orthogonally with its opposing skew face at the semi-angle, which is $\theta = 35.26^\circ$ for the cube corner. A rotation from the surface faces around x and y by $\pm 35^\circ$ yield these skew surfaces. The eight by 35°inclined faces around the three-sided indenter pyramid are completely represented with only two images for symmetry reasons of the bcc cubic crystal under (100) (Fig. 8.6) and under (110) (Fig.8.7). This facilitates the understanding of the differences for crystallographic reasons.

The crystal face on (100) and the skew faces under it in Fig.8.6 under (100) stand for the higher exothermic phase-transition of α-iron. The cube corner opposes all of the eight faces almost orthogonally that are devoid of channels. That means, there is no energy lost by the migration of phase transformed material. The gained exothermic energy remains highly negative.

Conversely, Fig. 8.7 with Fe on (110) with the lower exothermic phase-transition energy shows the skew faces by rotations of $\pm 35^\circ$ from it. Four of the eight exhibit open channels orthogonally to the indenter. Therefore, part of the gained transition-energy is used up for migration of the phase transformed material, leaving less of the gained energy by phase-transition. The channel face is here fortuitously the {111} faces across the crystal. Only the other four faces impede migrations.

The analogous analysis has been successful with the exothermic phase-transition of α-SiO_2 with cube corner in [19], where 4 different faces were studied: the absence of channels retains exothermic negative transition energy. Everything is thus well understood by the straightforward analysis in the case of exothermic phase-transition.

As already shown for the endothermic phase-transitions of silicon in Section 3.3, the analysis of the strontiumtitanate using Berkovich with $\theta = 65.3^\circ$ is equally successful (not imaged here, due to many images that are required). The minimal endothermic work (6.5 μNnm/μN) is required under (100), where channels are available on the skew faces to facilitate the conversion. Conversely,

under (111) the strongest endothermic energy (14.8 μNnm/μN) is observed, as there are no channels at the skew faces that enforce the transition to stay blocked in space, which increases the endothermic work. Consistently, under (110) the value (7.0 μNnm/μN) stays between the extremes, as there are some smaller channels allowing for minor migration of the transformed material. Again, channels facilitate migrations for the endothermic phase-transitions and decrease the endothermic work. When migrations are blocked more work is required for the phase-transition. The face-dependency of phase-transition energies is thus well understood by crystal structure analysis.

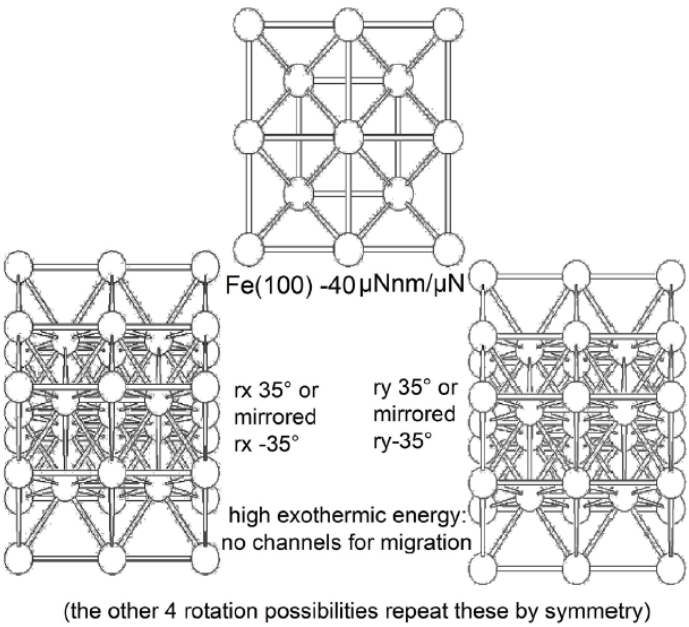

Fig. 8.6. The α-iron (100) face and those as obtained by rotations from it by rx = 35° and ry = 35°, modelling all eight skew surfaces that surround the penetrated cube corner indenter for symmetry reasons, leaving no channels for migrations

8.3.5 Phase-Transition Energies of Superalloys

The sudden first order sharp phase-transitions form polymorph interfaces that are shifted away from the indenter after their onset when the load increases. These polymorph interfaces are preferential sites for the nucleation of large far-distant cracks. This has already been imaged in connection with the multiple consecutive phase-transitions of sodium chloride in [20]. These circumstances are most important for the occurrence of catastrophic failures of superalloys at work. Clearly, polymorph interfaces must be avoided with materials under

mechanical and thermal stress. We must therefore urgently look for phase-transition onsets and transition energies of published loading curves of some superalloys (also called entropic alloys). This shall convince industries that they must complement their Vickers, Brinell, Rockwell, etc. hardness measurements with physical depth-sensing macroindentations' control. Only these provide the necessary phase-transition information. The problems might occur primarily after multi-1000-fold load and unload both mechanically and thermally. The thermal stress calculation requires the activation energy of the phase-transitions that can also be obtained by physically correct temperature dependent indentations [13]. The transition energies W_{trans} in Table 8.5 are purposely given in μNnm/μN units, in order to show that such phase transformations can also here occur at comparatively low loads and depths. There were no "pop-ins", which could disqualify the alloy's use beforehand. However, these published examples do certainly not represent alloys that are in practical use, as the actual alloys are secret and only available to the industrial personnel.

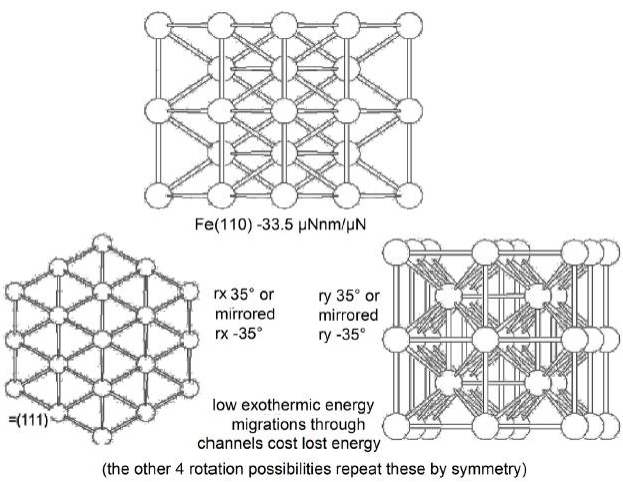

Fig. 8.7. The α-iron (110) face and those as obtained by rotations from it by rx = 35˚ and ry = 35˚, modelling by symmetry all eight skew surfaces that almost orthogonally surround the penetrated cube corner indenter, four of them (here fortuitously {111}) with open channels for migrations

Table 8.5 starts with the 68/32 γTiAl alloy, because a propeller blade close to the turbine each out of a "titanium-aluminium alloy" or an "Al-Li-alloy" from 2 identical airliners broke away, during flight within one year in 2017 and 2018. Both blades hit the body of the airliners, unfortunately killing a woman passenger. The alloy of publicly unknown composition contained certainly several other components. The data of Table 8.5 show however comparably low force and energy values for the phase-transition of the Al alloy base. It is seen: the way for obtaining high enough phase-transition onset and endothermic transition energy for a good Al alloy must probably have been too long. It appears important to study the Al-Li-

alloys with respect to their phase-transition properties. The other alloys of Table 8.5 exhibit much higher values, but these alloys are certainly not the secret alloys for airplanes. There are means to engineer alloys by trial and error with ductilizer.

Ductilizers give for example by oxide dispersion strengthening ODS-super-alloys with Y_2O_3, ThO_2, La_2O_3, Al_2O_3, etc. [28]. Also, carbon and further materials have been widely used as additives. Here is now the still not industrially used (legal ISO-ASTM standard certification!) more systematic way to improve superalloy compositions for best performance. All what's required is the easy and reliable physical indentation analysis with respect to phase-transitions. The hardness of materials is again a poor guide for judging the phase-transition onset force ranges and the phase-transition energies. For example, the by far best alloy in Table 8.5 is Vileroy-105 with a comparably low hardness (k_1= 0.90332 $\mu N/nm^{3/2}$ or with other units 29.652 $mN/\mu m^{3/2}$) that are much smaller than those of $Fe_{43}Cr_{16}Mg_{16}C_{15}B_{10}$ (k_1= 7.21378 $\mu N/nm^{3/2}$ or with other units 228.12 $mN/\mu m^{3/2}$), while the $W_{transition}$ ratio is 291/87, respectively. The Newton-range is almost reached with Vileroy-105. Its first transition is at highest force and also the transition energy is highest, whereas the well-known iron-based superalloy surmounts the kink force only at its second phase-transition but with much lower transition energy. The magnesium based alloy is inferior and the copper-based alloy has two phase-transitions at still lower forces and transition energies.

The here achieved maximal loading forces (0.5 N, corresponding to HV 0.05) are at or below the lower level of industrial Vickers, Brinell, Rockwell, etc. hardness measurements. These are certainly highly standardized by ASTM, but unable to detect phase-transitions. It is to be expected that further as yet undetected phase-transitions will occur at the much higher loads (for example from Vickers hardness HV 0.5 to HV 10) in all cases.

The field of superalloys for technical constructions is widespread and extremely important, and so is the improvement of the stability of superalloys when being at work. Any alloy must only be admitted to forces below its first phase-transition onset. Both the onset force and the transition energies must be as high as possible. We present here a simple systematic way to improve the engineers' efficiency, but this depends on the profound change of the present ISO and ASTM standards that are the basis of the manufacturer's certification. Physical mathematically proved standards must be urgently created, edited, and enforced. Present ISO-ASTM hardness or indentation moduli are not physical quantities and they are unsuitable for the safety. Their biggest flaw is their inability to detect or even know of phase-transitions under load. The here described improvements are, of course, worldwide indispensable, but unfortunately not easily achieved for various unscientific reasons.

8.4 CONCLUSION

We showed here that undeniable sacrosanct basic calculation rules prove the physically founded Equation (8.1) [7] for pyramidal (or conical) indentations. These lead to the detection and energetic characterization by calculations with proof of the universal evaluation formulas. Phase-transition onset and phase-transition energies have been calculated across all material types. These include

multiple transformations and surface dependent ones at various load conditions. Special effects are detected and corrected because bulk qualities are aimed at. Instrument builders are urged to offer the corresponding software for automatic calculation of these quantities. It is impossible to judge the ranges of phase-transition onset forces and energies from hardness and elastic moduli that violate the energy law [14,21,22]. The wrong exponent 2 on h and the violation of the energy law are intolerably incomprehensible and must be pitiless rejected. The whole world should no longer be forced to assume that the elastic pressure deformation plus all of the pressure induced plastic deformations can be obtained from nothing. The presented measurements indicate again that phase-transitions of materials under mechanical or thermal stress facilitate catastrophic breakages [20]. ISO and ASTM must thus normatively require the detection of the onset and transition energies for all technically used materials. And for safety reasons, admission of all materials must be restricted to forces (temperatures) well below their first phase-transition. For thermal stress, the activation energy of the first phase-transition [13] must be calculated and its constancy after the long running routines equally secured. The ISO 14577 standard must urgently be changed. In the meantime, Certification Agencies must stop using ISO 14577 for the certification procedure of industrial companies. Only that stopping will enable them to perform the required use of the calculation rules with depth sensing (macro) indentations for the search of phase-transition onsets and energies. This is, of course, additionally required after the standard stretching and bending tests for all materials. It will also be necessary upon the legally prescribed maintenance routines and particularly for a posteriori tests after the recent catastrophic events of e.g. broken off propeller blades in front of turbines, etc. It will clarify the reasons and avoid further risks with replaced materials for safety reasons. This paper shall help in that endeavor. Future research must also routinely include reliable low and very low-temperature indentations of technical materials to search for embrittlements (no pile-up allowed) and additional low-temperature phase-transitions. First examples at −63°C [29] and −113°C [30] are already available, but the proved mathematical analyses were not used. We try cooperation at an applied instrument with such capabilities and continue with worldwide lecturing on this important subject.

COMPETING INTERESTS

Author has declared that no competing interests exist.

REFERENCES

1. Kaupp, G. and Naimi-Jamal, M.R. (2013) Penetration Resistance and Penetrability in Pyramidal (Nano)Indentations. Scanning, 35, 88-111. https://doi.org/10.1002/sca.21038
2. Love, A.E.H. (1939) Boussinesq's Problem for a Rigid Cone. The Quarterly Journal of Mathematics (Oxford), 10, 161-175. https://doi.org/10.1093/qmath/os-10.1.161

3. Sneddon, I.N. (1965) The Relation between Load and Penetration in the Axisymmetric Boussinesq Problem for a Punch of Arbitrary Profile. International Journal of Engineering Science, 3, 47-57.
https://doi.org/10.1016/0020-7225(65)90019-4
4. Oliver, W.C. and Pharr, G.M. (1992) An Improved Technique for Determining Hardness and Elastic Modulus Using Load and Displacement Sensing Indentation Experiments. Journal of Materials Research, 7, 1564-1583.
https://doi.org/10.1557/JMR.1992.1564
5. Kaupp, G. and Naimi-Jamal, M.R. (2004) Nanoscratching on Surfaces: The Relationships between Lateral Force, Normal Force and Normal Displacement. International Journal of Materials Research, 95, 297-305.
https://doi.org/10.3139/146.017952
6. Naimi-Jamal, M.R. and Kaupp, G. (2005) Quantitative Evaluation of Nanoindents: Do We Need More Reliable Mechanical Parameters for the Characterization of Materials? International Journal of Materials Research, 96, 1226-1236.
https://doi.org/10.3139/146.101166
7. Kaupp, G. (2016) The Physical Foundation of $F_N = k\ h^{3/2}$ for Conica/l pyramidal Indentation Loading Curves. Scanning, 38, 177-179.
https://doi.org/10.1002/sca.21223
8. Kaupp, G. (2013) Penetration Resistance: A New Approach to the Energetics of Indentations. Scanning, 35, 392-401.
https://doi.org/10.1002/sca.21080
9. Liu Z, Wang S, Zhang S, Feng Y, Peng Y, Gong J. Deformation response of gradient low-temperature gaseous carburized case in austenitic stainless steel during cyclic nanoindentation. Materials Today Communications. 2021 Sep 1;28:102714.
10. Bernachy-Barbe F. A data analysis procedure for phase identification in nanoindentation results of cementitious materials. Materials and Structures. 2019 Oct;52(5):1-2.
11. Kaupp G. Indentation onto Stishovite (SiO2), MgO, and a Covered Superalloy: “Pop-In” Repair, Phase-Transition Onsets, Polymorph Energies, and Transition-Energies. Advances in Materials Physics and Chemistry. 2020 Mar 25;10(3):77-95.
12. Merle, B., Maier, V. and Durst, K. (2014) Experimental and Theoretical Confirmation of the Scaling Exponent 2 in Pyramidal Load Displacement Data for Depth Sensing Indentation. Scanning, 36, 526-529.
https://doi.org/10.1002/sca.21151
13. Kaupp, G. (2014) Activation Energy of the Low-Load NaCl Transition from Nanoindentation Loading Curves. Scanning, 36, 582-589.
https://doi.org/10.1002/sca.21158
14. Kaupp, G. (2017) The ISO Standard 14577 for Mechanics Violates the First Energy Law and Denies Physical Dimensions. Journal of Material Sciences and Engineering, 6, 321-328.

https://doi.org/10.4172/2169-0022.1000321

15. Zeng, K. and Chiu, C.H. (2001) An Analysis of Load-Penetration Curves from Instrumented Indentation. Acta Materialia, 49, 3539-3551.
    https://doi.org/10.1016/S1359-6454(01)00245-2
16. Hainsworth, S.V., Chandler, H.W. and Page, T.F. (1996) Analysis of Nanoindentation Load-Displacement Curves. Journal of Materials Research, 11, 1987-1995.
    https://doi.org/10.1557/JMR.1996.0250
17. Troyon, M., Abbes, F. and Garcia Guzman, J.A. (2012) Is the Exponent 3/2 Justified in Analysis of Loading Curve of Pyramidal Nanoindentations? Scanning, 34, 410-417.
    https://doi.org/10.1002/sca.21025
18. Soare, S., Bull, S.J., Oila, A., O'Neill, A.G., Wright, N.G. Horsfall, A. and dos Santos, J.M.M. (2005) Obtaining Mechanical Parameters for Metallization Stress Sensor Design Using Nanoindentation. International Journal of Materials Research, 96, 1262-1266.
    https://doi.org/10.3139/146.101172
19. Kaupp, G. (2019) Phase-Transition Energies, New Characterization of Solid Materials and Anisotropy. Advances in Materials Physics and Chemistry, 9, 57-70.
    https://doi.org/10.4236/ampc.2019.94006
20. Kaupp, G. (2018) Six Polymorphs of Sodium Chloride upon Depth-Sensing Scanning Macroindentatiom with Unusual Long-Range Cracks Requiring 30 N Load. Journal of Material Sciences and Engineering, 7, 473-483.
    https://doi.org/10.4172/2169-0022.1000473
21. Kaupp, G. (2017) Dilemma between Physics and ISO Elastic Indentation Modulus. Journal of Material Sciences and Engineering, 6, 402-405.
22. Kaupp, G. (2017) Challenge of Industrial High-Load One-Point Hardness and of Depth Sensing Modulus. Journal of Material Sciences and Engineering, 6, 348-355.
    https://doi.org/10.4172/2169-0022.1000348
23. Keller, E. (1997) Schakal 97. Kristallographisches Institut der Universität Freiburg i. Br., Germany.
24. Lin, J.F., Degtyareva, O., Prewitt, C., Dera, P., Sata, N., Gregoryanz, E., Mao, H.K. and Hemley, R.J. (2004) Crystal Structure of a High-Pressure/High-Temperature Phase of Alumina by In-Situ X-Ray Diffraction. Nature Minerals, 3, 389-393.
    https://doi.org/10.1038/nmat1121
25. Thurn, J., Morris, D.J. and Cook, R.F. (2002) Depth-Sensing Indentation at Macroscopic Dimensions. Journal of Materials Research, 17, 2679-2690.
    https://doi.org/10.1557/JMR.2002.0388

26. Bradby, J.E., Williams, J.S. and Swain, M.V. (2003) In Situ Electrical Characterization of Phase Transformations in Si during Indentation. Physical Review B, 67, Article ID: 085205.
https://doi.org/10.1103/PhysRevB.67.085205
27. Page, T.F., Oliver, W.C. and McHargue, C.J. (1992) The Deformation Behavior of Ceramic Crystals Subjected to Very Low Load (Nano)Indentations. Journal of Materials Research, 7, 450-473.
https://doi.org/10.1557/JMR.1992.0450
28. Kaupp, G. (2011) Reactive Milling with Metals for Environmentally Benign Sustainable Production. CrystEngComm, 13, 3108-3121.
https://doi.org/10.1039/c1ce05085k
29. Wang, S., Liu, H., Xu, L., Du, X., Zhao, D., Zhu, B., Yu, M. and Zhao, H. (2017) Investigation of Phase Transformation in Monocrystalline Silicone at Low Temperatures via Nanoindentation. Scientific Reports, 7, Article No. 8682.
https://doi.org/10.1038/s41598-017-09411-x
30. Lee, S.W., Meza, L. and Greer, J.R. (2013) Cryogenic Nanoindentation Size Effect in [0 0 1]-Oriented Face-Centered Cubic and Body-Centered Cubic Single Crystals. Applied Physics Letters, 103, Article ID: 101906.
https://doi.org/10.1063/1.4820585

DISCLAIMER
This chapter is an extended version of the article published by the same author(s) in the following journal.
Advances in Materials Physics and Chemistry, 9:103-122, 2019.

Chapter 9
Print ISBN: 978-93-5547-921-1, eBook ISBN: 978-93-5547-922-8

The Loading Curve of Spherical Indentions is Not a Parabola and Flat Punch is Linear: Scientific Explanation

DOI: 10.9734/bpi/mono/978-93-5547-921-1/CH9

ABSTRACT

The goal of this paper is to physically deduce the loading curves for spherical and flat punch indentations, especially since the one exponent parabola assumption appears to be impossible for not self-similar spherical impressions. By taking into account the work done by elastic and plastic pressure work, these deductions avoid the still common first energy law violations of ISO 14577. The misleading though hitherto generally accepted "parabolas" exponents on the depth *h* ("2 for cone, 3/2 for spheres, and 1 for flat punches") are still the unchanged basis of ISO 14577 standards that also enforce the (false for cone and sphere) up to 3 + 8 free iteration parameters for ISO hardness and ISO elastic indentation modulus. Since the elastic and inelastic pressure work cannot be created out of nothing, almost all of these common practices are now refuted by physical mathematical proof of exponent 3/2 for cones, which also dispels the myths about indentation against a flat projected surface (contact) area with violation of the first energy law. The impression of a volume that is associated with pressure formation, which results in elastic deformation and a variety of plastic deformations, is physically accurate. Only the loading parabola for cones, pyramids, and wedges follows the exponent 3/2. It appears impossible that the geometrically not self-similar sphere loading curve is an $h^{3/2}$ parabola. Hertz did only deduce the touching of the sphere and Sneddon did not get a one-exponent parabola for the sphere. The radius over depth ratio is not constant with the sphere. The sole exponent 3/2 on h (Johnson's formula) for the spherical indentation loading curve does not hold up against the ostensibly strong correlation of such parabola graphs at large R/h ratios and low *h*-values. Such graphs do not represent the sphere physically, and so, attempted regression results point to data manipulations using at least one published data fitting formula. Unbiased algebraically we now deduce with the exponential factor $h^{3/2}$ and a depth-dependent dimensionless correction factor containing the R/h ratio as result the closed physical formula for the spherical indentations. Even with huge radius/depth-ratios at the shallow indents, the $h^{3/2}$ against force plot utilizing published data is concavely bent. Thus, the benefits of conical, pyramidal, and wedged indentations are negated. For experimental nano- and micro-indentations, these details are listed. Spherical indentations showing linear data regression for force versus $h^{3/2}$ plots do not agree with physical reality. They are

useless and reveal the data-fitting. This emphasizes the need for simple deductions of the right relationships based on indisputable calculation procedures and indisputable fundamental physical knowledge that don't require fitting or iteration. Therefore, in addition to formulas for the physical indentation hardness, indentation work, and applied work for these indentations, the simple physical deduction of the flat punch indentation is also supplied. A macroindentation serves as an illustration.

Keywords: Closed formula for spherical indentation; CHALLENGE OF ISO14577; mathematical proofs; volume instead of area; correct flat indentations; physical indentation hardness; hardness dependence on indenter shape; data treatment detection.

9.1 INTRODUCTION

The two-dimensional handling of the three-dimensional impression into solids is the most serious fallacy in the powerful (nano) indentation sector. Since 1992, this practice has gained widespread praise on a global scale. The force-depth curves for conical and spherical indenters, respectively, are still viewed as parabolas with the exponents 2 and 3/2, and serve as the foundation of ISO 14577 [1,2,3]. It seemed to be an unbreakable norm for indentations. This misleading hypothesis is “supported” and widely accepted in academia [1], textbooks [2], and business [3]. Despite being aware that the spherical indentation is not "geometrically self-similar," they continue to utilize a "parabola with exponent 3/2 for spheres" (ratio of impression radius or diagonal over depth is not constant). Furthermore it is used for defining the size of their always used correction factor “ε” [4], for their iteration of the projected contact area according to the work by [1], and by ISO 14577 for “refining” their ISO-hardness (H [N/m^2 or GPa]) and ISO-elastic modulus E calculations. These include false exponent and energy-law violation and undue “Young’s modulus” claim by ([1], etc.) and ISO 14577, as first disproved in [5,6]. Spherical indentions cannot physically be described by a F_N - $h^{3/2}$ parabola (F_N = normal force, formerly often called “P”), even though experimental plots of $h^{3/2}$ versus F_N appear to be linear for very high R/h values (sphere radius over depth) and low depth ranges. Some updates in this area are available elsewhere and may find attention of the readers [7-9]. [7] describes the Hertzian theory of 1882 in combination with an asymptotic modelling. Also [8] analyzes detailed sphere to sphere indentations. [9] uses sole exponents on h and determines its value between 1 to 1.5 on the basis of FE-simulations, but at the expense of the universal equation that is our unique mathematical physics formula (9.7). from 2019 that cannot be denied.

However, a physical background was missing. H. Hertz deduced an equation with exponent 3/2 for the mathematical touching of a sphere and a flat surface or a second sphere, and for horizontally sliding of solid bodies without pressure [10]. Hertz himself literally stressed the validity of his deduction in [10] only for the mathematical touching (not indenting) at one single point in [11], and Sneddon’s solution for spheres is not a one-exponent parabola [12]. Nevertheless, the unproved parabola has also been used for the determination of

the tip rounding of pyramidal indenters. Uncountable AFM (atomic force microscopy) publications reported on the "spherical Hertzian exponent 3/2" without citing Hertz work and without giving their equation for the impression contact under force. No force-depth relation with exponent 3/2 can be found in [11] and Hertz's hardness definition does not help either. This can not at all be taken as a description of indentations under load. In addition, the authors of [1] and ISO 14577 took over the force-less contact for spherical indentations under force for indentations. Also the textbook [2] explained the inconstant a/R ratio (R = indenter radius, a = radius of the impression), for not self-similarly penetrating spheres in its Figs. 1.1and 1.4 for angles between 0 and at least ±33° from the normal line. The author did not consider that such angle would not be proportional to the depth of spherical indentations. Users were nevertheless taught that they can go deeply onto the surface with such a parabola. Interestingly, while the exponent 2 for conical indents of Sneddon [12] (his pre-exponential constant differed from the one of Love [13]) and exponent 1 for flat indents were welcomed in [1] and by ISO 14577, but Sneddon's non-parabola solution for spheres with after all three members and three different exponents on h (2, 1, and 0) after rewriting of his formula was disregarded (inappropriate [10] was preferred). One just took what is liked and disregarded what is disliked for the sphere in [12]. However, we do not agree with the solution of Sneddon for spheres as the false premises of [12] were the same as those that ended with the false exponent 2 for cones.

The universal correct exponent for cones is in fact 3/2 as undeniably proved in [14] on the basis of sacrosanct calculation rules. This is also not in accord with the still common "iron rule" of ISO etc. Unfortunately, the "iron rule" was not abandoned since 1965 and more so when "h^2" for cones" was experimentally replaced by $h^{3/2}$ in 2004 [15], even though the elegant and simple physical deduction (finally published in 2016 [14]) was ripe for deduction. But the false exponent "2" for cones/pyramids/wedges is still defended by biased anonymous reviewers who fight against the $F_N = kh^{3/2}$ plot for conical/pyramidal/wedged indentations and unduly call it "Kaupp-fitting" (it must therefore now be called Kaupp-plot). Furthermore, they use and cite easily traced juggler tricks from published papers revealing unbelievable lack of mathematical knowledge of very basic calculation rules. These include unequal dimension on both sides of equations, or not realizing that the proportionality factor of loading parabolas has a dimension that depends on the exponent of h as does its value, or by defining indentation hardness as force over surface area, and then claiming a "theoretical confirmation of h^2" for the cone and pyramid, as deduced from such definition. Unfortunately, this includes ISO 14577 officials, authors, editors, and biased anonymous peer reviewers. Nevertheless, ISO 14577 and numerous recent publications still claim the so-called "Hertzian exponent" on a "parabola with exponent 3/2" on h_{sphere}. Others simply claim to use an unspecified "Hertzian theory" but without citing the original (e.g. [10] and [11]) and not telling what they mean with that, when spheres are penetrating into flat surfaces.

Before having the here disclosed solution the present author expressed however on his worldwide lectures the opinion that the spherical loading curves might at

best only approximate the exponent 3/2 on h for experimental spherical indentations, for large R/h ratios and shallow indents [1,2], as in ISO 14577. This speculation deserves the straightforward physical deduction, because $h^{3/2}$ cannot at the same time be valid for geometrically self-similar cones/ pyramids/wedges and the not self-similar sphere [14]. But even the present author obtained good correlations with $F_N = k\ h^{3/2}$ plots in the analyzed spherical indentations from the literature. He added the word “apparently” to this exponent of a parabola [16] and that these slopes cannot be compared with the ones from pyramids [16]. But the reported k_1-value from the nickel-superalloy (published R = 269 nm) [17] and the k-value from PDMS ((polydimethylsiloxane) (R = 192 µm) ([18], in [16] are no longer penetration resistances, because the now deduced Equation (9.7) excludes a parabola for spherical indentation. $F_N = k\ h^{3/2}$ plots for spherical indentations are physically in error, irrespective of the linear correlations with their large radius/dept ratios and narrow depth ranges. This will be shown in this paper. We deduce in this work the physical load-depth behavior for spheres on the same basis as the deduction in [14] by Kaupp with respect to the impressed volume but not with respect to a projected flat basal contact area, and check both of these correct and incorrect approaches. By doing so, we will also complete the story with the physical proof of the (correct) exponent 1 for flat punch indentations. A consistent theoretical understanding is achieved. Both spherical indentations were reanalyzed in Section 9.3.2.2. and 9.3.2.3.

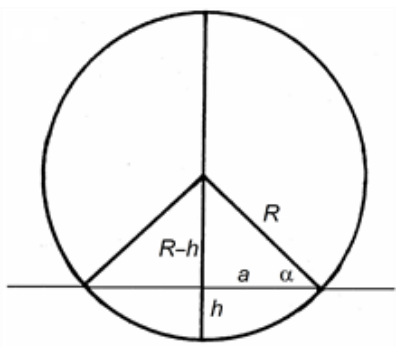

Fig. 9.1 Schematic representation of a sphere partly immersed beneath an initial plane surface with an angle α that is differently defined as the one mentioned in Section 1 of [2]

Fortunately, the unprecedented new results did not affect our elegant and correct calculation of the PDMS adhesion energy with $0.5\ F_N\ h$ in [5], which corrected the complicated JKR (Johnson, Kendall, Roberts) [19] iterative process in [18] by a factor of 2.66 [5].

9.2 MATERIALS AND METHODS

The indentation onto a hard metallic nickel superalloy with a blunt Berkovich indenter with claimed end radius of 269 nm was selected, because its calculated

cone depth $h_{\text{cone}} = R\left(1-\sin\beta\right)$ [16]) of 15.75 nm was very close at 15.9 nm. The final depth of only 50.3 nm allowed for the safe collection of 13 data pairs after a minor surface effect. Conversely, the data of a soft PDMS sample (polydimethylsiloxane) in combination with a huge spherical indenter radius and providing both 54 "experimental" and 54 fitted data pairs at considerable depths were calculated and printed with Excel®. The data collections were from the digitized published loading curves with the Plot Digitizer 2.5.1 program; http://www.softpedia.com/. The calculations of Equation (9.7) used a pocket calculator with 10 figures to avoid rounding errors and the results reasonably rounded in the Tables and text.

9.3 RESULTS AND DISCUSSION

9.3.1 The Force-Depth Parabola of Conical/Pyramidal/Wedged Indentations

We repeat here the physical deduction of the exponent for the loading parabola of self-similar conical, pyramidal and wedged indenters to remind the elegant straightforward technique. Indentations create two connected processes: the volume formation and the total pressure [14]. This has hitherto been disregarded or ignored, even though the retained part of the pressure (not transformed for plasticizing) has been amply used from the beginning for the elastic modulus iteration from the unloading curve by [1], ISO 14577. It remained unconsidered that even elastic pressure creates work that is generated by the force. We have therefore to start with a normal force (F_N) parabola $F_N = k\ h^x$ with two components, one for volume (V) and the other for pressure (p):

When doing so we have to consider that the total pressure (p_{total}) (remaining pressure plus loss of pressure in case of all of the different modes of plastic conversions) must be used. The exponents m and n must sum up to 1 for obtaining F_N. As p_{total} is undoubtedly proportional to the indented volume of the indenter under the originally flat surface we have for the cone with its mathematical volume at the depth h the equation $p_{\text{total}} = KV = K\pi\left(\tan\alpha\right)^2 h^3/3$. The conversion of h r^2 into $(\tan\alpha)^2\ h^3$ is self-evident. Similarly, we have h^3 also for the volumes of pyramids and wedges. As p_{total} is proportional to h^3 also $F_{\text{N-}p} \propto h^3$, and h relates to $F_{\text{N-}p}^{1/3}$, which is lost for the indentation depth, but it tells us that $F_{\text{N-}V}^{m} = F_{\text{N-}V}^{2/3}$. So we have physically on the basis of arithmetic calculation rules $F_{\text{N-}V}^{2/3} = \text{const}h$ or $F_{\text{N-}V} = kh^{3/2}$ (Equation (9.1) [14] where k denotes the chemo-physical properties of the material in question. This describes in detail the deduction of the universal exponent 3/2 for conical/pyramidal/wedged indentations with hard indenters (diamond), independent of the materials, as could be finally published in 2016 (9.2).

(9.1)

$$F_{\text{N-}V} = kh^{3/2} \tag{9.2}$$

9.3.2 The Force-Depth Curve of Spherical Indentations

9.3.2.1 Theoretical Considerations, Deduction of Equation (9.7)

The spherical indentation is generally though falsely assumed (ISO14577, [1,2,3,4]) to occur as parabola with exponent 3/2. The non-indentation but only touching deduction of Hertz [10,11] was taken as theoretical background, but there is concern, whether cones/pyramids/wedges could have the same exponent for loading parabolas. Experimentally it appeared that such behavior would be also valid for spherical indentations, but only for large R/h values and the low penetrations that are achieved. Also the present author Kaupp obtained good correlations with $F_N = kh^{3/2}$ plots from the published "spherical" indentations that he analyzed, but the word "apparently" was added to this spherical exponent [16] and an initial approximation was claimed. As already mentioned, Sneddon [12] did not get a simple parabola at all, but this deduction was disregarded in [1,2,3,4]. The solution of Sneddon is as follows when his equation "6.13" is substituted in "6.15" on page 54 of [12]. By now using the common letters for the corresponding subjects one obtains $F_N = \left[E/(1-\nu) \right] \left[\left(a^2 + R^2 \right) 2h/a - aR \right]$ with strongly varying h/a- ratio = cotgβ (for β cf. Fig. 9.1) as a three-membered "solution". From there with $a = h/\cot\beta$ one obtains $F_N (1-\nu)/E = 2h^2/\cot\beta - hR/\cot\beta + 2R^2 \cot\beta$ This is not a parabola but cotβ is variable (*E* = "Young's" modulus, ν = Poisson's ratio). Experimental results are not in agreement with the solution of Sneddon, as it depends on his undue premises (area instead of volume) that also led to the disproved exponent 2 for cone/ pyramid/wedge. The physical solution is now deduced.

When starting with using volume instead of area as shown in Section 9.3.1, we reformulate the mathematical volume of the immersed calotte (9.3A) by multiplication with 1 = h/h and obtain the form of (9.3B), which separates h^3 and a dimensionless though h-dependent correction factor. Further forms are (9.3C) with two different exponents on h and finally for the angle α dependence (9.3D). According to Fig. 9.1 is $(R-h)/R = \sin\alpha$ so that $h/R = (1-\sin\alpha)$ or $R/h = 1/(1-\sin\alpha)$ This can be substituted in (9.3B) to obtain (9.3D), so that one can also check the angle ranges of the depressions. All 4 forms A-D of (9.3) are equal.

$$V = \pi h^2 (R - h/3) \tag{9.3A}$$

$$V = \pi h^3 \left(R/h - 1/3 \right) \tag{9.3B}$$

$$V = \pi h^2 R - \pi h^3/3 \tag{9.3C}$$

$$V = \pi h^3 \left[1/\left(1 - \sin\alpha\right) - 1/3 \right] \tag{9.3D}$$

We first show how much the dimensionless volume factor of (9.3D) changes for various angles α between 30° (very deep impression) and 89.5° (very flat impression) in Table 9.1. They indicate the strong non-linear variation of the volume factor with the indention depth.

Table 9.1 Clearly shows the enormous variation of the dimensionless factor for Equations 9.(3B), which excludes a physical parabola exponent for spherical indentation load-depth curves. It is only valid for every single point of such curve with its own R/h ratio in accord with the physical deduction in Section 9.3.1, because the point by point changing pre-exponential dimensionless factor multiplies with the penetration resistance k_{sphere} [N/m$^{3/2}$] (cf. (9.2)). The claimed parabolas seem to be excluded under these conditions. There is the proviso that so named "experimental data" could have been somehow iterated and fitted. We do not invoke the sphere quality here. It is clearly seen at (9.3), that the calotte volume is not only described by h^3 as we had it with the cone (pyramid, wedge) where we deduced the exponent 3/2 on h in Section 9.3.1. There is now a dimensionless factor that changes with the R/h ratio (9.3B).

Table 9.1. Formal analysis of the volume factor $\pi[1/(1-\sin\alpha) - 1/3] = \pi(R/h - 1/3)$ **at varying angle α**

α °	sin α	1 − sin α	π [1/(1 − sin α) − 1/3]
30	0.5000	0.5000	0.5236
40	0.642787609	0.35721239	7.7475
50	0.766044443	0.23395556	13.4282
60	0.866025403	0.13397460	23.4492
70	0.93969262	0.06030738	52.0930
80	0.984807753	0.01519225	207.7429
89.5	0.999961923	0.00003808	82,499.8071

The physical deduction of the spherical loading curve using (9.3B) starts with the evidently coupled processes of volume formation and pressure formation. As in Section 9.3.1 it means (9.1) Both factors relate to the immersed volume and n + m must give 1 (9.1). The total pressure (p_{total} is the sum of p that remains plus p for all plastic deformations) has to be considered, as it leads to reversible and to plastic deformations. It is without any doubt that p_{total} is proportional to the impressed volume V. Thus $p_{total} \propto h^3 \pi \left(R/h - 1/3 \right)$

and thus also $F_{N\text{-}p}$ are proportional to $\pi h^3\left(R/h-1/3\right)$ (4). So. we obtain the exponent n = 1/3 when h is expressed in (9.5) and m = 2/3 because both exponents must add to 1. As the pressure part of the force is lost for the impression, it follows that $F_{N\text{-}V}^{2/3}$ is proportional to $h\pi^{2/3}\left(R/h-1/3\right)^{2/3}$ (9.6), and thus for the impression $F_{N\text{-}V}=kh^{3/2}\pi\left(R/h-1/3\right)$ (9.7) where **k** takes care of the relevant chemo-physical properties of the material in question. $F_{N\text{-}V}$ controls the depth and can now be abbreviated as F_N in relation to the depth) (9.7) of the not self-similar spherical indenter. The calculation of α indicates the angle range of the experimental loading curves. Equation (9.7) shows that the penetration resistance $k\pi\left(R/h-1/3\right)$ [N/m$^{3/2}$] of spherical indentations is not constant and it cannot be easily compared with the k-values of pyramidal indentations. The latter are normalized for their cone angles [16]. The physical deduction uses the undeniable fact that the indenter volume is immersed into the material and that the force is in part used for pressure stress that produces elastic and plastic work. This pressure stress is not part of the depth formation that determines the immersed indenter volume. Earlier deductions [12] did not care for the pressure part and they thus violated the first energy law [1,2,3] and ISO 14577. Such unphysical "deductions" were mathematically very complicated [12,18,19] and yielded false results. The physical deduction in this work does not need more than basic calculation rules in (9.1) and (9.3) through (9.7) for the spherical indentation with its inconstant penetration resistance $k\pi\left(R/h-1/3\right)$ [N/m$^{3/2}$]) with its materials factor *k* and the geometrical factor that also depends on the depth. Equation (9.1) , is also the start point for the spherical indentationon.

p_{total} and thus also $F_{N\text{-}p}=\pi h^3\left(R/h \quad 1/3\right)$ (9.4)

$$F_{N\text{-}p}^{1/3}\propto h\pi^{1/3}\left(R/h-1/3\right)^{1/3} \tag{9.5}$$

With n = 1/3 and m = 2/3 it follows that $F_N^{2/3}$ is proportional to the depth h, and with the h-dependent dimensionless geometrical factor π(R/h − 1/3) one obtains:

$$F_{N\text{-}V}^{2/3}\propto h\pi^{2/3}\left(R/h-1/3\right)^{2/3} \tag{9.6}$$

After rewriting and inclusion of the materials factor k one obtains:

$$F_N=kh^{3/2}\pi\left(R/h-1/3\right) \tag{9.7}$$

The closed Equation (9.7) is the physical description of the loading curve for spherical indentations. However, there are further experimental reports telling that the exponent 3/2 describes spherical indentation parabolas sometimes without reliable knowledge of the conospherical radius. And there are rather useless "spherical indentations" when so called "effective radii" are continuously changed along the loading curve with power-law fitting [20]. We therefore analyze only "experimental" measurements without such and other fittings or iterations. These appear to be the loading curves of a Ni-based superalloy with nominal largely rounded Berkovich up to the cone-point of 15.9 nm and a PDMS nominal experimental spherical indentation. Both exhibit large R/h ratios that decrease rapidly with the depth *h*. By doing so we compared the now disproved parabola approach using the Kaupp plot of Equation (9.2) [5,14,16] and the physical loading curve Equation (9.7) for comparison purposes. The results are collected in Table 9.2 and Table 9.3, respectively, in Sections 9.3.2.2 and 9.3.2.3.

We have to stress here, that the adhesion energy by jump below the surface of PDMS or similarly in force experiments with AFM, as 0.5 F_Nh for the negative F_N-region stays valid independent of the loading curves' shape [5] and that it continues to correct the erroneous JKR iterations, as e.g. in [18] (Section 9.3.2.3).

9.3.2.2 The Presumed "Spherical" Nickel-Superalloy Indentation

Spherical indentations can be obtained with blunted conical/pyramidal indentations below the cone point depth, when the depth in the following "cone region" is only short. A typical example is the nickel-superalloy loading curve from [17].

The determined F_N and $h^{3/2}$ data below the cone point are listed in Table 9.2. The published end radius of the Berkovich indenter was 269 nm. After removal of the initial effects the *R*/*h* ratios are from 284.867 to 21.350. The value of

[16] is 15.75 nm, where β is the effective cone angle of

the Berkovich. (but see Chapter 16). The observed h_{cone} is at 15.9 nm, which corresponds closely to the calculated value in apparent accord with a spherical indentation part. The Kaupp-plot for the postulated parabola (not shown) gives a straight line with a slope of 3.873 µN/nm$^{3/2}$ (r^2 = 0.9997). This can however not be a confirmation of the $h^{3/2}$ parabola for spheres, because the physical correction factor of $\pi\left(R/h-1/3\right)$ in (9.7) has not been applied. The

physically correct plot (9.7) with the same data points gives the covalently bent

loading curve of Fig. 9.2. The comparison of these different outcomes is difficult, but we try with a provisional trendline for the Fig. 9.2 curve, the slope of which calculates to 0.0688 µN/nm$^{3/2}$. This gives at least a rough hint for the enormous error (despite the high correlation) when the unphysical parabola assumption ([1] and ISO14577) for spherical indentations is applied. However, the change of R/h (Table 9.2) or sinα

(Table 9.1) is undeniable and the hard to explain apparent "parabolas" bear the risk that their slopes be interpreted as being real for further applications. The first goals of indentations are hardness and elastic modulus and when these are unphysical, their errors are perpetuated in the there from defined further characterization of the materials. For example 12 different applications of the indentation modulus from viscoelasticity to fracture toughness are listed in [21].
The apparent slopes of unreal spherical indentation parabola plots cannot be interpreted as physical indentation hardness and used for face transition energies and activation energies as in the case of conical/pyramidal/wedged indentations (Section 9.3.1). Also the k-value of this nickel-superalloy sample that was published in [16] is invaluable. It is no longer the penetration resistance for spherical indentations. It would suggest far too high constant hardness instead of the changing hardness when the depth increases. The reason is the particular formula (9.3) for the penetration calotte volume, even in the very narrow ranges. One has to use Equation (9.7) for a correct result. The authors of [17] unduly called their cone point at 15.9 µm a "pop-in" "marking the transition from elastic to plastic deformation". When *R* would be 269 nm it would however be the change from spherical to pyramidal indentation. There is however the proviso: this kink would most likely indicate a harder surface layer with about 15 nm height on the bulk, provided that the pyramidal end-radius was actually sharp. This tip-radius might have been determined as the second free parameter (C_1 with the dimension of a length) of the second iterated term C_1h_c from the eight parameter iteration of the contact area from [1] and ISO 14577. This technique is often performed and leads to undue very large "radii", so that this is the most likely explanation as a parabola from a sharp pyramid. There is almost no opposition against this tip rounding iteration technique in the literature in addition to [16,22] -----. Tip radii must not be iterated but measured with tapping mode AFM [16]. This indentation should be repeated with a certified sharp Berkovich indenter to finally clarify these points. Table 9.2 and Fig. 9.2 contain the results showing the shape of the plot that would describe the spherical indentation when R is indeed 269 nm (9.7). It clearly confirms the non-parabola for such spherical indentation.

9.3.2.3 The Spherical PDMS Indentation

The result with the Ni-superalloy requires also the analysis of a much deeper indentation with a huge sphere radius and much deeper penetration with very compliant materials. A published nominal "experimental" PDMS spherical indentation (the sphere radius was R = 192 µm) and the JKR iterated and fitted unloading curve [18] (the fitting formula is published in [18]) were analyzed for comparison. Both provide F_N-$h^{3/2}$ parabolas against (9.7). The jump below the surface requires starting from the so formed negative force minimum, but the adsorption energy does not disturb the analyses [5,16]. The R/h ratio varies from 480 to 53.33 (Table 9.3). Also the present author had analyzed these loading curves with respect to the claims of ISO 14577 and [1,2,3,4] by applying the Kaupp-plot. Kaupp calculated and published apparently well correlating k-values [5,16] that can however no longer be considered as being valid, because they violate the physical deduction of the closed formula (9.7) (Section 9.3.2.1). The slope of the (unphysical) F_N-$h^{3/2}$ data (not shown here) was 0.04912 mN/µm$^{3/2}$

= 0.9999 with 54 data points). Also for the JKR-fitted unloading curve the corresponding correlation with a slope of 0.0560 mN/µm$^{3/2}$ calculated with r = 0.9999. This appears to be a good fit, but it does not prove anything, because it does not correspond with the physical Equation (9.7). We try to explain these features against physical evidence and analyze the experimental loading curve with Equation (9.7) in Table 9.3 and Fig. 9.3. There remains the proviso that the loading curve named "experimental" was perhaps also JKR iterated and fitted to correspond with the prescribed parabola of [1] and ISO 14577. Again there are increasing values of h$^{3/2}$ multiplied with decreasing correction factor values. The plot according to (9.7) is again concavely bent. Comparison can again only be tried with the provisionally calculated trendline in Fig. 9.3. Its slope is 0.0005 mN/µm$^{3/2}$. The so judged error of the unphysical parabola is almost twice as much as in the nickel-superalloy in Section 9.3.2.2. Such JKR-iterations and fittings are detrimental treatments of experimental data, as already challenged in [5]. Here the JFK iterations and fittings calculated what the authors wanted to see: an "iron-rule" parabola with exponent 3/2 as prescribed by ISO 14577 and ([1], etc.), which is clearly disproved by (9.7). Our provisional green trendline does not mean that the original experimental data would lie close to it or on it. Iterated and fitted data cannot be reconstructed.

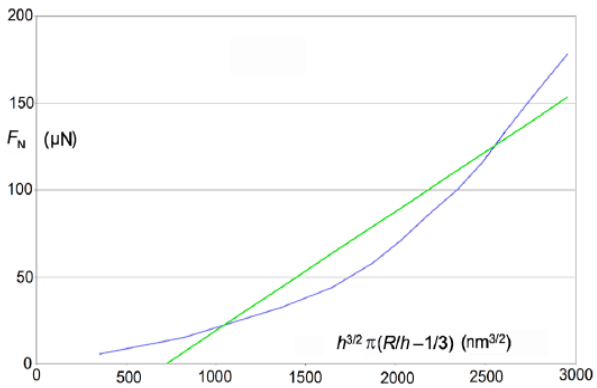

Fig. 9.2. F_N versus plot (9.7) of a Ni-based superalloy with a rounded Berkovich (claimed R = 269 nm) after the removed initial effect (first point at 30 µN load) up to the cone point at 180 µN; the green line is the provisional trendline (only for comparison) with a slope of 0.2169 µN/nm$^{3/2}$

Our physical analysis is important, because any non-physical direct plot $F_{N\text{-sphere}}$ versus h$^{3/2}$ would give vastly different false indentation hardness values as already exemplified with the Ni-based superalloy in Section 9.3.2.2. Clearly, spherical indentations are unable to obtain hardness values. They would change

from depth to depth for every R/h-value (Table 9.3). Also, the hitherto used older formula of [1] $S = 2E_{\mathrm{r}}A^{1/2} / \pi^{1/2}$ is incorrect for spherical indentations.

It must be noted here that our AFM (atomic force microscopy) loading curve of polystyrene with a silicon cantilever (typical apex radii 10 - 15 nm) in [16, 22] is the result of a pyramidal indentation, but not of a “spherical indentation”. After an initial effect well below 100 nm depth the pyramidal indentation proceeded down to 550 nm depth with 16 µN load.

Table 9.2 Analysis of a Ni-based superalloy indentation of a blunt Berkovich up to the cone point depth as it would be with R = 269 nm) according to (9.7)

h (nm)	$h^{3/2}$	R/h	$\pi (R / h - 1 / 3)$	$h^{3/2}\pi (R / h - 1 / 3)$	F_N (μN)	α (˚)
0.17728	0.07464	1517.37	4765.91126	355.7276	5.5039	87.9198
0.94430	0.91763	284.867	893.888878	820.2593	15.1171	85.1978
2.74338	4.43902	98.0542	306.999157	1362.7753	32.2638	81.8102
3.83473	7.50935	70.1484	219.330501	1647.0295	43.9297	80.3140
4.95573	11.0322	54.2806	169.480337	1869.7410	57.6617	78.9850
5.87044	14.2235	45.8228	142.909374	2032.6715	71.4031	78.0081
6.81462	17.7894	39.4740	122.296389	2175.5794	85.1433	77.0758
7.84709	21.9818	34.2802	106.647301	2344.2996	100.51	76.1268
8.88041	26.4636	30.2914	94.1160423	2489.0205	116.75	75.2368
9.82479	30.7953	27.3797	84.9686669	2616.6356	135.004	74.4671
10.9166	36.0687	24.6414	76.3661338	2754.4427	153.183	73.6211
11.7138	40.0910	22.9644	71.0975929	2850.3736	165.001	73.0293
12.5993	44.7218	21.3504	66.0270623	2952.8491	178.254	72.3947

Table 9.3. Analysis of a spherical indentation onto PDMS with a Borosilicate glass ball (R = 192 μm) of [18], according to Equation (9.7)

h (μm)	$h^{3/2}$	R/h	π (R/h − 1/3)	$h^{3/2}$π (R/h − 1/3)	F_N (mN)	α (˚)
0.0					−0.02759	90
0.4	0.2529822	480	1506.91729	381.2232	−0.00919	86.3009
0.8	0.7155418	240	752.93505	538.7565	0.019923	84.7678
1.2	1.3145341	160	501.60764	659.3803	0.055012	83.5908
1.6	2.0238577	120	375.9448	760.8588	0.094993	82.5980
2.0	2.8284271	96	300.54640	850.0736	0.141720	81.7229
2.4	3.7180640	80	250.28022	930.5579	0.248921	80.9313
2.8	4.6852962	68.57	214.37182	1004.3955	0.239081	80.2030
3.2	5.7243340	60	187.44837	1073.0171	0.298851	79.5247
3.6	6.8305198	53.33	166.49395	1137.2402	0.350958	78.8873

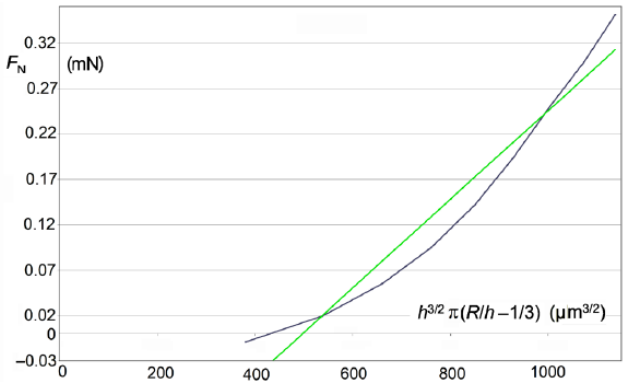

Fig. 9.3. F_N versus $h^{3/2}\pi\left(R \quad h-/ \quad 1/3\right)$ plot of the "experimental dat a" ofthe PDMS polymer with a Borosilicate glass ball (R = 192 μm) [18] according to (9.7); it starts at the minimum after jump below the surface; the green line is the provisional trendline (only for comparison) with a slope of 0.0005 mN/μm$^{3/2}$

9.3.3 The Force-Depth Relation of Flat Cylinder or Beam Indentations

It is widely accepted that the flat indenter (either column or beam) proceeds linearly ([1,2,3] and ISO 14577). According to Sneddon the cylinder penetrates with "$F_N = 2rhE/\left(1-\nu\right)^2$" [12] (here r as column radius, h depth, E Young's modulus. and v Poisson's ratio). The exponent on h is thus 1, but we need a clear-cut deduction without Young's modulus avoiding the premises of Sneddon. This has however never been studied before. As there is also the volume formation coupled to pressure formation one starts the deduction as in Section 9.3.1, which tells that one does not indent towards a projected basal indenter face, but against the volume formation by the indenter. Any almost negligible compression of the very hard indenter is part of the pressure action. The volume of the cylinder $V = \pi r^2 h$ or of the beam $V = a^2 h$ (here a means the edge), has only the h as the variable. In that situation both the pressure and the immersed volume are both directly proportional to the depth. The pressure part is again lost for the depth and we get directly $F_{N\text{-}flat} = k_{flat}\, h^1$ (9.8). The applied force and thus work is the area of the F_N-h triangle (9.9). It is 1:1 divided between pressure work $W_{flat\text{-}pressure}$ and the indentation work $W_{flat\ indent}$. The latter is thus the area of the F_N-h triangle (9.9). $W_{flat\text{-}indent}$ is thus 1/4 $F_{N\text{-}max}\, h_{max}$ (9.10), again in accordance with the first energy law [5,6]. The penetration resistance k_{flat} is here the physical indentation hardness with the dimension [N/m], which is also the full flat loading stiffness (S). And $k_{flat}/2$ is the energy corrected flat impression

hardness = stiffness. The definition of [1] $S = 2E_r A^{1/2} / \pi^{1/2}$ is also here in error, because it relies on the unsuitable premises of Sneddon by using area instead of volume [12].

$$F_{\text{N-flat}} = k_{\text{flat}} h \tag{9.8}$$

$$W_{\text{flat-applied}} = 1/2 F_{\text{N-max}} h_{\max} \tag{9.9}$$

$$W_{\text{flat-indent}} = 1/4 F_{\text{N-max}} h_{\max} \tag{9.10}$$

Load versus depth curves of flat punches onto visco-elastic materials seem to be rare, as creep and moduli were the prevailing points of interest. However, load-depth curves with cylinder of 0.5 cm radius onto F82 H steel at different temperatures (92˚C to −196˚C) used loads up to 600 N and were linear up to 100 N at about 30 µm depths. They continued at first with moderate bending up to 250 N and further so up to 600 N towards 1 mm depth. The first part up to about 50 N or 0.5 GPa with a poorly resolved kink was reported as “fully reversible”. The kink was followed linearly up to 150 - 200 N or 1.5 - 2 GPa, depending on the temperature. This experimentally confirms the indentation law h^1_{flat} for the low resolved initial parts. The bending above these loadings was interpreted with three different plastic stages [24]. As such bending is not in accord with (9.8) it has to be concluded that the experimental control was lost at such high loads, most probably by macroscopic undetected cracks and perhaps chemical transformations of the different components. The following bending starts with protruding of material around the imprint or chemical reactions [24]. Regular pile-up would not destroy the physical law (9.8) [5,25]. Interestingly, these results are comparable with the yield stress of tensile tests, the values of which are about 3 times smaller than the stress at the start of the bending for 16 tested metallic materials [24]. The elastic moduli have been obtained from the slopes of the initial linear part of the unloading curves from 120 - 110 µm without iterations. But energy law corrections that should be the factor 0.5 according to (9.9) and (9.10) [5, 6] have not been considered. The obvious comparability of flat macro-indentation with tensile tests appears interesting for further applications.

9.4 CONTINUATION

For later found not data-treated spherical indentations in accord with eqn. (9.7) see Chapters 11 and 13. The presented deductions of physical equations for conical/pyramidal/wedged, spherical, and flat indentations must urgently replace the false historical equations of ISO 14577 with their energy law violations for obtaining reliable mechanical parameters and to enable the new applications (detection of phase-transition onsets, their transition energies and activation energies) that were previously not possible. Further applications are to be developed particularly at very low temperatures for airplanes and spacecraft

vehicles. The spherical indentations are the most complicated and least rewarding ones. The spherical work of indentation by integration of Equation (9.7) does not provide a rational ratio with the total work of indentation, as comparable with the 4/5 ratio in the case cones/pyramids [5]. This complicates the important energetic evaluations and the not self-similar spherical indentations are thus more difficult than the indentations with the self-similar indenters. The same is true for paraboloids of revolution for which [1] falsely claimed loading parabolas (but see also Chapter 13) with exponent 3/2. They are centrosymmetric but not self-similar. Also ellipsoids and two-sheet-hyperboloids of revolution are centrosymmetric but not self-similar indenters that would complicate their advanced use.

The possibilities of flat punch indentation require further development and promise interesting further applications beyond the creep determinations. ISO must be further urged to thoroughly revise and modernize ISO 14577 on the physical basis without iterations and data-fittings. This will remove the falsely obtained mechanical materials parameters; which is of urgent importance for avoiding the risks with technical products in daily life. The certification of industrial producers must be based on physical reality rather than on historical errors to enable the use of the correct novelties and the development of improved materials and confidence in a correct way, so that catastrophic mechanical failures can be avoided or at least minimized. Responsibilities can no longer be shifted to ISO 14577 and from there to historical researchers.

9.5 CONCLUSIONS

The most severe misconceptions in the powerful (nano) indentation field have been reported in this paper. It is the two-dimensional treatment of the three-dimensional impression into solids, with its now obsolete “iron-rule” (“cone exponent 2, sphere exponent 3/2, and flat exponent 1”). The main problem was the impossible equality of exponent 3/2 for conical/pyramidal [14] and for spherical indentation loading curves [1,2,3]. This had to be solved despite the common ISO 14577 standards. Only the exponent 1 for flat punch indentation was not debated, but it also required the deduction of a correct Equation (9.8). By prescription of [1] and ISO 14577 the conical parabola should have the exponent 2 on h instead of 3/2. Therefore, believing researchers tried to question the universality of $h^{3/2}$ for cones/pyramids/wedges and iterated huge tip roundings with 8 free parameters for indenters, while proposing exponent 3/2 parabolas for s pheres. By doing so, these researchers had to iterate and fit their data from s pherical indentation for example with JKR techniques, in order to obtain treated d ata, providing four-nines-correlations that only exhibited what they expected to ob serve. Both detrimental techniques (iteration of excessive tip radii and iterative dat a-fitting treatments) are uncovered in this work. It could be done because the und eniably deduced physically formulas cannot be overcome. Also CSM Inst ruments Application Bulletin 35 advocates for FEA (finite element models). and JKR iterations for spherical indentations on the basis of “$h^{3/2}$ parabolas for spheres”. A respective very complicated data-fitting formula is cited and written down in the Introducion of Section 13 on page 185. The enormous errors of such fitting data treatments are roughly judged. Another iteration and fitting technique

is the continuous change of"effective radii" along the loading curve with pow er-law fitting [20]. It is particularly bothersome that the materials are false ly calculated (including violation of the energy law) and that phase-transition s under load cannot be traced with false exponent and the shape of the untreat ed loading curves. The correct value of the exponent is of utmost importance for i ncreased precision by regression, the calculation of materials' properties, the recognition of initial surface effects, gradients, and phase transitions with their tr ansition energies and activation energies [5,16,25,26,27,28]. The therein and in th is paper challenged behaviors create high risks and miss the important possi bilities for avoiding catastrophic failures by initiation of nucleation for cracks with catastrophic failures within the polymorph interfaces [25]. All of that is inaccessibl e with the unphysical exponents and iterations with data-fittings. The differentia tion between loading parabolas, non-parabolas, and straight lines is also im portant. The physical deductions of the loading curves use the volume of the indenters, rather than their basal surface area or "contact area", to obtain closed formulas without any iterations and data fittings in a very elegant and simple way as compared to previous work. A comprehensive understanding has be en achieved now for conical/pyramidal/wedged, spherical, and flat-punch indent ations. This has been shown for experimental nano- and micro-indentations. Fu rther applications are expected for AFM studies of visco-elastic-plastic bi ological and medical preparations. The universal exponent 3/2 on h for the lo ading parabola is only valid for cones/pyramids/wedges [14]. Spherical inde ntations provide non-parabola loading curves according to the now deduced Eq uation (9.7), and flat-punch indentations with exponent 1 follow the new Equation (9.8). The reason for the non-parabola at spherical indentations is the strongly var ying R/h ratio upon penetration of geometrically not self-similar sphere calottes.

Clearly, undeniable closed physical formulas based on sacrosanct calculation rules stands before regression analysis of a physically incorrect parabola that required data-fittings. This shows for spherical indentations that any published linear correlations without valid physical background require our techniques for the detection of data-treatments. Sorry to say: it might perhaps be easier for mainstream researchers, who do not dare to challenge ISO 14577, to please it and also its proponents.

The new unprecedented physical deductions rely on the indented volume (not on projected area) by using undeniable calculation rules [14]. All of the errors from the previous falsely believed (including violation of the energy rule) indentation exponents are to be abandoned. The still exacting of the world by the common ISO 14577 standards with the energy law violations derived from the unsuitable mathematical premises of [1,2,3,4,12,13] that did not consider that the "depth formation work" (projected area instead of volume) is coupled to the pressure work, which can however not be created from nothing. ISO 14577 and [1,2,3,4] are incorrect. They required, prescribed, or allowed data-fittings and iterations. These missed all of the named unprecedented further applications and cannot even detect the calibration errors in calibration standard indentions of [1] (five of the six standards with calibration error; two mix-ups of figure designations; ignoring phase-transitions). These experimental errors are not corrected and still

used in the ISO 14577 documents. The unprecedented novelties have already been applied for conical/pyramidal/wedged indentations [5,6,16,25,26,27,28], and further applications are expected for the Equations (9.2), (9.7) and (9.8) when ISO 14577 will be profoundly revised on sound physics but not on historical errors. Unfortunately, there are non-scientific problems for a rapid ISO decision, including severe liability questions [26].

COMPETING INTERESTS

Author has declared that no competing interests exist.

REFERENCES

1. Oliver, W.C. and Pharr, G.M. (1992) An Improved Technique for Determining Hardness and Elastic Modulus Using Load and Displacement Sensing Indentation Experiments. Journal of Materials Research, 7, 1564-1583.
https://doi.org/10.1557/JMR.1992.1564
2. Fischer-Cripps, A.C. (2002) Nanoindentation. Mechanical Engineering Series. Springer, New York.
https://doi.org/10.1007/978-0-387-22462-6
3. Chudoba, T., Schwaller, P., Rabe, R., Breguet, J.M. and Michler, J. (2006) Comparison of Nanoindentation Results Obtained with Berkovich and Cube Corner Indenters. Philosophical Magazine, 86, 5265-5283.
https://doi.org/10.1080/14786430600746424
4. Oliver, W.C. and Pharr, G.M. (2004) Measurement of Hardness and Elastic Modulus by Instrumented Indentation: Advances in Understanding and Refinements to Methodology. Journal of Materials Research, 19, 3-20.
https://doi.org/10.1557/jmr.2004.19.1.3
5. Kaupp, G. (2013) Penetration Resistance: A New Approach to the Energetics of Indentations. Scanning, 35, 392-401.
https://doi.org/10.1002/sca.21080
6. Kaupp, G. (2017) The ISO Standard 14577 for Mechanics Violates the First Energy Law and Denies Physical Dimensions. Journal of Material Sciences and Engineering, 6, 321-328; https://doi.org/10.4172/2169-0022.1000321
7. Argatov II, Jin X, Keer LM. Depth-sensing spherical indentation of an elastic sphere on an elastic substrate. Journal of the Mechanics and Physics of Solids. 2021 Apr 1;149:104297.
8. Argatov I, Jin X. Depth-sensing indentation of spherical particles on corrugated substrates—An asymptotic model. International Journal of Engineering Science. 2020 Sep 1;154:103349.
9. Ogar P, Gorokhov D, Zhuk A, Kushnarev V. Contact geometry during indentation of a sphere into an elastoplastic half-space. In MATEC Web of Conferences 2019 (Vol. 298, p. 00093). EDP Sciences.
10. Hertz, H. (1882) über die Berührung fester elastischer Körper. Journal für die reine und angewandte Mathematik, 92, 156-171.

https://doi.org/10.1515/crll.1882.92.156
11. Hertz, H. (1896) On the Contact of Rigid Elastic Solids and on Hardness. Macmillan and Co., New York. https://archive.org/details/cu31924012500306
12. Sneddon, I.N. (1965) The Relation between Load and Penetration in the Axisymmetric Boussinesq Problem for a Punch of Arbitrary Profile. International Journal of Engineering Science, 3, 47-57. https://doi.org/10.1016/0020-7225(65)90019-4
13. Love, A.E.H. (1939) Boussinesq's Problem for a Rigid Cone. The Quarterly Journal of Mathematics (Oxford), 10, 161-175.https://doi.org/10.1093/qmath/os-10.1.161
14. Kaupp, G. (2016) The Physical Foundation of $F_N = k\ h^{3/2}$ for Conical/Pyramidal Indentation Loading Curves. Scanning, 38, 177-179. https://doi.org/10.1002/sca.21223
15. Kaupp, G. and Naimi-Jamal, M.R. (2004) Nanoscratching on Surfaces: The Relationships between Lateral Force, Normal Force and Normal Displacement. International Journal of Materials Research, 95, 297-305. https://doi.org/10.3139/146.017952
16. Kaupp, G. and Naimi-Jamal, M.R. (2013) Penetration Resistance and Penetrability in Pyramidal (Nano)Indentations. Scanning, 35, 111. https://doi.org/10.1002/sca.21038
17. Wöllmer, S., Zaefferer, S., Göken, M., Mack, T. and Glatzel, T. (2003) Characterization of Phases of Aluminized Nickel Base Superalloys. Surface and Coatings Technology, 167, 83-96. https://doi.org/10.1016/S0257-8972(02)00843-5
18. Ebenstein, D.M. and Wahl, K.J. (2006) A Comparison of JKR-Based Methods to Analyze Quasi-Static and Dynamic Indentation Force Curves. Journal of Colloid and Interface Science, 298, 652-662. https://doi.org/10.1016/j.jcis.2005.12.062
19. Johnson, K.L., Kendall, K. and Roberts, A.D. (1971) Surface Energy and the Contact of Elastic Solids. Proceedings of the Royal Society of London. Series A, 324, 301-313. https://doi.org/10.1098/rspa.1971.0141
20. Ni, G., Cheng, Y.T., Cheng, C.M. and Grummon, D.S. (2004) An Energy-Based Method for Analyzing Instrumented Spherical Indentation Experiments. Journal of Materials Research, 19, 149-157. https://doi.org/10.1557/jmr.2004.19.1.149
21. Kaupp, G. (2017) Dilemma between O Physics and SO Elastic Indentation Modulus. Journal of Material Sciences and Engineering, 6, 402-405. https://doi.org/10.4172/2169-0022.1000402
22. Kaupp, G. and Naimi-Jamal, M.R. (2010) The Exponent 3/2 at Pyramidal Nanoindentations. Scanning, 32, 265-281. https://doi.org/10.1002/sca.20206
23. Malzbender, J. and de With, G. (2002) Indentation Load-Displacement Curve, Plastic Deformation and Energy. Journal of Materials Research, 17, 502-511. https://doi.org/10.1557/JMR.2002.0070

24. Riccardi, B. and Montanari, R. (2004) Indentation of Metals by a Flat-Ended Cylindrical Punch. Materials Science and Engineering: A, 381, 281-291.
https://doi.org/10.1016/j.msea.2004.04.041
25. Kaupp, G. (2018) Six Polymorphs of Sodium Chloride upon Depth-Sensing Scanning Macroindentation with Unusual Long-Range Cracks Requiring 30 N Load. Journal of Material Sciences and Engineering, 7, 473-483.
https://doi.org/10.4172/2169-0022.1000473
26. Kaupp, G. (2014) Activation Energy of the Low-Load NaCl Transition from Nanoindentation Loading Curves. Scanning, 36, 582-589.
https://doi.org/10.1002/sca.21158
27. Kaupp, G. (2019) Phase-Transition Energies, New Characterization of Solid Materials and Anisotropy. Advances in Materials Physics and Chemistry, 9, 57-70.
https://doi.org/10.4236/ampc.2019.94006
28. Kaupp, G. (2019) Physical Nanoindentation: From Penetration Resistance to Phase-Transition Energies. Advances in Materials Physics and Chemistry, 9, 103-122.
https://doi.org/10.4236/ampc.2019.96009

DISCLAIMER
This chapter is an extended version of the article published by the same author(s) in the following journal.
Advances in Materials Physics and Chemistry, 9: 141-157, 2019.

Chapter 10
Print ISBN: 978-93-5547-921-1, eBook ISBN: 978-93-5547-922-8

Indentation onto Stishovite (SiO_2), MgO, and a Covered Superalloy: "Pop-In" Repair, Phase-Transition Onsets, Polymorph Energies, and Transition-Energies: A Recent Study

DOI: 10.9734/bpi/mono/978-93-5547-921-1/CH10

ABSTRACT

In order to determine the phase-transition onset forces, indentation energies, and transition energies, the Berkovich indentation loading curves of the initially only extraterrestrial available polymorphs of SiO_2 are physically analysed using the now well-established F_N versus $h^{3/2}$ plots for conical/pyramidal indentations. These features are described for two phase-transitions of synthesised Stishovite that result in two polymorphs, one of which being Seifertite. For increasing load indentation, a third post-Stishovite polymorph is obviously projected. The anticipated third of them is waiting, and the two of them are currently available for further examination on Earth at room temperature. The force-depth curve had to be self-evidently repaired in order to eliminate the published "pop-ins." It appears to be the first time that the significance of published "pop-ins" has been clarified. There are numerous causes for bothering them and for the avoidance of them. They are mechanical artefacts rather than features of the materials. Although theoretical considerations suggest that the beginning of "pop-ins" involves an elastic-plastic conversion, published pop-ins has absolutely nothing to do with phase transitions. Spherical indentation analyses before them are obsolete and dangerous. Final support is inter alia that one of the two new MgO twinning transitions is within a published "pop-in excursion". The putting of a pop-in arrow at smooth loading curve without discontinuities in the F_N versus $h^{3/2}$ plot is criticized, as the transfer between chemically different phases is neither phase transition nor "pop-in". The onset forces, energies, and endothermic or exothermic phase-transition energies of the polymorph are described. Mechanochemical analysis is done on the formation of the Stishovite, post-Stishovite, and MgO polymorphs. For the safe use of technical materials like MgO for building or coated superalloys in things like aeroplanes, turbines, and other large machinery, high pressure polymorph energetic characteristics are crucial also for the earth's sub mantel investigations. The onset and transition energies need to be higher than the maximum permissible mechanical and thermal stress for them to be safe since breakage and catastrophic cracks are more easily initiated at polymorph interfaces.

Keywords: Berkovich indentation; catastrophic cracking; covered-superalloy; false historical concepts; MgO; phase-transition-energy; "Pop-In"; post-stishovite; stishovite; quartz.

10.1 INTRODUCTION

High energy polymorphs of quartz are one example of an extraterrestrial material that was initially found in meteorites from Mars and later gathered from the moon. These crystalline substances include the monoclinic quartz variant, orthorhombic Seifertite, and the tetragonal Stishovite polymorphs that appeared later. Each one of the three is metastable at normal temperature. Today, stishovite is also discovered in diamonds, ultrahigh pressure metamorphism rocks, atomic explosion craters, and other geological formations. Large enough single crystals of Stishovite are currently successfully crystallising using high-pressure, high-temperature syntheses, and Seifertite has also been obtained. They are yet the second hardest oxides. The indentation of Stishovite is of particular interest, as indentations of α-quartz undergo exothermic phase-transition into an amorphous phase but not endothermic into crystalline Coesite, another high pressure polymorph of SiO_2. Apart from amorphous phases one could expect exothermic formation of Coesite or endothermic Seifertite and the monoclinic variety from Stishovite. A still higher post-Stishovite polymorph's transition energy will be expected. Two microindentations with Berkovich diamond indenters have been reported. One of them reports three small pop-ins and the other one very late broad "pop-in". But smooth loading curves are necessary before physical (not iterative fitting) analyses are enabled for phase-transition onsets (depth and load), indentation work (W_{indent}), applied work ($W_{applied}$), and transition energy (W_{trans}). Such endeavor requires correct calculation, excluding rounding errors with the already long available simple closed formulas. Iterations converging to a false exponent on the depth h and the inexcusable violation of the energy law must be avoided. Rethinking of the "pop-in's" meaning and their removal or avoidance removes the still most complicated common misinterpretations.

Phase-transitions are revealed from physically analyzed [1] smooth force-depth curves of conical-pyramidal indentations not involving "pop-ins". The differences in the penetration resistances of the formed polymorphs provide sharp unsteadiness in the normal force vs. depth$^{3/2}$ plots (F_N vs $h^{3/2}$). Some still iterating opponents have disdainfully been calling it "Kaupp-plot" but we will take it up now respectfully. The Kaupp-plot gives the penetration resistance k with dimension [$N/m^{3/2}$] as physical hardness. It is the slope from conical, pyramidal, and wedged indentations [1]. It will be shown for the first time that "pop-in" is unintended autonomous force hold, while indentation depth values are falsely extrapolated and not corrected upon force resumption. There are several reasons for the avoidable show-up of "pop-ins". Frequent speculation in the literature still claims their being essential for elastic to plastic conversions of materials, which are however not phase-transitions [1]. Particular striking misuses of the "pop-in" term are arrows labeled "pop-in" that point to smooth loading curve sites where there is none. Furthermore, one must not use the Kaupp-plot (F_N vs. $h^{3/2}$) [1] without prior removal of published "pop-ins" (e.g. [2]), and beware of using it for spherical indentations. These are not simply parabolic. Only the Kaupp-plot reveals phase-

transitions with their onsets and energies. That is easy, fast, and reliable. Phase-transitions have only rarely been guessed by "pop-outs" that require particular unloading techniques for confirming spectroscopic or electric results from e.g. hydrostatic pressure experiments. Almost all actually occurring phase-transitions remain unknown, if the physical Kaupp-plot analysis [1] is avoided for historical reasons. This proved already extremely dangerous, as polymorph interfaces upon phase-transition are nucleation sites for initially small cracks that upon further force produce catastrophic cracking for example in airliners [3,4,5]. Remedy is indispensable for e.g. the titanium alloys of propeller blades that should be improved in composition or replaced by other improved superalloys in airliners. Their phase-transition onsets and endothermic phase-transition energies must be far beyond the maximal forces that occur during turbulent flight. Some updates in this area are accessible elsewhere and can attract the readers' attention [6-8]. [6] provides a review of the vapor-liquid phase-transition of confined fluids in the pores of solids. [7] studies the phase-transitions of plastic crystal salts. [8] analyses the high-pressure polymorphism phase-transition process with hexahedron pressure equipment and uses synchrotron diffraction up to 40.4 GPa. After the author's complaints in [4,5] that phase-transition under load facilitates catastrophic cracking of titanium-aluminium alloys, there is now a response. The chosen faster "remedy" is apparently not replacement of the alloy by a better one. It is now the placing of devices in front of the airliners' turbine propellers for impeding rotating broken off propeller blades from exiting at their higher speed in forward direction and shortly thereafter hit penetrating at the fuselage. In the meantime, small cracks at the pickle-fork (wing-connection to fuselage) and cracks at the fuselage were searched for and detected. Hundreds of airliners were long term grounded at once.

This paper puts forward the physical analyses of widespread Berkovich indentations for clarifying erroneous reports in the literature on the basis of common calculation rules, but not iterations with up to 3 + 8 free parameters. It disproves the unfortunately continued toleration of the ISO (International Standardization Organization) violation of the energy law, which impedes to even think of phase-transitions (creating polymorph interfaces for crack initiation), not to speak of their detecting by the F_N vs. $h^{3/2}$ curve. This paper exemplifies the new application possibilities (the phase-transition activation energy requires temperature-dependent indentations). It analyzes the indentation onto Stishovite (SiO_2), magnesium oxide, and a covered superalloy. It requires only the physical loading curve analysis for obtaining the phase-transition onset and its energy. The calculation uses basic algebraic calculation rules but no iterations for the secure use of existing and advanced materials. The ease of the indispensable physical analysis of indentations is particularly favorable. Also the necessity for precise direct calibrations will be stressed. Unfortunately, the ISO "standards" that were obtained with false force calibration, materials' mix-up, inconsideration of the phase-transitions, and excessive multi-parameter iterations (as revealed in [5]) are unacceptable. But fortunately, these standards are not required at all. Only the absolute force and depth calibrations and the proper execution prescription of the indentation experiment are essential. That part of the calibration and its reliability is apparently in good hands at ISO or at the

instrument builders, as shown by the successful physical analyses. Any occurring false calibration of instruments is fortunately immediately recognized, when experimental data do not concur with the undeniable general algebraic formulas. Examples are poor force linearity at higher loads or defective indenter tips, or manipulated published data, or iterated and fitted curves. Any false reports facilitate disastrous results when checks of their content are omitted. False experiments require repetition. Advanced materials require the use of indentations with physical analysis with all of the new possibilities for their characterization. This is exemplified in this paper.

10.2 MATERIALS AND METHODS

When force vs depth indentation curves from the literature were analyzed for phase-transitions, all published "pop-in excursions" were removed and the falsely extrapolated depth readings were subtracted for joining the depths from before and after the shown-up distortion. A continuous smooth loading curve was obtained by joining the loading parts that were interrupted by the force hold. This self-evident repair (Section 3.1) enabled the physical analysis with the Kaupp-plot. The k-values (penetration resistances = physical hardness) were not affected by the repair, whatever the reasons for the "pop-in" might be because creep errors were by far too small. The original data-point pairs were taken from the printed figures that were enlarged to abscissa lengths of 15 to 20 cm for that purpose. They were directly loaded to Excel® for the calculation of Figure 10.1 through Figure 10.3 and listed in Table 10.1. The calculations according to the already repeatedly published short and easily proved equations (numbers 3 - 7 in [5]) must not be repeated here. Due to high sensitivity and for avoiding rounding errors, all values throughout were calculated with 10 significant figures, for reasonable rounding in Table 10.1 and at the final results in the text. Due to its energy law violation of the mostly used "P" for the normally applied force we use F_N that is 0.8 P. The factor 0.8 is inherent in F_N for being compatible with the energy law. This avoids a complication of formulas. 0.2 F_N is the universal requirement for the elastic + plastic work of conical, pyramidal and wedged indentations [5] (Chapter10.7).

10.3 RESULTS AND DISCUSSION

10.3.1 "Pop-Ins": Appearance, Significance, Handling

So called "pop-ins" disturb the force-depth loading curves of indentations. If these appear, more careful repetition of the indentation experiment is required, or repair of the printed curve from a publication becomes necessary, prior to looking for the physical force-depth and energetic relations. At every "pop-in" production, the indenter electronics go autonomously in a force hold-mode, while the penetration loop continues in a pseudo creep mode with falsely reporting somehow extrapolated "fake depth" readings (not creep depression) until resumption of the loading loop, when too deep penetration depth value readings continue. The joining together of the loading parts requires subtraction of the

"fake-values". Such correction must be manually executed, as there is no automatic correction when the force loop autonomously resumes after some time. It is hard to understand why that was not seen before. The real depth is the same at both ends of the horizontal "pop-in", notwithstanding some minimal creep that is often too small for being corrected, due to the short and comparably low constant-force action. Autonomous force holding ("pop-in") is a purely instrumental error. Unfortunately, common practices still continue to concede the pop-ins a physical significance (elastic to plastic conversion) that must be urgently challenged now. For example, pop-ins have nothing in common with the onset of "a sudden and strictly plastic punching" and it is not "an entirely plastic deformation process" [9]. Correspondingly, it has been claimed that "the onset of full plastic yielding at the indenter site is to be marked at the pop-in point" or that the "Hertzian elastic stress" ends at the pop-in [10].

Published pop-ins appear primarily when nanoindentation instruments are not cased for protection from environmental influences. For example they appear upon audible, ultra and infra sound, shaking, or switching of heat sources. To say it again: the force control stops during the published pop-in, while depth values are further extrapolated and recorded instead of a creep mode switching. Other distortions of the force control can be roughness, e.g. when the descending indenter tip hits with its skew sides or edges to a terrace step or other obstacle, or when it falls into a micro-hole. These events might sufficiently arrest the very sensitive constant force increase loop. It takes thereupon some time for autonomously resuming the force loop. Remedy is repetition of the experiment at a different site of the sample, or at another time, or at a larger distance from previous impressions or sample edges. The suggested distance of 10-fold indentation width should better be 20-fold [3]. Loading curves without pop-ins are achieved when following these hints.

Nevertheless, published pop-ins have continuously been interpreted as a purely elastic to plastic conversion, even though such published pop-ins started at different forces, often occurred multiply within the same indent, and varied considerably in their time for resumption. The elastic to plastic conversion does not change at such event and that is physically proved [1]. Furthermore, the "cone-point" {$h_{cone} = R\,(1 - \sin\alpha)$, where R is apical radius and α half-angle} is much smaller than the start of the shown-up pop-in with common Berkovich indenters. Examples for such errors are manifold in the literature. Most intriguing are claims of "pop-ins" when these are not present in the smooth F_N vs h curves. Some authors even try to misuse the term "pop-in" by inserting an arrow with such label at the smooth Berkovich loading curve. And that is tried to justify with the disproved "Hertzian theory" for spheres. For example the authors of [11] try to support their false belief with a large tip radius R. By using the iterative ISO 14577 techniques for the iteration of their tip end-radius they used a fused quartz indentation and both 3 + 8 free parameter iterations for comparison with equally treated and fixed standards. But they did not consider the numerous challenging reports telling that such "calibration" leads to far too high values, when compared with direct tapping-mode AFM measurements. The published iterated "tip radius" in [11] amounts to 269 nm. Such rounding would indicate an effective cone

height of 15.75 nm for a Berkovich, which is almost the same as the kink position of the Kaupp-plot in [12]. The authors of [11] assumed elastic to plastic conversion at 15.9 nm depth for their Al-covered Ni-based superalloy diffusion zone and used a so-called "Hertzian approach", falsely believing in a spherical indentation up to this point. However, as already told above, spherical indentations do not proceed with a simple parabola [12]. The rightfully found parabola with exponent 3/2 is the result of conical and pyramidal behavior [1]. The iterated tip rounding of 269 nm is thus disproved and the tried application of the "Hertzian approach" is obsolete. In fact, elastic work and all kinds of plastic work relate in the same way to force and energy [1]. The historical views are unphysical and a half-sphere indentation (calotte before the cone-point) would require the physically correct non-parabola $F_N = k\pi\ (R/h - 1/3)\ h^{3/2}$ [12]. Nevertheless, the authors of [11] put an arrow labeled with "pop-in" at their smooth loading curve where there was none. One cannot better manifest the widespread false unphysical belief than by putting a "pop-in arrow" to a smooth curve in the absence of any pop-in! Clearly, our physical analysis with the Kaupp-plot of the smooth Al-covered Ni-superalloy loading curve reveals a very minor initial surface effect and two straight lines before and after the kink position (both with R = 0.9999 regression) in Fig. 10.1. That is evidence for $h^{3/2}$ parabola loading curves. This proves pyramidal behavior. The not spherical behavior before the kink has already graphically been shown in [12]. The Berkovich of [11] must have been sharp (commonly 50 - 100 nm) [12]. Only the correct analysis of such published curves of [11] is valid. The kink at 15.4 nm and 252 µN force does not indicate an elastic to plastic conversion and neither so a phase-transition. It clearly characterizes the crossing over two chemically different phases. This corrects the previous interpretation of the kink in Fig. 10.1 as a "sphere to effective cone conversion" in [13] when the physical analysis of spherical indentations in [12] was not yet available and the "Hertzian" parabola for spheres appeared still credible. Unfortunately, the widespread misuse of the pop-in term in connection with iterative analyses is still widely used. That's very dangerous, when used for technical materials under mechanical load, as phase-transition inreases the probability for cracking

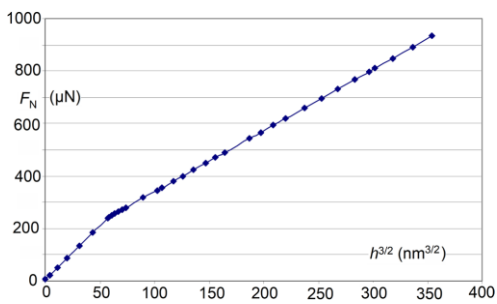

Fig. 10.1. The physical analysis of the Berkovich indentation onto the "matrix phase" (10 µm thick) within the diffusion zone (25 µm thick) of an Al-coated Ni-superalloy; the load vs displacement curve data were taken from the Fig. 10.10 in [11] from 0 - 50 nm depth

10.3.2 Stishovite, Seifertite and Monoclinic Polymorph of SiO_2

Stishovite is tetragonal SiO_2, with Rutil-type space group ($P4_2/mnm$). It is named after Sergey H. Stishov, Russia, for its first synthesis from α-quartz (density of 2.65 g/cm^3) at 20 GPa and 1100°C [14]. A more recent synthesis treated fused quartz at 20 GPa and 1100°C [15]. It is one of the densest (4.287 g/cm^3) polymorphs known from SiO_2 [16]. It had first been found together with Coesite in meteors from Mars and later collected from Moon [17], or from atomic bomb explosion craters, in some diamonds and now in ultrahigh pressure metamorphism rocks around the Globe.

Orthorhombic Seifertite (Pbcn) with unusual six-fold Si-O coordination (named after Friedrich Seifert, Bayreuth, Germany), was described in [16]. 3 years later, space group Pbcn or Pb2n and 4.29 g/cm^3 were discussed by [18], and it was synthesized in 2013 (see below). A monoclinic post-Stishovite was identified together with Seifertite (not orthorhombic $Pca2_1$, but monoclinic $P2_1/c$) was identified by [17,19] in the Martian Shergotty meteorite. All of them are metastable at ambient conditions. It appears intelligible, that the first phase-transition of Stishovite proceeds to Seifertite with still higher density and again with the unusual 6-fold coordination of the silicon atoms. The first hint for a second phase-transition from Stishovite leads to the structurally identified $P2_1c$ polymorph again with six-fold coordination and the density of 4.30 g/cm^3. The energetic sequence of these is not certain. The minor density differences cannot secure the chosen sequence that awaits structural characterization by indentation with synchrotron X-ray analysis close to the indented Berkovich, or (less reliable) calculations of the energy and suppressiveness. It appears impossible that the about 15 known further crystalline polymorphs (known α- and ß-forms are counted) at much lower density (1.7 to 2.62 g/cm^3) and fourfold coordination could have been formed upon indentation of Stishovite. However a caveat remains, because 8 highest-pressure polymorphous structures of silica are listed with references in the Review [17] as CaF_2, Fe_2N, α-PbO_2, I2/a, $CaCl_2$, Pa-3, GeO_2, TiO_2 structures. These structures have been obtained by hydrostatic pressurizing or theoretical calculations, but some of them might only exist under high pressure. The orthogonal $CaCl_2$-typ (Pnnm) was found by a second order transition of Stishovite [20,21] by hydrostatic pressure in a diamond anvil, but it is not quenchable and immediate first order transitions occur around 45 GPa. An inhomogenity at nearly hydrostatic pressure change in the rather gradual Raman frequency shift has been interpreted to occur from the TiO_2-structure into the non-quenchable $CaCl_2$ structure at 27°C [21]. An earlier paper with (quasi) hydrostatic experiments reported evidence for the $CaCl_2$-structure of a post-Stishovite polymorph by synchrotron X-ray experiments. But only one phase-transition above Stishovite was found [22].

The situation changed with the detection of the quenchable Seifertite and $P2_1/c$ polymorphs. Seifertite could be synthesized from Cristobalite at 20 GPa and 900°C [23]. Here we will rely on "quenchable" crystalline polymorph structures. The unloading curves [24] have smooth shapes, and the fast strain rate of the indentations with sharp onset would disfavor the possible $CaCl_2$ structure under

these conditions and favor Seifertite and $P2_1c$ polymorphs. Indentations should be a useful tool for the formation and energetics of post-Stishovite polymorphs and the transition energies. Also the formation of still higher pressure polymorphs at room temperature can be envisaged.

10.3.3 The Indentation onto Stishovite

Indentations and hydrostatic compressions detect the polymorphs as they exist under pressure, and they include unquenchable (pressure-less not metastable) polymorphs. Both techniques can be performed at various temperatures. Only indentation is useful for the calculation of the important phase-transfer activation energies [25,26], but temperature dependent indentations of Stishovite wait for their execution. Both techniques have been used for structural analysis with highly focused synchrotron X-ray analysis. The much slower hydrostatic pressure increase allows for equilibrations and the structural elucidation with X-ray analyses under pressure is easier also with various spectroscopic analyses. Raman spectroscopy has also been used with indentations. Syntheses with fast quenching (temperature and pressure) obtain only the quenchable polymorphs. Either indentation or hydrostatic pressing alone cannot distinguish all useful qualities.

10.3.3.1 The Indentation of Stishovite: Indentation Work and Transition Energies for 2 Post-Stishovites Despite 3 Published Pop-Ins

The Berkovich indentation onto (110) of a synthesized Stishovite single crystal [24] provided a loading curve with three short pop-ins at 0.98 mN (with 25.80 nm), at 8.53 mN (with 104.49 nm), and at 18.58 mN (with 160.13 nm) force (with depth). They are 1.0, 0.5, and 2.7 nm wide, respectively. However [24] deals only with the first of its 3 published pop-ins. Only the repaired published loading curve could be physically analyzed. The Kaupp-plot reveals a short (<40 nm) initial surface effect (including tip rounding) and two phase-transitions, indicating 3 polymorphs up to 22.5 mN load. The regression line data are given as inserts in Fig. 10.2. They contain the penetration resistance values (physical hardness) as the slopes and the force axis cuts. The equalization of the regression formulas provides the phase-transition onset kinks. The first kink (phase-transition onset) is at 9.71 mN with 110.74 nm, the second kink at 17.25 mN with 152.89 nm. There is, of course, no correspondence at all with the first of the published pop-in. The second published pop-in is 1.19 mN before the first phase-transition. The third published pop-in is 1.33 mN after the second phase-transition. Clearly, none of phase-transition values correspond with the published pop-in values. All phase-transitions occurred without any pop-in contribution, and published pop-ins are therefore not connected with phase-transitions, and they are not a prerequisite for phase-transitions. The reasons for published pop-ins have been discussed in Section 10.3.1, and their missing significance is again confirmed by these results. Perhaps some distortions by inhomogeneities, or disorders would have required the use of different crystal sites for indentation. The two phase-transitions indicate two post-Stishovite polymorphs as formed endothermic with higher penetration resistance (Table 10.1) and a third one would be at a third

kink as expected for an indentation at higher load. At the first kink we have #1 and #2 and at the second #2 and #3 polymorphs. The #3 polymorph compression proceeds towards a firmly predicted #4 polymorph that is however not reached at a higher force kink point, due to the cut off of the indentation load. 22.5 mN is not very high for microindentation. The regression line equations are used for the calculation of indentation work W_{indent} and transformation energies W_{trans}. These results and their normalized values are listed in Table 1.

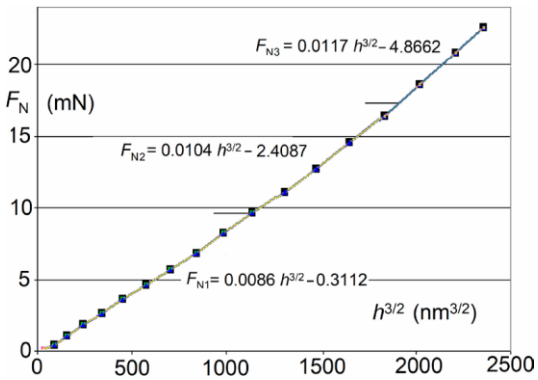

Fig. 10.2. The physical F_N vs $h^{3/2}$ plot (Kaupp-plot) from the indentation with Berkovich onto the (110) Stishovite after removal of the pop-in excursions and correction of the penetration values with inserted regression equations; the short horizontal lines indicate the kink positions (phase-transition onsets) where the regression lines (not drawn) intersect; the original force-depth data are taken from [24]

The phase-transition onsets are clearly seen and marked at the sharp though shallow kinks in Fig. 10.2. All transitions are endothermic and a projected third post-Stishovite is not reached due to the cupping of the indentation force. The phase-transition onset forces do not closely correlate with the transition energies. But what are the structures of these post-Stishovite polymorphs? More answers are provided by the calculated indentation work W_{indent} and the also calculated transformation energies W_{trans} that have been arithmetically calculated without iterations and without requiring the common energy-law violations of ISO-standards [25].

One has to distinguish indentation work W_{indent}, applied work $W_{applied}$, and transition energy W_{trans}. Before calculations, the published loading curves must be repaired from any pop-ins by removing such instrumental hold-periods with adjustment of the depth readings. Only required are the well-known formulas, as repeatedly published in [4] (their formulas 3 - 7). These correct for surface effects (axis cut F_a) of the physically analyzed loading curves. They calculate from the phase-transition onsets the balance of full $W_{applied} - \Sigma W_{applied}$ of the involved polymorphs. Such calculations have amply been published before [3,4,5,25,26]. The results are collected in Table 10.1.

Table 10.1. Berkovich micro-indentations; the arithmetically calculated indentation, application, and transition energies of Stishovite-SiO_2 with 2 post-Stishovite polymorphs and of MgO with 2 post-MgO polymorphs

Stishovite#1 onto (110)	**h_{kink} nm**	**F_{Nkink} mN**	**W_{indent}/mN mNnm/mN**	**$W_{applied}$ mNnm**	**Σ $W_{applied}$ mNnm**	**Full W_{appl} mNnm**	**W_{trans} mNnm**	**normalized W_{trans} mNnm/mN**
#1 to #2	110.7354	9.71019	49.1884	520.40020	520.40020	537.63062	17.23042	1.77447
#2 to #3	152.8857	17.2513	32.1117	692.46215	1212.8624	1318.7383	105.87597	6.13727
#3 up to 522.588 mN	176.30[a]	22.588[b]	20.5818	581.12649	1793.9889	1991.1322	197.14335	8.72779
MgO N˚1 onto (001)								
N˚1 to N˚2	99.29877	13.8862	25.662655	705.9483	705.9483	689.43882	243.99447	17.57107
N˚2 to N˚3	243.7261	29.9345	102.93585	3851.6663	4557.6146	3647.9229	−909.691	−30.38941
N˚3 up to 70 mN	475[a]	70.0[b]	273.5352	23,934.433	28,492.047	15,771.663	−8122.15	−116.0307

[a] h_{end}; [b] F_{Nend}

The general calculation sequence is clear from Table 10.1. One obtains $W_{applied1}$ from the triangle 0-F_{Nkink1}-depth h. The $W_{applied2}$ requires integration of the loading curve for the corresponding range to obtain the $W_{indent2}$ values that are multiplied with 1.25 to get the $W_{applied2}$ values. Their corresponding sum and the full $W_{applied}$ value are obtained as for the $W_{applied1}$ with the corresponding triangles. The balance is obtained by subtraction (full $W_{applied}$ − Σ $W_{applied}$) to obtain the W_{trans} values that are normalized by division through the corresponding force ranges. The W_{indent} values are not listed for space reasons, because they are easily obtained as 0.8 $W_{applied}$ [25]. The normalized W_{indent}/mN values show the energy differences of the three polymorphs. It decreases from Stishovite#1 to #2 and #3. Conversely, there is much increase in the required phase-transition work the higher the energy of the polymorph. Such energetic properties are not available by other techniques and should be an empiric basis for the test of quantum mechanical calculations.

It is also seen in Table 10.1, that both phase-transitions of Stishovite (describing the three polymorphs) are highly endothermic and that the normalized transformation energies here with respect to the transition onset force are increasingly high. Every one of the three polymorphs has its particular quality that is increasing with the normal force and thus pressure. The normalized transition energy values W_{trans} per mN of Stishovite are independent of the length of their stability ranges (the last one is cut off).

We can now ask, whether the proposed sequence of #2 before #3 is correct. The in Section 3.2 described quenchable orthorhombic Seifertite (Pbcn; 4.303 g/cm^3) is the first guess for #2 in Table 10.1. The second guess for #3 is the also quenchable monoclinic polymorph ($P2_1/c$; 4.30(2) g/cm^3) [19]. The reported densities are too close for deciding which one should be #2 or #3 in Table 10.1. And there is the possibility for as yet unknown unquenchable post-Stishovite polymorphs. A safe answer to these questions can only provide the onsite indentation at a synchrotron with highly focussed X-ray analyses. It is however certain that both of these endothermic formed polymorphs maintain the six-coordination of the silicon atoms. This excludes all of the numerous lower energy polymorphs with four-coordination to the silicon atoms. However, their transition energy contents are rather large in Table 10.1 and that should be helpful for decisions by calculations, as long as the synchrotron studies are lacking. The multitude of proposed structures is described in Section 10.3.2. Further indentation experiments with higher loads than 25 mN are advisable for finding still higher polymorphs of SiO_2. The big advantage of indentation is the energetic characterization that is only possible with this technique. The reason why (post)Stishovite does not exothermic react to give the 4-fold coordination of Coesite etc, or α-quartz that transforms exothermally to an amorphous phase with k_1 = 2.5443 and k_2 = 1.8609 μN/nm$^{3/2}$ [5] is their enormous density due to 6-fold coordination of Si. That makes any internal expansion difficult and prefers cooperative transitions with minimal internal movements by retaining the 6-fold coordination and retaining the high density. This view is also supported by the very high penetration resistance values k from the Kaupp-plot (the physical

hardness) of 0.0086 to 0.0117 mN/nm$^{3/2}$ (Fig. 10.2). These values reach and surmount the ones of superalloys [4].

10.3.3.2 The Stishovite Indentation with Published Broad Late Pop-In

It appears of course appropriate to compare the indentation of Section 10.3.3.1 with the 3 years older indentation, again onto (110) of Stishovite, and again with a Berkovich indenter. Smaller polycrystalline Stishovite grains (50 - 200 µm wide) were used and the results "should be regarded as for single crystals" [27]. These authors published one late large "pop-in" (20 nm wide) starting at 14 mN load and 128 nm depth. After the repair of the loading curve, the Kaupp plot revealed again two phase-transitions very close to the ones in Section10.3.3.1, with the very similar but slightly larger k-values of 0.0092, 0.0116 and 0.0133 mN/nm$^{3/2}$. The kink values are at lower loads (8.464 and 15.273 mN). After removal of the pop-in and the corresponding depth correction, the phase-transition depths (h_{kink}) are calculated lower at 97.757 and 134.136 nm than in Section 3.3.1. One of the phase-transitions is situated very far before and the other 6.8 nm behind the published pop-in from the 128 - 148 nm excursion length before the repair of the loading curve. That is again in support to the self-evident removal of pop-ins. The differences of the three k-values from Fig. 10.2 increase from +6% to +12%. All of that points to a calibration problem of the unspecified indentation instrument due to the iterative ISO 14577 calibration [28]. An "error of ±5% for the calibration" has been claimed. As the precise conditions are not reported in [27] (e.g. sample purity, origin of instrument, compliance correction, calibration of force and depth), we refrain from the energetic calculations but rely on the apparently better defined measurements: In [24] the tip radius was measured with tapping mode AFM, the single crystal was larger, the distances between the several impressions were 20 instead of only 10 µm, and the tests were at constant strain-rate of 0.05/s. Instrument calibrations should be direct but not indirect by using ISO 14577 standards that were obtained by two consecutive iterations the first with 3 and the second with 8 free parameters [28]. And there were experimental errors at the force linearity and severe mix-up of standard materials in [28], as revealed in [5].

It is again very clear that the removal of the pop-ins from published loading curves works well, whatever their appearance might be. They might be absent, broad, or multiply narrow, early, later, and very late.

10.3.4 The Published Huge "Pop-In" of Periclase MgO

While the behavior of the highly energetic and rarely available metastable materials in Section 3.3.with unusually high six-coordination to silicon atoms might appear somewhat special, one has to check at least one indentation of a normal stable material with pop-in accordingly. For example, the names Periclase for the MgO mineral (NaCl-type structure) already denotes easy cleavage all around its crystal, which can be a weak point for cracking and for pop-in production. Nevertheless, the B1 into B2 phase-transition of MgO upon hydrostatic pressure occurs between very high pressures of 429 and 562 GPa at

room temperature or at much higher temperatures [29]. One could therefore not safely expect a phase-transition by a Berkovich micro-indentation onto magnesium oxide. However the reported terraces on its indented freshly cleaved (100) plane should increase the probability for pop-in production when the descending tip hits a terrace step with its skew side or edge. This has already been pointed out in Section 3.1. Micro-cracking upon Periclase indentation far from the tip edges could be excluded, as there was none of the short depressive spikes in the smooth loading curve, which are known from [3]. The authors of [9] called their published pop-in at 9.501 mN from 75 - 125 nm a "kind of accident" at the conversion from "elastic deformation" to "elasto-plastic behavior". The comparison with an indentation of Al without pop-in in [9] is misleading: there were no terraces on it. The published loading curve of MgO required therefore its elucidation. A smooth loading curve was obtained for the physical analysis after removing the published pop-in and the corresponding correction of the penetration values. Following an initial surface effect up to <30 nm depth, the Kaupp-plot from the so repaired smooth loading curve with its regression lines can now obtain the kink positions by equalizing the corresponding regression lines (the initial effects including tip rounding are of course not part of the regression). The first exothermic phase-transition is at 99.299 nm. It is marked with the first vertical line in Fig. 10.3. This is the depth-corrected position within the now removed autonomous decoupled instrumental hold period. Therefore, the phase-transition force of 13.886 mN is above the previous hold-force (9.501 mN) of the removed pop-in, as expected. Clearly, the phase-transition did neither occur at the start of the published pop-in, nor at its end. The regression lines cover data points from before and from after the force-hold-period. This observation proves: the published pop-in did not at all influence the exothermic phase-transition onset. This is an especially lucky feature. It undoubtedly confirms the new recognition of the missing significance of "pop-ins" that must be avoided or removed. It certifies the undisturbed calculation of the indentation works and the transition energies despite published pop-ins. Published loading curves with "pop-ins" must indeed be repaired for any physical analysis both for exothermic and endothermic phase-transitions (Table 10.1).

Our process is highly precise. While the plot from the first kink (first vertical line) to the end point might be judged uniformly (this would correlate with R^2 = 0.9996). However, the differently drawn data points of the Excel calculation indicate another very shallow kink of two regression lines (not drawn) that correlate with R^2 = 0.9998 and 0.9997, respectively. The physical analysis thus reveals three polymorphs up to at least 76 mN load. The first transition produces exothermic the first post-MgO polymorph. And this polymorph produces at higher force exothermic the second post-MgO polymorph. A projected third post-MgO kink is not reached due to the cupped off indentation force. The transition energies are listed in Table 10.1. The energetic data were again arithmetically calculated with the well-known closed formulas in [3,5].

For the structures of post-MgO polymorphs we have to consider that an early B1 (NaCl type) to B2 (CsCl type) structural transformation of MgO at 13.9 and up to 30 and up to 70 mN load of a Berkovich indenter (Table 10.1) is not imaginable in

view of the required super-high hydrostatic pressure for this phase-transition [29]. The early transition onset of the first transition should therefore only reach a first twinned MgO, requiring the high mechanical stress due to high crystal energy of B1-MgO (3795 kJ/mol [30]) and that the first MgO-twin upon further stress transforms exothermic to a different second twin, which is stable to more than 67 mN load at the cut-off. Further post-MgO polymorphs require higher load indentations.

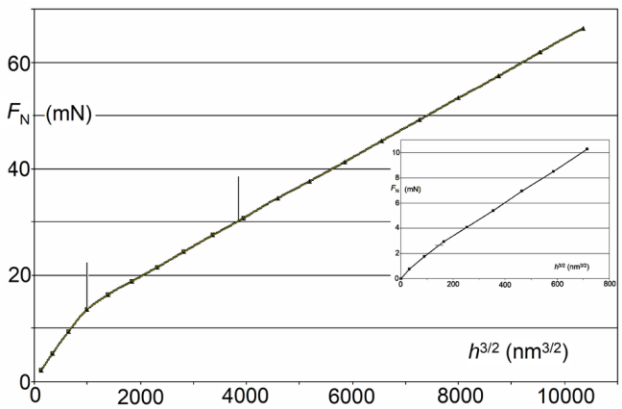

Fig. 10.3. Kaupp-plot of the Berkovich loading data onto (100) of MgO as calculated from the F_N vs h curve of [9] after removing the pop-in and adjusting the penetration values; the vertical lines indicate the intersection of the regression lines; the insert ($F_N = 0.0133h^{3/2} + 0.7258$; $R^2 = 0.9998$) shows the higher resolved initial part including initial effect before the horizontal line

Supporting evidence for these conclusions are the synthesized MgO-twins by epitaxial pulsed laser deposition from (111) faces in [111] direction [31] or by sintering of MgO (m.p. 2800˚C), at 2200-2300˚C into a structurally known monoclinic MgO-twin (a 6.443, b 5.9385, c 5.699, ß 91˚16') [32]. Two different deformation twins of MgO from {110} to [110] and from {111} to [112] slip systems have also been calculated [33]. This can provide a hint for the energetic sequence of the ones from micro-indentation in Table 10.1. Such twinning was apparently overlooked in the hydrostatic experiments.

The differences between the energetic data of metastable Stishovite and stable MgO are striking. While the penetration resistances are surprisingly pretty close, the first phase-transition energy W_{trans} of MgO is about 10 times higher. Conversely, the indentation energy W_{indent} of Stishovite is about twice as high. Clearly, both chemical and crystallographic effects play their decisive role. Stishovite has its unusual six-coordination of oxygen to silicon that cannot be abandoned at increasing pressure. Actually the compression of the Si-O bonds enforced the six-fold coordination of Stishovite under drastic conditions for

optimal space-use. The post-Stishovite polymorphs had to retain this unusual six-fold coordination and retain that feature when producing higher energy structures with minimal internal migrations in cooperative processes. Further post-Stishovite structures will be highly interesting and should be created by indentation at higher load. Conversely, MgO with its high crystal energy retains as much as possible of its favorable structure by internal migrations for the twinning at high pressure. The further constrained first twin continues at higher load with exothermic transition to the more stable twin. Apparently more demanding internal migrations reach the more stable second twin of MgO. One does not yet know the necessary force for the transition from coordination number 6 to 8 that is required for the projected phase-transition to B2-MgO. Interestingly, all of these exothermic migrational transitions of MgO require much more applied work for exothermic transitions than the endothermic phase-transitions of Stishovite. Chemical bond energy changes upon bond-length compression and the size and electronic structure of the central atoms (Mg or Si) in combination with crystal energies play their roles for these phase-transitions.

10.4 CONCLUSIONS

This paper reports two phase-transitions, each of micro indentation loading curves from the metastable Stishovite and from magnesium oxide. The projected third post-Stishovite and the projected third post-MgO are not reached due to the cupped indentation forces, but the way to them has been paved. These further polymorphs are firmly predicted for indentations up to higher loads. The published "pop-ins" within the loading curves had to be removed. The here described repair technique is highly important for the physical use of important published force vs. depth curves onto extremely precious materials, such as a good single crystal of Stishovite. Autonomous force holding ("pop-in") is a purely instrumental distortion. In the case of an Al-coated Ni-superalloy "diffusion zone" there is not a phase-transition but the crossing over two chemically different phases. It occurred without a published "pop-in", despite such strangest claim. Also in that case the widespread false belief on elastic-plastic conversion with "pop-in" had to be challenged. Unfortunately, the widespread belief in "pop-ins" is very dangerous. The change from elastic to plastic indentation does not change the smoothness of the loading parabola $F_N = k\ h^{3/2}$ of all normal conical or pyramidal indentations, but phase-transitions produce unsteadiness that is detected as sharp kinks in the F_N vs. $h^{3/2}$ Kaupp-plot. The so enabled search for phase-transitions for all solid materials is of practical importance. Phase transitions lead to polymorph interfaces that are sites for cracks' nucleation with catastrophic failures.

Published "pop-ins" are evidently due to the hype with them and the complicated theories about them with claiming spherical indentation just at their show-up, while spheres give no parabola and the so used exponent 3/2 on h is exclusively valid for cones, pyramids, and wedges. However, "pop-ins" are machine generated force holding with extrapolation of apparently not recognized fake depths. "Pop-ins" must be avoided by repetition of the measurement in the absence of the external or internal disturbing factors. If such distortions are

published at whatever position, they are not at all indicating any materials' properties. Published "pop-ins" are not resulting from the elastic to plastic conversion. They must and can be removed with the adjustment of the depth readings by subtraction of the produced fake-depths. Such self-evident repair of published loading curves is essential and simple, as outlined in Section 10.3.1. Creep correction during the short force hold at low force is mostly too small for its execution requirement. The arithmetically calculated phase-transition onsets, as revealed by using the Kaupp-plots for the repaired loading curves, are before, within, and after published "pop-in excursions". Phase-transitions are not accompanied by "pop-ins". This apparently for the first time achieved new cognition replaces all false historical claims that are unfortunately still pursuit with enormously complicated untenable argumentations. Several reasons for instrumental distortions are listed for the first time in Section 10.3.1.

This paper also points out that the correct calibration of the indentation equipment is important for correct numerical results. Secondary calibrations with the ISO 1457 standards are unsuitable, because of the mix-up of materials that occurred upon their generation with poor force calibration, inconsideration of their phase-transitions and iterations with at first 3 and then 8 free parameters, as revealed in [5] by checks with the Kaupp-plot. Such standards cannot be accepted for physical calibrations. But materials' standards are not necessary for the absolute physical analyses. ISO, instrument suppliers and certification agencies are required to use and enforce primary direct calibrations of the indenter instruments.

The two structurally known meteorite post-Stishovite polymorphs Seifertite and the monoclinic post-Stishovite can now easily be prepared for further investigation by microindentations onto Stishovite. Higher energy post-Stishovite polymorphs' onsets and energies are safely expected by higher force micro-indentation, and if necessary by depth sensing macro-indentation. The single crystal that has been used for Fig. 10.2 was already large enough for indentations at higher load micro- or macro-indentation above 25 mN. Also the B1 to B2 phase-transition onset and energies of MgO await further indentations at higher well calibrated loads.

It will be important for earth sub mantel explorations to indent all of the mayor minerals occurring in the lower earth mantle and study their high and highest energy phase-transition onsets and energies also temperature dependently. This will lead to a better understanding of the earth crust with its tectonic properties and influences. It will also be important to study all old and advanced technical and constructional materials for phase-transition onsets and energies to help avoiding catastrophic crashes of e.g. airliners, all types of fast running propellers, turbines, bridges, buildings, commodities, etc. Cracking is facilitated at polymorph interfaces. Their mechanical and thermal stress must be well below their as yet unknown phase transition onsets. As these remained undetermined for historical reasons they have now to be elucidated by physical indentation.

10.5 OUTLOOK

For the future, it will be important that industry shall be enabled to use the here described results and physical analysis techniques for the correction of false characterizations of technically important materials and for producing physically correct results. To reach that goal, the independent academic teachers must abandon their very complicated historical thinking and teaching that prevents them from disagreeing with the striking energy violation of ISO. As universally deduced in [25], the violation is 20% for the correct loading exponent 3/2 on h— or it calculates to 33.33% upon use of the incorrect exponent 2 on h of the undeniable pressure work. It cannot be created workless from nothing! However ISO 14577 still enforces to believe that all applied force is used for the penetration. ISO calls the normal force "P", which in fact means 1.25 F_N (see Section 2). This severe violation of the energy law is responsible for prescribing the false exponent 2 on h for cones and pyramids, which impedes phase-transition detections with their onsets and energies. It also falsifies dimension and value of ISO hardness, the values of ISO modulus, and the numerous mechanical parameters that are deduced from them. This must no longer be taught in classes for students and should help for complaints against ISO 14577 and also against handbooks of the indentation equipment suppliers. Such complaints shall be directly addressed towards ISO 14577 agents in addition to the present author who continues with direct complaining at ISO in Germany. It is certainly a difficult task for worldwide ISO to thoroughly modernize their 14577-Standards for complying with the physical basis at the expense of historical belief against elementary physics. Physically sound standards are indispensable for the instruction of the certification agencies, (between agencies and them) for their requiring this states-of-the-art upon the certification of the producing industries. The latter are of course bound to their certification documents and cannot act against them. Also instrument builders must change their handbooks and provide the physical calculation routines for the physical characterization techniques and extensions to the before not even thinkable applications. This will not only increase the value of the indentation techniques, but it is a requirement for daily safety to produce physically correct data. In the meantime independent researches are urged to use the here presented and cited new physical possibilities and publish their data on phase-transition onsets and energies. That includes the here not addressed temperature dependent indentations for the activation energies of phase-transitions. After all, liability problems cannot be excused with disproved historical beliefs any more.

COMPETING INTERESTS

Author has declared that no competing interests exist.

REFERENCES

1. Kaupp, G. (2016) The Physical Foundation of $F_N = k\ h^{3/2}$ for Conical/Pyramidal Indentation Loading Curves. Scanning, 38, 177-179. https://doi.org/10.1002/sca.21223

2. Page, F., Oliver, W.C. and McHargue, C.J. (1992) The Deformation Behavior of Ceramic Crystals Subjected to Very Low Load (Nano)Indentations. Journal of Materials Research, 7, 450-473. https://doi.org/10.1557/JMR.1992.0450
3. Kaupp, G. (2018) Six Polymorphs of Sodium Chloride upon Depth-Sensing Scanning Macroindentation with Unusual Long-Range Cracks Requiring 30 N Load. Journal of Materials Science and Engineering, 7, 473-483. https://doi.org/10.4172/2169-0022.1000473
4. Kaupp, G. (2019) Physical Nanoindentation: From Penetration Resistance to Phase-Transition Energies. Advances in Materials Physics and Chemistry, 9, 103-122. https://doi.org/10.4236/ampc.2019.96009
5. Kaupp, G. (2019) Phase-Transition Energies, New Characterization of Solid Materials and Anisotropy. Advances in Materials Physics and Chemistry, 9, 57-70. https://doi.org/10.4236/ampc.2019.94006
6. Adidharma H, Tan SP. Experiments of Vapor–Liquid Phase Transition of Fluids Confined in Nanopores: Implications on Modeling. Industrial & Engineering Chemistry Research. 2022 Jul 7.
7. Qian Y, Wang YM, Xu L, Yao WW, Shao DS, Ren XM. Formation of organic ion cocrystals, phase transition and ion conduction. CrystEngComm. 2022;24(21):3962-71.
8. Zhang L, Yu P, Fan J, Li Y, Gao Y, Li G. High pressure induced the polymorphism phase transition in the Fe40Mn40Co10Cr10 multi-principal element alloy. Intermetallics. 2021 Sep 1;136:107268.
9. Tromas, C., Girard, J.C., Audurier, V. and Woirgard, J. (1999) Study of the Low Stress Plasticity in Single-Crystal MgO by Nanoindentation and Atomic Force Microscopy. Journal of Material Science, 34, 5337-5343. https://doi.org/10.1557/JMR.1992.0450
10. Armstrong, R.W. and Elban, W.L. (2010) Macro- to Nano-Indentation Hardness Stress-Strain Aspects of Crystal Elastic/Plastic/Cracking Behaviors. Experimental Mechanics, 50, 545-552. https://doi.org/10.1007/s11340-009-9246-5
11. Wöllmer, S., Zaefferer, S., Göken, M., Mack, T. and Glatzel, T. (2003) Characterization of Phases of Aluminized Nickel Base Superalloys. Surface and Coatings Technology, 167, 83-96. https://doi.org/10.1016/S0257-8972(02)00843-5
12. Kaupp, G. (2019) The Loading Curve of Spherical Indentions is not a Parabola and Flat Punch Is Linear. Advances in Materials Physics and Chemistry, 9, 141-157. https://doi.org/10.4236/ampc.2019.98012
13. Kaupp, G. (2013) Penetration Resistance and Penetrability in Pyramidal (Nano)Indentations. Scanning, 35, 88-111. https://doi.org/10.1002/sca.21038
14. Stishov, S.M. and Popova, S.V. (1961) A New Dense Modification of Silica. Geokhimiya, 10, 837-839.
15. Leger, J.M., Haines, J., Schmidt, M., Petitet, J.P., Pereira, A.S. and da Jamada, J.A.H. (1996) Discovery of Hardest Known Oxide. Nature, 383, 401. https://doi.org/10.1038/383401a0
16. Sharp, T.G., El Goresy, A., Wopenga, B. and Chen, M. (1999) A Post-Stishovite SiO2 Polymorph in the Meteorite Shergotty: Implications for

Impact Events. Science, 284, 1511-1513. https://doi.org/10.1126/science.284.5419.1511
17. Hemley, R.J., Prewitt, C.T. and Kingma, K.J. (1994) High Pressure Behavior of Silica, Chapter 2. In: Heaney, P.J., Prewitt, C.T. and Gibbs, G.V., Eds., Mineralogy, Volume 29, The Mineral Society of America, New York, 41-73.
18. Dera, P., Prewitt, C.T., Boctor, N.Z. and Hemley, R.J. (2002) Characterization of a High-Pressure Phase of Silica from the, Martian Meteorite Shergotty, Alpha-PbO2-Like. American Mineralogist, 87, 1018-1023. https://doi.org/10.2138/am-2002-0728
19. El Goresy, A., Dubrovinsky, L., Sharp, T.G., Saxena, S.K. and Chen, M. (2000) A Monoclinic Post-Stishovit Polymorph of Silica in the Shergotty Meteorite. Science, 288, 1632-1634. https://doi.org/10.1126/science.288.5471.1632
20. Tsuchida, Y. and Yagi, T. (1989) A New, Post-Stishovite High-Pressure Polymorph of Silica. Nature, 340, 217-220. https://doi.org/10.1038/340217a0
21. Kingma, K.J., Cohen, R.E., Hemly, R.J. and Mao, H.K. (1995) Transformation of Stishovite to a Denser Phase at Lower-Mantle Pressures. Nature, 374, 243-245. https://doi.org/10.1038/374243a0
22. Andrault, D., Fiquet, G., Guyot, F. and Hanfland, M. (1998) Pressure Induced Landau-Type Transition in Stishovite. Science, 282, 720-724. https://doi.org/10.1126/science.282.5389.720
23. Page, M.E., Ohtani, E., Suzuki, A., Asahara, Y. and Saxena, S. (2013) Synthesis of Seifertite and Its Applications to Shocked Meteorites. American Geophysical Union, No. 213, Abstract ID: P41F-1983.
24. Dub, S.N., Brazhkin, V.V., Novikov, N.V., Tolmachova, G.N., Litvin, P.M., Lityagina, L.M. and Dyuzheva, T.I. (2010) Comparative Studies of Mechanical Properties of Stishovite and Sapphire Single Crystals by Nonoindentation. Journal of Superhard Materials, 32, 406-414. https://doi.org/10.3103/S1063457610060067
25. Kaupp, G. (2013) Penetration Resistance: A New Approach to the Energetics of Indentations. Scanning, 35, 392-401. https://doi.org/10.1002/sca.21080
26. Kaupp, G. (2014) Activation Energy of the Low-Load NaCl Transition from Nanoindentation Loading Curves. Scanning, 36, 582-589. https://doi.org/10.1002/sca.21158
27. Luo, S.N., Swadener, J.G., Ma, C. and Tschauner, O. (2007). Examining Crystallographic Orientation Dependence of Hardness of Silica Stishovite. Physica B, 399, 138-142. https://doi.org/10.1016/j.physb.2007.06.011
28. Oliver, W.C. and Pharr, G.M. (1992) An Improved Technique for Determining Hardness and Elastic Modulus Using Load and Displacement Sensing Indentation Experiments. Journal of Materials Research, 7, 1564-1583. https://doi.org/10.1557/JMR.1992.1564
29. Dubrovinskaia, N., Petitgirard, S., Chariton, S., Tucoulou, R., Garrevoet, J., et al. (2019) B1-B2 Phase Transition in MgO at Ultra-High Static Pressure. Cornell University, Ithaca, NY. arXiv.org>cond-mat>Xiv: 1904.00476
30. Lide, D.R. (2005) CRC-Handbook of Chemistry and Physics. 86th Edition, CRC-Press, Taylor & Francis, Boca Raton, FL. https://www.crcpress.com

31. Stampe, P.A. and Kennedy, R.J. (1998) X-Ray Characterization of MgO Thin Films Grown by Laser Ablation on Yttria-Stabilized Zirconia. Journal of Crystal Growth, 191, 472-477. https://doi.org/10.1016/S0022-0248(98)00163-8
32. Toda, N. (1965) On the Sintering Mechanisms of Magnesium Oxide. Mineral Journal, 4, 356-373. https://doi.org/10.2465/minerj1953.4.356
33. Yang, B., Huang, C., Yin, D., Zhao, Y., Sun, S., Yue., X., Fu.T. (2018) Investigation of Impurity Induced Twinning in MgO from First Principles Calculations. Computational Materials Science, 150, 390-396. https://doi.org/10.1016/j.commatsci.2018.04.039

DISCLAIMER
This chapter is an extended version of the article published by the same author(s) in the following journal.
Advances in Materials Physics and Chemistry, 10: 77-95, 2020.

Chapter 11
Print ISBN: 978-93-5547-921-1, eBook ISBN: 978-93-5547-922-8

Valid Geometric Solutions for Indentations with Algebraic Calculations

DOI: 10.9734/bpi/mono/978-93-5547-921-1/CH11

ABSTRACT

This chapter analyzes the force vs depth loading curves of conical, pyramidal, wedged and for spherical indentations on a strict mathematical basis by explicit use of the indenter geometries rather than on still world-wide used iterated “contact depths” with elastic theory and violation of the energy law. The loading curves, which have now been accurately examined, offer undetected phase-transition. This contains a clear correction for the variable depth/radius ratio, which was previously ignored, for the spherical indentations. Fortunately, no data-fitting, simplification, or fake simulations must be utilised in the determination of a material's properties; only algebraic formulas. By equating the linear regression lines from the mathematically linearized loading curves, the penetration resistance differences of the materials' polymorphs offer accurate intersection values as kink unsteadiness. The phase transition onset values for depth and force are indicated by these intersections. Energy and phase-transition energy calculations are made possible by the accurate and precise estimation of phase-transition onsets. The derivation of the novel algebraic equations is most straightforward and reproducible mathematically. There are no limitations on the behaviour of elastic or plastic materials, and no need to utilise distinct formulas for various force ranges. This is now also achieved for spherical indentations. Their formula as deduced for plotting is reformulated for integrations. The unique indentation formulas provide previously unattainable access to the phase-transitions' onset, energy, and transition energy. (W_{indent}) allows now for comparing spherical with pyramidal indentation phase-transitions. Only low energy phase-transitions from pyramidal indentation may be missed in spherical indentations. The spherical calottes' relatively shallow penetration depths are calculated extremely closely for both cap and flat area values. As a result, the indentation phase-transition onset pressure may be calculated and successfully compared to the results of hydrostatic anvil pressurising. Low energy phase-transitions are frequently overlooked beneath the anvil; therefore, this is highly beneficial for their interpretations and further supports the unparalleled simplicity of the indentation experiments. The numerical examination of previously published germanium data has compared pyramidal, spherical, and hydrostatic anvil stresses. The preexisting, commonly accepted theories and guidelines for historical indentation are contested. It is easiest to check falsely generated and even published so-called "experimental" indentation data from the literature. Due to their mathematical inadequacies and the pressing need for daily safety with stressed materials, they must be corrected. The issue of faulty ISO 14577

standards for inaccurate and inadequate material categorization is what spurred the author to write this essay. By employing our closed formulas, which are founded on indisputable geometric and algebraic calculation laws, we can reinforce and advance the mathematical truth while minimising catastrophic failures, such as in aviation.

Keywords: Geometry of indenters; algebraic solutions; false mathematic concepts; germanium; pyramidal and conical indentation; spherical indentation; anvil pressuration.

11.1 INTRODUCTION

A challenging mathematics issue involving normal indentations on flat surfaces was first addressed by Boussinesq in 1882 [1]. Starting with elasticity theory has traditionally been the approach taken to try to solve the load/depth relation. The materials by indentations with the total applied force for a (since 1992 iterated) indentation area were improperly described by Young's modulus E (that is unsuited for indentations) and Poisson's ratio ν. Hertz's influential paper from 1882 [2] only discussed the mathematical touching between balls (with radius R) and balls with flat surfaces, but not penetration. He deduced a contact pressure $p = k\alpha^{3/2}$ where α describes the impact area. He repeated that he did not describe penetration in [3], but all followers who refined this approach kept with a force P per indentation area a (circle of contact) when the half-sphere penetrated at increasing force. They had to deal with an additional parameter the indentation depth h and kept with the exponent 3/2 on the penetration depth ($h^{3/2}$). Much effort was put to the refinement in the early 1900ies, but advancements became over complicated, and also conical indentation had to be mathematically described. Really useful equations for practical use had to wait until 1939, when Love in [4] very laboriously deduced formulas for rigid cones. His approach was again "elastic theory" and force per area and his solution is $P = h^2\pi \mathrm{tg}\alpha E/2(1-\nu^2)$ (below we replace P by F_N for normal force and do not violate the energy law). Thus, the depth was squared for cones and pyramids in [4]. Only the proportionality factor was changed in 1965 with the very laborious deduction of Sneddon in [5] to read $P = h^2 \cdot 2E\cot\alpha/\pi(1-\nu^2)$ that has been widely accepted. He also deduced a "solution" for spherical indentation by using Hankel transforms and the theory of dual integral equations. His formula (6.15) for spheres is $P = E(1-\nu)^{-1}\{(a^2+R^2)2\,h/a - aR\}$, where $a^2 = R^2 - (R-h)^2$. It at least shows that the situation is much more difficult than "Hertzian theory". When the substitution is made one obtains an equation $P = E(1-\nu)^{-1}(2Rh - h^2)^{-1/2}(5R-2h)h^{3/2}$ with a multitude of terms and with numerous different exponents on h. Only this part of Sneddon's work was ignored. 20 years later Johnson came back in [6] with a formula by "summarizing Hertzian theory" to read $F = 4/3\,E^*R^{1/2}h^{3/2}$ (where E^* is reduced elastic modulus) for the sphere. This again did not consider the particular geometry of the sphere calotte. Interestingly, Oliver and Pharr cited in [7] the reference [5] but formulated "$P = \alpha h^m$ for spheres "with m = 1.5", arguing that the sphere can be described as a solid of revolution giving "a smooth function". But they did not tell that this was Johnson's "summarized" formula in [6]. Unfortunately, the geometrically unsound

formulas in [7] and in [6] became ISO-ASTM standard (International Standardization Organization-American Society for Testing of Materials) that is still generally enforced. For example, the authors of [8] calculated modulus values E from the elastic contact with spherical indentation “according to the classical Hertzian theory” with Johnson’s formula in [6] (“below the yield point”). It did not help that the experimental loading curves were at variance with these formulas. The exponents were just believed but not checked. Such checking was at least possible since 2004 as shown in [9] and thereafter with the F_N vs $h^{3/2}$ plot from the present author’s group. This plot (later from believers disdainfully termed as “Kaupp-plot”) disproved and disproves the more than 1000-fold falsely claimed exponent “2” on h (as enforced by ISO) for all conical, pyramidal and wedged indentations. It also discloses whether published spherical indents were truly spherical. However, several researchers continued to simulate spherical indentations as one exponent parabola with $h^{3/2}$ according to Johnson’s formula in [6] and claimed that their “experimental curves” would support such claims. Fortunately, such published “results” of “spherical indentations” have been and can be disproved by exponent check with the F_N vs $h^{3/2}$ plot (we now also call it “Kaupp-plot”), which, of course, cannot give straight lines neither for the simulation and nor for the published so called “experimental” curves. Such publications are disastrous and some examples for such clearly manipulated data are published in [10,11]. Some updates in this area are available elsewhere and may find attention of the readers [12-14]. We refrain from listing further examples; they are easily checked in the literature. [12] is a Book Section review paper for the common ISO 14577 approach of indentations onto biological material with some critics that adhesive contact is often not properly applied. [13] uses FEM simulations for "Young's modulus" determination from unloading curves on the basis of pseudo cones and tries to circumvent differences with experiment by using a new factor ß. [14] deals with "approximate analytical formulas" for indentation pile-up from sphere and cone. We might question whether it is worth publishing more and more reviews of the ISO 14577 related fittings, iterations, and simulations rather than either reporting correction of dangerous tabulated unphysical mechanical properties of undetected polymorphs, instead of those from pristine materials for more reliable AI. Particularly rewarding would be reports of indentations on the basis of universal physically sound and repeatable calculation rules for the finite avoidance of polymorph interfaces under stress for safety reasons. The here cited disclosures and our papers with mathematical deductions on the basis of undeniable closed mathematical equations for indentations have not yet occasioned ISO-ASTM to thoroughly revise their incorrect ISO 14577 standards, falsely enforcing the producing industries via the Certification Agencies. We therefore extend our mathematical deductions for conical, pyramidal, wedged and spherical indentations and report various unprecedented application. This also allows for comparison of unchanged spherical indentations with hydrostatic techniques.

11.2 THE GEOMETRICAL DEDUCTIONS OF INDENTATION FORMULAS EXCLUDING ITERATIONS

All mathematical deductions in the Introduction started with the indented surface area, and by applying the elasticity theory. They ran into enormous mathematical

problems that could for a long time not be solved since 1882 with practically useable formulas. Only the still incorrect formulas of Love in [4] or one of them from Sneddon in [5] and of Johnson in [6] were used by Oliver-Pharr [7] in 1992 by using standard materials that they characterized by two iterations with 3 followed by 8 free parameters. These iterations were taken up by ISO and refined as ISO 14577 standards for performing and analyzing indentations. These physically unsound but binding standards had not been challenged before 2004 [9] when the present author's group started to empirically prove with the Kaupp-plot that such standards did experimentally not concur. It was undeniably deduced in 2013 [15] that the standards violated the energy law because not all applied force and energy is used for the volume formation. Finally, the mathematical foundation of the F_N vs $h^{3/2}$ parabola for cones was geometrically deduced in 2016 using basic algebra in [16]. The projected or iterated contact area related formulas are thus finally disproved for conical, pyramidal and wedged indentations. Rather the volume of the indenter has to be used and everything is very simple. Previous thinking is thus obsolete. We must now comprehensibly repeat the geometrical deduction despite their simplicity, as the incorrect ISO 14577 standards are still used by teachers, and enforced to Certification Agencies, and thus also for the producing industries.

11.2.1 The Energetics and the Correct Exponent of Conical Indentations

The normal force vs depth curves are empirically described since 2004 in [9] and also theoretically since 2016 in [16] as parabolas with exponent 3/2 on the depth as Formula (11.1). F_N is the normal force (we do not use "P" as in the formulas of the Introduction), h (µm) is the depth, and k (mN/µm$^{3/2}$) is the material's penetration resistance. The indentation work W_{indent} (mNµm) in Formula (11.2) is obtained by integration. The constantly increased normal force from zero to the same force gives the applied work $W_{applied}$ (mNµm) in Formula (11.3). For the maximal force F_{Nmax} we substitute F_N of Formula (11.1) in Formula (11.3) and obtain the $W_{applied}/W_{indent}$ ratio of 5/4, which is universally valid for all materials upon conical, pyramidal and wedged indentations. Clearly 20% of $W_{applied}$ (and thus F_N) is not used for the penetration with a cone, pyramid or wedge. The non-consideration is the already mentioned violation of the energy law that led to a false exponent on h, which is still enforced by ISO, but urgent subject to change. This is the reason why we use F_N and not "P" for the normal force.

$$F_N = kh^{3/2} \tag{11.1}$$

$$W_{indent} = 0.4k\ h^{5/2} \tag{11.2}$$

$$W_{applied} = 0.5F_N h \tag{11.3}$$

The geometric deduction of the correct exponent (3/2 but not 2) in [16] has to consider that the penetration of the cone under force is a coupled process of volume- and pressure-formation. In practice there is not always only elastic pressure but there are mostly all kinds of plastic deformations. We thus sum up

all of it to "total pressure". It creates the 20% loss of force and energy for the volume formation with its depth. One has to multiply the force for volume formation F_{Nv} with the force for total pressure formation F_{Np} in Equation (11.4). Now one considers that the total pressure must be proportional to the immersed volume of the cone in Equation (11.5), so that F_{Np} is proportional to h^3 and h proportional to $F_{Np}^{1/3}$ When the exponent n is 1/3 the exponent m must be 2/3 and Equation (11.4) becomes Equation (11.6). As $F_{Np}^{1/3}$ is lost for the indentation only $F_{Nv}^{2/3}$ is proportional to the depth in Equation (11.7). The deduction is completed with inclusion of the materials property factor, which is the penetration resistance or the physical hardness k_v or k = 1.25k_v (mN/µm$^{3/2}$) as the proportional constant to give Equation (8_v) and by its multiplication of both sides with the $W_{applied}/W_{indent}$ ratio = 1.25 that is herewith also deduced. Equation (8_v) is used when only the volume formation must be considered as e.g. in Section 5. Equation (1) thus describes the whole indentation.

$$F_N = F_{Nv}^m \, F_{Np}^n \tag{11.4}$$

$$V_{cone} = h^3 \pi \tan \alpha^2 / 3 \tag{11.5}$$

$$F_N = F_{Nv}^{2/3} F_{Np}^{1/3} \tag{11.6}$$

$$F_{Nv}^{2/3} \propto h \text{ or } F_{Nv} \propto h^{2/3} \tag{11.7}$$

$$F_{Nv} = k_v h^{3/2} \tag{11.8}$$

Equation (11.1) is generally valid for all materials, pyramids and wedges. Normalization of these is possible when different indenter geometries among these must be compared. The k_v value of Equation (11.8_v) is the physical hardness with respect to the force F_{Nv} that is responsible for the volume formation. A perhaps technically more important k_{tot} = 1.25 k_v value of Equation (11.1) is the physical hardness for the whole indentation k_{tot} with $F_{N\text{-}tot}$ = 1.25F_{Nv}. We thus distinguish two different physical hardness values. This $F_{N\text{-}tot}$ has to be taken into account for the comparison of e. g. pyramidal indentations with spherical ones with inconstant $W_{applied}/W_{indent}$ ratios. Unlike iterations for false "ISO-hardness" we obtain from the correct analysis of Equation (11.1) by plotting F_N vs $h^{3/2}$ (the "Kaupp-plot") linear regression lines via Excel(R) calculation and detect the phase-transition onsets at the kink unsteadiness of intersecting regression lines, because different polymorphs exhibit different k-values. The calculated intersection points by equalization of the regression lines at F_{Nkink} and $h_{kink}^{3/2}$ reveals also the practically important indentation energies [cf Equation (11.2) and Equation (11.3)]. Furthermore, the phase-transition energy can be calculated by using the Equation (11.9) through (11.13). The application of Equation (11.9) and Equation (11.11) contain the corrections for axis-cut F_a when not zero. All of these have been deduced and are repeated here in modified form [17,18] for direct comparison with the spherical situation in Section 2.2.

$$W_{applied1} = 0.5h_{kink}(F_{Nkink} \quad (11.9)$$

$$W_{indent1} = 0.8W_{applied1} \quad (11.10)$$

$$W_{indent2} = 0.4(h^{5/2} - h_{kink}^{5/2}) + F_{a2}(h_2 - h_{kink}) \quad (11.11)$$

$$\text{full } W_{applied} = 0.5F_{N2}h_2 \quad (11.12)$$

$$W_{transition} = \text{full } W_{applied} - \Sigma W_{applied} \quad (11.13)$$

The fast calculation of $W_{applied1}$ for cones, pyramids and wedges with Equation (11.10) avoids the integration of Equation (11.1). Higher phase-transition $W_{indents}$ must be integrated from kink to the next kink etc. The F_{N2}-h_2 pair can be freely chosen above the kink$_1$. In the case of several phase-transitions one proceeds from kink to further kink and after the last phase-transition there is free choice for the F_{Nn}-h_n pair. A practical example will be calculated in Section 3.

11.2.2 The Correct Loading Curve and the Energetics of Spherical Indentations

A one member "parabola with exponent 3/2" for spheres in [6], [7] and ISO is impossible, because such parabola with exponent 3/2 is only valid for cones, pyramids and wedges. The geometric deduction of the correct F_N vs h curve of sphere calottes (with sphere radius R and calotte radius r) is more involved, because the depth related *R*/*h* ratio is changing during the penetration as shown in [10]. As in the conical case one starts again with Equation (11.4) to distinguish pressure and volume. The sphere-calotte volume formula is $V = h^2\pi(R - h/3)$. It is modified by multiplication with 1= h/h to give the more easily handled Equation (11.14) that is more similar to Equation (11.5) containing h^3 but with the varying dimensionless *R*/*h* term for its $\pi(R/h - 1/3)$ correction. This correction term can be treated like a variable factor that has to be separately applied for every force point of the plot, according to Equation (11.18) that is not at all a one-member parabola. The sequence of the deduction is now similar to the one for cones. We consider again that the total pressure must be proportional to the immersed volume of Equation (11.14) and we get the Formulas (11.15). Equation (11.18) is obtained for F_{Nv} after multiplication with the material's proportionality factor k_{sv} ($_s$ for sphere; $_v$ for volume) (see also Chapter 12). Equation (11.18$_v$) describes only the volume formation and it is used when the penetration part F_{Nv} must be exclusively considered. Equation (11.18) for the whole indentation is obtained by multiplication of both F_{Nv} and k_v. Equation (11.18) is used for plotting F_N vs $\{h^{3/2}\pi(R/h - 1/3)\}$. One obtains the penetration resistance values k_{s1} and k_{s2} (mN/µm$^{3/2}$), the phase-transition onset with F_{Nkink}, the $\{h^{3/2}\pi(R/h - 1/3)\}$value and the $W_{applied1}$ at the kink position from the intersection of the regression lines. The necessary h_{kink} must not be calculated. It is available from the F_N vs *h* curve for $F_N = F_{Nkink}$.For the now necessary calculation of W_{indent} we reformulate Equation (11.19) and add the axis cut F_a (+, 0, or -) to give (11.20). Its integration gives

Equation (11.21) for W_{indent}. The $W_{applied2}$ is calculated from F_{Nkink} to F_{N2} (here chosen at F_{Nmax}). The balance of full $W_{applied}$ − Σ $W_{applied}$ is the phase-transition energy $W_{transition}$ as in Equation (11.13). A practical example will be calculated in Section 11.4. Equation (11.18_v) will be used in Sections 4, 5, and 6.

$$V = h^3\pi(R/h - 1/3) \tag{11.14}$$

$$F_N \propto h^3\pi(R/h - 1/3) \tag{11.15}$$

$$F_{Nv} = k_{sv}h^{3/2}\pi(R/h - 1/3) \tag{11.18_v}$$

$$F_N = k_s h^{3/2}\pi(R/h - 1/3) \tag{11.19}$$

$$F_N = k_s\pi R h^{1/2} - k_s\pi h^{3/2}/3 + F_a \tag{11.20}$$

$$W_{indent} = \int F_{Nkink}\mathrm{d}h = 2/3 \cdot k_s\pi R h^{3/2} - 2/15 \cdot k_s\pi h^{5/2} + \Delta F h \tag{11.21}$$

11.3 THE PYRAMIDAL INDENTATION CALCULATION OF GERMANIUM

For the numerical exemplification, the published data of the semiconductor germanium are chosen from the literature. This covers pyramidal (Berkovich diamond), spherical (diamond) indentations, and hydrostatic anvil compression. The analysis of the Berkovich indentation onto cubic germanium from [19] according to Equation (11.1) is depicted in Fig. 11.1 with the inserted regression line equations after a short initial surface effect (including the inevitable tip rounding). The proportionality of W_{indent} = 0.8$W_{applied}$ (Equation (11.2) and Equation (11.3)) for a loading parabola with exponent 3/2 in [15] makes it particularly easy to calculate W_{indent} for every chosen work so that normalization per force unit provides comparable values for different materials. The phase-transition kink position by equalization of the regression lines is at 4.149 mN and 0.151 µm. The pristine polymorph withstands a phase-transition up to 0.1342 mNµm applied work and $W_{indent1}$ is thus 0.1074 mNµm. With $W_{applied2}$ = 1.7927 and full $W_{applied}$ = 2.3059 mNµm the phase transition energy into the second polymorph calculates easily as full $W_{applied}$ − Σ $W_{applied}$ (Equation (11.13)) to give $W_{transition}$ = 0.37898 mNµm from kink to 15.25 mN load. These are after normalization per mN 0.03414 mNµm/mN. Such transition energies based on physically valid application of geometry and arithmetic calculation rules are not available by any other means. Unfortunately, we could not search for further phase-transitions of germanium, due the smoothness lack by the repeated load-unload sequences at higher loads in [19].

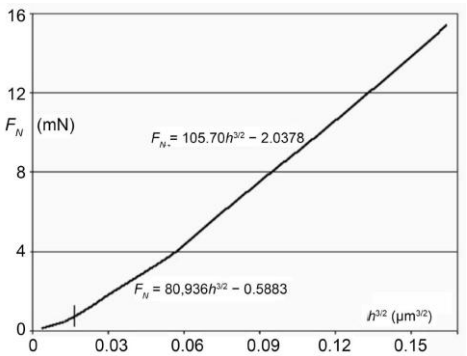

Fig. 11.1. Normal force vs depth$^{3/2}$ plot upon Berkovich indentation onto germanium with inserted regression line equations; the vertical line cuts off the initial surface effect; F_{Nkink} is at 4.149 mN; the original data from the F_N vs h curve are taken from Fig. 11.5(a) in [19], but only up to 0.3 μm depth (at 15.25 mN) before numerous load-unload sequences that detract from the smoothness of the further force-depth curve.

11.4 THE SPHERICAL INDENTATION CALCULATION OF GERMANIUM

The spherical indentation onto germanium at a rate of 7 mN/s follows Equation (11.18) and Equation (11.19), but not Johnson's equation of a one exponent $F_N \propto h^{3/2}$ parabola for spheres in [6]. The publication of [20] depicts in its Fig. 1(a) the loading curve of crystalline germanium onto (100) from a sphere with radius R ≈ 4.2 μm. This was certainly a good sphere at least up to 4 μm depth. The so-called "pop-ins" of the F_N vs h curve far away from the phase-transition position are not corrected for, because there is no force hold interruptions and there are no "discontinuities" in the F_N vs h curve of [20]. Our trial Kaupp-plot in Fig. 11.2 does not result in a straight line as it should if the "Hertzian analysis" of [20] would be correct. The convex curve has only some discontinues that must however not be interpreted as exothermic events. It proves the obvious failure of the false ISO and Johnson equation for spheres that must be strongly rebuffed. The data of the published F_N vs h curve are fortunately in [20] *not* data-fitted. That is proved by our plot according to Eq. (11.19) for spherical indentations (Fig. 11.3), providing two linear branches from the actually very prominent endothermic phase transition. So, we can really tell and exclude or prove data fittings, which should be highly welcomed (see also Chapter 13). Apart from the following energetic calculations below, we provide the easiest way for the detection of phase transitions under mechanical load: While our physically correct two-exponent parabola plot for spherical indentations in Fig. 11.3 gives after the initial surface effect two straight lines with a very pronounced kink, indicating the endothermic phase-transition, even though a phase transition was "excluded" by [20] with Raman spectroscopy. Only a "pinning of slip bands" and or "multiple discontinuities" by "plastic deformation" were suspected in [20]. In

Fig. 11.3 we plot the normal force F_N vs $\{h^{3/2}\pi(R/h - 1/3)\}$ for germanium, according to Equation (11.19). It visualizes the linearity for obtaining the penetration resistance values k (mN/μm$^{3/2}$) at the kink-point with respect to the spherical tip with radius 4.2 μm. The phase-transition onset is clearly seen by the kink and the very different k-values of the polymorphs. The regression line results are inserted. The slightly steeper data above the horizontal shut-off line are not included in the regression.

We do not dare to claim a “second kink” at about 46 mN load due to the short pen etration length, but did not include the data pairs above 40 mN load, due to the s hort penetration length. There is also a risk of spheres’ quality at higher dept hs. The 4.2 μm diamond sphere was however in good shape, at least up to about 0.4 μm depths. The inserted regression lines give the materials’ dependent penetr ation resistance values ks (mN/μm$^{3/2}$) of the respective polymorphs, because the uninterruptedly varying geometric factor is taken care of by the R/h ratios in Equation (11.19). The equalization of the (not drawn) regression lines provide the sharp phase transition onset at the kink position at 5.197{h3/2p(R/h-1/3)

.

One obtains F_{Nkink} = 10.703 mN by insertion in any one of the two regression line equations. With the F_{Nkink} value one obtains h_{kink}= 0.124 μm from the F_N vs h loading curve and according to Equation (11.9) also $W_{applied1}$ = 0.67704 mNμm. The integrated Equation (11.21) provides $W_{indent1}$ = 0.4756 mNμm.

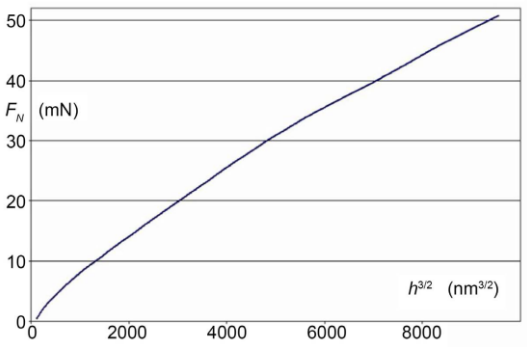

Fig. 11.2. Normal force vs depth$^{3/2}$ trial-plot of the spherical (R = 4.2 μm) indentation onto germanium, disproving the so-called “Hertzian theory” ofJohnson [6] that has been claiming a one-exponent h$^{3/2}$ parabola as that would require to proceed linearly in that plot; the loading data were taken from [20]

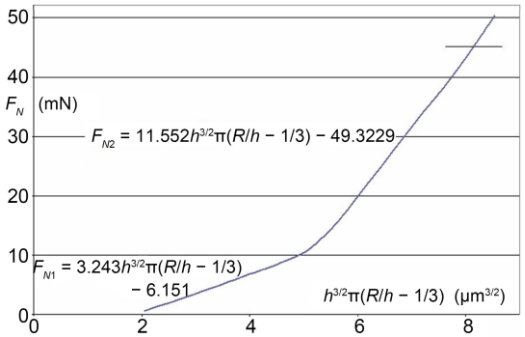

Fig. 11.3. Normal force vs point by point corrected depth$^{3/2}$ plot of germanium upon spherical indentation (R = 4.2 μm) onto germanium with the inserted regression line equations; the initial surface effect data and the data above the horizontal line are not part of the regressions; the phase-transition onset is at 10.703 mN; the loading data were taken from [20]

The $W_{indent}/W_{applied}$ ratio is here not 0.8 as in the case of conical, pyramidal, and wedged indentations (cf Section 3). It changes for every point at spherical indentations as in Fig. 11.3. We need the integrated Formula (11.21) for the transformed polymorph of germanium. It can be calculated for any force with its depth above the kink value for the calculation of $W_{indent2}$ and $W_{applied2}$. In the absence of a second kink within the loading range we integrated from F_{Nkink} to F_{Nmax} at linearly interpolated 50 mN and the interpolated depth of h_{max} = 0.4444 μm. Equation (11.21) provides $W_{indent2}$ = 7.07438 mNμm for the sphere with radius 4.2 μm. Equation (9) is correspondingly used for (50 − F_{Nkink1}) and (h_{max} − h_{kink}) to give $W_{applied2}$ = 8.8219 mNμm up to 50 mN load for the sphere of radius 4.2 μm. The sum ($W_{applied1}$ + $W_{applied2}$) is 9.4989. As the full applied work (Equation (11.12)) from 0 to F_{Nmax} and h_{max} is 11.1111 mNμm one obtains the endothermic balance as full $W_{applied}$ − $\Sigma W_{applied}$ = $W_{transition}$ = 1.6122 mNμm, according to Equation (11.13) for the phase transition energy of germanium at the kink onset position for the whole indentation force.

It should be noted that the energy calculations for spheres are with respect to the R/h value at the kink position. The non-constancy of the correction factor in Equation (11.19) prevents a normalization of the energy values per mN. Every energy value must be separately calculated when compared with the values from conical, pyramidal, or wedged indenters. Only for the latter is it possible to interpolate and even interconvert energy values. This disadvantage of spherical indentations is outweighed by the pressure distribution over an almost plane area. The sphere calotte radius for R = 4.2 μm and h = 0.124 μm is easily calculated with $\sin\beta = (R - h)/R$ and $\cos\beta = r/R$ to give r = 1.01327 μm. Thus, the flat π r^2 area is here 3.226 μm^2, which is similar to the calotte-cap 2πRh surface area of 3.272 μm^2. For the pressure calculation we need the force part for the penetration of Equation (11.19_v), in accordance with the energy law. At

the phase transition onset position, the $W_{indent1}/W_{applied1}$ ratio is 0.4756/0.67704 = 0.70247. Therefore, also $F_{Nindent1}/F_{Napplied1}$ = 0.70247. When this factor is multiplied with the whole force of 10.703 mN one obtains the force at the phase-transformation onset that is only responsible for the penetration and calculates to 7.5185 mN. The penetration force/area is thus 2.331 or 2.298 mN/µm^2 (which is better known as GPa). We do not decide which of the two surfaces give the better value, but upon rounding both read 2.3 GPa. The almost perfect correspondence of this pressure value with much more difficultly obtained hydrostatic anvil pressurization results is discussed in Section 11.6.

11.5 COMPARISON OF THE PYRAMIDAL AND SPHERICAL INDENTATIONS ONTO GERMANIUM

It is certainly more precise to indent with diamond indenters like for example with Berkovich indenter, the smooth diamond faces of which are everywhere uniform. Its inevitable tip rounding ends at the very low $h_{cone} = R(1 - \sin 70.3)$ and it is mostly hidden within the diverse surface effects that are abandoned. Conversely, ideal spherical diamond tips require more expertise at their production and control of a constant radius for a certain guarantied height. Such radii are not very precisely known and hardly reproducible. The next difference is the penetration mathematics that is very easy for cones, pyramids, and wedges, but more complicated for spheres. These questions could be answered now with the Equation (11.18) and Equation (11.19). Different are the penetration depths with pyramids and spheres. The kink values of the phase-transitions for Berkovich are 4.149 mN at 0.151 · 0.8 µm (Equation (11.8_v)) and for the sphere 10.703 mN at 0.124 · 0.70247 µm [Equation (11.18), we must here use the penetration force]. The corresponding $W_{indent1}$ values are at 0.10736 mN and 0.4756 µm for Berkovich and sphere, respectively. Also, the comparison of the corresponding phase-transition energies of 0.2487 and 1.6217 mNµm shows that we cannot clai m without further data that these phase-transitions did produce the sa me polymorph. The Berkovich should have reached a much deeper penetra tion depth than the sphere and the values of W_{indent} and $W_{transition}$ better comparabl e. It
might be twinning of germanium as had been suggested in [19] for the Berkovich. Unfortunately, we could not analyze the smoothness-lacking multi load-unload curves of [19] up to 40 mN so that we probably missed the force for the more demanding phase-transition, as it was reached for the sphere. Furthermore, the lower force for twinning at low depths of the sphere, could have been lost due to zero-point problems at the start and extremely large R/h values of Equation (11.19) at very low force. This is a disadvantage of spherical indentations. Low energy phase-transitions must be detected with pyramidal indentations. On the other hand, high energy phase-transitions are easier with ideal spheres at lower depths. We detected here two phase-transitions with different transition energies for germanium, the further characterization of these requires X-ray diffraction or more advanced spectroscopic techniques.

11.6 COMPARISON OF THE SPHERICAL INDENTATION WITH RESULTS FROM ANVIL PRESSURIZING OF GERMANIUM

An important advantage of the sphere calotte geometry is its flat πr^2 area value that is very similar to the one of the $2\pi Rh$ cap area at low depth (here 3.226 and 3.272 μm^2, respectively). One calculates reliable force over area pressure values ($mN/\mu m^2$, better known as GPa). These do not contain the errors of extensive simulations for ISO hardness for indentations in [7] by assuming pristine standards by denying the phase-transitions that had occurred at their loads, not to speak of the numerous further technical errors as revealed and listed in [21]. The present spherical onset force at F_{Nkink} = 10.703 × 0.70247 mN gives 2.321 or 2.298 $mN/\mu m^2$ (GPa) transition pressure when divided by the penetration area at the phase-transition onset (Section 11.4). This pressure value is smaller than those of the most cited anvil experiments that require about 8 to 11 GPa, depending on the hydrostatic purity of the pressure transfer in [22]. That seems to exclude in the present spherical case a transformation of Ge-I (cubic, diamond, Fd3m) into non-quenchable Ge-II {(tetragonal, space group $I4_1/amd$, ß-tin)}. But one has to consider that Ge-III (body centered tetragonal) is formed from Ge-II in the anvil case upon pressure release from 12 - 14 GPa down to 7.6 GPa and lower, where it thermally reverts to Ge-I and Ge-III. Very important in this respect is the long-time (weeks) anvil-pressurizing of Ge-I at 2.5 GPa to obtain Ge-III at room temperature. This is known since 1965 [23] and has been confirmed in [24]. This value corresponds very well with the rapidly reached phase-transition pressure value of 2.3 GPa by spherical indentation. We conclude that there was enough pressure for the phase-transition under the sphere to yield the Ge-III polymorph. But we cannot exclude that this might have occurred via Ge-II that thermally diverted rapidly to Ge-I and Ge-III at the pressure of 2.3 GPa. Both anvil and spherical indentation techniques require X-ray diffraction analyses. Indentation is much easier and probably more precise than anvil pressurizing.

11.7 CONCLUSIONS

This paper compares the mathematical descriptions of conical, pyramidal and wretched indentations with the spherical ones and it numerically exemplifies them with literature data from germanium. The geometrically based mathematical deductions result in arithmetic formulas and application equations. Unprecedented applications are developed. The physically correct formulas are up to replace the false formulas of ISO 14577 that rely on false premises that are still violating the energy law by using elastic theory and iterated projected (contact) area. We therefore urgently ask to abandon historical beliefs. ISO 14577 still standardizes incorrect standards and procedures that do not match with reality. The reasons for the inconsistencies for more than a century are unrepeatable extremely complicated “mathematical deductions”. In addition to that ISO-ASTM use experimentally false standards not only due to not considering phase-transitions under load—that they cannot detect with their false formulas—, but also with poor force linearities and mix-ups of the standards. It is therefore clear that they could not create valid closed equations for indentations.

Rather the false belief required numerous iterations, approximations, data-adjustments, and simulations. Any control of experimental data had been impeded and did not occur in the mainstream. It produced false thinking and encouraged various data manipulations. Some striking examples are challenged in [10] and [21]. These can only now be easily detected and often corrected by using our mathematically correct closed equations. We sincerely advocate to after all accepting the easiest application of geometry and arithmetic calculation rules for the correct analyses of indentation data.

We complete and extend in this paper the geometric solutions for conical, pyramidal, wedged and spherical indentations by physically sound use of the indenter volume for the coupled pressure and penetration events and we deduce valid formulas and application equations. The calculation of the energies and transition energies of phase transitions upon indentation with the Berkovich indenter is calculated in the usual way as in [11,15,17,18,21] up to 16 mN load. It confirmes the loading curve $F_N = k\,h^{3/2}$ from [16].

The unfortunately still worldwide accepted ISO and Johnson equation for spherical indentations ("$P = 4/3\,E^* R^{1/2} h^{3/2}$") has again been disproved with a trial Kaupp-plot F_N vs $h^{3/2}$ that is not linear.

The spherical loading curve does not at all proceed as a one exponent parabola, because the volume of the sphere calotte $V = h^2\pi(R - h/3)$ can be transformed into $V = h^3\pi(R/h - 1/3)$ by multiplication with 1 = h/h. In correspondence to the deduction of Equation (11.4) into Equation (11.8) [16] one obtains (11.19) as the plottable equation with a point by point variable dimensionless correction term. It provides the materials constants k_{s1} and k_{s2} (mN/µm$^{3/2}$) and the onset values of the phase-transition at the intersection of the regression lines. For the energetic terms one transforms Equation (11.19) into Equation (11.20) $F_N = k_s\pi R h^{1/2} - k_s\pi h^{3/2}/3 + \Delta F$ for the integrations by taking care of their ranges to obtain the indentation energies $W_{indent1}$ at the intersection point and $W_{indent2}$ at an arbitrary point. The chosen point must be the same for the full applied work (full $W_{applied} = 0.5F_{N2}h_2$). The unprecedented phase-transition energy $W_{transition}$ is then simply the balance of full $W_{applied}$ minus ($W_{applied1}$ + $W_{applied2}$).

The unprecedented indentation energy and the phase-transition energy also for spherical indentations enabled the comparison of Berkovich indentations with spherical ones. This was only possible with the penetration and thus also with the corresponding $W_{indent1}$ values. Only these are comparable and the spherical $W_{applied}/W_{indent}$ ratios are depth dependent.

The indentations onto germanium were exemplified and the outcome is different with Berkovich at 4.149 mN load and with 42 µm sphere radius at 10.703 mN load. These are different phase-transitions. The low energy transition (most likely twinning) must have been lost in the spherical case where one detects the Ge-I into Ge-III transition.

Importantly, the spherical indentation reveals a reliable pressure calculation for the comparison with published hydrostatic anvil results, because the flat calotte

surface at the low penetration depths is only slightly smaller than the cap surface (here 1.4%). The average calculated force/μm^2 value of the phase-transition pressure amounts to 2.3 mN/μm^2 (GPa) in excellent correspondence with the published anvil value of 2.5 GPa. These results support the interpretation of the hydrostatic and long questioned anvil results. Such now possible comparisons are very rewarding.

The presented geometric results are not only comprehensive for academia, but the search for phase-transition onset and energy under load is of immense importance for practical applications and safety, because polymorph interfaces are prominent sites of cracking and crashing as imaged in [17]. False historical science must urgently be abandoned for the sake of sound mathematics with undeniable calculation rules. This helps in minimizing the risk for catastrophic crashes. One must now apply the geometry-based indentation in addition to the macroscopic pulling and bending tests. Indentations on the geometric mathematical basis is the only way for detecting materials' phase-transition onsets and energies and temperature-dependent including activation energies [25]. The phase-transition onsets for stressed materials must be well above the highest imaginable stresses when they are at work. The search for them is indispensable. This includes the physical indentation control after long stress exposure terms, because a good phase-transition onset can become worse, as material grain structures can change by various influences. There are certainly liability problems, but it's up now for an urgent revision of the still obligatory ISO 14577 standards that enforce false "State-of-the Art" techniques to certification agencies and from them to the producing industries. That is world-wide required for the sake of daily security, not only for the aviation.

COMPETING INTERESTS

Author has declared that no competing interests exist.

REFERENCES

1. Boussinesq, J. (1885) Applications des Potentiels a l'Etitude de l'Equilibre et du Mouvement des Solides Elastiques, Gauthier-Villiars, Imprimeur-Libraire, Paris; Book digitized by Google from the library of the University of Michigan and uploaded to the Internet Archive by user tpb. Openlibrary edition OL20553862M.
2. Hertz, H. (1882) On the Contact of Rigid Elastic Solids and on Hardness 1882. Macmillan and Co., New York. https://archive.org/details/cu31924012500306
3. Hertz, H. (1896) On the Contact of Rigid Elastic Solids and on Hardness 1896. Macmillan and Co., New York. https://archive.org/details/cu31924012500306
4. Love, A.E.H. (1939) Boussinesq's Problem for a Rigid Cone. The Quarterly Journal of Mathematics (Oxford), 10, 161-175. https://doi.org/10.1093/qmath/os-10.1.161

5. Sneddon, I.N. (1965) The Relation between Load and Penetration in the Axisymmetric Boussinesq Problem for a Punch of Arbitrary Profile. International Journal of Engineering Science, 3, 47-57. https://doi.org/10.1016/0020-7225(65)90019-4
6. Johnson, K.L. (1985) Contact Mechanics. Cambridge University Press, Cambridge. https://doi.org/10.1017/CBO9781139171731
7. Oliver, W.C. and Pharr, G.M. (1992) An Improved Technique for Determining Hardness and Elastic Modulus Using Load and Displacement Sensing Indentation Experiments. Journal of Materials Research, 7, 1564-1583. https://doi.org/10.1557/JMR.1992.1564
8. Sangwal, K., Gorostiza, P., Servat, J. and Sanz, F. (1999) Atomic Force Microscopy Study of Nanoindentation Deformation and Indentation Size Effect in MgO Crystals. Journal of Materials Research, 14, 3973-39829. https://doi.org/10.1557/JMR.1999.0537
9. Kaupp, G. and Naimi-Jamal, M.R. (2004) Nanoscratching on Surfaces: The Relationships between Lateral Force, Normal Force and Normal Displacement. International Journal of Materials Research, 95, 297-305. https://doi.org/10.3139/146.017952
10. Kaupp, G. (2019) The Loading Curve of Spherical Indentations Is Not a Parabola and Flat Punch Is Linear. Advances in Materials Physics and Chemistry, 9, 141-157. https://doi.org/10.4236/ampc.2019.98012
11. Kaupp, G. (2020) The Use of Geometry Leads to Easy Mathematical Solutions of Indentations. Advances in Materials Physics and Chemistry, 10, 77-95. https://doi.org/10.4236/ampc.2020.103007
12. Jin X, Li P, Borodich FM. Indentation tests of biological materials: Theoretical aspects. Contact problems for soft, biological and bioinspired materials. 2022:181-98.
13. Kovář J, Fuis V, Čtvrtlík R, Tomáštík J. The discrepancy between the indentation curves obtained by the finite element method calculation with a Berkovich and a conical indenter. Journal of Materials Research. 2022 May 9:1-2.
14. Nikas GK. Approximate analytical solution for the pile-up (lip) profile in normal, quasi-static, elastoplastic, spherical and conical indentation of ductile materials. International Journal of Solids and Structures. 2022 Jan 1;234:111240.
15. Kaupp, G. (2013) Penetration Resistance: A New Approach to the Energetics of Indentations. Scanning, 35, 392-401. https://doi.org/10.1002/sca.21080
16. Kaupp, G. (2016) The Physical Foundation of $F_N = k\ h^{3/2}$ for Conical/Pyramidal Indentation Loading Curves. Scanning, 38, 177-179. https://doi.org/10.1002/sca.21223
17. Kaupp, G. (2018) Six Polymorphs of Sodium Chloride Upon Depth-Sensing Scanning Macroindentation with Unusual Long-Range Cracks Requiring 30 N Load. Journal of Material Sciences and Engineering, 7, 473-483. https://doi.org/10.4172/2169-0022.1000473

18. Kaupp, G. (2019) Physical Nanoindentation: From Penetration Resistance to Phase-Transition Energies. Advances in Materials Physics and Chemistry, 9, 103-117. https://doi.org/10.4236/ampc.2019.96009
19. Gogotsi, Y.G., Domnich, V., Dub, S.N., Kailer, A. and Nickel, K.G. (2000) Cyclic Nanoindentation and Raman Microspectroscopy Study of Phase Transformations in Semiconductors. Journal of Materials Research, 15, 871-879. https://doi.org/10.1557/JMR.2000.0124
20. Bradby, J.E., Williams, J.S., Wong-Leung, J., Swain, M.V. and Munroe, P. (2002) Nanoindentation-Induced Deformation of Germanium. Applied Physics Letters, 80, 2651-2653.https://doi.org/10.1063/1.1469660
21. Kaupp, G. (2019) Phase-Transition Energies, New Characterization of Solid Materials and Anisotropy. Advances in Materials Physics and Chemistry, 9, 57-70. https://doi.org/10.4236/ampc.2019.94006
22. Menoni, C.S., Hu, J.Z. and Spain, I.L. (1986) Germanium at High Pressures. Physical Review B, 34, 362-368.https://doi.org/10.1103/PhysRevB.34.362
23. Bates, C.H., Dachille, F. and Roy, R. (1965) High-Pressure Transitions of Germanium and a New High-Pressure Form of Germanium. Science, 147, 860-862. https://doi.org/10.1126/science.147.3660.860
24. Nelmes, R.J., McMahon, M.I., Wright, N.G., Allan, D.R. and Loveday, J.S. (1993) Stability and Crystal Structure of BC8 Germanium. Physical Review B, 48, 9883-9886. https://doi.org/10.1103/PhysRevB.48.9883
25. Kaupp, G. (2014) Activation Energy of the Low-Load NaCl Transition from Nanoindentation Loading Curves. Scanning, 36, 582-589. https://doi.org/10.1002/sca.21158

DISCLAIMER
This chapter is an extended version of the article published by the same author(s) in the following journal.
Advances in Pure Mathematics, 10: 322-336, 2020.

Chapter 12
Print ISBN: 978-93-5547-921-1, eBook ISBN: 978-93-5547-922-8

Erratum to "Valid Geometric Solutions for Indentations with Algebraic Calculations"

DOI: 10.9734/bpi/mono/978-93-5547-921-1/CH12

ABSTRACT

The original online version of this article (Gerd Kaupp 2020) Valid Geometric Solutions for Indentations with Algebraic Calculations, (Volume, 10, 322-336, https://doi.org/10.4236/apm.2020.105019) needs some amendments and clarification.

12.1 THE DEDUCTION DETAILS FOR THE SPHERICAL INDENTATIONS EQUATION

The incorrect proportionalities (16) and (17) in the published main-text are useless and we apologize for their being printed. They were not part of the deduction of the Equation (18_v). The deduction of (18_v) follows the one for the pyramidal or conical indentations (4) through (8). The only difference is a dimensionless correction factor $\pi(R/h - 1/3)$ that must be applied to every data pair due to the calotte volume. The detailed deduction of (18_v) = (6S), is therefore supplemented here.

Upon normal force (F_N) application the spherical indentation couples the volume formation (V) with pressure formation to the surrounding material + pressure loss by plasticizing (p_{total}). One writes therefore Equation (1S) (with m + n = 1)

$$F_{\mathrm{N}} = F_{\mathrm{N}v}^{m} F_{\mathrm{N}p-\mathrm{total}}^{n} \tag{1S}$$

There can be no doubt that the total pressure depends on the inserted calotte volume that is $V = h^2\pi(R - h/3)$. It is multiplied on the right-hand side with 1 = h/h to obtain (2S). We thus obtain (3S) and (4S) with n = 1/3.

$$V = h^3\pi(R/h - 1/3) \tag{2S}$$

$$F_{\mathrm{N}p\mathrm{total}} \propto h^3 \tag{3S}$$

$$F_{\mathrm{N}p\mathrm{total}}^{1/3} \propto h_{p-\mathrm{total}} \tag{4S}$$

(4S) with pseudo depth "$h_{p\text{-total}}$" is lost for the volume formation. It remains (5S) with m = 2/3 on F_{Nv} or the exponent 3/2 on h_v.

$$F_{\mathrm{N}v}^{2/3} \propto h_v \text{ or } F_{\mathrm{N}v} \propto h_v^{3/2} \tag{5S}$$

The proportionality (5S) must now result in an equation by multiplication with the dimensionless correction factor $\pi(R/h - 1/3)$ and with a materials' factor k_v (mN/μm$^{3/2}$) to obtain Equation (6S) that is Equation (18) in the main paper.

$$F_{\mathrm{N}v} = k_v h^{3/2} \pi(R/h - 1/3) \tag{6S}$$

For plotting of (6S) for obtaining k_v the $\pi(R/h - 1/3)$ factor is separately multiplied with $h^{3/2}$ for every data pair.

An additive term F_a can be necessary for the axis cut correction if not zero due to initial surface effects of the material.

COMPETING INTERESTS

Author has declared that no competing interests exist.

DISCLAIMER
This chapter is an extended version of the article published by the same author(s) in the following journal.
Advances in Pure Mathematics, 10, 545-546, 2020.

Chapter 13
Print ISBN: 978-93-5547-921-1, eBook ISBN: 978-93-5547-922-8

Study on Real and Fitted Spherical Indentations

DOI: 10.9734/bpi/mono/978-93-5547-921-1/CH13

ABSTRACT

The physically accurate mathematical formula and its integration, which take into consideration the radius over depth changes upon penetration, are used to assess spherical indentations that rely on the original date. For germanium, zinc-oxide, and gallium-nitride, linear plots, phase-transition onsets, energy, and pressures are obtained algebraically. Low pressure phase transitions can either be resolved by hydrostatic anvil onset pressures or they cannot. By comparing the polymorph structures to known structures from pulsed laser deposition, molecular beam epitaxy, and twinning, makes it possible to attribute the polymorph structures. The easiest method for creating and characterising polymorphs that are now available in pure form under diamond calotte and in contact with their equivalent less dense polymorph is to use a spherical indentation. Loading curves from experimental data are needed to account for the novel outcomes and new opportunities, which open-up new horizons for the synthesis of new polymorphs, not available under anvil pressurization. These are now easily distinguished from data that are “fitted” to make them concur with widely used unphysical Johnson’s formula for spheres (“$P = (4/3)\ h^{3/2}R^{1/2}E^{*}$”) not taking care of the *R/h* variation. Its challenge is indispensable, because its use involves even published “fitting equations” for making the data concur. These misleading reports (which do not include any "experimental" data) offer risky incorrect moduli and ideas. For PDMS, GaAs, Al, Si, SiC, MgO, and Steel, the fitted spherical indentation reports with radii ranging from 4 to 250 m are identified. Characteristic elements are revealed by the thorough analysis.

Keywords: Spherical indentations; correct formula; phase-transition onset pressure; false Johnson formula; detection of data fittings.

13.1 INTRODUCTION

H. Hertz did not specify the spherical indentations; instead, he simply reasoned that the pressure of a contacting sphere is proportional to the "impact" area/3, but not to the depth (h) of the indentation [1,2]. All researchers engaged attempted to use "elastic theory" with regard to the area after taking the penetration depth into account (but not to the volume). With hundreds of complex equations and a variety of the most advanced mathematical procedures, the unusable mathematical formalism became so complex that it appeared to be readable only to highly skilled mathematicians. Also, Sneddon reported in 1965 a still very complicated hardly usable multi-term and multi-exponent equation in [3] that was

forgotten, when Johnson in 1985 presented his simple (but false) " $P = (4/3)h^{3/2}R^{1/2}E^*$ " formula for spherical indentations [4]. It offered a straightforward analysis, a shortcut to the smaller "Young's modulus," and an escape from extremely difficult math. This received widespread recognition and was later incorporated into the ISO 14577 standard. This formula was thus used by most authors for spherical indentations by citing [1,2,4] without checking content and validity. That is rather strange, because the experimental data of spherical indentations exclude the validity of this formula and every simple circle directly shows its incorrectness: it does not consider the enormous *R*/*h* changes during the penetration. For example, the *R*/*h* ratios in [5] vary from >1500 to 20 (for h_{max} = 20 nm) or from >480 to 50 (for h_{max} = 3.6 µm (Chapter 9). Every researcher should have immediately seen that any *R*/*h* term is missing in Johnson's formula and that a cone or a pyramid behaves different from a sphere. The second obvious error is claiming "Young's modulus" that is a unidirectional property, totally different from an indentation modulus. A very complex "equation for fitting" of the depth values is published as equation (9) in [6]:

$$\delta - \delta_{\text{contact}} = a_0^2/R\,\{[1 + (1 - P/P_{\text{adh}})^{1/2}/2]\}^{4/3} - 2a_0^2/3R\,\{[1 + (1 - P/P_{\text{adh}})^{1/2}/2]\}^{1/3}$$

The δ in [6] is penetration depth; *P* is "load" (force). The "fit parameters" are a_0 and P_{adh}. This data-falsification is published in [6] together with a series of crazy modulus values, relying on them. Related other fitting equations might also be in use. Only few authors published true experimental data of spherical indentations. These publications will be analyzed and the wealth of their loading curves is used in Section 13.4 on the basis of the physically and mathematically correct Equation (1), as deduced in [5,7]. These honest papers concentrate on Bradby's group of 2002 (e.g. [8]). Correct data for Ge, ZnO, and GaN will be analyzed and compared with hydrostatic anvil pressurizations. Several by fitting falsified spherical indentations from peer reviewed publications will be analyzed in Section 13.4 They are largely prevailing and all of them are worthless in all respects. But we present easy and strict methods to sort them out. Some updates in this area are accessible elsewhere and can attract the readers' attention [9-11]. But these authors use very complicated fittings, iterations, and simulations instead of starting with the long known undeniable course of spherical indentations (Formula (1) as cited from [5] and [7]. And they do not detect any phase-transformation. Furthermore, the use of unidirectional "Young's modulus" for the simulation of the loading curve to result in the false Johnson equation is incorrect. The data fitting for concurring with it are severe falsification. The therefrom determined "Young's moduli" are dangerously misleading. The enormous trouble when Young's moduli are equalized with indentation moduli has been amply exemplified in [12]. The publication of moduli from "fitted" data [6] adds another aggravation to these problems. The unsound theories that emerged from falsified data are, of course, also completely worthless. The purpose of this work is to ask Authors, Peer Reviewers, and Editors to reject papers that use data that are falsified by data-fitting. Unfortunately, such publications are the basis of certificates for industries, from which these must not deviate. Therefore, numerous false materials' properties create a daily risk for failure upon mechanical stress [5,13]. Our sorting out techniques below for recent false reports, are clearly developed in this paper. They shall help to repeat the

mechanical characterization with true experimental data, when these are unavailable from the recent authors for genuine publications. Falsified results must no longer be used. The below cited and further authors of falsified reports on spherical indentations obtain the possibility to revisit their published data and the connected non-physical theories. The publication of their experimental data for obtaining correct important materials' properties will be highly welcomed. The false theories and the severe risks from incorrect mechanical properties of technical materials in daily life must be removed.

13.2 METHODS

The loading data of the materials are taken from the published curves that were enlarged to A4 size. The cone depths were checked with $h_{cone} = R\ (1 - \sin\beta)$ where β is the half angle of the cone and R the sphere radius. When pop-ins was present these were repaired [13]. 20 data points were used and pocket calculator with10 decimals. The results are suitably rounded in text and Table 1. The calculations according to the Equation (13.1), Equation (13.2), and Equation (13.3) or the arithmetic routines including the energy correction are comprehensibly published in [7]. The r-values for the immersed calotte area are easily available by the combined use of $\sin\alpha = (R - h/R)$ and $\cos\alpha = r/R$. The analysis of the spherical loading data used Equation (13.1) [5,7]. The indentation work W_{indent} results from the integrated Formula (2) [7]. The detection of data fittings was with plots of the published data according to the Equations (13.1) and (13.3) [14], even though (13.3) is only valid for pyramidal and conical indentations and would correspond to the false often cited Johnson's equation that must be denoted here as an inequality $F_{Ns} \neq (4/3)h_s^{3/2}R^{1/2}E^*$.

$$F_{Ns} = k_s \pi h_s^{3/2}(R/h_s - 1/3) \tag{13.1}$$

$$W_{indent} = 2/3 \cdot k_s \pi R h_s^{3/2} - 2/15 \cdot k_s \pi R h_s^{5/2} + \Delta F_{as} h_s \tag{13.2}$$

$$F_{Npy} = k_{py} h_{py}^{3/2} + F_{apy} \tag{13.3}$$

The indices in the Equations (13.1) (13.2) (13.3) are N for normal, s for spherical, a for axis cut when not zero, and py for pyramidal or conical.

The area of the immersed calotte for the onset of the phase-transition pressure calculations is given by its flat surface (πr^2) or by its cap surface ($2\pi Rh$). The radius r is easily obtained by the combination of $\sin\alpha = (R - h)/R$ and $\cos\alpha = R/r$ when looking at the geometric situation for the penetration of the calotte from the sphere with radius R [5].

13.3 RESULTS AND DISCUSSION

13.3.1 Germanium Spherically Indented

The spherical indentation analysis of germanium [7],[8] is reported here for comparison with the further examples in Table 1. Figure 1 provides the basic data from the F_N vs $\pi h^{3/2}(R/h - 1/3)$ plot and by using Equations (13.1) and (13.2). It shows the penetration resistances k_1 and k_2 as the slopes for the two phases up to 50 mN load.

Table 13.1. Mechanic and energetic data of spherical indentations (R = 4.2 µm) onto Ge, ZnO, and GaN that are reasonable rounded

Material	F_{Nkink} (mN)	h_{kink} (µm)	W_{indent} (mNµm)	$W_{applied}$ (mNµm)	full W_{appl}	$W_{transition}$ (mNµm)	Areas: $\pi r^2/2\pi Rh$ flat/cap	$_{transition\text{-}onset}$ mN/µm^2 (GPa)
Ge[a)]	10.7029	0.1243	0.4756	6.80929	10.9251	4.1158[b)]	3.226/3.272	2.331/2.298
ZnO	22.3800	0.22059	2.16661	7.54011	14.6431	7.1030[c)]	5.6684/5.8212	3.7325/3.6344
ZnO	56.6290	0.51716	11,0579	15.8916	26.4440	10.552[d)]	12,807/13.648	4.0438/3.7948
GaN	38.8406	0.1455	2.12467	12.3876	22.8151	10.428[e)]	3.7731/3.8397	10.294/10.116
GaN	118.397	0.3854	24.7506	33.8652	59.7898	25.925[f)]	9.7038/10.171	12.201/11.641

[a)]Data taken from [7]; [b)]up to 50 mN; [c)]up to 56.6 mN; [d)]up to 100 mN; [e)]up to 117.5 mN; [f)]up to 250 mN.

The phase-transition onset of Fig. 13.1 is at 10.703 mN. The energetic data give the indentation work W_{indent} = 0.4756 mNμm and the transition energy $W_{transition}$ = 4.1157 mNμm, as calculated up to 50 mN load. The transformation pressure is also calculated to give the good correspondence of 2.3 GPa with the anvil pressurizing phase-transition at 2.5 GPa. A nevertheless published trial plot in [7] with F_N vs $h^{3/2}$ (not shown here) for excluding the sole $h^{3/2}$, as prescribed by ISO standards and false Johnston's formula, for spherical indentations gave a convex plot instead of linearity. Fig.13.1) repeats the correct plot according to (13.1) and reveals a prominent endothermic phase transition. A further endothermic phase-transition is already indicated at the end of the second straight line, subject to investigation at higher loads.

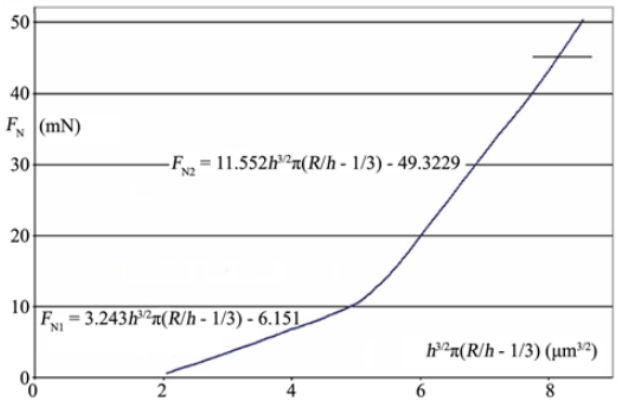

Fig. 13.1. Normal force vs $\pi h^{3/2}(R/h - 1/3)$ plot of a spherical indentation (R = 4.2 μm) onto germanium, showing the required linearity (regression lines not drawn) and the kink of the Ge-I to Ge-III transition; linear regression equations are inserted; image taken from [7]

13.3.2 Zinc Oxide Spherically Indented

The spherical indentation onto ZnO with wurtzite structure follows Equation (13.1) and it reveals two phase-transitions. The analysis had to be performed after repair [13] of the published pop-ins in [15]. The plotted data are in Fig. 13.2, where the included regression data are the basis for the calculations.

The spherical indentation onto ZnO exhibits two phase-transitions, distinguishing 3 polymorphs in the force range up to 100 mN load, as revealed with the plot by application of Equation (13.1) to the published original load-depth data. The inserted linear regression equations are the basis for the calculation of the energetic terms and the pressure data in Table 13.1.

13.3.3 GaN Spherically Indented

The spherical indentation onto a GaN epilayer (R = 4.2 μm) was reported in 2002 [16] and the analysis (after pop-in repair [13]) with Equation (13.1) gives the

linear plot with two phase-transitions (three linear branches) as shown in Fig. 13.3. These published F_N vs h curves represent original, not data-fitted, data.The inserted regression formulas allow for the calculation of the onset forces, the energetic terms, and onset pressures in Table 13.1.

The more recent spherical indentation onto a single crystal of GaN [17] cannot be compared. Unfortunately, the analysis of these data with Equations (13.1) and $F_N \propto h^{3/2}$ for cones and pyramids using the techniques for the various further materials in Section 13.4 shows that these published depth data are fitted according to the ISO14577 standard to concur with the disproved Johnson's formula. These data and conclusions are totally at variance. It would be nice to see the original untreated data. Unfortunately, numerous more recently published spherical loading curves are data-fitted and follow the unphysical formula of ISO and Johnson. It is therefore very important to check the validity with our plots for not being mislead. I can only discuss some of these here. It could be that the published data-fitting formula or related ones are inserted into more recent instrumented indenter's software, so that data-fitted F_N - h curves directly ensue (see also Chapter 11). The here deduced formulas should be used by the users to check for it and try to obtain and publish unfitted original data.

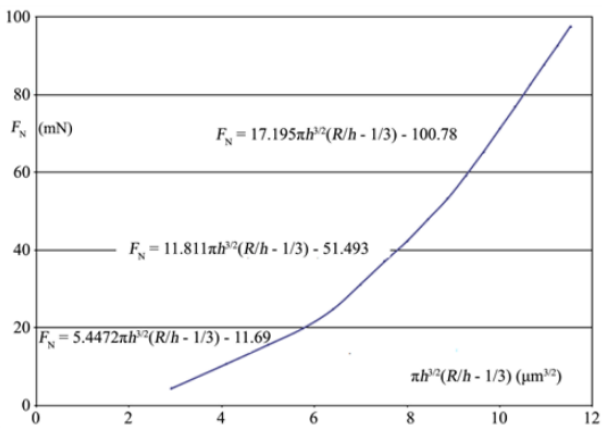

Fig. 13.2. Normal force vs $\pi h^{3/2}(R/h - 1/3)$ plot of a spherical indentation (R = 4.2 µm) onto ZnO; data taken from Fig. 1 in [15] after repair of the pop-ins [13]; linear regression equations are inserted; kink positions in Table 13.1

13.3.4 Comparison of the Results from Ge, ZnO, and GaN

The results with Ge, ZnO, and GaN are compared in Table 13.1.

These materials cover maximal loads that are 50 mN for Ge, 100 mN for ZnO, and 250 mN for GaN. More phase-transition onsets are to be expected at higher

loads. The force for the first phase-transition onset describes the sensitivity of the materials for their stability with respect to mechanical interactions. It is equally reflected by the sequence of the penetration resistance values k_1 (physical hardness) in Figs. 13.1-13.3. The penetration depth values are not in the same sequence and neither so the first indentation work that are required for reaching the transition onset. But the transition work values are for the first and second transition of ZnO and GaN in the same sequence as the F_{Nkink} values. The data reflect the situation of spherical indentations with the same radius covering one or two phase-transitions per sample. The depths are always very low. The results are calculated from 0 to kink, from kink to kink, and from kink to the maximal force. The transition-energy and the onset pressure values can also be calculated for every force of interest, but they cannot be normalized per force as in the pyramidal case. The energy law requires multiplication of the phase-transition F_{Nkink} values with $W_{indent}/W_{applied} = F_{Nindent}/F_{Napplied}$ [7,18] when only the penetration is addressed, for obeying the energy law. The advantage of experimental spherical indentations is the reliable pressure calculations at the transition onsets. The close similarity of flat surface and cap surface for the low depths is very favorable. It allows the comparison with hydrostatic pressurizing and new insights are therewith achieved.

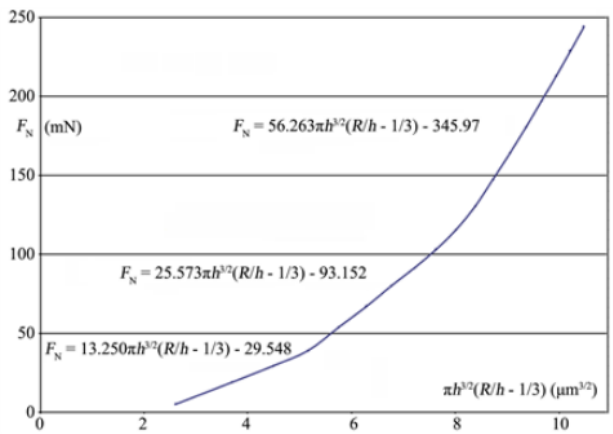

Fig. 13.3. Normal force vs $\pi h^{3/2}(R/h - 1/3)$ plot of a spherical indentation (R = 4.2 μm) onto GaN; data taken from Fig. 1 in [16], showing the required linearity and the kinks for two phase-transitions, ready for the calculation of the results in Table 13.1; kink positions in Table 13.1

13.3.5 Comparison of the Spherical Indentation with Hydrostatic Pressurizing Data and with Synthesized Polymorphs

The pressure data of germanium has already been compared with anvil pressure as combined with X-ray diffraction date. The low anvil pressure of 2.5 GPa required enormous effort for being detected and was long disregarded, as outlined and discussed in [7]. It corresponds with the onset pressure of 2.3 GPa

in Table 13.1. The present analysis of the spherical indentation is by far easier than anvil experiments but we profit from the X-ray proof for the low-pressure GeI to GeIII phase-transition in a highly rewarding manner. The pressure values for ZnO in Table 13.1 up to 100 mN load are not large enough for the B4 to B1 (NaCl-type) transition, because the hydrostatic pressure for that phase-transition are reported to start at 9 GPa [19] or 9.8 GPa [20]. There are numerous reports on theoretically calculated caged ZnO polymorphs [21] that are not better space-filling than the wurtzite structure (B4) of these materials and need not to be considered here. The theoretical calculations of 7 bulk polymorph structures of ZnO with respect to expected optical properties is also not helpful, because these lack density predictions [22] and none of these possible structures have been found by anvil pressurizations. The difficulties with resolving low pressure transitions under anvil are already discussed above with germanium. There remain the zinc-blende (=sphalerite) B3 phase and formations of twinned polymorphs. The more highly pressurized of these (onset at 4 GPa) is most likely the (B3) phase of ZnO that could already be epitactically grown on (001) of GaAs on a ZnS substrate at 500°C. The growth of the film was by metalorganic molecular-beam epitaxy with diethylzinc + O_2, "using electron cyclotron resonance plasma source to excite high density oxygen plasma with low-ion energy of 10 - 20 eV". The lattice constant of 4.463 ± 0.015 Å was obtained from the RHEED (high-energy electron diffraction) pattern [23,24]. The fact that the growing of the film succeeded indicate that the pressure for its formation must be rather low. We can thus confidently claim having detected the first synthesis technique for the bulk ZnO B3 polymorph under the diamond calotte cap for further investigation. It is provisionally attributed to the 4 GPa onset pressure. The spacious wurtzite tetrapod with its complicated twinned shape including legs, as obtainable from thermal "vapor deposition on a polymer decorated silicon substrate" [25], must be excluded. The high tendency of ZnO to form twin structures is known [26]. A ZnO twin had already been synthesized by pulsed laser deposition [26]. It can also be obtained by electro-deposition on indium doped tin oxide (ITO) [27]. Again, spherical indentation appears to be the easiest synthesis of this species. These attributions must be confirmed by on-site X-ray diffraction at a synchrotron, or spectroscopically. This will include their further characterization. The spherical indentation results of ZnO reveal that the hydrostatic anvil pressurizing experiments did not resolve these lower pressure phase-transitions. The almost uniform pressure distribution in the low depth spherical indentations is particularly suitable for the suggested investigations.

The GaN B4 phase (wurtzite) transforms upon hydrostatic pressurizing at 47 GPa into the GaN B1 phase (rock-salt) [28]. Another report found this transition pressure at 37 GPa [29]. These publications do not report on transitions at lower pressures that are again not remarked under anvil pressurizing. Thus, the B4 to B3 (zinc-blende = sphalerite) transition pressure was not known. The ab-initio calculations of [30] predict a pressure of 11.45 GPa for the B4 into B3 transition. This value is close to our 12 GPa value in Table 13.1 and we assign accordingly. Very interesting is our 10 GPa value in Table 13.1. When compared to ZnO this phase-transition occurs at 0.65 times the depth at 1.75 times the force and at 2.75 times the pressure. This may at first glance indicate twinning of GaN, but

why should that require so much force and pressure? Another attribution comes to mind: it could be the formation of the rhombohedral phase (R3m) of GaN that has recently be found in the B3 (zinc-blende, F-43m) phase of GaN epilayers, as grown on sapphire by molecular beam epitaxy [31]. This would prevent the twinning by pressurizing upon spherical indentation. Unfortunately, no energetics is available for the rhombohedral phase. The rhombohedral GaN (R3m) forms also via migration enhanced encapsulation growth by encapsulation between silicon and graphene [32]. It is thus easily formed. This would also support our attribution of the first phase-transition onset pressure of GaN to the rhombohedral polymorph with space group R3m. Clearly, experimental spherical indentation extends the knowledge from hydrostatic anvil pressurizing. Both assignments should be checked by Synchrotron X-ray diffraction together with the now far easier further analyses under the diamond calotte of these elusive and now easily available polymorphs.

13.4 CHALLENGE OF SIMULATIONS AND DATA-FITTING FOR SPHERICAL INDENTATIONS

It appears that after publication of the false Johnson's formula requiring an $F_N = 4/3 \cdot h^{3/2} R^{1/2} E^*$ relation, the ISO standard 14,577, several textbooks, and publications believed in it (Section 1). A first glance on that Formula (from the beginning in 1985) should have evidenced that it does not take into account the self-evident change of the *R*/*h* ratio during penetration. As the experimental data did not concur with the assumed $F_N - h^{3/2}$ relation for spheres, Authors did not hesitate to simulate spherical loading curves by using Young's modulus and Poisson's ratio of the material with e.g. the JKR procedures [33] to produce such relation. Thereafter, the experimental depths have been fitted to concur with it by using published "fitting formulas" (e.g. Equation (9) in [6] with "fitting parameters", as is written out in Section 13.1). That is in fact severe data-treatment. Related other fit-equations might also be in use. But most of the involved scientists stopped with publishing their experimental spherical indentation depths in favor of publishing "fitted depths".

They so avoided the inefficient formula for spheres from [3] and credulously thought to have a simple means for direct determination of the reduced elastic modulus. When doing so they agreed with data manipulation, not recognizing that it was against scientific ethics or practical value. However, anonymous Referees and Editors of books and papers did not stop such data treatments. There were though the important correct publications with Germanium, ZnO, and GaN from 2002 that are cited and successfully analyzed in Section 3. These pioneering papers contain experimental spherical load-depth curves that were apparently neglected, but they rightfully did not agree with Johnson's formula. So, we urge on their revival here.

The "fitting" of depth data is the creation of fake data for making them obey the falsely prescribed F_N vs $h^{3/2}$ relation for spherical indentations. That relation is however only valid for cones and pyramids [5,14]. It is more than misleading to unpardonably call the depth values in [6] "experimental data" instead of fitted

ones, as in their Figure 4 for a spherical (R = 200 or 192 µm) indentation onto PDMS. The exponent analysis according to $F_N \propto h^{3/2}$ gave a perfect straight line with a correlation R^2 = 0.9999 (no phase-transition seen!) [34]. This was already complained against in [5] (with apology for not expressively having criticized the false $F_N \propto h^{3/2}$ relation for spherical indentations in [34]). When the correct F_N vs $\pi h^{3/2}(R/h - 1/3)$ plot according to Equation (13.1) is applied to fitted spherical indentations onto materials, one obtains concave curves. That is imaged below for GaAs, Al, and Si. It is also typical for all the further analyzed materials in this Section 13.4 (including the fitted curve for GaN from [17] in Section 3.3). These plots are the most compelling proof of data-fittings. When data were fitted to concur with Johnson's formula they must, of course, provide straight lines when plotted according to Equation (13.3). Such trial plots indicate less sharply that the fitting had not completely wiped out any phase-transition unsteadiness. But one must not use such plots of manipulated data for phase-transition characterizing. It would be completely misleading to do so: we show with all of the analyzed examples in this Section 13.4 that one would always falsely claim exothermic behaviors while the phase-transitions are in in their correct physical indentation data endothermic.

It appears that most recently published spherical indentations were "fitted" to obey the incorrect Johnson's formula with its false promise to obtain "Young's moduli" values that are however also incorrect fake values, not to speak of the fact that Young's moduli are unidirectional moduli. Fortunately, we can easily distinguish valid from fitted invalid spherical indentation reports by simply checking their loading curves with plots according to the Equations (13.1) and $F_N \propto h^{3/2}$.

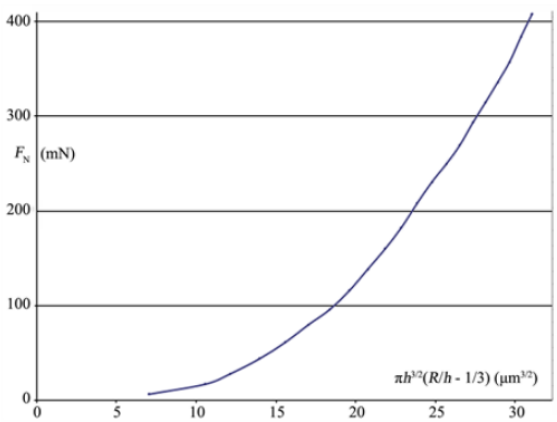

Fig. 13.4. Plot according to Equation (13.1) for spherical indentations of the published clearly fitted data as taken from [35] for a spherical indentation with R = 10 µm onto GaAs, proving the data fitting for concurrence with the disproved Johnson's equation, as no straight line ensued

We do not further deal here with the details of the JKR simulations [33] and the data-fitting techniques concerning the spherical indentations, because that is unscientifically false. Such data treating is dangerous and against scientific ethics. The falsified outcome will now be further exemplified with some unbelievably manipulated published loading curves of varied types. It is hoped that this somehow difficult task will help to positively develop this important field of materials' analyses.

13.4.1 Gallium Arsenide "Spherically" and Pyramidally Indented

The spherical indentation (R = 10 µm) of GaAs in [35] does not follow the equation for spherical indentations (13.1) and the Authors cited paper [4]. The analysis of the published loading curve—after repair of the "pop-in" in their Fig.1(a)—with Equation (13.1) for spheres does not give a straight line, but the concave curve of Fig. 13.4. This indicates the belief of the authors in Johnson's formula from 1985 and the application of a fitting procedure to the original loading data to concur with such formula.

Conversely, the application of $F_N \propto h^{3/2}$ for cones and pyramids as falsely claimed by Johnson to the data of [35] leads, after a short initial effect, to two straight lines, the first steeper as the second by forming a kink. This is shown in Fig. 13.5. The disproved Johnson's formula requires, of course, linearity with the exponent 3/2 on h for fitted spherical indentations. However, the so received putative exothermic event does not represent the endothermic phase-transitions of GaAs, and also the slopes are simulation and fitting-iteration artefacts without any value. There is thus a risk of pitfalls with linear plots using Equation (13.3) from loading curves published in the literature, because some of the phase-transition unsteadiness is not fully extinguished by the data-fitting of spherical indentations. It must therefore be clear that the authors' indenter specification was correct, when the phase-transition analysis comes out exothermic as in Figure 13.5. We must therefore note here, that our so revealed "exothermic phase-transitions" are from a faked data-fitted curve of [35]. The wealth of our double check deserves full appreciation, rather than criticism.

This data check proved the already complained data fitting. It appeared therefore necessary to compare the values in the caption of Fig. 13.5 with the ones from the correct analysis of Berkovich indention loading curves onto GaAs. These are taken from Fig. 1 in [36] at low penetration (up to 4.5 mN) and from Fig. 3(a) of [37] at high penetration (up to 600 mN). These genuine experimental curves were analyzed to yield kink points for endothermic phase-transitions at 2.517mN for loads up to 5 mN and 218 mN for loads up to 600 mN. The first of these with onset at 2.517 mN is not resolved at this loading range. The second of these loads in Fig. 13.6 starts pretty close to the one in Fig. 13.5, but the calculated mechanical data are principally different. The second branch is steeper than the first one, indicating the endothermic phase-transition with the onset (kink position) at 218 mN load and 1.40 µm depth. The normalized Berkovich indentation transition-energy with onset at 218 mN is endothermic at +0.161 mNµm/mN [this work], as deduced with $F_N \propto h^{3/2}$ for cones and pyramids and its

integration in [7,14]. Thus, the spherical indentation with R = 10 µm onto GaAs is a misleading fitting artifact showing again the data treatment in [35]. The importance of the argument deserves the printing of the Berkovich indentation analysis of the experimental result from [37] in Fig. 13.6.

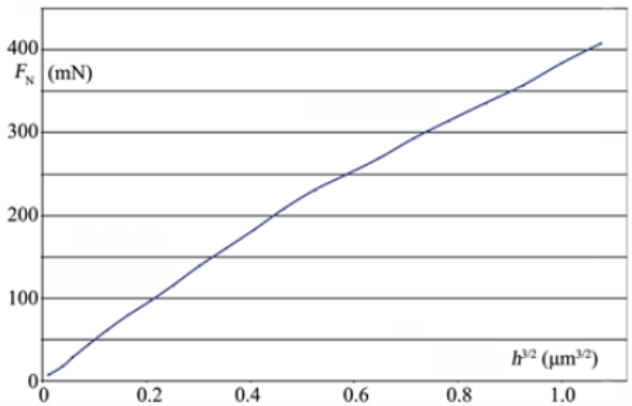

Fig. 13.5. Trial plot ($F_N \propto h^{3/2}$) with the data as in Fig. 13.4 from the spherical indentation (R = 10 µm) onto GaAs (100) with the clearly fitted data as taken from [35], showing after an initial effect two straight lines with trial regression lines of $F_{N1} = 433.6h^{3/2} + 6.6$ and $F_{N2} = 325h^{3/2} + 57.9$ mN that would falsely simulate an exothermic transition event with an onset at 213 mN and a here provisionally calculated impossible transition energy per mN of −0.101 mNµm/mN. This exothermicity is dangerously in error and the slopes in Fig. 13.5 have no physical meaning

Fig. 13.6 where $F_N \propto h^{3/2}$ is correct for the pyramidal indentations and the Kaupp-plot [14] proves undoubtedly that the phase-transitions of GaAs under load are endothermic.

As we present strong arguments, we must check whether further fitted spherical indentation exhibit the corresponding behavior.

13.4.2 Aluminum "Spherically" Indented

The analysis of the spherical indentation onto aluminum [38] reveals a similar outcome as with GaAs. The sphero-conical indenters are precisely described with a cone half angle of 45° and nominal radii of 10 µm and 5 µm. Scanning electron microscopic images indicated "well formed" radii of 8.5 and 5 µm down to depths of 2.5 and 1.5 µm, respectively. The nominal radius of 10 µm corresponds to h_{cone} = 2.93 µm. This is considerably larger than the maximal depth of <1 µm) for the indentation data of pure Al. Again, the analysis with Equation (1) for spheres does not give a straight line but the concave curve

of Fig. 13.7, which clearly indicates a data fitting for concurring with Johnson's formula and unfortunately ISO standard.

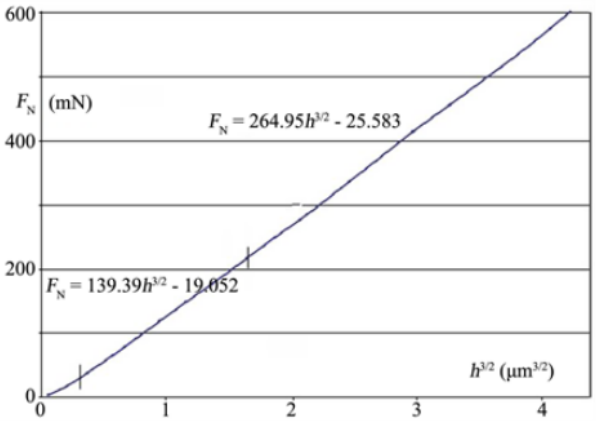

Fig. 13.6. Analysis with the Kaupp-plot ($F_N \propto h^{3/2}$) of the Berkovich indentation onto GaAs (data taken from Fig. 3(a) in [37]) showing after an initial unresolved part two linear branches with the inserted regression equations that both correlate with $R^2 = 0.9999$; the slopes of the pyramidal indentation in Fig. 13.6 are the penetration resistance values of the two polymorphs

The trial plot with $F_N \propto h^{3/2}$ to the spherical indentation in Fig. 13.8, using the same fitted data as for Fig. 13.7 is linear with after the extended initial effect two straight lines. These simulate an exothermic event, because the second branch has the lower slope. This is the false and dangerous result of the fitting error as above with GaAs (Fig. 13.5): the phase transition of aluminum under load is endothermic, as was already shown with Berkovich indentations onto aluminum in [34].

Again, the calculations of elastic moduli according to false Johnson's formula and its discussion are useless and misleading. The data fitting is again safely confirmed with Fig. 13.7 and Fig. 13.8. The previous branch is again steeper than the following one, simulating a false exothermic event. The known phase-transition of aluminium upon Berkovich indention has the endothermic phase-transition onset at close to 40 mN load (two different sources) [34]. The similarity with the above GaAs case repeats the falsifications by the fittings. Again, the falsified data for an $h^{3/2}$ loading parabola retain only the information that there must be a phase-transition at a similar force, as characterized with a Berkovich indentation.

Data fitting destroys the value of spherical indentation and excludes any use of them. "Fitted" data points must not be told or suggested as being "experimental" ones.

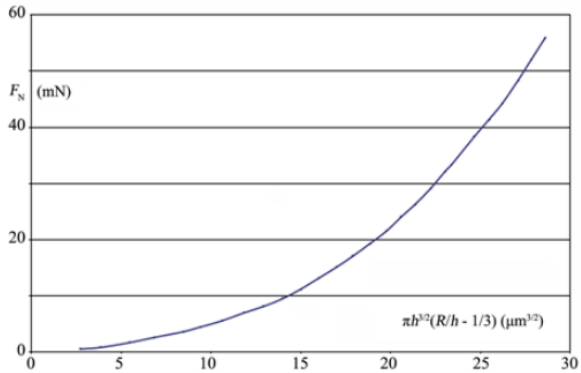

Fig. 13.7. Analysis of the published fitted data from the spherical indentation with a nominal radius of 10 µm onto pure aluminum according to Equation (1); data are taken from the upper data points of the multiple partial loading Fig. 13.12(b) in [38]; the concave bending does not agree with Equation (1) and proves the data-manipulation

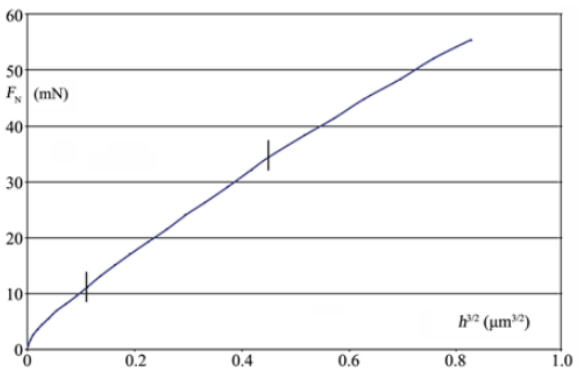

Fig. 13.8. Trial Kaupp-plot according to $F_N \propto h^{3/2}$ for the spherical indentation onto aluminium substantiating the undue "fitting" of the original experimental data; this plot appears as if it were the result of a conical or pyramidal indentation instead of a spherical one with R = 10 µm; after the initial effect (oxide and polishing) two extended straight branches with unsteadiness at about 33 mN loads that would simulate an exothermic event, but not the endothermic phase-transitions of aluminium; the "averaged" data crosses are taken from Fig. 13.12(b) in [38]; the slopes in Fig. 13.8 have no physical meaning

13.4.3 Silicon "Spherically" Indented

Spherical indentations (R = 8.5 µm) of silicon were published in [39]. Photos of a sphere and a description of their indenter setup as "*All of the force-*

displacement measurements were made on a UMIS-2000 instrument", and also the copious description how "*The indentations were carried out*" are indicating that they might have been without data-fitting. Only the cone angle of the conoidal indenter was not disclosed. However, the authors relied in their text on the incorrect Johnson's formula with the impossible F_N vs $h^{3/2}$ relation for spherical indentations. This must again be severely challenged. Our analysis of the published "experimental" data pair crosses from their Fig. 4(a) (similarly in the further images) give again no straight line when the Equation (13.1) for spheres is applied to the published data. The concave curve in Fig. 13.9 is obtained instead.

The data-fitting is again additionally secured with the trial Kaupp-plot (F_N vs $h^{3/2}$) in Fig. 13.10, using the so called "observed" but in reality, fitted loading curve data pairs (the data crosses next to the simulated curve in [39]). This second proof is evident by the linearity with exothermic unsteadiness at about 30 mN and very pronouncedly at 80 mN load.

As shown with GaAs and aluminium, the residual information of "exothermic unsteadiness" tells only that phase-transitions will be found by Berkovich indentation. The steepness of the preceding lines in Fig. 13.10 is again higher than that of the following ones. This seems to be indeed typical for the undue fitting procedure. The genuine silicon phase-transitions are all endothermic: the Berkovich indentation onsets of Si (100) at 4, 15 and 25 (data taken from [40]) or 29 and 81 mN (data taken from [41]) were analyzed in [42]). They reveal endothermic phase-transitions.

Unfortunately, the more recent spherical indentation onto silicon with R = 5 µm of [43] also used Johnson's formula and the Authors do not disclose their cone angle. We therefore do not discuss it here.

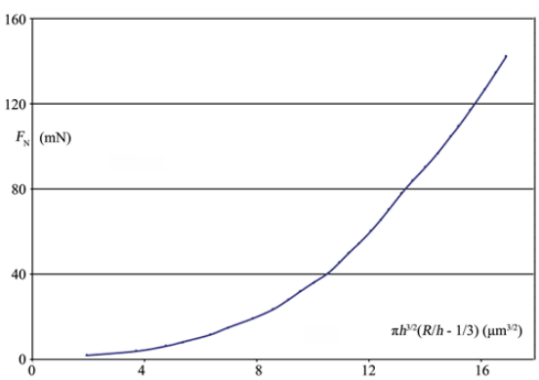

Fig. 13.9. Plot of the spherical indentation (R = 8.5 µm) onto silicon (100) according to Equation (1); the concave form instead of the required linearity proves the data-manipulation in Fig. 4(a) of [39], from where these were taken

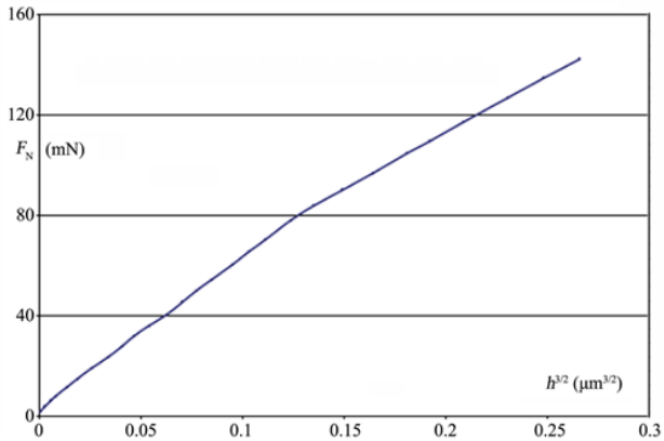

Fig. 13.10. Trial plot of the spherical indentation (R = 8.5 µm) onto silicon (100) according to $F_N \propto h^{3/2}$, showing linearity with kinks at about 30 and 80 mN loads that mimic exothermic event, whereas the phase-transitions at such forces must be endothermic; the lower force onset of silicon requires a ruler; the artificial slopes in Fig. 13.10 have no physical meaning, due to obvious data-fitting from a sphere with a radius of 8.5 µm to follow Johnson's formula

13.4.4 Silicon Carbide "Spherically" Indented

Datye et al. in [44] published spherical indentation data of silicon carbide (SiC). They used their SiC-N brand "*that is similar to* (0001) *of the single crystal*". With their sphere radii of 25 µm and 7.5 µm they reached fully elastic or elastic and plastic indentations, respectively. The data were "fitted" to "*Hertz spherical contact solution*", which means: the disproved Johnson's equation was again the fitting target. These published load-depth curves with fitted depths do again not follow the Equation (1) for spherical indentations. They give the concave curve when tested with Equation (1) and they analyze linear with the trial Kaupp-plot (that is only valid for pyramids and cones) according to $F_N \propto h^{3/2}$ without unsteadiness up to 475 mN load. After short initial effect, the simulated slopes of 1030 (R = 7.5 µm) mN/µm$^{3/2}$ or 3742 (R = 25 µm) mN/µm$^{3/2}$ are obtained with correlation coefficients of 0.9997 or 0.9999, respectively. These do however not describe any materials' property, but only reflect the fitting efficiency. We nevertheless determined these slopes despite the data-fitting, for provisionally checking the influence of the tip radius influence. Interestingly, despite the fitting treatment of the depths, the ratio of these slopes (3.7) is similar to the ratio of the radii (3.3). It should be further studied whether such a relation holds also for spherical indentations with untreated experimental depth data. The mayor errors of the simulating procedure appear to be the modulus E^* as calculated with the false Johnson formula of ISO 14577.

The phase-transition pressures of SiC have been calculated to 102 and105 GPa (hexagonal 6H to 1B) or (cubic 3C to 1B = sodium chloride) phase, respectively, and the experimental shock data have them at about 100 GPa [45]. This is far from being reached with the maximal force of 500 mN in [44].

There seems to be the same data fitting techniques in all of the here analyzed cases, but we still need further analyses with a crystalline oxide.

13.4.5 Magnesium Oxide "Spherically" Indented

The authors of [46] used a polished and rinsed (001) surface of MgO for a "*spherical indenter in diamond*" with an iterated radius of 9.5 µm. Their published Fig. 1(c) in [46] is completely reversible up to 300 mN load and 0.4 µm depths. The data fitting is clearly revealed by their reference to [4] and again by the concave plot that results by application of Equation (1) to the published force-depth curve (not shown here). We need thus not deal any further with this report.

13.4.6 Steel "Spherically" Indented

For rounding up our knowledge of the falsifying effects of data-fitting spherical indentations we also need the analysis of a technical multi-component material. A spherical indentation onto a standard microhardness steel block (500 HV30; H/E = 0.04), using a sphero-conical tip with radius of 7.2 µm [47] and cone half angle of 45° [38] (we calculate h_{cone} = 2.11 µm) (formula in Section 13.2) appeared appropriate. Actually, the nominal radius of 5 µm ± 6.6 nm (we calculate h_{cone} = 1.46 µm) was increased by a "*well-fitting simulation*" to 7.2 µm. And the "*nominal values of* 210 GPa *and* 0.3 *were assumed for Young's modulus and Poisson's ratio in all simulations*". The load-depth data were taken from Fig. 5(a) in [47]. The application of Equation (1) for spherical indentation is valid for every tip radius as long as the h_{cone} value is not surpassed. But the depth values for a certain force are strongly dependent on the tip radius (cf. Section 13.4.4.). Again, concave curves (not shown here) but not straight lines are obtained both for nominal 5 µm or iterated 7.2 µm radius. These analyses tell that our already multiply complained data-fitting was again performed in [47]. Fig. 13.11 ensued, when the Kaupp plot according to $F_N \propto h^{3/2}$ was applied to the clearly fitted loading data. It exhibits three linear branches that simulate two unsteadiness points both with misleading exothermic behavior. Neither the slopes nor the exothermicities are usable. The known phase-transitions of steels and iron are endothermic. A numerical comparison with their onset forces would require a Berkovich indentation of this particular multi-component steel. It should be stressed that the radius R must be measured but never be simulated. It plays an important role for the outcome of experimental spherical indentations.

The unsteadiness onsets in Fig. 13.11 cannot be termed phase-transition values, as they would falsely claim "exothermic" behavior and the slopes are worthless. They are equally false as in the cases for GaAs, Al, and Si. Despite the obvious errors of data-fitting for obeying ISO 14577 standards, the authors of [47] relied

on the false Johnson formula for "Young's modulus" determinations from a simulated loading curve. These are nothing else than faked results.

Very strange is the publication of Fig. 3 in [47]. The tip radius had been shifted from 50 µm ± 1.4 nm to 115 µm, because the data could "only be well fitted" to the simulated Johnson loading curve with R = 115 µm. Such behavior is absurd. The Authors of [47] did not at all recognize that the course of a spherical indentation strongly depends on the radius R. They tried to justify their shifting with the inconceivable claim that "*a slight flattening of the spherical shape over the* 4.5 µm *radius contact region*, *arising from as little as* 0.11 µm *at the center*, *is sufficient to produce an increase in spherical radius of this amount*" (from R = 50 µm ± 1.4 nm into R = 115 µm!). Tip radii are mechanical values that cannot be shifted by iterations "as necessary". While all of that already proves the multiple data treatment, we nevertheless checked the fitted data with our reliable test methods. The application of Equation (1) give the differently sized concave curves (not imaged here) for the data pairs with R = 115 µm and for the simulated curve with nominal R = 50 µm ± 1.4 nm. This confirms the data fitting, as in all of the other tested cases in Section 4.

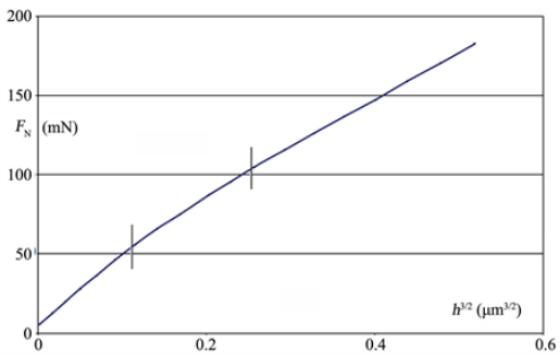

Fig. 13.11. Trial plot according to $F_N \propto h^{3/2}$ for the spherical indentation (iterated R = 7.2 µm) onto the steel with H/E = 0.04, as taken from Fig. 5(a) in [47] by using their fitted data point crosses; the force vs depth$^{3/2}$ plot—only valid for conical or pyramidal indentations—shows three linear branches simulating two exothermic events due to the data-manipulations, while phase-transitions of steels are endothermic; the slopes in Fig. 13.11 have no physical meaning

Furthermore, both simulated curves for the spherical indentation "*of a steel standard hardness block* (900 *HV*30 *nominal*" with H/E = 0.4 in Fig. 3 of [47]) give linearity when trial plotted according to $F_N \propto h^{3/2}$. The simulated R = 50 µm radius curve gives an exothermic unsteadiness at about 100 mN and 0.150 µm (not imaged here) with our calculated pressure of p = 2.11 GPa. Conversely, the simulated R = 115 µm curve in [47] gives the single straight line in Fig. 13.12 again with the maximal force at 200 mN from the first to the last data point

without any unsteadiness. This only tells the high fitting precision that is obtained with the published equations in e.g. [6] (as written down in Section 1). Our calculated pressure in Fig. 13.12 at its end with 200 mN load gives p = 1.58 GPa. This clearly misses the unsteadiness at p = 2.11 GPa with R = 50 µm, as such a high pressure is not reached with a more than twice as high radius R. It stresses however the enormous influence of the tip radius. In the present case one must be alerted of not mixing up the fitted spherical indentation (that is totally worthless) with a pyramidal or conical indentation that would give a totally different slope (yet unknown for steel 900 H/E 0.4). It appears rather strange that the paper [47] could pass the Reviewers and Editors for its publication in the Journal of Materials Research. Fortunately, our mathematically sound analyses are now able to detect the invalid simulations, fittings, and iterations, by using Equation (1).

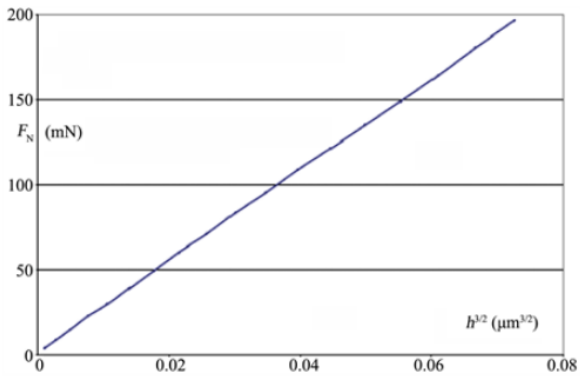

Fig. 13.12. Trial Kaupp-plot according to $F_N \propto h^{3/2}$ for the spherical indentation (iterated R = 115 µm) onto a steel standard hardness block (900 HV30 H/E = 0.4); the clearly fitted "data" are taken from Fig. 3 in [47]; it shows a perfect straight line without unsteadiness, as the data-fitted spherical indentations falsely require an F_N vs $h^{3/2}$ relation; the onset pressure of the unsteadiness is not reached; the slope in Fig. 13.12 has no physical meaning

The plot in Fig. 13.12 again underlines the unique power and necessity of checking publication data from spherical indentations with the correctly deduced Formula (1) in [5] and [7]. It reveals: both of the manipulated data in Fig. 13.3 of [47] (R = 115 µm or of nominal 50 µm) are totally worthless due to various simulations, iterations, and data-fittings for concurring with the disproved Johnson equation that does not take care of the depth-dependent R/h ratio during the penetration. Even worse, the influence of the tip radius to the applied pressure was not acknowledged when nominal tip radii were changed by iterations (5 into 7.2 or 50 into 115 µm).

A recent report deals with the spherical indentation of several steels with a ball of radius 250 µm, in e.g. Fig. 10 of [48]. The Authors used the techniques of [38] and published several "experimental" indentation curves. We analyzed the one for DC01 steel. The test with Formula (1) for spheres gives the concave curve (not imaged here) corresponding to the ones that we always obtained when the spherical indentation data were fitted. This paper [48] covers high loads up to almost 200 N. The trial test with $F_N \propto h^{3/2}$ for conical or pyramidal indentations gives three linear branches at very high load with two unsteadiness points, simulating again worthless exothermic behavior. This F_N vs $h^{3/2}$ plot in Fig. 13.13 proves that the simulation, iteration, and fitting techniques from 1993 [47] and 1995 [38] are unfortunately still in active use.

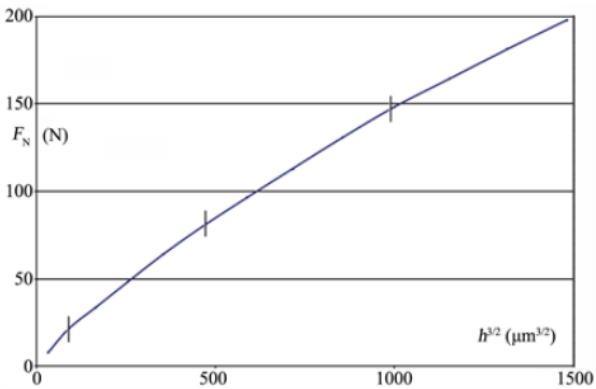

Fig. 13.13. Trial Kaupp-plot according to $F_N \propto h^{3/2}$ for the high-load spherical indentation (*R* approximately 250 µm) onto steel DC 01, using the fitted data as taken from Fig. 10 in [48]; it presents after the unresolved initial effect two unsteadiness kink-points that would misleadingly indicate exothermic events; the reasons are the undue simulation, iteration, and data-managing techniques for complying with the incorrect Johnson's equation and with the present ISO-14577 standard; the slopes in Fig. 13.13 have no physical meaning

13.5 CONCLUSIONS

A prerequisite for the analysis of spherical indentations is the use of the correctly deduced force-depth relation (Equation (1) that takes into account that the *R*/*h* ratio changes strongly during the penetration. Equation (1) describes experimental (not fitted) spherical indentation loading curves. Unfortunately, data-treatment with simulations and data-fittings are still (2020) used by ISO 14577 prescriptions with the false Johnson Formula (here as an inequation $F_N \neq (4/3)h^{3/2}R^{1/2}E^*$) that does not care for the *R*/*h* changes. Typical loading curves from spherical indentations with (untreated) experimental data for Ge, ZnO, and GaN are successfully analyzed. The unprecedented results

demonstrate the unexpected wealth of spherical indentations. The plot of the experimental data according to Equation (1) is linear with kinks at the phase-transition onset points (one, or two within the loading ranges). In addition to the onset force and onset pressure one obtains the phase-transition energy. These values are of great value for the rating of the materials' compliances and for avoiding phase-transitions with their dangerous polymorph interfaces by overloading. These are mayor advances of experimental spherical indentations. The transition onset pressures can be compared with available anvil pressure onsets, because we are close to hydrostatic conditions. In the case of germanium, our calculated onset pressure favorably supports the results of the anvil experiment that had formerly been questioned. It turns out that low-pressure phase-transitions under anvil pressurizing are either not resolved, or too rapidly overrun, or simply overlooked. Our detected polymorphs under the sphere calotte are also reasonably attributed. The most favorable uses of experimental spherical indentations are the expansion of the mechanical characterization of materials and the controlled synthesis of the various polymorphs that is much easier than by any other technique. The polymorphs are located at a most favorable site under the sphere calotte cap, clean and next to their preceding less dense polymorph. That opens new horizons for their structure elucidation by X-ray diffraction and spectroscopy. This should become the method of choice for the characterization of other solid materials with their polymorphs.

Any trust in the historical concepts and formulas is unsuitable and dangerous. Despite their apparently general use, one must strongly reject the false ISO-Johnson formula and all connected false theories that neglect the R/h dependency. It should have been seen before by Authors, Reviewers and Editors, when looking at the abounding printed circles in most of the relevant papers. There is no excuse when black-box routines in their instruments might have automatically simulated, iterated, and data-fitted. Furthermore, the technical users who apply the JKR technique for the evaluation of adhesion properties (cf [6]) should also be alerted for checking, whether they use experimental or falsified force-depth related quantities, for obtaining reasonable results.

We finally state that valid reported spherical indentations are very useful for complementing the highly demanding and less sensitive hydrostatic pressurizing experiments. They reveal also the lower-force phase-transition pressures that might have been hydrostatically overlooked under the anvil. It will be possible now to recognize and stop the widespread data falsifying techniques not only for regaining the scientific reputation in the field of indentations. Peer Reviewers must no longer support data falsifying fake papers. It is not enough when historical authors are cited with their paper titles, but without referring to their antiquated content, or when black-box manipulations produce exact coherency with erroneous equations. The risk of false technical materials' properties will be removed by the sorting out of falsified data and by urgent repetition of the corresponding indentations, if the original experimental data are no longer available for revised publication. The various new possibilities with experimental spherical indentations provide all of the further important characteristics of phase-transitions. They open new horizons for creation and structural

characterization of yet unknown polymorphs of materials. For technically used materials they tell how to avoid dangerous cracking, originating from polymorph interfaces, which often continue to disastrous crashes [5,13] in daily life upon overloading. General help is required for reaching physically sound indentation analyses. Applications for the urgent replacement of the incorrect loading equations with the physical and mathematical correct formulas (1) and (3) have been filed by the author for a hopefully soon coming revision of ISO 14577.

COMPETING INTERESTS

Author has declared that no competing interests exist.

REFERENCES

1. Hertz, H. (1882) über die Berührung fester elastischer Kärper. Journal für die reine und angewandte Mathematik, 92, 156-171. Translated Work: On the Contact of Elastic Solids, #5 in Miscellaneous Papers by H. Hertz, Ed. P. Lenard. Physics Publisher London: New York Macmillan and Co., New York, 1896, 146-162.
https://archive.org/details/cu31924012500306
https://doi.org/10.1515/crll.1882.92.156
2. Hertz, H. (1896) Translated Work: On the Contact of Elastic Solids and on Hardness, #6 in Miscellaneous Papers by H. Hertz, Ed. P. Lenard. Physics Publisher, London, New York Macmillan and Co., New York, 163-183.
https://archive.org/details/cu31924012500306
3. Sneddon, I.N. (1965) The Relation between Load and Penetration in the Axisymmetric Boussinesq Problem for a Punch of Arbitrary Profile. International Journal of Engineering Science, 3, 47-57.
https://doi.org/10.1016/0020-7225(65)90019-4
4. Johnson, K.L. (1985) Contact Mechanics. Cambridge University Press, Cambridge.
5. Kaupp, G. (2019) The Loading Curve of Spherical Indentations Is Not a Parabola and Flat Punch Is Linear. Advances in Materials Physics and Chemistry, 9, 141-157.
https://doi.org/10.4236/ampc.2019.99012
6. Ebenstein, D.M. and Wahl, K.J. (2006) A Comparison of JKR-Based Methods to Analyze Quasi-Static and Dynamic Indentation Force Curves. Journal of Colloid and Interface Science, 98, 652-662.
https://doi.org/10.1016/j.jcis.2005.12.062
7. Kaupp, G. (2020) Valid Geometric Solutions for Indentations with Algebraic Calculations. Advances in Pure Mathematics, 10, 322-336.
https://doi.org/10.4236/apm.2020.105019 Erratum in 10, 545-546.
https://doi.org/10.4236/apm.2020.109034
8. Bradby, J.E., Williams, J.S., Wong-Leung, J., Swain, M.V. and Munroe, P. (2002) Nanoindentation-Induced Deformation of Germanium. Applied Physics Letters, 80, 2651-2653.
https://doi.org/10.1063/1.1469660

9. Kontomaris SV, Stylianou A, Malamou A. Is It Possible to Directly Determine the Radius of a Spherical Indenter Using Force Indentation Data on Soft Samples? Scanning. 2022 Feb 17;2022.
10. Huang FY, Liu YW, Kuo JC. Uncertainties in the representative indentation stress and strain using spherical nanoindentation. Applied Nanoscience. 2021 Mar;11(3):895-909.
11. Weng P, Yin X, Hu W, Yuan H, Chen C, Ding H, Yu B, Xie W, Jiang L, Wang H. Piecewise linear deformation characteristics and a contact model for elastic-plastic indentation considering indenter elasticity. Tribology International. 2021 Oct 1;162:107114.
12. Kaupp, G. (2017) Dilemma between Physics and ISO Elastic Indentation Modulus. Journal of Material Sciences and Engineering, 6, 402-405. https://doi.org/10.4172/2169-0022.1000402
13. Kaupp, G. (2020) Indentation onto Stishovite (SiO2), MgO, and a Covered Superalloy: “Pop-In” Repair, Phase-Transition Onsets, Polymorph Energies, and Transition Energies. Advances in Materials Physics and Chemistry, 10, 77-95. https://doi.org/10.4236/ampc.2020.103007
14. Kaupp, G. (2016) The Physical Foundation of $F_N = k\ h^{3/2}$ for Conical/Pyramidal Indentation Loading Curves. Scanning, 38, 177-179. https://doi.org/10.1002/sca.21223
15. Kucheyev, S.O., Bradby, J.E., Williams, J.S. Jagadish, C. and Swain, M.V. (2002). Mechanical Deformation of Single-Crystal ZnO. Applied Physics Letters, 80, 956-958. https://doi.org/10.1063/1.1448175
16. Bradby, J.E., Kucheyev, S.O., Williams, J.S., Wong-Leung, J., Swain, M.V., Munroe, P., Li, G. and Phillips, M.R. (2002) Indentation-Induced Damage in GaN Epilayers. Applied Physics Letters, 80, 383-385. https://doi.org/10.1063/1.1436280
17. Huang, J., Xu, K., Gong, X.J., Wang, J.F., Fan, Y.M., Liu, J.Q., Zeng, X.H., Ren, G.Q., Zhou, T.F. and Yang, H. (2011) Dislocation Cross-Slip in GaN Single Crystals Under Nanoindentation. Applied Physics Letters, 98, Article ID: 221906. https://doi.org/10.1063/1.3593381
18. Kaupp, G. (2013) Penetration Resistance: A New Approach to the Energetics of Indentations. Scanning, 35, 392-401. https://doi.org/10.1002/sca.21080
19. Duzynska, A., Hrubiak, R., Drozd, V., Teisseyre, H., et al. (2012) The Structural and Optical Properties of ZnO Bulk and Nanocrystals Under High Pressure. High Pressure Research: An International Journal, 32, 354-363. https://doi.org/10.1080/08957959.2012.700308
20. Decremps, F., Zhang, J. and Liebermann, R.C. (2000) New Phase Boundary and High-Pressure Thermoelasticity of ZnO. Europhysics Letters, 51 268-274. https://doi.org/10.1209/epl/i2000-00347-0

21. Vins, F., Lamiel-Garcia, O., Illas, F. and Bromley, S.T. (2017) Size Dependent Structural and Polymorphic Transitions in ZnO: From Nanoclusters to Bulk. Nanoscale, 9, 10067-10074. https://doi.org/10.1039/C7NR02818K
22. Shabbir, S., Shaari, A., Bakhtiar, Haq, U., Ahmed, R. and Ahmed, M. (2020) Investigations of Novel Polymorphs of ZnO for Optoelectronic Applications. Optik, 206, Article ID: 164285. https://doi.org/10.1016/j.ijleo.2020.164285
23. Ashrafi, A.B.M.A., Ueta, A., Avramescu, A., Kumano, H. and Suemune, I. (2000) Growth and Characterization of Hypothetical Zinc-Blende ZnO Films on GaAs (001) Substrates with ZnS Buffer Layers. Applied Physics Letters, 76, 550-552. https://doi.org/10.1063/1.125851
24. Ashrafi, A. and Jagadish, C. (2007) Review of Zincblende ZnO: Stability of Metastable ZnO Phases. Journal of Applied Physics, 102, Article ID: 071101. https://doi.org/10.1063/1.2787957
25. Ding, Y., Wang, Z.L., Sun, T. and Qui, J. (2007) Zinc Blende ZnO and Its Role in Nucleating Wurtzite Tetrapods and Twinned Nanowires. Applied Physics Letters, 90, Article ID: 153510. https://doi.org/10.1063/1.2722671
26. Steplecaru, C.S., Martín-Gonzalez, M.S., Fernandez, J.F. and Costa-Krämer, J.L. (2010) How to Prevent Twin Formation in Epitaxial ZnO Thin Films Grown on c-Plane Sapphire. Thin Solid Films, 518, 4630-4633. https://doi.org/10.1016/j.tsf.2009.12.047
27. Bai, R., Pandaya, D.K., Chaudhary, S., Dhaka, V., Khayrudinov, V., Lemettinen, J., Kauppinen, C. and Lipsanen, H. (2019) Site-Specific Growth of Oriented ZnO Nanocrystal Arrays. Beilstein Journal of Nanotechnology, 10, 274-280. https://doi.org/10.3762/bjnano.10.26
28. Perlin, P., Jauberthie-Carillon, C., Itie, J.P., San Miguel, A., Grzegory, I. and Polian, A. (1992) Raman Scattering and X-Ray-Absorption Spectroscopy in Gallium Nitride under High Pressure. Physical Review B, 45, 3-89. https://doi.org/10.1103/PhysRevB.45.83
29. Xia, H., Xia, Q. and Ruoff, A.L. (1993) High-Pressure Structure of Gallium Nitride: Wurtzite-to-Rocksalt Phase Transition. Physical Review B: Condensed Matter and Materials Physics, 47, 12925-12928. https://doi.org/10.1103/PhysRevB.47.12925
30. Saad Saoud, F., Plenet, J.C., Louail, L. and Maouch, D. (2011). Mechanism of the Phase Transition in GaN under Pressure Up to 100GPa. Computational and Theoretical Chemistry, 964, 65-71. https://doi.org/10.1016/j.comptc.2010.11.037
31. Selke, H., Kirchner, V., Heinke, H., Einfeld, S., Ryder, P.L. and Hommel, D. (2000) Polytypism in Epitaxially Grown Gallium Nitride. Journal of Crystal Growth, 208, 57-64. https://doi.org/10.1016/S0022-0248(99)00462-5

32. Al Balushi, Z.Y., Wang, K., Ghosh, R.K., Vila, R.A., Eichfeld, S.M., Caldwell, J.D. Qin, X., et al. (2016) Two-Dimensional Gallium Nitride Realized via Graphene Encapsulation. Nature Materials, 15, 1166-1171. http://www.nature.com/naturematerials https://doi.org/10.1038/nmat4742
33. Johnson, K.L., Kendall, K. and Roberts, A.D. (1971) Surface Energy and the Contact of Elastic Solids. Proceedings of the Royal Society A: Mathematical, Physical and Engineering Sciences, 324, 301-323. https://doi.org/10.1098/rspa.1971.0141
34. Kaupp, G. (2013) Penetration Resistance and Penetrability in Pyramidal (Nano)Indentations. Scanning, 35, 88-111. https://doi.org/10.1002/sca.21038
35. Meinhard, H. and Grau, P. (2004) Viscosity of Glass at High Contact Pressure during Indentation Experiments. International Journal of Materials Research, 95, 326-334. https://doi.org/10.3139/146.017957
36. Le Bourhis, E. and Patriarche, G. (2005) Nanoindentation Investigation of Solid-Solution Strengthening in III-V Semiconductor Alloys. International Journal of Materials Research, 96, 1237-1241. https://doi.org/10.3139/146.101167
37. Xu, L., Kong, L., Zhao, H., Wang, S., Lu, S. and Qian, L. (2019) Mechanical Behavior of Undoped n-Type GaAs under the Indentation of Berkovich and Flat-Tip Indenters. Materials, 12, 1192-1201. https://doi.org/10.3390/ma12071192
38. Field, J.S. and Swain, M.V. (1995) Determining the Mechanical Properties of Small Volumes of Material from Submicrometer Spherical Indentations. Journal of Materials Research, 10, 101-112. https://doi.org/10.1557/JMR.1995.0101
39. Weppelmann, E.R., Field, J.S. and Swain, M.V. (1993) Observation Analysis and Simulation of the Hysteresis of Silicon Using Ultra-Micro-Indentation with Spherical Indenters. Journal of Materials Research, 8, 830-840. https://doi.org/10.1557/JMR.1993.0830
40. Page, T.F., Warren, C.O. and McHarger, J. (1992) The Deformation Behavior of Ceramic Crystals Subjected to Very Low Load (Nano)Indentation. Journal of Materials Research, 7, 450-473. https://doi.org/10.1557/JMR.1992.0450
41. Hainsworth, S.V., Chandler, H.W. and Page, T.F. (1996) Analysis of Nanoindentation Load-Displacement Loading Curves. Journal of Materials Research, 11, 1987-1995. https://doi.org/10.1557/JMR.1996.0250
42. Kaupp, G. (2019) Physical Nanoindentation: From Penetration Resistance to Phase-Transition Energies. Advances in Materials Physics and Chemistry, 9, 103-122. https://doi.org/10.4236/ampc.2019.96009
43. Shiwa, M., Weppelmann, E., Munz, D., Swain, M.V. and Kishi, T. (1996) Acoustic Emission and Precision Force-Displacement Observation of

Pointed and Spherical Indentation of Silicon and TiN Film on Silicon. Journal of Materials Science, 31, 5985-5991. https://doi.org/10.1007/BF01152149

44. Datye, A. and Lin, H.T. (2017) Energy Analysis of Spherical and Berkovich Indentation Contact Damage in Commercial Polycrystalline Silicon Carbide. Ceramics International, 43A, 800-809. https://doi.org/10.1016/j.ceramint.2016.10.011
45. Gorai, S. and Bhattachara, C. (2019) Shock Induced Phase Transition in SiC Polytypes. Journal of Applied Physics, 125, Article ID: 185903. https://doi.org/10.1063/1.5090808
46. Montagne, A., Tromas, C., Audurier, V. and Woirgard, J. (2008) A New Insight on Reversible Deformation and Incipient Plasticity during Nanoindentation Test in MgO. Journal of Materials Research, 24, 883-889. https://doi.org/10.1557/jmr.2009.0127
47. Field, J.S. and Swain, M.V. (1993) A Simple Predictive Model for Spherical Indentation. Journal of Materials Research, 8, 297-306. https://doi.org/10.1557/JMR.1993.0297
48. Idriss, M., Bartier, O., Mauvoisin, G. and Hernot, X. (2019) Determining the Stress Level of Monotonic Plastically Pre-Hardened Metal Sheets Using the Spherical Instrumented Indentation Technique. Journal of Mechanical Science and Technology, 33, 183-195. https://doi.org/10.1007/s12206-018-1218-1

DISCLAIMER
This chapter is an extended version of the article published by the same author(s) in the following journal.
Advances in Materials Physics and Chemistry, 10, 207-229, 2020.

Chapter 14
Print ISBN: 978-93-5547-921-1, eBook ISBN: 978-93-5547-922-8

Undue Hardness/Modulus Ratio Claims instead of Physical Penetration Resistance and Applications with Mollusk Shells: A Recent Study

DOI: 10.9734/bpi/mono/978-93-5547-921-1/CH14

ABSTRACT

A precise method for revealing mechanical properties is nanoindentation. However, such elucidation calls for physically based loading curve interpretation, which is largely still not done. The most significant phase-transitions under load, which happen often, cannot be detected by using indentation hardness H and indentation modulus Er. The assertion that H vs E plots always correspond linearly is neither experimentally supported nor properly inferred. It is most hazardous and misleading because it produces incorrect material properties. It is incorrect to employ H/E, commonly known as the "elasticity index," in complex calculations for the brittle parameter, yield strength, toughness, and so-called "real hardness." Without taking into account phase-transitions under load, which necessitate the correct exponent 3/2 on h for the loading curves, the usage of H/E cannot show the true attributes of materials (instead of disproved 2). The physical data of various mollusk shells that go through phase transitions, a novel bionics model, and various contributions for their strengthening serve as examples of this. The information is contrasted with that of aragonite, calcite, and vaterite.

Keywords: Nanoindentation; H/E ratio challenge; phase-transitions; penetration resistance; mollusk shells; aragonite; calcite; bionics-model.

14.1 INTRODUCTION

The recent publications of Labonte, Lenz and Oyen [1] which include hardness and moduli data from indentations onto calcite, aragonite, and nacre, and a multitude of other materials, or the one of Teniswood, Roberts, Howard and Bradby on the pyramidal nanoindentation onto aragonite of pteropod shells [2] are unphysical and burden with historical errors despite long known physical knowledge on the basis of simple arithmetic [3]. Since 2004 [4] and 2013, with extensive tables for all types of materials [5] it has been empirically known and undoubtedly physically deduced one year before 2016 [3] and also in 2020 [6] that pyramidal and conical indentations follow the exponent 3/2 on the depth h (but not 2) in the force (F_N) vs depth curves, the slope of which is the penetration

resistance, that is the physical hardness. It was deduced in 2013 [7] and in 2017 [8] that the Oliver-Pharr iterations that are still ISO 14577 standard violate the energy law for hardness H [7] and in 2017 [8] also for E_r since 2017 [9] (ISO denotes International Standardization Organization). Furthermore, elastic moduli from indentations are not "Young's moduli", as used in [1] and [2]. Both quantities should not rely on the three and eight free parameters iterations. And one does not know which of the polymorphs of the material under the applied force was probed. The detection of such polymorphism is only possible by using the F_N vs $h^{3/2}$ relation [3,4,5]. It is known since 2010 how unsteadiness kinks in F_N vs $h^{3/2}$ plots detect important phase transitions upon indentations in [10], in 2018 [11], and in numerous further publications of the present author. The calculation of phase-transition energies was developed in 2013 [7], in 2014 [12], in 2019 [13,14], and in 2020 [15], the calculation of activation energies of phase transitions in 2014 [12]. Some updates in this area are accessible elsewhere and can encourage the readers' judgement [16-18]. 16] continues with still critisizing the work of [3,7,14] by using the disproved ISO 14577 method. Also [17] does not follow the undeniable deduction of $F_N = k\ h^{3/2}$. It again uses the disproved ISO-H and ISO-E_r values for bio-mimetic studies on keratin with the aim to improve the fracture toughness. [18] performs interesting nanoindentations on the explosive ß-HMX for the anisotropy study of the indentation moduli, which might be dangerously misleading, as unfortunately still the unphysical exponent 2 on h is used for the Berkovich impressions. But all of the physical and arithmetical deduced facts have been disregarded by the criticized authors who refer to Oliver-Pharr [19] and prefer the corresponding errors and energy law violations rather than checking the exponent on h of their loading curves (it is in all cases 3/2 and not 2). The numerous undeniable listed applications are not at all available with the physically false assumed exponent. Such H and E_r are fake-values and so are there from created theories of [1] and [2] that must be urgently criticized.

14.2 MATERIALS AND METHODS

The published Berkovich indentation loading curves from the *Limacina Helicina Antarctica* and *Haliotis rufescens* mollusks were scanned and enlarged to A4 size. 25 to 42 data points were taken for the Excel calculation of F_N vs $h^{3/2}$ diagrams. The regression lines of the linear branches provide the slopes as k-values (the physical hardness) for the precise calculation of the kink position (phase-transition onset). These are the basis for the calculation of indentation work (W_{indent}), applied work ($W_{applied}$), full applied work (full $W_{applied}$) and phase-transition energy ($W_{conversion}$), using a pocket calculator (10 digits before final rounding). We normalize them per µN to make them comparable. The necessary equations are well known as repeatedly published in [3,6,14], and earlier publications of the present author. The criticized log-log diagrams from [1] are checked for its missing validity even within the long disproved ISO-H and ISO-E_r world.

14.3 RESULTS AND DISCUSSION

14.3.1 The Still Believed *H*/*E* ("Elastic Index") Claims

The methods of [1] are for various reasons questionable and useless. The authors do not explain why they claim proportionality between ISO-H and ISO-E_r (here for Berkovich). The according to [19] defined ISO-H is F_N per contact area A_{hc} that is geometrically $27.15h_c^2$. The dimension is (force/depth^2) usually reported as GPa. The elastic property is experimentally measured as stiffness $S = \Delta F_{Nmax}/\Delta h$ with the different dimension (force/depth). To obtain an ISO-E_r with the same dimension as the ISO-H, one multiplies the stiffness S with $0.5\ \pi^{1/2}\ A_{hc}^{-1/2}$. This provides the further h_c^{-1} for the dimension of ISO-E_r as force per area (GPa). But the A_{hc} value requires one iteration with 3 and another iteration with up to 8 free parameters (also + or − sign selection) according to [19]. The plots of log H vs log E_r numbers, suggesting a "≈0.05 ratio of H/E_r" for uncountable published Berkovich indentations would at best indicate very poor worldwide measurements of indentations over the years if that would be reality. It cannot be used for the calculation of E_r from H numbers with a "statistical confidence of 95%" and $R^2 = 0.96$. For example, a hardness number H of 0.6 GPa in Fig. 14.1 of [1] contains a spread from 6-30 GPa for the moduli E_r of the densely overlapping entries. Or an entry at $H = 7 \times 10^{-5}$ GPa has a data triangle value of about 1.05×10^{-2} GPa for E_r, while the corresponding H value on the H/E_r line for that E_r is at 4.8×10^{-4} GPa, which is an about 6.9-fold higher hardness number. These examples show drastically that the claimed linear relation between the ISO hardness H and ISO modulus E_r numbers is not correct. And it will be shown in Section 14.3.2 why it cannot be correct. The claimed statistic confidence of 95% for the log-log plot is useless and dangerous. In the Figs. 1, 4a, and 4b of [1] there must be selective choices of data from old papers and tables (often not the more recent ones) with questionable reliability. And even in the more recent papers it was never considered or known which polymorph of the sample had been probed under load, because their onsets could never been seen or excluded. We also must complain that the used entries in Fig. 1 of [1] are not cited and the materials not named. It appears that numerous of these are unpublished own values. This must also be concluded from the caption of Fig. 14.4 in [1], where, unlike the H/E_r plot, straight linear plots are imaged. These are for spherical and for Berkovich indentations without any visible deviations. Beware from the risk of H vs E_r plots in view of Fig. 1 of [1] and beware from predictive uses from there!

Particularly risky and dangerous are the use of H/E_r plots or values for the evaluation of brittleness characterizations, critical load ratios, strengthening, toughness, and "true hardness". For example Fig. 14.4a in [1] describes linear correlations of the brittleness parameter against the load ratio, which rests on $(H/E_r)^2$ numbers, and the normalized characteristic indentation dimension vs critical normalized cracking load ratios are plotted in Fig. 4b of [1]. Only some wet and dried materials are named here and the authors of [1] cite hardly checkable data collections and unpublished own data (which ones?). For example they did not cite the soda lime glass values from [19], which are still a present ISO-

standard for H_I and E_I, even though they repeatedly invoked the "Oliver-Pharr analysis" or "-model". And only a few entries are directly cited, but almost none of these disclosed published original loading curves that could be checked and used for the calculation of real properties like physical hardness, iteration-free elastic moduli and phase-transitions under load.

Furthermore, the authors of [1] try to define and calculate a so-called "true hardness" $H_{true} = H/\{1 - (H/E)^{1/2} (2/\tan ß)^{1/2}\}^2$, where ß is the cone angle of the indenter. This shall be the "resistance to plastic deformation" or "resistance to irreversible deformation", which "depends on the ratio between indentation hardness and indentation modulus". It is strangely claimed that "a large indentation hardness does not imply a large resistance to irreversible deformation *per se*". This hard to understand basis by using the H/E_r fraction is exemplified in [1] as follows: H = 1.07 GPa and E_r = 10.5 GPa shall imply "true hardness" of 17.8 GPa"; or H = 3.12 GPa and E_r = 87.02 GPa shall imply "true hardness" of 10.8 GPa". The H/E_r fraction is contained in such calculations. And the other formulas are in the appendix of [1]. These need not be depicted here, due to the incorrect physical basis from the beginning. Such "true hardness" with exorbitantly misleading high values adds further to misleading confusion without any physical merit.

14.3.2 The Physical Errors of the *H*/*E* Ratio Claims with Their Uses

The proportionality claims of ISO-H with ISO-E_r in [1] and the therein appropriate citations are physically wrong. They cannot be valid for basic physical reasons! The only correct physical hardness of conical or pyramidal indentations is the penetration resistance k [force/depth$^{3/2}$] from the slope of the so named Kaupp-plot F_N vs $h^{3/2}$. None of the cited and used H_I and E_I values tells which polymorph of the material was probed, because their onset forces cannot be found with the wrong exponent 2 on h. One needs such linear plots for the detection of polymorph formation onsets [4,10-15]. And every polymorph has its own mechanical properties. With other words:

All of these H and E_r values are unphysical and so are their ratios, because they rely on the disproved exponent 2 on h (instead of the F_N vs $h^{3/2}$ relation) and require data-fitting iterations [19]. For correct analysis of loading curves for pyramidal and conical indentations see [3] and [6]. Spherical indentations are more complicated [6], but some of the examples in Fig. 14.1 of [1] are from unphysical interpreted spherical indentations or Vickers hardness as in e.g. [20] with similar H/E ratios containing log/log plots. Unfortunately, E_r numbers are not well defined and depend strongly on the details of their detection, as outlined in [9], so that one has to choose from sometimes extremely different values for E_r when comparing different methods.

The Oliver-Pharr technique and the still present ISO 14577 standard assume the physically disproved exponent 2 on h for the loading curves instead of undeniably physically deduced $h^{3/2}$ [3], and they violate the energy law [6] [8]. Therefore the authors of [1] cited H and E_r values that are entirely unphysical parameters. If

indentation hardness have to be compared with indentation modulus one should only take physically sound values from the so named Kaupp plots (F_N vs $h^{3/2}$) that most easily provide penetration resistance onsets and differentiate the properties of every polymorph under load. And it provides directly measured indentation moduli (E_{phys}) without any iteration. All of the trouble in Section 14.3.2 originates from the widespread refusal to check the exponent of their loading curves. These F_N vs h loading curves follow always the physically correct relation $F_N = kh^{3/2}$ and spherically $F_{N\text{-}s} = k_s \pi h_s^{3/2} (R / h_s - 1/3)$. All of the respective authors stay with the physically disproved h^2, apparently until ISO and the authors of [19] correct their basic errors with public announcements.

14.3.3 The Wealth of Penetration Resistance for the Physical Analysis as Exemplified for the Marine Mollusks Case

The claims of linear relations between ISO-hardness H and ISO-modulus E_r include nacre, eggshell, aragonite, calcite, hydroxyapatite, enamel, dentine, bone, etc in the unphysical and incorrect log/log plots in [1]. But their data are selective and none of them reveals which polymorph was probed under what applied load. Furthermore, it is not told which of the triangle data points around the regression line in Fig. 14.1 of [1] belong to which materials. These data are without any value.

We show now that hitherto unthinkable materials' properties are straightforwardly obtained on the physical analysis of indentations from correctly cited publications. This will be exemplified for the case of two mollusk varieties with their aragonite shells, including the distribution of the organic materials. The physical analysis of the indentation loading curve onto the polar pteropod *Limacina Helicina Antarctica* shell, as recently published with Fig. 4 in [2], yields the F_N vs $h^{3/2}$ diagram of Fig. 14.1. One recognizes an initial surface effect up to about 300 µN load (from its water content) and three linear branches that are connected by smooth transition zones between them. This was not seen in their F_N vs h curve and it does never show up in the unphysical F_N vs h^2 relation with its false exponent 2 on h. The authors of [2] did thus not see that their calculation of ISO-H and ISO-E_r values [19] do not at all relate to properties of their sample but to the third polymorph of it that is present at their maximal force. Our three linear regression lines with (R^2 = 0.9994, 0.9993, and 0.9993, respectively) have the equations that are inserted in Fig. 14.1. The kink positions, as obtained by equation of two adjacent regression equations, at 1182.08 and 2958.895 µN loads are phase-transition onsets. With these experimental values we calculate the phase transition energies with the simple well-known arithmetic equations that are most recently comprehensively published in [6] and [14], and earlier publications of the present author. The obtained normalized per µN values are 0.01496 µNµm/µN and 0.14879 µNµm/µN. Clearly, there are three different polymorphs up to a loading range of 5 mN load with a Berkovich. Interestingly these values are similar to the ones of calcite in Table 1 of [14] that are at 0.01599 and 0.10692 µNµm/µN, respectively, although at their mN ranges. It is clear that we have the phase transitions with the *Limacina Helicina Antarctica* shell.

The smooth transition zones rather than sharp kinks that are here only seen by the intersecting regression lines reveals a gradual change of the strengthening organic material between the different polymorphs. This is certainly a bionics model for avoiding the crack increasing risk when unavoidable polymorph interfaces contact smoothly [11]. This appears to be further studied and used for modifying the negative effect of phase-transitions also with technical materials.

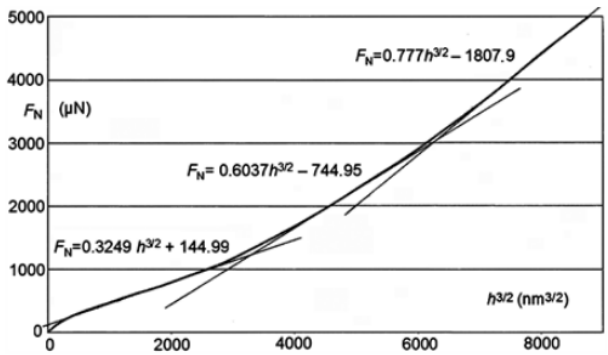

Fig. 14.1. Linear plot of a "typical" Berkovich indentation onto the pteropod *Limacina Helicina Antarctica* shell with thinner intersecting regression lines, exhibiting an initial surface effect and three straight branches with comparably smooth transition zones between them. The inserted steepness constants *k* are in μN/nm$^{3/2}$; the original force vs load data are taken from Fig. 4 in [2]

The precise distribution of the about 5 wt% of organic material is certainly worth further studies. Conversely, the unphysical H and E_r measurements led to the claim of "essentially homogenous distribution throughout the shell for "strengthening the cell" [2]. Furthermore, the rather strong variation of the averaged ISO-H and ISO-E_r values in Fig. 14.5 of [2], or the report that some indentations were going down to 700 nm depth and others down to only 200 nm depth, or the observation of rough and smooth areas would also suggest a thorough new and physically analyzed indention. All of these strongly deviating results must be reproduced and separately analyzed rather than averaged as in [2]. Comparison of the so available penetration resistance k-values (mN/μm$^{3/2}$) of the different polymorphs up to the same load maximum would tell, whether there are zones with more or less organic material also laterally distributed. In the case of micro-caverns empty or filled with water, these would show-up as spurious pop-ins [15]. The physical analysis technique is the only means for the distinction of soft and hard regions that cannot be visibly traced.

It is particularly unsuitable that the authors of [2] did not compare their findings with the physical analysis of the Berkovich indentation onto the lamellar pteropod structure of the red abalone *Haliotis rufescens* in [5]. This pteropod shell exhibits

distinct well defined stepwise organic layers between the aragonite lamellas and the indentation curves of them are physically correct analyzed in [5]. The non-appreciation of the well documented different strengthening bionics model is misleading, even though the introduction of paper [2] cites numerous old and very old papers on different pteropod varieties with prismatic helical and lamellar aragonite structures, but unduly questioned the paper of [21]. We must therefore resume our analyses here with the calculations on the correct physical basis. These add to a much better understanding of the pteropods stability with reliable parameters instead of iterated H and E_r that are against physics.

The averaged Berkovich indentation curve of the red abalone *Haliotis rufescens* shell from Baja, California [21] was physically analyzed in [14]. The exterior nacre shell of 250 - 300 nm thickness with $k_{\text{first-aragonite-shell}}$ = 0.9058 µN/nm$^{3/2}$ is sharply distinguished by the organic layer with k_{organic} = 0.274 µN/nm$^{3/2}$ and the following inner apatite layer with $k_{\text{inner-aroganite-shell}}$ = 1.1495 µN/nm$^{3/2}$. The stepwise behavior is also shown in the original F_N vs h plot from Fig. 14.7 in [21]. Clearly both aragonite layers are sharply separated by the soft organic layer. The F_N vs $h^{3/2}$ plot in Fig. 14.2 with the inserted regression equations, as calculated up to 400 nm depth (8000 nm$^{3/2}$) with the inserted regression lines is totally different from Fig. 14.1. After a minor initial surface effect that is not part of the regression (5 points) two aragonite layer lines are separated by the organics line. The larger k-value of the first inner aragonite layer starts at a 26.9 per cent higher load and at higher $h^{3/2}$. Therefore at least some of this k-value increase represents the shift relative to the end of the first aragonite layer. The thinner strengthening organic layer is considerably softer. The 16.8% difference between the k-values of the two aragonite layers cannot solely be responsible for their displacement. The second aragonite layer should also be phase-transformed at the increased force with an onset right above the organic layer at 4312 µN. The regression line values of the hard branches correlate both with R^2 = 0.9997.

However, there are difficulties for the calculation of the phase-transition energy, because we do not have a kink-point between the displaced aragonite layers. We must try to secure that the inner aragonite layer is a polymorph by a phase-transition. Fig. 14.2 indicates that the first branch ends very close to the lower end of the organic layer at 4000 µN load and 287 nm depth (4853 nm$^{3/2}$). The second aragonite branch starts directly at the upper end of the organic layer at 4312 µN. This data point is already part of the regression line for the steeper (harder) branch. The 4000 µN load would thus be the phase transition onset point if the organic layer was not there. Unlike the repair of pop-ins [15], our phase-transition energy calculation technique is not applicable for such separation by a different material. A shift of the upper layer line for joining with the lower line at 4000 µN by formally removing the organic layer is not allowed. And it would not solve the problem: the steepness of the second hard layer is influenced both by higher F_N and by higher $h^{3/2}$ values at its start. This influence on the steepness cannot be undoubtedly judged and also minor corrections in that sense would strongly influence our precise and highly sensitive calculations. A phase transition part from about 4500 µN load of the hard nacre shell is however most likely. That judgment is in view of the k_1 and k_2 values of the softer

Limacina Helicina Antarctica shell that experiences the phase transition and the k_1 and k_2 values of the *Haliotis rufescens* shell that are in the same order of magnitude even though the shells of *Limacina Helicina Antarctica* are softened by the embedded organic layers. Final proof would require comparison with an indentation of pure aragonite at forces up to about 7000 µN load. Unfortunately we did not find accessible reliable Berkovich indentation curves of pure aragonite at such a loading range with smooth loading curves that are not interrupted by continuously repeated unloads. There is however a phase-transition within a 500 µN loading range of pelletized aragonite from [22] that occurs with an endothermic phase-transition at 348 µN load We interpret it as an endothermic twinning of aragonite and calculate the normalized conversion energy to 0.02922 µNµm/µN. Clearly this interesting twinning transition cannot be remarked at an indentation range of 7000 µN of the mollusks indentations.

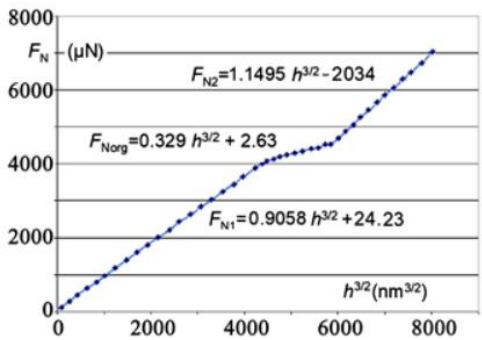

Fig. 14.2. Linear plot of Berkovich indentation onto the red abalone *Haliotis rufescens* shell from Baja, California [21]; image taken from [5] and with complete inserts that denote the penetration resistance *k* (their physical hardness (µN/nm$^{3/2}$) with the axes cuts of the hard and the soft layers [3,6]

We must report here how one can identify and exclude experimentally false reported data by the calculation of transition energies. The reported Berkovich indentation onto (001) of aragonite up to 1000 µN load from the Fig. 1 of [23] revealed a minor exothermic transition at F_{Nkink} = 408.6 µN when physically analyzed. Thus, Fig. 15b in [5] would exhibit exothermic transition energy of −0.00276 µNµm/µN [14]. This putative strange twinning of aragonite appeared to be a specialty of the (001) face of aragonite. It was hardly resolved in the indentations of nacre up to 7000 µN load and must be cancelled now in Table 1 of [14]. This failure is an important application of the calculation of phase-transition energies, because it helps to eliminate undue measurements. The work of [23] failed, because the loading curves were averaged and pop-ins was also reported with three imaged individual curves on the probed surface. Their inclusion in the curves averaging constructed the exothermic event. It is still not widely recognized that pop-ins are instrumental errors due to distortions that must be repaired or eliminated from further use [15]. The pop-in generation in the present case was probably by touching of tip sides with terrace steps on the

probed surface (further reasons of pop-in distortions are listed in [15]). Any averaging of experimental curves must be strictly avoided. Only the results from all individual undistorted curves should be averaged. The curve for (001) in Fig. 14.1 of [23] and its analysis in Table 14.1 of [14] must be disregarded.

The behavior of aragonite must now be compared with the other ambient modifications of $CaCO_3$. Hexagonal calcite, orthorhombic aragonite, and hexagonal vaterite crystallize in the respective space groups R3−c, Pbm6n, and $P6_3/mmc$. Their X-ray densities are 2.71, 2.93, and 2.93 g/cm^3, respectively. The most frequent twins of calcite occur along (10 - 11) by mechanical stress on (01 - 12) and those of aragonite on (110) by mechanical stress on (010) [24]. So there is the possibility of mechanical twinning by pressure. Such twins of aragonite are orthorhombic Pmcn. Vaterite twins have been found in pearls [25]. All three modifications occur as minerals. Aragonite and vaterite (with some organic material) are primarily of biological origin as in pearls or mollusk shells, and vaterite in gallstones and nephritic stones and plants (e.g. [26]). An important point is the repair of deformed Gastropodes' aragonite shells with vaterite attachments [26]. The loading curves of calcite up to 10 mN [27] and up to 40 mN [28] have been analyzed in [14] to give conversion energies of 0.01599 mNμm/mN and 0.1069 μNμm/μN for the second phase transition.

14.4 CONCLUSIONS

It appears more than surprising that a paper like [1] is still prepared (and can even be published) that rests on disproved historical errors. Since these are against physics, their mechanical parameters required data manipulating iterations and more and more extremely complicated theoretical treatments, as shown here in Section 3.1. Such behavior is still not stopped by the International Standardizing Organization with its ISO 14577. This Organization is very slow with the revision of their standards that still enforce industries for being certified. It did not yet help that the easily empirically found (since 2004) [4] and straightforwardly deduced (convincingly published in 2016 [3] and in 2020 enhanced [6]) physical equations can be simple reproduced. They are successfully published and provide numerous unprecedented arithmetic applications. But influential people, who stick to history and did or taught it always historically, are restrictive. Unfortunately, the false characterization of mechanical properties is continuously leading to catastrophic disasters. But for perhaps obvious responsibility reasons, it is not tried to assign the reasons for these disasters to poor alloys in need of improvement for airplanes, for public bridges, and all further construction materials. Upon catastrophic events, one just refers to obeying ISO standards and tries for example in the case of continuing airliner crashes only to blaming pilot errors or deficient piloting control software, but not also to unfit physically incorrectly analyzed materials. Thus, indentations revealing phase-transition onset control of the materials upon mechanical (cf. Fig. 14.1) and thermal (cf. [12]) stress are disregarded, ignored, or denied. But why not avoid braking turbine propeller blades with improved alloys that withstand higher forces before phase-transition onsets occur [14]. We also complain the cracking between wing and fuselage (pickle fork) and hundreds of

grounded airliners with multiple clefts on fuselage, etc. These are materials' failures. Pickle forks must not just be repaired, but constructed with improved alloys and replaced. The checking and improving of the alloys must be for increasing the phase-transition onsets forces and energies. Polymorph interfaces from phase transitions are sites for cracks' nucleation with catastrophic failures [11,12,13,15]. The detection of phase transitions under load is still not part of ISO 14577, because it cannot achieve them by using the false exponent 2 on h instead of 3/2 from indentation loading curves.

An H/E_r ratio (also called "elasticity index") is unphysical, as are ISO-H and ISO-E_r. Physical hardness is $H_{phys} = k = F_N / h^{3/2}$ (k in force/depth$^{3/2}$) for conical and pyramidal indenters. And the not iterated physical modulus is $E_{rphys} = (d1.25F_N / dh) / A$. [8, 29] for obeying with the energy law. Modern instrumentation provides enough data points for the initial linear slope that is stiffness S of the unloading curve. The assumed but not physically deduced linearity between H and E_r has not been demonstrated by the log-log plot in Fig. 1 of [1] with a "statistical confidence of 95%" and $R^2 = 0.96$ for the selected materials by not considering their undetermined phase-transitions that are however most frequent for all kinds of materials upon load. Even under these unsuitable conditions the actual deviations are very often enormous. However, most materials have to be again indented when neither original data, nor published F_N vs h loading curves had been published. ISO-H and ISO-E_r values cannot reinstall the physical indentation results, due to the exhaustive data fitting iterations. It has to be rejected that the H/E_r ratio is used for defining a so-called "true hardness" with extremely high useless values of hardness and moduli. Also the revival of the complicated formulas, using H/E_r ratios for brittle parameter, yield strength, and toughness, is misleadingly incorrect and useless. Correct unprecedented qualities of materials (as exemplified in Section 3.3.) are to be deduced from a physically sound basis. The easily obtained experimental achievements on the basis of the physical analyses of indentations are withheld in [1] from its audience of biologists, pharmacists, physicians, theoreticians, and other readers.

The exemplarily analysis of the indentations onto seawater mollusks shows that ISO-H and ISO-E values are unable to differentiate between the construction principles of different mollusk shells. The aims to solve important biological questions are not attained and so are the theoretical speculations. It requires the so named Kaupp-plot (F_N vs $h^{3/2}$) for most easily and rewardingly revealing the striking differences. In the case of *Limacina Helicina Antarctica* the linearized loading curve undergoes two phase-transitions in the load ranges up to 5 mN. The within aragonite distributed material cushions shocks so that the shells are protected. We quantified the phase-transition onsets and energies that reflect the details for the lattice conversion in Section 14.3.3. A new bionics model is extracted from the shell behavior. Its cell strength is achieved by mitigation of the dangerous effects of polymorph interfaces by softening with gradual approach to polymorphs interface from the unavoidable phase-transitions. This bionics model should become most useful for technical materials that are exposed to mechanical forces that induce phase-transition onsets in e.g. ballistics or earthquakes etc. Furthermore, these results open up new technical and

biological insights. Further indentations onto *Limacina Helicina Antarctica*, as requested in Section 14.3.3 will in the future facilitate the crystallographic understanding of these phase-transitions with eventually further bionics models. Totally different is the already known bionics model of *Haliotis rufescens*. It uses alternating layers of the thin soft organic material between thicker aragonite layers for cushioning. Also further studies with the numerous further mollusks become worthwhile and promising now. Variations of the layer thickness and detailed structures in the not layered varieties with respect to environmental conditions will provide biological answers. Also snail-shell indentations should be physically analyzed, but not with the disproved and unable techniques in Figs. 14.1 and 14.2 of [1], as discussed in Section 14.2.

Further advances of the physical analyses, in addition to the precise detection of phase-transition onset forces and energies for explaining and avoiding catastrophic failures, are the sorting out of initial surface effects, the detection and elimination of experimentally false reports with the calculation of phase-transition energies and the distinction of phase-transition onsets from those of different material layers. When measured at various temperatures one can also calculate the activation energies of phase-transitions [12]. None of these achievements are available from H, E_r, H/E_r and there from deduced obsolete techniques, because they are all unphysical.

The future will detect and understand further phase-transition onsets and energies from all kinds of materials. This opens their discussion for the widening of their understanding and applications, and the search for further bionics models appears promising.

It is hoped that not only biologists, pharmacists, physicians, and also industrial Engineers take their chance to increase and revise their knowledge for preventing dangerous disasters by using the penetration resistance instead of ISO-H and ISO-E_r. The revision of ISO-14577 must also be accelerated. It is strongly hoped that ISO 14577 and the authors of [19] correct their basic errors with public announcements as soon as possible for a safer world.

COMPETING INTERESTS

Author has declared that no competing interests exist.

REFERENCES

1. Labonte, D., Lenz, A.K. and Oyen, M.L. (2017) On the Relationship between Indentation Hardness and Modulus, and the Damage Resistance of Biological Materials. Acta Biomaterialia, 57, 373-383. https://doi.org/10.1016/j.actbio.2017.05.034
2. Teniswood, C.M.H., Roberts, D., Howard, R. and Bradby, J.E. (2013) A Quantitative Assessment of the Mechanical Strength of the Polar Pteropod Limacina Antarctica Shell. Journal of Marine Science, 70, 1499-1505. https://doi.org/10.1093/icesjms/fst100

3. Kaupp, G. (2016) The Physical Foundation of $F_N = k\,h^{3/2}$ for Conical/Pyramidal Indentation Loading Curves. Scanning, 38, 177-179.https://doi.org/10.1002/sca.21223
4. Kaupp, G. and Naimi-Jamal, M.R. (2004) Nanoscratching on Surfaces: The Relationships between Lateral Force, Normal Force and Normal Displacement. Zeitschrift für Metallkunde: International Journal of Materials Research and Advanced Techniques, 95, 297-305.
5. Kaupp, G. (2012) Penetration Resistance and Penetrability in Pyramidal Nanoindentations. Scanning, 35, 88-111. https://doi.org/10.1002/sca.21038
6. Kaupp, G. (2020) Valid Geometric Solutions for Indentations with Algebraic Calculations. Advances in Pure Mathematics, 10, 322-336. (Erratum (2020) Advances in Pure Mathematics, 10, 545-546.) https://doi.org/10.4236/apm.2020.105019 https://doi.org/10.4236/apm.2020.109034
7. Kaupp, G. (2013) Penetration Resistance: A New Approach to the Energetics of Indentations. Scanning, 35, 392-401. https://doi.org/10.1002/sca.21080
8. Kaupp, G. (2017) The ISO Standard 14577 for Mechanics Violates the First Energy Law and Denies Physical Dimensions. Journal of Material Sciences & Engineering, 6, 321-328. https://doi.org/10.4172/2169-0022.1000321
9. Kaupp, G. (2017) Dilemma between Physics and ISO Elastic Indentation Modulus. Journal of Material Sciences and Engineering, 6, 402-405. https://doi.org/10.4172/2169-0022.1000402
10. Kaupp, G. and Nami-Jamal, M.R. (2010) The Exponent 3/2 at Pyramidal Nanoindentations. Scanning, 32, 265-281. https://doi.org/10.1002/sca.20206
11. Kaupp, G. (2018) Six Polymorphs of Sodium Chloride upon Depth Sensing Macroindentation with Unusual Long-Range Cracks Requiring 30 N Load. Journal of Material Sciences and Engineering, 7, 473-483. https://doi.org/10.4172/2169-0022.1000473
12. Kaupp, G. (2014) Activation Energy of the Low-Load NaCl Transition from Nanoindentation Loading Curves. Scanning, 36, 582-589. https://doi.org/10.1002/sca.21158
13. Kaupp, G. (2019) Phase-Transition Energies, New Characterization of Solid Materials and Anisotropy. Advances in Materials Physics and Chemistry, 9, 57-70. https://doi.org/10.4236/ampc.2019.94006
14. Kaupp, G. (2019) Physical Nanoindentation: From Penetration Resistance to Phase-Transition Energies. Advances in Materials Physics and Chemistry, 9, 103-122. https://doi.org/10.4236/ampc.2019.96009
15. Kaupp, G. (2020) Indentation onto Stishovite (SiO_2), MgO, and a Covered Superalloy: “Pop-In” Repair, Phase-Transition Onsets, Polymorph Energies, and Transition-Energies. Advances in Materials Physics and Chemistry, 10, 77-95. https://doi.org/10.4236/ampc.2020.103007

16. Yan C, Bor B, Plunkett A, Domènech B, Schneider GA, Giuntini D. Nanoindentation of Supercrystalline Nanocomposites: Linear Relationship Between Elastic Modulus and Hardness. JOM. 2022 Apr 15:1-6.
17. Wang B, Huang Y, Zhou B, Li W, Chen H. Nanoindentation and Hierarchy Structure of the Bovine Hoof Wall. Materials 2021, 14, 289.
18. Olokun A, Dillard T, Dhiman A, Tomar V. Experimental study of anisotropic constitutive behavior of β-HMX crystals via nanoindentation and small-scale dynamic impact. SN Applied Sciences. 2021 Dec;3(12):1-1.
19. Oliver, W.C. and Pharr, G.M. (1992) An Improved Technique for Determining Hardness and Elastic Modulus Using Load and Displacement Sensing Indentation Experiments. Journal of Materials Research, 7, 1564-1583.
https://doi.org/10.1557/JMR.1992.1564
20. Rhee, Y.W., Kim, H.W., Deng, Y. and Lawn, B.R. (2001) Brittle Fracture versus Quasi Plasticity in Ceramics: A Simple Predictive Index. Journal of the American Ceramic Society, 84, 561-565.
https://doi.org/10.1111/j.1151-2916.2001.tb00698.x
21. Katti, K.S., Mohanty, B. and Katti, D.R. (2006) Nanomechanical Properties of Nacre. Journal of Materials Research, 21, 1237-1242.
https://doi.org/10.1557/jmr.2006.0147
22. Sevcik, R., Sasek, P. and Viani, A. (2018) Physical and Nanomechanical Properties of the Synthetic Anhydrous Crystalline CaCO3 Polymorphs: Vaterite, Aragonite and Calcite. Journal of Materials Science, 53, 4022-4033.
https://doi.org/10.1007/s10853-017-1884-x
23. Kearney, C., Zhao, Z., Bruet, B.J.F., Radovitky, R., Boyce, M.C. and Ortiz, C. (2006) Nanoscale Anisotropic Plastic Deformation in Single Crystal Aragonite. Physical Review Letters, 96, Article ID: 255505.
https://doi.org/10.1103/PhysRevLett.96.255505
24. Anthony, J.W., Bideaux, R.A., Bladh, K.W. and Nichols, M.C. (Eds.) (2003) Handbook of Mineralogy. Mineralogical Society of America, Vol. 5.
https://www.handbookofmineralogy.org
25. Qiao, L. and Feng, Q.L. (2007) Study on Twin Stacking Faults in Vaterite Tablets of Freshwater Lacklustre Pearls. Journal of Crystal Growth, 304, 253-256.
https://doi.org/10.1016/j.jcrysgro.2007.02.001
26. Spann, N., Harper, E.M. and Aldridge, D.C. (2010) The Unusual Mineral Vaterite in Shells of the Freshwater Bivalve Corbicula fluminea from the UK. Naturwissenschaften, 97, 743-751.
https://doi.org/10.1007/s00114-010-0692-9
27. Guillonneau, G., Kermouche, G.K., Bec, S. and Loubet, J.L. (2012) Determination of Mechanical Properties by Nanoindentation Independently of Indentation Depth Measurement. Journal of Materials Research, 27, 2551-2560.
https://doi.org/10.1557/jmr.2012.261
28. Presser, V., Gerlach, K., Vohrer, A., Nickel, K.G. and Dreher, W.F. (2010) Determination of the Elastic Modulus of Highly Porous Samples by

Nanoindentation: A Case Study on Sea Urchin Spines. Journal of Materials Science, 45, 2408-2418. https://doi.org/10.1007/s10853-010-4208-y

29. Kaupp, G. (2020) Real and Fitted Spherical Indentations. Advances in Materials Physics and Chemistry, 10, 207-228. https://doi.org/10.4236/ampc.2020.1010016

DISCLAIMER
This chapter is an extended version of the article published by the same author(s) in the following journal.
Advances in Materials Physics and Chemistry, 11: 45-57, 2021.

Chapter 15
Print ISBN: 978-93-5547-921-1, eBook ISBN: 978-93-5547-922-8

Recent Updates on Volume, Side-Area, and Force Direction of Berkovich and Cubecorner Indenters

DOI: 10.9734/bpi/mono/978-93-5547-921-1/CH15

ABSTRACT

To shed new light on this crucial area of study and application, a thorough explanation and extension of the iteration-free physical description of pyramidal indentations using closed mathematical equations are provided. All computations are easily repeatable and ought to be encoded into instruments by their manufacturers to make general use even simpler. The resulting forces and force directions are inferred and presented, along with formulas for the volumes and side-areas of Berkovich and cubecorner as functions of depth. The full comparison of various indenters on the mathematical reality is made possible by all of these. The values of pyramids are significantly different from those of so-called "equivalent cones." The worldwide use of such pseudo-cones is in severe error. Disproved is the previously asserted and employed 3 times greater displacement volume with cube corner than with Berkovich. At the same applied force, both move the same amount. Experimental evidence is used to support the previously unreported mathematical findings for both the sharp-onset phase transitions and the physical indentation hardness. Phase-transition energies are calculated. New fundamental insights are provided by comparing the two indenters. The phase transition onset force is identical for isotropic materials, but the transition energy is greater at the cube corner due to a higher force and flatter force direction. The cube corner is now eligible for studies on fracture toughness. The alleged "friction with the indenter" is not what causes the pile-up. Under pressure, sliding along cleavage planes and channels occurs in anisotropic materials both internally and externally. The depression volume is increased by their volumes. These quantities are crucial for managing pile-ups in the best possible way. Crack-nucleating polymorph interfaces are created during phase transitions. Technical materials must be created with onset forces greater than the maximum stresses imaginable (at airliners, bridges, etc.). This requires urgent revision of ISO 14577-ASTM standards.

Keywords: Closed mathematical formulas; force direction; indenter volumes and side-areas; iteration-less calculations; equal base-area cones; pile-up; phase-transition-onset and -energy.

15.1 INTRODUCTION

15.1.1 The Force vs Indentation Depth Relation

Physical and mathematical innovations that described (nano)indentation by considering the energy conservation law and the penetration volume of the submerged indenter, rather than the basal indenter area, were made in 2013 and 2016. The experimentally discovered $h^{3/2}$ vs applied normal force (F_N) connection rather than h^2 for pyramidal and conical indentations from 2004 [3] was conclusively demonstrated by [1] and [2] to be true. Additionally, 22 linear F_N vs $h^{3/2}$ plots using virtually every type of material had already been reported in [4]. This rightfully opposes to the nevertheless still common belief in incorrect "h^2", losing all information from it (no physical hardness, no initial surface and tip rounding effects, no phase transitions, no possible gradients). Similarly, the iteration of the loading curve exponent for best-fitting of the loading curve etc wipes out all these information. Still worldwide believed is the using h^2 derived ISO 14577-ASTM hardness (International Standardization Organization and American Society for Testing and Materials) from conical and pyramidal indentations that is used in available tabulations, peer-reviewed scientific publications, and industries. It is unduly defined as force over projected basal contact area. But why is that so? The applied force does not press to the basal area of the indenter! It must be the result of the still retained wrong exponent for the loading curve. The readers may be interested in certain updates in this topic that are available elsewhere [5-7]. While [5] presents the investigations arithmeticly, [6] is using "fundamental physics instead of the typical rigorous mathematical process" for AFM but is still claiming "Young's modulus", and [7] still depends on simulations. And [8] is the complete background of ISO 14577-ASTM.

15.1.2 ISO and ASTM Hardness and Modulus

According to [8], the area function of the "perfect" Berkovich is $A_{hc} = 24.5h_c^2$ where h_c indicates contact height. The constant had been checked with the compliance C (inverse stiffness) vs $A^{1/2}$ plots from the "two highest" (120 mN) indentations in aluminium of [8]. A_{hc} is iteratively "refined" for the not ideal indenter to give the fitted "contact area" A_{hc} for other materials. At first the unloading curve exponent is iterated with 3 free parameters (fitted unloading steepness). Secondly, the area is iterated with 8 free parameters C_1 - C_8. The first guess of them is $24.5h_c^2$ and the further 8 exponents on h_c decrease via 1 to 1/128 for fit with the aluminum data. For smaller depths the fit is for the corresponding fused quartz data. That leads to the fitted contact depth $h_c = h_{max} - \varepsilon F_{Nmax}/S$. The ε is a disputed factor. The necessary stiffness S is defined after differentiation of the fitted unloading curve as dF_N/dh_{max}, and the fitted reduced elastic modulus is $E_{r\text{-}fitted} = S\pi^{1/2}/2A_{hc}^{1/2}$ This does not consider that only part of F_{Nmax} is responsible for the depth h [1]. All of these iterations from [8] are the ISO 14577-ASTM International standard. They are automatically executed with the commercial indenters to provide iterated ISO-hardness H [N/depth^2].

Furthermore, the equally iterated E_r [N/depth^2] is not at all the claimed "Young's modulus". The latter is, of course, a strictly unidirectional property out of the 6 by 6 matrix of Young's moduli that finally, depending on crystal symmetries, gives 9, 7, 6, or in the cubic case 3 independent always very different Young's moduli. That is generally known and communicated, but here falsely disregarded.

The common use of the false exponent on *h* followed by exhaustive iterations and false definitions is dangerous. All of that creates false materials properties and it denies phase-transitions under load with their polymorph interfaces. Unfortunately, that is still enforced by ISO 14577-ASTM for technical materials with catastrophic risks.

15.1.3 The Mathematics with the Correct Exponent 3/2 on the Depth *h*

The undeniably [2] correct physical hardness from conical and pyramidal indentations is obtained as k ($F_N/h^{3/2}$), which is the penetration resistance as slope of the experimental linear F_N vs $h^{3/2}$ plot (also called "Kaupp-plot" since 2004 and 2016) as Equation (15.1). It must be corrected for any axis cut F_a to give (15.2). Such axis cuts can be positive or negative due to various surface effects. They are excluded from regressions. The various reasons for initial surface effects have been amply discussed in preceding publications. Sample surfaces are not always free of layers (twins, oxides, hydroxides, chemical and mechanical pre-treatment such as polishing etc). Their separate elucidation requires indentations with very small depth ranges. Axis cuts are corrected for in a straightforward way.

It is the iteration-free and undeniable mathematics that reaches correct physical data of materials and totally new ones from (nano)indentations. Examples are the physical indentation hardness [1,2,3,4], the previously undetectable phase-transitions under load as kink unsteadiness on the F_N vs $h^{3/2}$ plot (e.g. Fig. 15.2 [2]), and the phase-transition energies. The phase-transition energies are now normalized per depth region. Unfortunately, the presently still used concept of "work hardening" with iterated exponential functions is meaningless, dangerous, and obsolete. The formed polymorphs can be spectroscopically identified and they create dangerous interfaces after their sharp onset with the non-transformed material. Polymorph interfaces are sites for crack nucleation.

For the mathematical description of the pyramidal or conical indentations on a physical basis the formulas from [1] are below extended and completed, and their use is outlined. For their deduction it was first necessary to distinguish applied work $W_{applied}$ from indentation work W_{indent} [1]. The latter is the work for the impression. The former contains additionally the work for pressure formation to its environment and all types of plasticizing. The whole indentation process subdivides 80% of the applied force for the inverted pyramid or inverted cone formation and 20% of it for pressure and all kinds of plasticizing. This always mathematically precise 4:1 ratio in (15.3) has been mathematically deduced in 2013 [1]. In the case of phase-transition upon indentation the sharp kink

unsteadiness occurs in the F_N vs $h^{3/2}$-plot, separating linear branch 1 from linear branch 2 with different slopes k_1 and k_2. These are the different penetration resistances (hardnesses), in e.g. mN/μm$^{3/2}$ units of the involved polymorphs. The h_{kink} and the $F_{N\text{-}kink}$ values for $W_{1\text{-}applied}$ are easily obtained by equation of the regression line formulas from the two branches for the triangle Equation (15.4). For the $W_{2\text{-}applied}$ value one has to integrate (15.2) to give (15.5) that is multiplied with 1.25 according to (15.3) and it is added to $W_{1\text{-}applied}$ for obtaining $\Sigma\ W_{applied}$. The latter is subtracted from full $W_{applied}$ to obtain the transition work $W_{transition}$ up to h_2 [1,9] (h_2 is freely chosen; perhaps at the depth where another kink deviation starts). The transition-energy is calculated according to (15.7). Its normalization is now by division through the depth difference (15.8) (no longer through the force difference) for better comparison of different indenter tips.

An analogous procedure is applied for multiple phase-transitions from kink to kink. That purely algebraic sequence of calculations has been performed to numerous materials by the present author for endothermic and exothermic phase transitions under load. These will now be augmented with different materials and comparison of two different indenters. Again, phase-transitions cannot be obtained by iterative fittings including finite element calculations. Their onset forces and transition energies are important for daily life security, because the formation of polymorph interfaces can be sites of catastrophic initiations of crashes.

$$F_N = kh^{3/2} \tag{15.1}$$

$$F_N = kh^{3/2} + F_a \tag{15.2}$$

$$W_{indent} = 0.8\ W \tag{15.3}$$

$$W_{indent} = 0.8W_{1\text{-}applied} = 0.5h_{kink}F_{N\text{-}kink} \tag{15.4}$$

$$W_{2\text{-}indent} = 0.4k_2(h_2^{5/2} - h_{kink}^{5/2}) + F_{2\text{-}a}(h_2 - h_{kink}) \tag{15.5}$$

$$\text{full}\ W_{applied} = 0.5F_{N-max}h_{max} \tag{15.6}$$

$$W_{transition} = \text{full}\ W_{applied} - \Sigma(W_{applied}) \tag{15.7}$$

$$\text{normalized}\ W_{transition} = W_{transition}/(h_2 - h_{kink}) \tag{15.8}$$

15.2 MATERIALS AND METHODS

A fully calibrated Hysitron Inc. Triboscope® Nanomechanical Test Instrument with 2D transducer, leveling device, and direct combination with a Nanoscope II atomic force microscope (AFM) was used for the author's (nano)indentations. Loading times were 30 sec, force-controlled in contact mode. The radii of the cubecorner (55 nm) and Berkovich (110 nm) diamond indenters [4] were directly measured by non-contact AFM at a Park NX20 atomic force microscope from

Park Systems. Highly resolved microscopic images were obtained with a digital 3D microscope from Keyence Ltd., model VHX - 100 K with almost uniform coaxial vertical illumination through optical fiber, ring lenses, and 45˚ half mirror. A CCD-camera recorded the light of the halogen lamp, as coaxially reflected back by the sample through the half mirror. The chosen focal depth steps were down to 1 µm.

Most preferable for the analysis of AFM loading curves is the direct calculation of all instrumental data points (about 20,000) according to (15.2) as loaded to Excel®. For published loading curves, with reasonable experimental description, the data digitization is obtained after paper filling enlargement with the plot digitizer 2.5.1 program (https://www.softpedia.com/) giving 50 - 70 data-pairs, or manually 20 to 30 data pairs. Visual inspection of the printed Excel® F_N vs $h^{3/2}$ plots look for the linear ranges, surface effects, obvious gradients, and other peculiarities (e. g. non-linear force application). The kink is sharp, but there might be some short soft transitions in buffering biological materials [10] or at too rapid penetration. The bearing analysis routine [11,12] is used for the measurement of depression and pile-up volumes with respect to the plane through the respective edges and corners. We did not use the complicate formulas with numerous assumptions of [13].

Fig. 15.1 looks quite smooth but Fig. 15.2 shows a much extended initial effect, some minimal displaced points in the kink region and a deviation above 90 mN load. The initial effect study would require separate indentation to about 20 mN load. It is possible that there is another transition, as perhaps twinning. Endothermic twin formation of tungsten is indeed initiated by application of shear-force to tungsten [14]. The final deviation must here be excluded from further consideration, because it also occurs comparably with 6 materials all above 90 mN load in [8]. But for k_1 and k_2 there exists no ambiguity due to correlation coefficients R^2 of 0.9995 and 0.9996. It appears to be a poor instrumental compliance above 90 mN or non-linear force application from that point. This has been revealed in [15]. Our analysis is versatile enough to reliably determine the phase-transition energy despite such particular difficulties. This technique is not of the Arrhenius type and does not require indentations at different temperatures as with activation energies from indentations as in [16].

The formulas (15.1) through (15.7) contain all information, but a step-to-step description of the calculation is also necessary. Due to exponents, sums and differences it appears necessary to calculate with 10 figures, so that the experimental errors are not increased by the calculations. For the transition energies we equate the regression lines (R^2 must be >0.9995) $F_{N\text{-}1} = k_1 h^{3/2} + F_{a\text{-}1}$ and $F_{N\text{-}2} = k_2 h^{3/2} + F_{a\text{-}2}$ to obtain $h_{kink}^{3/2}$, h_{kink}, $h_{kink}^{5/2}$, and $F_{N\text{-}kink}$. $W_{1\text{-}applied}$ is then calculated according to (15.4). *W* stands for work or energy. The subscript "kink" describes the sharp intersection of the regression lines that is the "kink-unsteadiness" at the onset point (depth and force) of the phase-transition.

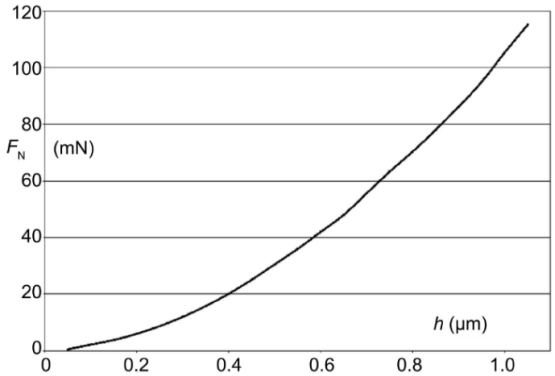

Fig. 15.1. Force vs depth image with Berkovich onto tungsten from Fig. 15.9 in [8]

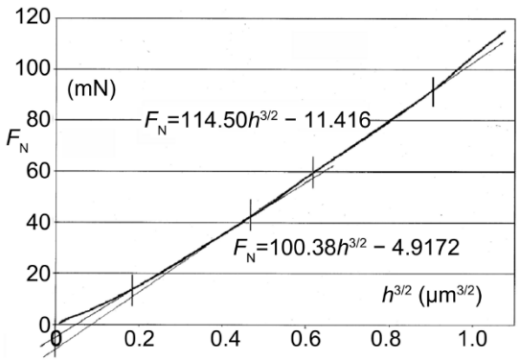

Fig. 15.2. F_N vs $h^{3/2}$ plot according to (15.2) of the curve in Fig. 15.1) with regression equations in the selected ranges (kink at 0.460254957 μm$^{3/2}$ and 41.28319258 mN); the slopes are the physical hardness k (mN/μm$^{3/2}$); the initial part is cut off and should be separately studied with lower force range; a short intermediate range around the kink point is not part of the regression

The force value F_{end} (>$F_{N\text{-}1}$) for the calculation of $W_{2\text{-applied}}$ can be chosen at will (in the case of a following higher phase-transitions one chooses the value for $h_{max} = h_{kink\text{-}2}$). One then calculates $h_{max}^{3/2}$, h_{max} and $h_{max}^{5/2}$ for $F_{N\text{-}max} = k_2 h_{max}^{3/2} + F_{a\text{-}2}$ .With these and obtains $\Delta h^{5/2} = h_{max}^{5/2} - h_{kink}^{5/2}$ and $\Delta h = h_{max} - h_{kink}$. One has thus all mathematical values for the calculation of the indentation work. $W_{2\text{-indent}}$ according to (15.5) gives $W_{2\text{-applied}}$ = 1.25$W_{2\text{-indent}}$ according to (15.3), so that Σ $W_{applied}$ can be formed. The value of full $W_{applied}$ is 0.5F_{Nend} h_{end}, because the previous calculations corrected for both axes cut $F_{a\text{-}1}$ and $F_{a\text{-}2}$.

The transition-energy (15.7) $W_{\text{transition}} = \text{full}\, W_{\text{applied}} - \Sigma W_{\text{applied}}$ is then divided by Δh to finally obtain normalized $W_{\text{transition}}/\mu\text{m}$ (mNμm/μm) values. These characterize the phase-transition onset of the material in question. Different materials can be compared and calculations for any wished depths and forces are possible. A corresponding sequence applies for higher phase-transitions at higher forces.

15.3 RESULTS

15.3.1 Verification of the Transition-Energy Calculations

The determinations of the phase-transition energies are tested at a practical example from the literature. For example, Fig. 15.1 shows the F_N vs h curve that is the basis of the still used iterative ISO-hardness (H_{ISO}) and ISO-modulus of tungsten, which is used as indentation standard, and not considering the phase-transition unsteadiness for calibrations up to 120 mN, even though compliance or linearity are unfortunately miscalibrated (also for the other standard materials in [8]) and despite the particularly pronounced flaws that are challenged in the Introduction. We open the possibility for nevertheless using such published experimental loading curves for the non iterative penetration resistance (k mN/μm$^{3/2}$) calculation and detection of phase-transitions with their onset force and phase-transition energy in the valid regions.

The purely arithmetic calculations remove the initial effects, less precise data-pairs close to the kink point, and deviations due to non-linear force applications. After these strict precautions it can be tested whether the same result is obtained for $W_{\text{transition}}/\mu\text{m}$ when the different selected forces at 60 and 90 mN are chosen from the tungsten curves in the Fig. 15.1 and Fig. 15.2. Table 15.1 collects the test results as calculated according to (15.1) - (15.8) with 10 figures. The calculated values of $W_{\text{transition}}/\Delta h$ from the different end forces confirm the correctness of our formula scheme. The very low differences of 0.665×10^{-6} % (due to rounding) also confirm that the errors by the calculation using exponents, summations and subtractions strongly disappear in relation to unavoidable experimental errors.

It is therefore advisable to perform a computer program for the calculation of phase-transition energies in the future. However, the independent expert scrutiny by using the physically correct F_N vs $h^{3/2}$ plot of the experimental data from conical or pyramidal indentations remains indispensable. The situation with unfitted data of spherical indentations is described in [17] and [18].

This Table 15.1 indicates the calculation procedure and the precision of the calculations with 10 significant figures for at the end obtaining reasonably rounded results. The normalization of the transition energy at the onset kink point is now per depth region ($h_{\text{final}} - h_{\text{kink}}$).

Table 15.1. Calculation test from $F_{N\text{-}1} = 100.38h^{3/2} - 4.9172$ and $F_{N\text{-}2} = 114.50h^{3/2} - 11.416$ for $W_{transition}$ of tungsten at different chosen end forces from Fig. 15.2

F_{end}	60 (mN)	90 (mN)
h_{kink} (µm)	0.596118111	0.596118111
F_{Nkink} (mN)	41.28319258	41.28319258
$W_{applied\text{-}1}$ (mNµm)	12.30482939	12.30482939
Δh (µm)	0.133888326	0.326171522
$\Delta h^{5/2}$ (µm$^{5/2}$)	0.180953682	0.542532597
$W_{indent\text{-}2}$ (mNµm)	6.759209506	21.12441884
$W_{applied\text{-}2}$ (mNµm)	8.449011820	26.40552356
S$W_{applied}$ (mNµm)	20.75384127	38.71035295
Full $W_{applied}$ (mNµm)	21.90019311	41.50303349
$W_{transition}$ (mNµm)	1.14635184	2.792680535
$W_{transition}/\Delta h$ (mNµm/µm)	8.561999946	8.561999889

15.3.2 Phase-Transition Energies

It is important to distinguish the modification of the indented material and the indented surface of crystals. For example quartz (SiO_2) occurs as amorphous fused quartz and *α*-quartz (rocksalt), the latter with surface twins that can be cautiously removed by polishing if necessary. Also water layers will form at ambient atmosphere. Furthermore, Cristobalite, Coesite, Stishovite, and Seifertite are at ambient conditions metastable polymorphs of quartz. The latter two have been synthesized and are also known as Meteor crystals. The indentation onto Stishovite produced probably Seifertite and another still higher energetic as yet unknown polymorph, but none of the lower energy polymorphs of SiO_2. All of these give different results upon indentation [9].

The amorphous to amorphous transition of fused quartz is well known. Nevertheless the present ISO 14577 still uses fused quartz for indentation-instrument calibrations, which is another source of error when not taking care of it. The phase-transition energies can be negative (exothermic) or mostly positive (endothermic). The exothermic ones of iron (100) and (110) as well as of $InGaAs_2$ have been published in [15] and [19]. Also the 5 indented different faces of *α*-SiO_2 undergo the phase-transition exothermically [15] and [19].

The already published indentations with endothermic phase-transitions of superalloys including aluminium and *γ*Ti-6Al-4V in [19] are of particular importance in view of flying safety and require most scrutiny. Light titanium-aluminium-vanadium alloys are the preferred materials for airplane constructions. The present author complained in his publication [19] and in preceding world-wide lectures the low phase-transition onset forces and the low phase-transition energy of *γ*Ti-6Al-4V alloy that are much inferior with respect to pure aluminum and superalloys. For example, the phase-transition onset of the Vitreloy-105 metallic glass occurs at 58 fold higher onset force and at 108-fold higher phase-transition energy. All of the various researchers who indented onto and published

on this and related TiAlX alloys did not check for phase transition onsets, but they persisted on the unphysical ISO-ASTM standards. They are urgently asked to reanalyze and publish their original experimental data. The present author urgently exacted and exacts that the builders of airliners must check and improve their technical alloys by physical indentation ($h^{3/2}$ not h^2 and no iterations). Phase-transitions under load must be recognized, detected, and characterized. Their onset force and transition energy must be increased with improved alloys for much higher phase-transition onset forces and transition energies. Phase-transition polymorph interfaces are crack nucleation sites that must be avoided upon operation [20]. The justification of these urgent reports followed soon: propeller blades, one with a deadly accident, broke twice from a turbine and hit the fuselage within one year from the same type of airliner. Obviously alerted by [19] and [20] hundreds of airliners were together grounded for months due to scratches even at the pickle forks between wings and fuselage, but several catastrophic airliner accidents still occurred. Unfortunately, sharp onset phase-transitions under mechanical load with their polymorph interfaces formations are not detectable with the disproved [2], but still binding ISO-ASTM standards that continue to be an enforcing part of the industrial certification. This must be urgently and immediately changed, for safer flying and safer daily life. ISO and ASTM representatives are being personally informed since long ago.

Numerous further phase-transition onsets and endothermic transition energies are published in [19] for calibration standards, silicon (two faces), strontium titanate (3 faces), numerous salts, polymers, wood, and organic crystals. These cannot be repeated here.

15.3.3 The Comparison of Berkovich with Cubecorner Phase Transitions Using the Indenter Volumes and Side-Areas

While the Berkovich indenter is ISO standard in indentation testing, the steeper cubecorner has advantages for the study of fracture toughness. Actually, the cubecorner appears more appropriate for the fracture toughness measurement by indentation and we can explain it. Fracture toughness is commonly calculated as $K = 0.036(E/H)^{1/2}(F_N/c^{3/2})$ where c is the crack length, H and E are ISO hardness and ISO falsely so-called “Young’s elastic modulus”. The 0.036 is an empirical constant “from a fit” for cubecorner, but the E/H values are taken from Berkovich indentations [21]. Clearly, Berkovich and cubecorner indentations provide different results. The strange claims in that paper of the Oliver-Pharr group that the “hardness measured with the two indenters should be about the same” and the unpardonable claim that “the cubecorner geometrically displaces more than 3 times the volume of the Berkovich” at the same force are nevertheless unduly acknowledged. For example, it is used in [21] with citation of [8]. Also Wang [23] falsely claims that the cube-corner transforms more than 3 times the volume of the Berkovich “for a given load, and thus produces “higher stress beneath the indenter”. On the other hand [24] claims that “the Berkovich indenter probes a volume approximately 8-times bigger than the cube-corner” and “the Berkovich indenter distributes the load over a wider area with respect to the sharp cube-corner indenter”. All of these contradictionary published claims are more than disturbing. Clearly, the physical hardness (k-value as slope of the

F_N vs $h^{3/2}$ plot [2]) and indentation modulus from cubecorner and Berkovich results are different. Also ISO-hardness *H* and ISO-so-called "Young's" modulus *E* depend on the indenter acuteness [24]. Numerous fitting simulations exist, but experimental comparisons on the basis of published experimental loading curves are rare. It was however not taken into account, that the cubecorner must create the same indentation volume (plus eventual pile-up volume) than the Berkovich at the same force, because the energy law cannot be disregarded. The same applied work creates the same volume. This can be seen in Table 15.2 and Table 15.3. It is not seen by Bor et al. [24] who simulated fracture toughness again with *H* and *E* from Berkovich and cracking with cubecorner on the energy law violating 1:3 volume ratio basis with Berkovich and cubecorner. This paper tries to explain the differences upon indentations with the two-dimensional shape of broader Berkovich and more acute cubecorner and a poorly comprehensible "densification" of material at the steeper cubecorner apex. Clearly, the obvious fact is not considered that the material is displaced at the faces of the tip that penetrates much deeper than the Berkovich. Inverse triangular pyramids are formed in the material with different bases and depths. And again, their totally displaced volume must be equal at the same applied force, as the energy law must not be violated (see also Section 3.5). Thus, we cannot agree at all with the lengthy argumentation in [24].

It appears urgently important to deduce an undeniable mathematical basis for the explanation of the remarkable differences between the indenters, despite of the same displaced volume (including eventual pile-up volume). There were no mathematical formulas for the volumes of Berkovich and cubecorner diamond indenters as a function of depth. These pyramids are characterized with "equivalent" cone angles and with the known angles β from centerline to face (e.g. [24]). Unfortunately, the reason for different results has never been discussed with respect to indenter volumes. These angles β are 65.27° for Berkovich and 35.264° for cubecorner [25]. They have obviously never been used for the calculation of the indenter volumes as a function of the measured depths *h*. We need them to relate the normalized $W_{transition}$ values from indentations with the different indenters and for understanding the differing mechanical parameters. These include physical hardness, transition onset and transition-energy. Unfortunately, published experimental comparative loading curves with good precision for both indenters and suitable indentation forces at related or better equal force ranges are not very abundant. But the values from Table 15.3 indicate viable examples for the mathematical evaluation. The inclined 3D-sketch of an inverted pyramid in Fig. 15.3 with the equal-sided basal triangle on top indicates how the volume and side-area of three-sided straight pyramids as a function of the angle β can be mathematically described on the basis of elementary geometric formulas, by using basic trigonometry.

For the volumes of three-sided Berkovich and cubecorner we use the mathematical formula for the area of the basal equal sided triangle ($A_{triangle} = a^2 3^{1/2}/4$) and for the volume of the pyramid ($V_{pyr} = A_{triangle} h_{pyr}/3$), The central side length *a-value* has to be translated into the h_{pyr}-value of the pyramid with the aid of the characteristic β-angle values of the pyramids (β = 65.27° for Berkovich and 35.264° for cubecorner).

Table 15.2. Influence of indenter volume and side-areas of the indenter pyramids according to Equations (13) and (14), as tested with the force-depth curves of Zerodur® in Fig. 15.10 of [26]

Force F_N (mN)	Berkovich h (µm)[a)]	Cubecorner h (µm)	Berkovich V (µm^3)	Cubecorner V (µm^3)	Berkovich 3A (µm^2)	Cubecorner 3A (µm^2)
100	0.959	2.0300	7.2011	7.2446	24.8016	18.5443
200	1.380	2.9167	21.4580	21.4882	51.3570	39.0741
300	1.718	3.6333	41.4048	41.5357	79.5954	59.4046
400	1.974	4.1806	62.8046	63.2753	105.0838	78.6493
500	2.221	4.6944	89.4531	89.5897	133.0267	99.1694
600	2.449	5.1667	119.9268	119.4075	161.7407	120.1279

[a)] The final depths at 600 mN were 2.42769 µm for Berkovich and 5.15639 µm for cubecorner

Table 15.3. Comparison of Berkovich and cubecorner indentations from published loading curves; the calculations are with the units of the k-values followed by transformation into mN and µm units and rounding from initially 10 significant figures

n	Material	k_1 k_2	$h_{trans\ onset}$ (µm)	$F_{trans\ onset}$ (µm)	$W_{transition}$ (mNµm/Δh)	Data Source
1	Zerodur Berkovich	141.81 mN/µm$^{3/2}$ 189.24	1.54678	248.2246	86.8650	Ceram Internat, Elsevier, 2016, 42, 12740, Figure 10
2	Zerodur Cubecorner	46.121 mN/µm$^{3/2}$ 62.230	3.33355	250.1074	96.4875	
3	Fused SiO_2 Berkovich	1.5289 uN/nm$^{3/2}$ 1.8347	0.09016	1.19808	0.22610	Hysitron Handbook
4	Fused SiO_2 Cubecorner[a)]	0.4480 µN/nm$^{3/2}$ 0.5561	0.18883	1.12375	0.23926	Int J Mater Res 2005 96, 1226
5	Na_2O-Al_2O_3-SiO_2	1.8868 µN/nm$^{3/2}$	0.13679	3.10289	0.388391	J Amer Ceram Soc

n	Material	k_1 k_2	$h_{trans\ onset}$ (µm)	$F_{trans\ onset}$ (µm)	$W_{transition}$ (mNµm/Δh)	Data Source
	Glass Berkovich[b)]	2.2632				2018 101, 2930, Figure 2(A)
6	Na_2O-Al_2O_3-SiO_2 Glass Cubecorner	0.4765 µN/nm$^{3/2}$ 0.6119	0.36145	3.08279	0.84159	
7	2C22 Steel stress-free, Berkovich	45.814 mN/µm$^{3/2}$ 65.225	0.92967	34.20895	14.4435	Procedia Engineering 2011, 10, 3528, Figure 1(b)
8	2C22 Steel stress-free, Cubecorner	9.1998 mN/µm$^{3/2}$ 13.139	2.38606	33.29274	11.35050	
9	Nickel Berkovich	127.56 mN/µm$^{3/2}$ 167.96	0.60051	52.75485	19.05449	Philosophical Magazine 2016, 96, 3442
10	Nickel Cubecorner	25.124 mN/µm$^{3/2}$ 31.417	1.05640	26.24538	5.899987	
11	Germaniµm Berkovich	97.083 mN/µm$^{3/2}$ 128.58	0.27330	12.53433	4.377296	Appl Phys Lett 2005, 86, 131907
12	Germanium Cubecorner[c)]	29.085 mN/µm$^{3/2}$				
13	$Cu_{60}Zr_{30}Ti_{10}$[d)] Berkovich	2.1803 µN/nm$^{3/2}$ 2.6791	0.15718	4.01683	0.969275	Mater Sci Engin A 2006, 430, 350
14	Vitreloy-105[e)] Cubecorner	29.652 mN/µm$^{3/2}$ 36.139	2.53297	107.9909	28.29528	Phil Mag 2006, 86, 5715-5728

[a)]Now calculated with all of the 475 data points; [b)]sodium aluminosilicate glass; [c)]the published cubecorner loading curve cannot be analyzed for k_2 due to rough not repairable pop-in; [d)]a second transition is at about 9 mN and 0.25 µm; [e)]$Zr_{41}Ti_{14}Cu_{12.5}Ni_{10}Be_{22.5}$.

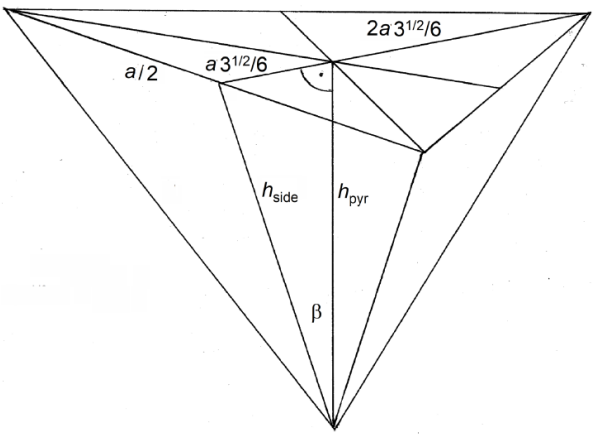

Fig. 15.3. Perspective view on a 3D wire model of an inverted straight three-sided pyramid without crossing lines. The triangles of the model are of course not distorted. The curve with a point shall indicate that there is actually a right angle at that site

For obtaining the requested formula we have to consider that the equal sided basal triangle height ($h_{\text{triangle}} = a \cdot 3^{1/2}/2$) subdivides in the 1:2 ratio at the center of the triangle, so that the short part $1/3\, h_{\text{triangle}} = a \cdot 3^{1/2}/6$ is used for $\tan\beta = a \cdot 3^{1/2}/6h_{\text{pyr}}$. One isolates *a* and obtains $a^2 = 36\tan^2\beta\, h_{\text{pyr}}^2/3$. By substitution of a^2 into A_{triangle} one obtains $A_{\text{triangle}} = 3 \cdot 3^{1/2}\tan^2\beta\, h_{\text{pyr}}^2$ and with $V = A_{\text{triangle}}h_{\text{pyr}}/3$ one obtains $V_{\text{pyr}} = 3^{1/2}\tan^2\beta\, h_{\text{pyr}}^3$ (9). The volumes of Berkovich (β = 65.27°) calculate thus as (15.10) for Berkovich and (15.11) for cubecorner (β =35.264°). Fig. 15.3 facilitates the survey of the trigonometric steps.

$$V_{\text{pyramid}} = 3^{1/2}\tan^2\beta\, h_{\text{pyr}}^3 \qquad (15.9)$$

$$V_{\text{Berkovich}} = 8.1647816h_{\text{pyr}}^3 \qquad (15.10)$$

$$V_{\text{cubecorner}} = 0.86600004h_{\text{pyr}}^3 \qquad (15.11)$$

Another point is the relation of the side-areas as a function of indentation depth that must be considered. The complete side-area $3A_{\text{side}}$ of the pyramids has not been used previously. We also determine their mathematical formula for checking how these depend on the tip angle. We use the mathematical formula for the areas of isosceles triangular side faces of the pyramid area that is $A_{\text{side}} = ah_{\text{side}}/2$. As above we first determine $a = 6\tan\beta\, h_{\text{pyr}}/3^{1/2}$. For obtaining h_{side} we use $\sin\beta = a \cdot 3^{1/2}/6h_{\text{side}}$, isolate h_{side} and substitute *a* twice to obtain after shortening out $h_{\text{side}} = \tan\beta\, h_{\text{pyr}}/\sin\beta$ these factors for *a* and h_{side} are in the

formula for A_{side}. This gives $3A_{\text{side}}$ for the Equations (15.12), or (15.13) and (15.14) with the numerical factors, for the complete inserted pyramidal side-faces.

$$3A_{\text{side}} = 3 \cdot 3^{1/2} \tan^2\beta \; h_{\text{pyr}}^2 / \sin\beta \tag{15.12}$$

$$3A_{\text{Berkovich}} = 26.96756 h_{\text{Berkovich}}^2 \tag{15.13}$$

$$3A_{\text{cubecorner}} = 4.0005 h_{\text{cubecorner}}^2 \tag{15.14}$$

We check now the experimental loading data of isotropic Zerodur® with great detail (calculation of the irrational numbers with 10 digits before reasonable rounding) in order to tell whether the inevitable tip rounding at the apex of sharp commercial quality indenters (radii about 50 nm for cubecorner and 100 nm for Berkovich) can be neglected, due to the always executed necessary axis-cut corrections. They can be neglected with this excellent published data. Clearly, blunt or broken indenters will not provide useful data; and simulated loading curves can be excluded when the calculated displaced volumes are not equal between the different pyramids or cones at the same force (but see Section 3.5).

The regression data as calculated from the load-depth curves in Fig. 10 of [26] for the calculation of the ceramic Zerodur properties are $F_{\text{N-1-Berkovich}} = 141.81h^{3/2} - 24.578$, $F_{\text{N-2-Berkovich}} = 189.24h^{3/2} - 115.82$ and $F_{\text{N-1-cubecorner}} = 46.121h^{3/2} - 30.604$, $F_{\text{N-2-cubecorner}} = 62.23h^{3/2} - 128.65$. The index 1 is before phase-transition, the index 2 after phase transition. The phase-transition onset is at 248.2246 mN for Berkovich and 250.1074 mN for cubecorner, which is practically the same value. The normalized transition energies are for Berkovich 86.8650 mNμm/Δ*h*, and for cubecorner they are 96.4875 mNμm/Δ*h*.

The corrections for the axis cuts $F_{\text{a-1}}$ and $F_{\text{a-2}}$ (15.2), which also include tip rounding, influence the calculation results considerably. They must therefore also be reported with the complete regression line equations.

The indentation onto fused quartz (n3 - n4) with Berkovich (μN, nm) gives the regression lines $F_{\text{N1}} = 1.5289h^{3/2} - 110.88$ and $F_{\text{N2}} = 1.8347h^{3/2} - 372.69$. The transition onset is at 1198.0844 μN load. The cubecorner (μN, nm) [27] gives by calculation with all of the 475 data points from the loading curve the regression lines $F_{\text{N1}} = 0.4480h^{3/2} - 38.762$ and $F_{\text{N2}} = 0.5561h^{3/2} - 319.010$ The transition onset is at 1123.7482 μN load.

For sodium aluminosilicate glass (n5 - n6) exist indentations with Berkovich and cubecorner in the same paper [22]. The published loading curve (Raw Glass-Air side) (μN, nm), as indented with Berkovich give the regression line $F_{\text{N-1}} = 1.88868h^{3/2} + 84.351$ and $F_{\text{N-2}} = 2.2632h^{3/2} - 517.82$ with a transition on-set at 3102.8851 μN load. The loading curve (Raw glass-Air side) with cubecorner (only usable up to 5000 of 9000 μN) gives the following regression lines: $F_{\text{N1}} =$

$0.4551h^{3/2} - 124.09$ and $F_{N2} = 0.581h^{3/2} - 879.33$ and the transition onset is at 2605.9316 µN load.

The Indentation of stress-free steel 2C22 (n7 - n8) has also been studied with both indenters (mN, µm) [28]. The published loading curve for Berkovich gives the regression lines $F_{N\text{-}1} = 45.814h^{3/2} - 1.8582$ and $F_{N\text{-}2} = 65.225h^{3/2} - 19.258$ mN, and the one with cubecorner $F_{N\text{-}1} = 9.1998h^{3/2} + 0.6152$ and $F_{N\text{-}2} = 13.139h^{3/2} - 15.134$ mN.

The indentation of nickel (n9 - n10) from [29] gives the regression lines from the published loading curve with Berkovich $F_{N\text{-}1} = 127.56h^{3/2} - 6.6057$ and $F_{N\text{-}2} = 167.96h^{3/2} - 25.406$ mN, and the one from cubecorner $F_{N\text{-}1} = 25.124h^{3/2} - 1.0337$ and $F_{N\text{-}2} = 31.417h^{3/2} - 7.665$ mN.

The indentation onto Germanium (n11 - n12) [30] gives the regression lines for Berkovich $F_{N\text{-}1} = 97.083h^{3/2} - 1.9363$ and $F_{N\text{-}2} = 128.58h^{3/2} - 5.8364$ mN. The k_2-value with Berkovich could not be reasonably determined from the published loading curve.

The loading curve (µN, nm) for the bulk of the $Cu_{60}Zr_{30}Ti_{10}$ alloy (n13) [31] gives the regression lines $F_{N\text{-}1} = 2.1803h^{3/2} - 301.72$ and $F_{N\text{-}2} = 2.6791h^{3/2} - 1289.7$. The transition onset is at 4016.830 mN, and the endothermic transition energy is 967.275 µNnm/Δh. A further transition onset follows at about 9000 µN load.

The loading curve of vitreloy (mN, µm) with the cubecorner (n14) [32] gives the regression lines $F_{N\text{-}1} = 29.652h^{3/2} - 11.605$ and $F_{N\text{-}2} = 36.139h^{3/2} - 37.756$.

Table 15.3 collects the results primarily from glassy ceramics (n1 - n6) for which both Berkovich and cubecorner indentations have been published. For comparison it also contains 2C22 steel alloy (n7 - n8) with an intermediate behavior, nickel (n9 - n10) as a crystalline metal, germanium (n11 - n12) with partly unsuitable data, and the metallic glasses (n13) and (n14) with "free volume" pores or shear bands formation even though these are only indented with one indented type, each. For glassy vitreloy (n14), here with the Δh normalization, we point to the possibility of partial crystallization and shear bands, as formed on the surface. It is one of the entropic metallic glasses with extremely high values of phase transition onset force and phase-transition energy. The examples (n13) and (n14) are necessary for pointing out that not all super-cooled amorphous materials solidify without pores or partial crystallization that allow for some pile-up. Such complications must also be taken care of. Fortunately, these features can now be easily determined by checking whether or not such material exhibits pile-up upon indentation or not.

The algebraically calculated mechanical results from loading curves of primarily glassy ceramics in Table 15.3 (n1 - n6) confirm the unfitted calculations from the

regression lines of F_N vs $h^{3/2}$ plots (15.1) for final applied forces from 2.5 mN (fused quartz) up to 600 mN (Zerodur®) or 500 mN (vitreloy-105). This rests on the now available volumes of Berkovich and cubecorner indenters as a function of the penetration depth. All phase-transitions in Table 15.3 are endothermic and pile-up is not possible in the isotropic materials (n1 - n6): they have no cleavage planes or channels for materials' slide. The crystalline porous alloy (n13) is an evident exception in this respect, due to pile-up formation via the pores. The 2C22 steel has still the very close correspondence with the phase-transition onset of both indenters.

Importantly, the earlier claimed 1 to 3 ratio of displaced material between Berkovich and cube corner ([21,24]) is clearly disproved. Despite the same displaced volume, the ratios of the physical hardness $k_{1\text{-Berkovich}}/k_{1\text{-cubecorner}}$ vary for the different glassy ceramics between 3.07 and 4.99 in Table 15.3 (n1 - n6). For crystalline nickel it is 5.09. It is thus not constant and cannot be related to the tanβ ratio of the indenters (3.0705), due to the different force directions and force powers. The phase-transition onset depths of the glassy ceramics vary from 0.090 or 0.189 µm of fused quartz to 0.137 or 0.362 µm of sodium aluminosilicate. But due to the displaced volume equality, the phase-transition onset forces are for these ceramics equal between Berkovich and cubecorner. The results with the glassy ceramics are particularly remarkable when the strong variations of the normalized phase-transition work from 0.23 - 96.5 mNµm/Δh are considered. The comparably very low value of fused quartz in connection with the low transition depth is a serious but mostly still not realized burden of its use as calibration standard for nanoindentations. Actually, it should only be used at forces below 1 mN for correct calibrations with Berkovich indenter and the ISO 14577 standard requires urgent revision. Conversely, Zerodur would be qualified as an indentation standard by its very high normalized transition work of 87 or 96.5 mNµm/Δh for resisting high mechanical and apparently also thermal stress in Ceran® cooking plates. The super-cooled 2C22 steel is with its 14.4 mNµm/Δh far away from that. Further published experimental curves are as yet missing. It is an interesting consequence of the energy conservation law and certainly an important tool for the ceramics industry.

The very closely identical values for the Berkovich and cubecorner volumes in Table 15.2 indicate that both indenters behave in the same way with the isotropic glassy ceramics that does not allow for slide of material that would require corrections for Equations (15.10) and (15.11). Corrections for tip rounding of sharp indenters and the compression of diamond indenters are also not necessary. These are not part of the mathematical Equations (15.9), (15.10), and (15.11). And they are at least very similar for both indenters. Our results are very close to the mathematical precision, because of the excellent mechanical qualities of the ceramics in question (e. g. Zerodur®). Any slight deviations are the result of low tip-angle precision and lack of the original data set for the data evaluation. We deal here with deep indentations and the tested materials are not super-hard. The sharp tip apex will stay sharp and its inevitable rounding is corrected together with the surface effects by F_a in (15.2). However, when indenting super-hard materials, the low elastic compliance of diamond would

require correction and the then increasing tip bluntness would have to be controlled over and over again with tapping mode AFM (but please not with the iterative penetration onto fused quartz).

We must now discuss the reasons for the differences between Berkovich and cubecorner indentations. Unlike equal displaced volumes V, the areas $3A_{side}$ of the Berkovich are about 1.3 times larger than the areas $3A_{side}$ of the cubecorner at the same force (Table 15.2), despite the much deeper penetration of the latter. The created polymorph cover upon phase transition will therefore be broader at the cubecorner side-areas than at the Berkovich side-areas at the same force. The different side face areas (15.13) and (15.14) do not change the phase-transition onset forces but they are certainly part of the differences between the transition works, as performed by Berkovich or cubecorner indentation. But the normalized phase-transition energy (15.8) values do not precisely correspond after division by the respective pyramidal surfaces $3A_{side}$ (15.13) and (15.14). The smaller transition energy value with the Berkovich indenter at the isotropic ceramics is thus not only due to its larger surface at the same indentation force. The cubecorner has to compress the same amount of the transformed polymorph from its smaller $3A_{side}$-area (Table 15.2) forming a broader cover over a much longer distance. And the polymorph is mostly less compliant than the bulk. Thus, the cubecorner has to add more compression energy for the same amount of transformed material to the endothermic phase-transition energy than the Berkovich. But this side-area influence cannot be the only reason for these differences of the $W_{tansition}$ values between the different indenters.

Perhaps more important than the side-area influence, is the force direction influence. The three-sided pyramids are three-sided "wedges" with the angle β (Fig. 15.3). The sideward force component F_{side} with influence to the phase-transition onset calculates with the simple wedge-force formula $F_{side} = F_{N\text{-}onset}/2\sin\beta$. For the phase-transition onset of e. g. Zerodur with Berkovich the direction of this force component is at the angle of 90 − 65.27 = 24.73°. One calculates $F_{\text{side-Berkovich}} = 248.2246/2\sin 65.27 = 136.6440$ mN. For the cube-corner phase-transition onset the direction of that force component is 90 − 35.246 = 54.754°. One calculates $F_{\text{side-cubecorner}} = 250.1074/2\sin 35.246 = 217.2346$ mN (1.59 times stronger than Berkovich). That is in both cases for every one of the 3 side-faces. At the phase-transition onset the cubecorner is roughly twice as deep as the Berkovich and the cube corner adds more force, which increases the endothermic transition energy over the one from the Berkovich. That is indeed observed for the glassy ceramics. The force direction is by far steeper for Berkovich and it compresses further down with lower resulting force than the cubecorner that compresses in a flatter way with higher resulting force. The graphical analysis provides 13.7° for Berkovich and 25.5° for cubecorner for the direction of the resulting force with respect to the indenter central line from the force parallelogram.

Importantly, its shallower compression direction is now also the straightforward explanation for the more efficient cubecorner indentations for fracture toughness determinations via cracks, when compared to Berkovich. These observations and

explanations clearly disprove the claim of [24] with compression of material at the apex of the cubecorner. Surprisingly, recent authors did not consider the force directional action when constructing their theories and simulations that are thus in error. Also the equal phase-transition onset forces for glassy ceramics and the different transition energies with the higher value from the cubecorner and the lower physical hardness *k* (15.1), (15.2) of the cubecorner are so reliably explained and comprehended. It's the force and the force direction from indenters that counts.

There are no problems with slide compliance in glassy ceramics. We note that all of these glasses indent without pile-up. In the absence of pile-up the phase-transition force must be equal for both indenters, and the quality of such indentations can be checked with this fact.

The novel mathematical insights are used without any correction necessity for the unprecedented facts and applications for glassy ceramics in Table 15.3 (n1 - n6). These basic insights are also valid for the further materials in Table 15.3 (n7 - n8), but further influences require corrections that are not included in the basic mathematical treatment. Pile-up and internal slide along cleavage planes would require their being reported, volumetrically measured, and crystallographically analyzed. Nothing of that is known yet, so that we need more research for developing techniques for the necessary corrections. A first partial solution is presented in Section 3.5.2. The steel in Table 15.3 (n7 - n8) is a borderline case, where the phase-transition onset force is almost the same for Berkovich and cubecorner. But the phase-transition energy value is now larger for Berkovich than for cubecorner. The differences with the ceramic examples increase enormously with anisotropic crystalline nickel with slide effects in Table 15.3 (n9 - n10). It provides a twofold difference in the phase-transition onset force between the indenters. Furthermore, the phase-transition energy is more than 3 times larger for Berkovich than for cube corner in that case. For an explanation one should at first know the different pile-up volumes for both indenters at the same force. Further difficulties with pile-up are discussed in Section 3.5.1. There is an unfortunate lack of comparative loading curves in that respect.

Before the discussion of pile-up in Section 3.5 we have to take care of reliable experimental data that must not be simulating fitted ones. The mathematical calculation of indenter volumes reveals unexpected further common errors by treating the pyramidal indenters as pseudo-cones. Unfortunately, equal base-area cones are not equivalent to the pyramids.

15. 3.4 The Undue Treatment of Pyramids as Pseudo-Cones

The now available volumes and side-areas of pyramidal indenters open new questions for the validity of the widespread use of pseudo-cones with equal base-area for the pyramids. ISO 14577 using [8], and so textbooks, and the so guided indentation research, including industrial technical applications, still believe in indentation ISO hardness *H*. Unfortunately, that relies on "projected area", or in refined form "contact area". The latter is obtained via two iterations

with 3 and then with 8 free parameters. Furthermore, it became common practice to treat the indenting pyramids as pseudo-cones with equal basal-area. This allows for easier calculations and huge savings in computer time for iterating simulations (e.g. [25] and [33]). The (half) opening angles of the pseudo-cones had been so calculated that the projected indentation area is indeed the same as with the corresponding pyramids. These almost always used angles are 70.2996° for Berkovich and 42.28° for cubecorner. But do pseudo-cone pyramids really penetrate to the same depths as pyramids? The previous Section 15.3.3 gives the answer and that is no! These so-called "effective" or "equivalent" models for pyramids are in fact (for quantification see Chapter 16) pyramidal phantoms. Their sideward force component direction angles are 90 − 70.2996 = 19.7004° (instead of 24.73°) and 90 − 42.28 = 47.72° (instead of 54.736°) for the Berkovich phantom and for the cubecorner phantom, respectively. This leads to errors in ISO-hardness and ISO-elastic modulus. Both pyramidal phantoms (Chapter 16) would give considerably flatter force direction and force power than the respective pyramids at the same applied force F_N. The resulting pseudo-cone phantom errors of the numerical data are huge. One may compare the depth differences at 600 mN load onto Zerodur (Table 15.3) between Berkovich and cubecorner of 2.73 µm, which depends on about 30° angle difference of the sideward force angle contribution. Here we have 5° or 7° smaller angles than the pyramids, which influences both depth and resulting force, as calculated via (15.15) and (15.16) at the same applied force F_N. Clearly, these "equivalent cones" are not at all equivalent to the pyramids. Our evident volume, side-area, and directional force effects have never been considered. The false use of the pseudo-cone phantoms has therefore never been challenged before.

The mathematical volume and side-area of the pseudo-cone phantoms as a function of depth calculates again straightforwardly. We use the corresponding half-opening angles α = 70.2996° and 42.28° for Berkovich and cubecorner phantomes, respectively. For the cone volume as a function of depth one starts with $V_{cone} = \pi r^2 h_{cone}/3$ and substitutes the basal r by h_{cone} via $\tan\alpha = r/h_{cone}$) to obtain without difficulty Equation (15.15). For the side-area of cones one uses $A_{side} = \pi r s$, where s is the side length. With $\sin\alpha = h_{cone}/r$ and $\tan\alpha = r/h$ followed by substitutions of r Equation (15.16) is obtained.

$$V_{pseudocone} = \pi \tan^2\alpha h_{cone}^3/3 \tag{15.15}$$

$$A_{pseudocone} = \pi \tan^2\alpha h_{cone}^2/\sin\alpha \tag{15.16}$$

Apparently, nobody figured out yet that such "equivalent cones" have not the same volume at the same force and angle as the pyramids. We test here with the pseudo-cone phantom of 70.2996° [34] for Berkovich. For cubecorner we test with the well-known old 42.28° but not with new 40.018°, as claimed in [25] (for avoiding an error of 16.2%). The numerical factors for $V_{pseudocone}$ in (15.15) for mimicking Berkovich are 8.168037 and for mimicking cubecorner (we test with the 42, 28° value) it is 0.865836. These numerical volume factors are within at most 0.04 % indistinguishable between pyramids and pseudo-cones. However, the respective volumes are different after their multiplication with the depth^3

values that are smaller with the pseudo-cones due to the lower depths (cf Berkovich and cubecorner in Chapter 16).

The numerical factors of $A_{\text{pseudocone}}$ (15.16) are 26.02765 for the Berkovich phantom and 3.86100 for the cubecorner phantom. The phantom values are thus smaller by 3.5% and by 14.2% respectively than those of the pyramids in Equation (15.13) and (15.14). This would after multiplication with the smaller depths^2 obtain smaller expected areas than with the pyramidal indents. Therefore, the equalization of pseudo-cone with pyramid and all simulations on that basis are in severe error also for that reason. The simulations of [25] are cited above. These facts are still not recognized by the simulation groups from [24,29,33,34], and many others.

The incorrect use of pseudo-cone pyramids adds to the further flaws of published experimental indentations that are now easily recognized by novel straight-forward testing. They appear often "influenced" by the hard-to-understand claims of the Oliver-Pharr group [21]. For example, further undue approaches argued with images of "broader" Berkovich coverage and "smaller" cubecorner coverage with complying material (actually after phase-transition onset it is polymorph). Their pressure distribution images [24] are more than questionable. Such claims are totally misleading and so are the extremely complicated discussions in that paper.
There were no reasons for challenging the pseudo cone phantom claims in 2017 [35-37]. The unexpected new results exclude the use of the so-called "equivalent cone angles" from that time and we apologize for their then bona fide use. All applications and conclusions are still correct in these 3 publications. Only the numerical values that depend on the α_{cone} angles of the pseudo-cone pyramids cones require correction (see Chapter 16).

15.3.5 The Pile-Up Influence

Pile-up upon indentation onto anisotropic nickel could not be corrected in Section 15.3.3, Table 15.3 (n9 - n10) due to pile-up formation. It is therefore now important to discuss the pile-up formations and effects. Anisotropic crystals with cleavage-planes and channels allow for sliding of materials along these and if they end at the indented surface, it is pile-up. Crystals are therefore the more compliant the better the force direction angle corresponds with the cleavage plane directions. That explains the anisotropy of indentation results upon indentations onto different crystallographic faces. Such sliding costs penetration depth that must be corrected for the penetration volume and it differs from material to material. Not all cleavage planes and channels end at the indented surface. There is also hidden sliding, and there are larger and smaller cleavage planes and channels with different sliding qualities in various directions. Sliding is also responsible for the differences between Berkovich and cubecorner indentations. This complicates the issue and requires detailed crystallography. The detailed crystallographic analysis of slide plane influences on not iterated physical hardness, phase-transition onset, and its energy has already been published for silicon onto (001) and (100), or α-iron onto (100), (110), and (111),

or $CaCO_3$ (three faces) in [19], or in the case of *α*-quartz onto 4 different faces. The anisotropy is explained with differently orientated channels in [15]. Crystallographic analysis of their 3D interlocking in crystals is important. One must detect the face of the crystal opposite to the skew indenter face. There might be channels that are too small for sliding but these facilitate the compliance and also induce anisotropy [15]. Some of these faces and channels end at the indented surface, others at the side faces. It might be even possible to find indentation directions on surfaces without exit from these, and sliding might end within the crystal. Furthermore, micro-porous materials will also produce pile-up.
There is no need to consider sink-in [1]. The depth of indentations is always measured from the height of the initial flat surface. And sharp pyramids like Berkovich or cubecorner indenters penetrate immediately upon contact. Their tip rounding can be neglected at sufficiently deep penetrations. Also initial surface effects are cut off by taking care of the axis cut in F_N vs $h^{3/2}$ plots [2] (Section 2).

15.3.5.1 The Common Interpretation of Pile-Up with Iterated Mechanical Properties

It is clear that the pile-up and hidden slide volume has to be added to the inverted pyramid volume, so that the mathematical depth requires correction for it. But the common ISO 14577 and ASTM guided discussion of the pile-up phenomenon for anisotropic materials does not consider cleavage planes and channels. It claims friction at the indenter instead. This must again be challenged, as it is not intelligible. The published ISO 14577 and ASTM guided publications claim that “no significant difference occurs between cubecorner and Berkovich measurements”. This has been “tested” for iterated ISO-modulus E_r and also for iterated ISO-hardness H with the pretended claim: “no fundamental difference is observed” [38]. Unfortunately, no experimental loading curves were supplied for obtaining not iterated data. The published data for 8 very different materials are within experimental error, on the basis of the 3 + 8 free parameters in the two consecutive iterations. This common ISO-ASTM procedure is still commonly used. Unfortunately, these claims would seem to include that numerous other mechanical qualities might also be without “significant difference”. Also phrases like “Friction does not significantly influence the simulation of the load-displacement response in indentations” [39] do not deny the challenged friction approach. And phrases like “Pile-up occurs due to isovolumetric plastic flow parallel to the indenter surface when the strain is concentrated directly below the indenter” [40] are incorrect. And so are the strange theories that are connected with it.

The averaged pile-up height around the indentation in [41] is obtained by AFM measurements of the indented surface, but this does not include the volume of the pile-up. Pile-up falsifies the ISO hardness H and ISO modulus E_r enormously (H up to 60% error, sometimes even 80% error, and E_r up to 30% error), because the “contact depth is falsified”. It is well-known, but most colleagues live with it. For example [42] complains it. But ISO-H and ISO-E_r values are nevertheless used in its finite element simulations. The current argumentation includes h_f/h_{max} ratio (h_f for $h_{max} + h_{pile\text{-}up}$), strain hardening coefficient n and E/σ_y, averaged pile-

up heights (instead of pile-up volumes), "indentation size effects" (instead of phase-transitions), and work hardening. All of that is published instead of considering the papers [1] and [2]. The contents of these were also long before discussed in numerous worldwide conferences.
Unfortunately, the faulty simulations of [42] stimulated the belief in even more extended simulations and iterations with finite element analysis. These include in their calculation not less than the complexity of h_f/h_{max} ratios, ISO-hardness H, ISO-modulus E_r, contact stiffness S, indentation size effect (ISE), pile-up height, strain hardening exponent, strain hardening coefficient, stress and strain, yield point, yield strain, yield stress, Poisson's ratio, equivalent strain energy elastic and elastoplastic, tip angle, cone model of Berkovich, deformed volume with Johnson's cavity model, total indentation work, and friction coefficient with numerous fitting constants [40]. Numerous of these building blocs are iterated ones. These more than complicated techniques are included in "inverse estimation iteration techniques".

Enormous iterations are used for describing the pile-up topography with an algorithm, but still not for the pile-up volume. Furthermore, there are different contradicting approaches and simulations. None of them help for understanding the pile-up events. And none of them invoke cleavage planes and channels of the materials. Such simulations did not distinguish between isotropic and anisotropic solids. Thus, all of these enormous diverting simulations and iterations are obsolete.

15.3.5.2 The Solution with Pile-Up Volume along Cleavage Planes

Fortunately, the physical hardness k [$F_N/h^{3/2}$] of pyramidal and conical (with cones) indentation, which is in accordance with the energy conservation rule [1], [2], is not invalidated by any pile-up. The latter is however influencing the steepness of the straight regression line. The failure of the simulations as challenged in Section 15.3.5.1 derives from their inability to take care of cleavage planes and channels, of directional force effects, and of phase-transitions. All pile-up considerations must additionally care for "free volume" pores, which also enable slide possibilities upon stress.

We must now more detailed discuss the reasons for pile-up. Cleavage-planes and or channels for the sliding of locally stressed materials are always present in the anisotropic crystalline matter. Slide possibilities along cleavage planes and channels must always be considered. They are revealed from proper crystallographic analysis and can facilitate the crystals compliance. Ample examples with crystal packing images are available in [15,19], and [43].

In order to prove the slide of material along the cleavage planes for pile-up, we looked for a suitable system with only one type of parallel cleavage planes that can be checked from different directions. And we determined the volume and shape of the pile-up. The organic molecule thiohydantoin crystallizes with parallel not interlocked molecular sheets in space group ($P2_1/c$) and melts at 230˚C. It is a particularly suitable example with 66˚ steep unimolecular sheets that have the

single cleavage plane direction for slide between them. The sheets and thus the parallel cleavage planes end on the (110) surface.

The model in Fig. 15.4 shows the different indentations with a cube corner indenter upon ramp scratching (indentation with increasing force along a predefined horizontal distance) in direction (a), (b), (c), and (d) from 0 - 400 µN load over a distance of 10 µm. The pile-up can now be freely selected from none, equal, and equal with perhaps slightly more than equal, as compared with the depression volume. The last possibility would mean that some broken edges added to the pile-up. The impressive interactive color images are freely available in [44].

The scratch against the sloping (dir. c) (Fig. 15.4) provides almost no pile-up, because the sheets are pushed down. The scratch with the sloping (dir. a) provides pile-up to both sides with a pile-up volume equal or perhaps slightly larger than the depression volume. Due to overlapping pile-up it does not leave well defined reference edges and corners. The volume can thus not precisely be quantified with AFM and the bearing analysis routine [11,12] in that case. Most interesting is the scratch along the sheets' direction. It depends on the orientation of the crystal whether all of the pile-up occurs to the left (dir. b) or upon turn of the crystal by 180˚ to the right side (dir. d) of the scratch direction onto the (110) face. In these cases, the pile-up volumes are equal to the depression volume. For example, the ratio for the measured dir. b direction is 2.661 μm^3 (pile-up) to 2.588 μm^3 (depression). No pileup is formed by normal indentation onto the (10-2) faces left or right of the crystal (Fig. 15.4). The sliding migrations from the penetrated sheets cannot exit the crystal in these cases. Such internal slide is "lost pile-up" that also detracts from the mathematical depth and volume values.

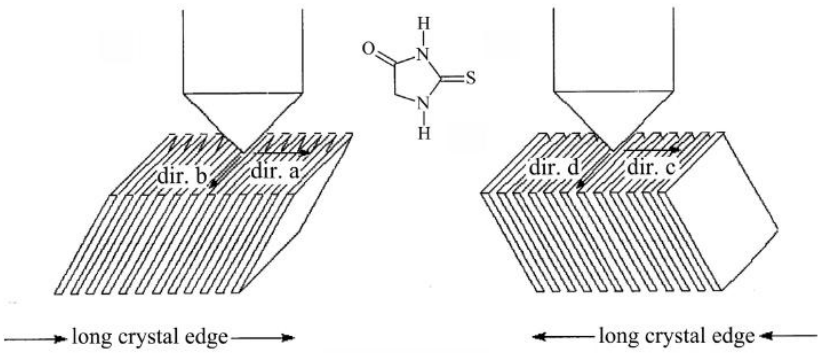

Fig. 15.4. Two geometric models at 0˚ and 180˚ orientation of the 66˚ skew monolayer sheet packing of thiohydantoin, indicating the four different indentation orientations for the ramp scratches with cubecorner indentation; the model is redrawn in part from [44]

This model is fundamental and convincing due to only one skew cleavage plane direction between unimolecular sheets. Further examples for pile-up to the right or to the left hand side, just by turning the crystals by 180°, are known from [44] and [45] for anthracene or for tetraphenylethene with their skew cleavage plane directions. These examples rest on their proper crystal structure analyses.

The situation is more complicated for crystals with more than one type of cleavage or channel directions. All of them require identification and indentation in the respective directions. Such as yet missing studies with crystalline materials (except from the present autor in the Chapters 5, 7, 8) will open the possibility to develop the corrections of the undeniable mathematical formulas for indenter volume and side-face. Practical applications will become unavoidable with that endeavor.

It is essential to always calculate the pile-up volumes (not only the average height) with the bearing analysis routine [11,12] on the basis of the plane through the respective corners. Unfortunately, such volume calculations are as yet not performed at the expense of only image topologies with AFM or of their simulation by using finite element calculation routines. Our striking results with thiohydantoin, anthracene, and tetraphenylethene disprove the validity of conclusions from pile-up height simulations. It's the volume that counts!

In fact, most crystalline materials of all types are much more complicated than thiohydantoin, anthracene, and tetraphenylethene due to numerous cleavage planes in different directions for sliding materials. All of these must be studied by indentations onto various faces to experimentally check their efficiency (angle and width). It might also be possible to find directions without pile-up. Hidden sliding occurs when cleavage planes or sufficiently wide channels cross the indentation direction.

A special case is remote pile-up about 50 to 200 µm from the indentation center. The Vickers impression onto crown glass at 50 N load is an example where these are symmetrically in line at right angle [26]. Clearly, there is materials slide along submicron cracks, as formed upon stress relief. In the case of flint glass such submicron cracks are unsymmetrical and so are the long-range pile-up features. Both glasses are amorphous and brittle though.

We remind here another long-range crack initiation and completion with the detection of the two-step nucleation in NaCl that happened upon depth-sensing Vickers indentation with the polymorph after its 5th phase-transition at 24.43 N load [20]. At 28.5 N load and 6.1 mm (!) from the indentation center occurred a mini-thin crack trace. It was detected at 5000X magnification with the 3D digital microscope. This tiny micro-crack nucleated a 5 µm short pre-crack with 1.68 µm width. Upon the further load the crack resumed from the continued micro-crack and completed without pile-up, while the load was continuously increased. At 29.8 N load the macroscopic crack was 8.5 µm wide. At 50 N load after 5.8 mm length the crack was 11.2 µm wide and 3.12 µm deep at the exit from the sample end. Clearly, long-range release of the stress due to the compacting imposed by

the indenter can be released along micro-cracks. Depending on the material there can be crack nucleation (crystal) or distant pile-up (glass).

Long-range pile-up is also possible with porous materials (e. g. the metallic glass $Cu_{60}Zr_{30}Ti_{10}$ with pores in Table 15.3 (n13). Isotropic materials like Zerodur or fused quartz help themselves by phase transition with polymorphs around the indenter.
The compression of the diamond indenter that is not corrected for, does not visibly affect the use of (15.9), as shown by the results of Table 15.3. Also the amorphous to amorphous phase-transitions (from floppy to rigid [4]) do not affect the results. But in case of pile-up we do not know yet. But see Chapter 16. Again, phase transitions are not seen in F_N vs h loading curves but only in there-from calculated F_N vs $h^{3/2}$ plots.

All of the here presented unprecedented facts can not be recognized by fitting simulations. Unfortunately, they are thus unthinkable by the common ISO 14577-ASTM standards that are still confined to the Oliver-Pharr iterations of 1992. And these are not obeying the energy conservation law (see [1] [2]).

Further comparisons of Berkovich and cubecorner indentations onto crystalline materials with forces well beyond the phase-transition onset are badly required.

15.4 CONCLUSIONS

The consideration of volume, side-area, and resulting force direction of pyramidal or conical indenters straightforwardly replaces numerous incorrect common dogmas with easy self-evident unprecedented cognition. This paper describes novelties from the mathematical treatment of indentations in great detail, so that it can be easily reproduced. Poor experimental data that do not give straight line F_N vs $h^{3/2}$ plots or fitted false linear F_N vs h^2 ones can be and must be excluded from consideration. Also, instrumental miscalibration, or denial of phase-transitions from [8] is still falsifying all of the 6 common calibration standards as reveled in [15]. Incredibly, the long-revealed phase transitions from all of them are still disregarded in the ISO 14577-ASTM standards! ISO-H and ISO-E_r are unphysical and thus very dangerous characterizations of technical materials. Only undeniable calculation rules characterize phase transition onsets (depth and force) and transition energies. The advanced normalization of phase-transition energies per $\Delta h = (h_{polymorph} - h_{onset})$ allows for mathematical comparison of Berkovich and cubecorner energies. The reliability of the precise calculations has been shown. They do not increase experimental errors by rounding errors.

Isotropic ceramics proceed without complications. They are particularly useful for understanding the differences between pyramidal or conical indentations. The formulas for the volumes, side-areas for pyramids and for cones as functions of penetration depth, and the angle dependent force directions are straightforwardly deduced and used. The sidewise wedge-type force of the indented cubecorner is 1.59 times stronger than the one of the Berkovich indenter at the same applied

force. Thus, cubecorner with higher force, flatter resulting force direction, and lower side-area is better for fracture toughness determinations than Berkovich at the same applied force.

The undeniable mathematical formulas are experimentally realized for ceramics lacking pile-up. The previous widely acknowledged claims of 3-times larger displaced volume for cubecorner as compared to Berkovich at the same indentation force is mathematically and physically disproved without using any iteration.

The very widespread mimicking of pyramids with "equivalent" cone angles for the same projected indentation area is in severe error (depth, force, angle, hardness, etc) and must be urgently cancelled (see Chapter 16). The straightforward consideration of basic physics and mathematics identifies the chimera.

The occurrence of pile-up with anisotropic crystalline material creates indentation volumes with different amounts for Berkovich and cubecorner. The pile-up requires a completely new understanding. The previous view of pileup claiming friction of indenter with material and the unintelligible nebulous claims of materials "slip" are straightforwardly rejected. Both pile-up to the surface and hidden "pile-up" within the materials use cleavage planes or channels or cracks for sliding under the mechanical stress. Several of these paths in different directions and with different widths produce different results on different faces (anisotropy) and with different indenters (force direction). That is demonstrated using the new insights from this paper and by stressing the crystallographic techniques. Pile-up is definitely not produced by friction with the indenter. The non-appreciation of the crystallographic facts by the ISO 14577-ASTM indenter community led to extremely complicated iterative worthless simulations that are not helpful for materials mechanics. Iterative pile-up simulations are extremely dangerous when applied to technical materials. These facts are experimentally confirmed with indentations including pile-up volume measurement. Pile-up management has been exemplified using skew single cleavage plane orientations in crystals.

The new insights from the indenter volume and side-area formulas have numerous practical applications. The arithmetic equations are valid both for isotropic and for anisotropic materials, covering physical hardness, initial surface effects, and phase-transition-onsets, -forces, and -energies. The comparison of Berkovich and cubecorner indenters at the same force has the physical indentation hardness ($mN/\mu m^{3/2}$) always smaller with the cubecorner, due to the deeper penetration. Only the ratio variations cannot be judged without further experimental data.

For isotropic materials the necessary phase-transition onset forces are equal for Berkovich and cubecorner, but the phase-transition energies are larger for the cubecorner due to its smaller β-angle (center line to side face) with flatter direction of the higher resulting force from the smaller side-area. For anisotropic materials the comparison of the different indenters is less predictable, because

pile-up and internal sliding volume has to be added to the impression volume, and the applied force to depth ratio is decreased. Different resulting forces meet the existing cleavage planes and channels at a different angle. Much more experimental research is required for finding appropriate predictive rules. The necessity to measure any pile-up volume (not only AFM topography) and to reveal cleavage planes, channels, and pores is stressed.

The previous errors and the ones from non-consideration of phase-transitions must and can be corrected with the novel insights from this publication. But there is presently a lack of comparative indentions with different indenters onto crystalline materials with applied forces beyond their phase-transition onsets. Further research on these lines will help for a safer daily life.

15.5 OUTLOOK

The present author asked ISO officials for early revision of ISO 14577, but that takes time for various non-mathematical reasons.

The unprecedented use of volume, side area, and force direction of pyramidal and conical indentations open numerous unexpected fields of research and unexplored applications. The background is undeniable calculation rules, but never simulative fitting of experimental data on the basis of incredibly difficult “theories”, which still violate the energy conservation law from the beginning.

The here described first novel results require further development with new experiments and development of computer programs beyond the common Excel® features. Fast data calculation in huge comparable indentation series will enable the development of technical materials with much better and physically correct mechanical properties. The data validity checks remain with the F_N vs $h^{3/2}$ plot. Examples are improved light alloys with systematically changing compositions for much better mechanical properties, particularly in view of phase-transition unsteadiness under load.

The indentation science and the involved industry must try to discard iterative simulations and try to correct the characterization of technical materials. It must no longer trust in unphysical though still enforcing ISO 14577-ASTM hardness and modulus with their numerous there from deduced and perpetuated unphysical materials parameters. We remind here the broken propellers-blades in front of the turbines hitting the fuselage of airliners, and also the hundreds of grounded airliners since 2019 with cracks at the fuselage, including cracks even at the pickle forks between wings and fuselage, most likely due to constructions with TiAlV alloy. And there were still several catastrophic airliner accidents. The TiAlX alloys exhibit comparably low phase-transition onset forces and energies, forming polymorph interfaces as sites for crack nucleation upon mechanical stress. Considerably improved alloys have to be immediately developed on the physical and mathematical basis, not only for the aviation industry.

Furthermore, unsolved problems promise unexpected new advancements and applications. The mathematical comparison of physical hardness (k-value $F_N/h^{3/2}$) between different indenters requires further investigations with new comparative indentation experiments. The angle β (Fig. 15.3) must certainly play an important role in that endeavor. Correction of the indentation volume with the pile-up volumes on all different materials surfaces can be helpful for structural decisions. Such studies promise important new materials properties that are not at all available by iterations.

It is to be hoped that young researchers, who are not caught with extremely complicated simulations and iterative data fittings, will continue with using undeniable self-explaining mathematics for the indentation research. By doing so, they will reveal further physical effects that are responsible for the transition energy differences between Berkovich and cubecorner. Further pyramidal or conical indenters for anisotropic materials should be included.

COMPETING INTERESTS

Author has declared that no competing interests exist.

REFERENCES

1. Kaupp, G. (2013) Penetration Resistance: A New Approach to the Energetics of Indentations. Scanning, 35, 392-401. https://doi.org/10.1002/sca.21080
2. Kaupp, G. (2016) The Physical Foundation of $F_N = k\ h^{3/2}$ for Conical/Pyramidal Indentation Loading Curves. Scanning, 38, 177-179. https://doi.org/10.1002/sca.21223
3. Kaupp, G. and Naimi-Jamal, M.R. (2004) Nanoscratching on Surfaces: The Relationships between Lateral Force, Normal Force and Normal Displacement. International Journal of Materials Research, 95, 297-305.
4. Kaupp, G. and Naimi-Jamal, M.R. (2010) The Exponent 3/2 at Pyramidal Nanoindentations. Scanning, 32, 265-281. https://doi.org/10.1002/sca.20206
5. Kaupp G. The Non-Equivalence of Pyramids and Their Pseudo-Cones: Important New Insights. Journal of Applied Mathematics and Physics. 2022 Apr 2;10(4):1158-66.
6. Kontomaris SV, Malamou A. Revisiting the theory behind AFM indentation procedures. Exploring the physical significance of fundamental equations. European Journal of Physics. 2021 Nov 30;43(1):015010.
7. Tang D, Zhao L, Wang H, Li D, Peng Y, Wu P. The role of rough surface in the size-dependent behavior upon nano-indentation. Mechanics of Materials. 2021 Jun 1;157:103836.
8. Oliver, W.C. and Pharr, G.M. (1992) An Improved Technique for Determining Hardness and Elastic Modulus Using Load and Displacement Sensing Indentation Experiments. Journal of Materials Research, 7, 1564-1583. https://doi.org/101557/JMR.1992.1564

9. Kaupp, G. (2020) Indentation onto Stishovite (SiO_2), MgO, and a Covered Superalloy: "Pop-In" Repair, Phase-Transition Onsets, Polymorph Energies, and Transition-Energies. Advances in Materials Physics and Chemistry, 10, 77-95. https://doi.org/10.4236/ampc.2020.103007
10. Kaupp, G. (2021) Undue Hardness/Modulus Ratio Claims Instead of Physical Penetration Resistance and Applications with Mollusk Shells. Advances in Materials Physics and Chemistry, 11, 45-57. https://doi.org/10.4236/ampc.2021.112005
11. Kaneko, R. and Hamada, E. (1993) Microwear Processes of Polymer Surfaces. Wear, 162-164, 370-377. https://doi.org/10.1016/0043-1648(93)90520
12. Han, Y., Schmitt, S. and Friedrich, K. (1999) Nanoscale Indentation and Scratch of Short Carbon Fiber Reinforced PEEK/PTFE Composite Blend by Atomic Force Microscope Lithography. Applied Composite Materials, 6, 1-18. https://doi.org/10.1023/A:1008812915701
13. Oila, A. and Bull, S.J. (2003) Nanotesting in Gear Steels. Zeitschrift für Metallkunde, 94, 793-797. https://doi.org/10.3139/146.030793
14. Wang, X., Wang, J., He, Y., Wang, C., Zhong, L. and Mao, S.X. (2020) Unstable Twin in Body-Centered Cubic Tungsten Nanocrystals. Nature Communications, 11, Article No. 2497. https://doi.org/10.1038/s41467-020-16349-8
15. Kaupp, G. (2019) Phase-Transition Energies, New Characterization of Solid Materials and Anisotropy. Advances in Materials Physics and Chemistry, 9, 57-70. https://doi.org/10.4236/ampc.2019.94006
16. Kaupp, G. (2014) Activation Energy of the Low-Load NaCl Transition from Nanoindentation Loading Curves. Scanning, 36, 582-589. https://doi.org/10.1002/sca.21158
17. Kaupp, G. (2019) The Loading Curve of Spherical Indentations Is Not a Parabola and Flat Punch Is Linear. Advances in Materials Physics and Chemistry, 9, 141-157. https://doi.org/10.4236/ampc.2019.99012
18. Kaupp, G. (2020) Real and Fitted Spherical Indentations. Advances in Materials Physics and Chemistry, 10, 207-229. https://doi.org/10.4236/ampc.2020.1010016
19. Kaupp, G. (2019) Physical Nanoindentation: From Penetration Resistance to Phase- Transition Energies. Advances in Materials Physics and Chemistry, 9, 103-122. https://doi.org/10.4236/ampc.2019.96009
20. Kaupp, G. (2018) Six Polymorphs of Sodium Chloride upon Depth-Sensing Macroindentation with Unusual Long-Range Cracks Requiring 30 N Load. Journal of Material Sciences and Engineering, 7, 473-483. https://doi.org/10.4172/2169-0022.1000473

21. Harding, D.S., Oliver, W.C. and Pharr, G.M. (1994) Cracking during Nanoindentation and Its Use in the Measurement of Fracture Toughness. MRS Online Proceedings Library, 356, 663-668. https://doi.org/10.1557/PROC-356-663
22. Li, X., Jiang, L., Mohagheghian, I., Dear, J.P., Li, L. and Yan, Y. (2018) New Insights into Nanoindentation Crack Initiation in Ion-Exchanged Sodium Aluminosilicate Glass. Journal of the American Ceramic Society, 101, 2930-2940. https://doi.org/10.1111/jacc.15465
23. Wang, Y. (2016) Effects of Indenter Angle and Friction on the Mechanical Properties of Film Materials. Results in Physics, 6, 509-514. https://doi.org/10.1016/j.rinp.2016.08.008
24. Bor, B., Giuntini, D., Domenech, B. Swain, M. and Schneider, G. (2019) Nanoindentation-Based Study of the Mechanical Behavior of Bulk Supercrystalline Ceramic-Organic Nanocomposites. Journal of the European Ceramic Society, 39, 3247-3256. https://doi.org/10.1016/j.jeurceramsoc.2019.03.053
25. Scordaris, G., Bouzakis, K. and Charalampous, C. (2018) A Critical Review of FEM Models to Simulate the Nano-Impact Test on PVD Coatings. MATEC Web of Conferences, 188, Article ID: 04017. https://doi.org/10.1051/matecconf/201818804017
26. Hervas, I., Montagne, A., van Gorp, A., Bentoumi, M., Thuault, A. and Iost, A. (2016) Fracture Toughness of Glasses and Hydroxyapatite: A Comparative Study of 7 Methods by Using Vickers Indenter. Ceramics International, 42, 12740-12750. https://doi.org/10.1016/j.cermint.2016.05.030
27. Naimi-Jamal, M.R. and Kaupp, G. (2005) Quantitative Evaluation of Nanoindents: Do We Need More Reliable Mechanical Parameters for the Characterization of Materials? International Journal of Materials Research, 96, 1226-1236. https://doi.org/10.3139/146.101166
28. Breuils, J., Krier, J., Pelletier, H. and Mille, P. (2011) Identification, Using Nanoindentation Tests, of Mechanical Behaviour of a 2C22 Steel Presenting a Residual Stress State. Procedia Engineering 10, 3528-3533. https://doi.org/10.1016/j.proeng.2011.04.580
29. Zhao, Y., Seok, M.Y., Lee, D.Y., Lee, J.A., Suh, J.Y. and Jang, J.I. (2016) Hydrogen-Induced Softening in Nanocrystalline Ni Investigated by Nanoindentation. Philosophical Magazine, 96, 3442-3450. https://doi.org/10.1080/14786435.2016.1159743
30. Jang, J. (2005) Evidence for Nanoindentation-Induced Phase Transformations in Germanium. Applied Physics Letters, 86, Article ID: 131907. https://doi.org/10.1063/1.1894588
31. Jiang, W.H., Liu, F.X., Wang, Y.D., Zhang, H.F., Choo, H. and Liaw, P.K. (2006) Comparison of Mechanical Behavior between Bulk and Ribbon Cu-Based Metallic Glasses. Materials Science and Engineering: A, 430, 350-354. https://doi.org/10.1016/j.msea.2006.05.042

32. Moser, B., Loffler, J.F. and Michler, J. (2006) Discrete Deformation in Amorphous Metals: An in Situ SEM Indentation Study. Philosophical Magazine 86, 5715-5728. https://doi.org/10.1080/14786430600627301
33. Huang, S. and Zhou, C. (2017) Modeling and Simulation of Nanoindentation. JOM, 69, 2256-2263. https://doi.org/10.1007/s11837-017-2541-1
34. Bucaille, J.L., Stauss, S., Felder, E. and Michler, J. (2003) Determination of Plastic Properties of Metals by Instrumented Indentation Using Different Sharp Indenters. Acta Materialia, 51, 1663-1678. https://doi.org/10.1016/S1359-6454(02)00568-2
35. Kaupp, G. (2017) The ISO Standard 14577 for Mechanics Violates the First Energy Law and Denies Physical Dimensions. Journal of Material Sciences and Engineering, 6, 321-328.
36. Kaupp, G. (2017) Dilemma between Physics and ISO Elastic Indentation Modulus. Journal of Material Sciences and Engineering, 6, 402-405. . https://doi.10.4172/2169-0022.1000402
37. Kaupp, G. (2017) Challenge of Industrial High-Load One-Point Hardness and of Depth Sensing Modulus. Journal of Material Sciences and Engineering, 6, 348-355. . https://doi.10.4172/2169-0022.1000348
38. Chudoba, T., Schwaller, P., Rabe, R., Breguet, J.M. and Michler, J. (2006) Comparison of Nanoindentation Results Obtained with Berkovich and Cube-Corner Indenters. Philosophical Magazine, 86, 5265-5283. https://doi.org/10.1080/14786430600746424
39. Bhattacharya, A.K. and Nix, W.D. (1988) Finite-Element Simulation of Indentation Experiments. International Journal of Solids and Structures, 24, 881-891. https://doi.org/10.1016/0020-7683(88)90039-X
40. Goto, K., Watanabe, I. and Ohmura, T. (2020) Inverse Estimation Approach for Elastoplastic Properties Using the Load-Displacement Curve and Pile-Up Topography of a Single Berkovich Indentation. Materials and Design, 194, Article ID: 108925. https://doi.org/10.1016/j.matdes.2020.108925
41. Zhu, L., Yu, B., Wang, H., Wang, C. and Yang, D. (2011) Measurement of Mechanical Properties of 1045 Steel with Significant Pile-Up by Sharp Indentation. Journal of Materials Science, 46, 1083-1086. https://doi.org/10.1007/s10853-010-4876-7
42. Gale, J.D. and Achuthan, A. (2014) The Effect of Work-Hardening and Pile-Up on Nanoindentation Measurements. Journal of Materials Science, 49, 5066-5075. https://doi.org/10.1007/s10853-014-8213-4
43. Kaupp, G. and Naimi-Jamal, M.R. (2013) Penetration Resistance and Penetrability in Pyramidal (Nano)Indentations. Scanning, 35, 88-111. https://doi.org/10.1002/sca.21038
44. Kaupp, G, Schmeyers, J. and Hangen, U.D. (2002) Anisotropic Molecular Movements in Organic Crystals by Mechanical Stress. Journal of Physical Organic Chemistry, 15, 307-313.

https://doi.org/10.1002/poc.487
45. Kaupp, G. and Naimi-Jamal, M.R. (2005) Mechanically Induced Molecular Migrations in Molecular Crystals. CrystEngComm, 7, 402-410. https://doi.org/10.1039/b503208n

DISCLAIMER
This chapter is an extended version of the article published by the same author(s) in the following journal.
Advances in Materials Physics and Chemistry, 11: 212-241, 2021.

Chapter 16
Print ISBN: 978-93-5547-921-1, eBook ISBN: 978-93-5547-922-8

Study on Non-Equivalence of Pyramids and Their Pseudo-Cones

DOI: 10.9734/bpi/mono/978-93-5547-921-1/CH16

ABSTRACT

It is challenged that simulating indentations using ostensibly "equivalent" pseudo-cones will take less computer time. Basic trigonometry and arithmetic rules out the mimicking of pseudo-cones with equal basal surface and depth with pyramidal indenters. The widely recognised angles of supposedly "identical" pseudo-cones cannot also assert that their depth is equal. The historical values of the often-employed half-opening angles of pseudo-cones are biassed, as evidenced by the answers provided for the problems to be answered. On that basis, it invalidates all simulations or findings. Not just for artificial intelligence, the large inaccuracies in the resulting hardness HISO and elastic modulus Er_{ISO} values are devastating. For equal basal surface and equal volume, the straightforward deduction for potentially ψ-cones (ψ for pseudo) without biassed depths' errors is presented. These *ψ*-cones would of course penetrate much more deeply than the three-sided Berkovich and cube corner pyramids ($r < a/2$), and their half-opening angles would be smaller than those of the respective pyramids (reverse with $r > a/2$ for four-sided Vickers). Additionally, the more sideways and their resulting downhill directions' opposite forces' direction angles are indicated. They are reflected by the parallelograms' diameters that are long and and their angles to the vertical axis. It is essential to have experimental loading curves before and after the phase-transition onsets. Quantitatively, imitation of pyramids and ψ-cones is likewise disallowed. For industrial and solid pharmaceutical materials, every simulation based on their assumptions would also be dangerously invalid.

Keywords: Basic mathematics; extreme errors; false cone angles; indentation; unphysical cone models for pyramids; undue simulations.

16.1 INTRODUCTION

When treating pyramids as comparable cones, simulations are made easier by the ubiquitous indentations associated with equilateral three-sided pyramids. Iterative simulations using the so-called "equivalent" cone model formulas are simpler and take a lot less time on the computer when simulating the pyramids (e.g. [1,2,3] etc.). That equal basal surfaces would result in "equal penetration depths" is a dubious "assumption." To pick between pyramids and "equivalent cones," guided textbooks and indentation simulation reports use ISO 14577, [3]. But how is the so-called “equivalency” of pyramid models founded? The

mathematical formulas for the areas $A_{triangle} = A_{circle}$ of equilateral triangle $(3^{0.5}/4)a^2$ and circle πr^2 (Fig. 16.1) are rightfully equated. But we showed in [4] that no "equivalent" behavior results in such commonly believed conditions. For a variety of reasons, pseudo-cones and pyramids behaved differently. But we could not yet quantify the sizes of the differences. Now, we search for accurate inferences.

The equal area radius r of the ψ-cone (ψ for pseudo) is transformed into the a-unit from the pyramid with correct mathematics. This will remain the handle for the calculation of equal volumes and unequal heights. These heights are equal to the penetration depths in the absence of pile-up and hidden internal migrations along cleavage planes or channels [4]. The readers may be interested in certain updates in this topic that are available elsewhere [5-7]. When cleavage planes are present, the penetration depth is smaller than the calculated, but these authors still use ISO-14577 Standards treatment with iterations, or deal only with business concerns, or they iterate and simulate the height and even H_{ISO} and $E_{r\text{-}ISO}$ [4]. The generally used angles of 70.2996° for Berkovich pseudo-cone, 42.28° for the cubecorner pseudo-cone, and 70.32° or 70.2996° for Vickers-pseudo cone in the literature are used for all time saving simulations. This has been challenged in [4] for various geometric reasons and will now be quantified.

16.2 METHODS

All calculations used a common scientific pocket calculator Rebell® SC2030 with 10 digits. All of them were used and results are reasonable rounded only when necessary. The worldwide unchangeable angles of diamond Berkovich and cube corner indenters were taken as fixed crystallographically approved quantities. Tip rounding is always removed in physically analyzed indentation curves as part of initial effects and did not interfere. Only undeniable trigonometry and mathematical formulas for the basal areas and volumes were used for the mathematical deductions without prejudice and without data-fitting.

16.3 RESULTS

The literature values of half opening angles of the pseudo-cones for Berkovich, cube corner, and Vickers indenters (of 70.2996°, 42.28°, and 70.32 or 70.2996° respectively) are incorrectly made to have the same basal areas, volumes, and heights as the pyramids. Historically, heights equivalence ("$h_{pyramid} = h_{cone}$") might have been a "necessity", because the indentation depths are used for ISO-hardness and ISO-indentation modulus. We deduce here equal basal area and equal volume for ψ-cones but unequal depths. The used terms are indicated in Fig. 16.1(a) (taken from [4]) and in Fig. 16.1(b). The three-times flat and totally different all around circular force fields alone should have halted using pseudo cones!

16.3.1 Error Discovery on the Deduction Ways of the Common "Equivalent" Pseudo-Cones

The comparison of the so-called "equivalent cones" with the corresponding three-sided normal pyramids requires straightforward basic algebra and trigonometry

with always 10 significant figures, due to numerous irrational numbers with numerous equations. We test on the basis of the known formulas for equal-sided triangle, circle, pyramid and cone by equating the triangle $A_{\text{triangle}} = a^2 3^{0.5}/4$ and circle areas $A_{\text{circle}} = \pi r^2$. Such equality is the basis for pseudo-cones. One obtains from the 2/1 ratio at the central cut of the equal-sided triangle heights $r^2 = 3^{0.5}a^2/4\pi = 0.1378322a^2$ and $r = 0.371257624a$ (Fig. 16.1). The pyramidal angle $\tan\beta = 3^{0.5}a/6h_{\text{pyr}}$ and the pyramidal depth $h_{\text{pyr}} = 3^{0.5}a/6\tan\beta$, where β is the well-known half-angle of the diamond Berkovich ($\beta = 65.27^\circ$) or of cubecorner ($\beta = 35.264^\circ$). For the pseudo-cone we have $h_{\text{pseudo-cone}} = r/\tan\alpha = 3^{0.25}a/2\pi^{0.5}\tan\alpha$.

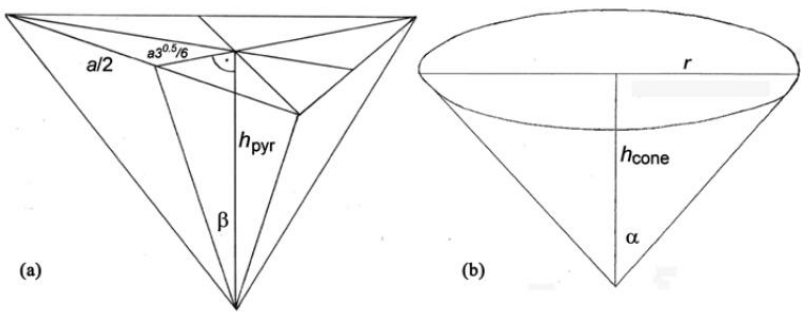

Fig. 16.1. Perspective images for (a) a three-sided pyramid and (b) a cone (not true to scale)

One obtains $h_{\text{pseudo-cone}}/h_{\text{pyr}} = 3^{0.25}a6\tan\beta/2\pi^{0.5}a3^{0.5}\tan\alpha$. For Berkovich with $\beta_B = 65.27^\circ$ and $\tan\beta = 2.171160716$ results $h_{\text{pseudo-cone}}/h_{\text{pyr}} = 2.792413659/\tan\alpha$. Here comes the historical error: Only by setting $h_{\text{pseudo-cone}}/h_{\text{pyr}}$ to 1, which is the same as dividing V_{cone} over V_{cone}, was the divisor h_{pyr} equal to the dividend h_{cone}. Such setting is absolutely cheating: It is putting a desired answer into the question. The dividend 2.792413659 is taken as an unbelievably biased "tanα" from the cone to give "$\alpha_{\text{cone}} = 70.29688723^\circ$" (undistinguishable from the less precisely calculated common 70.2996°; maybe historical equalization with Vickers?) in the case of Berkovich. It was falsely created, spread, and believed. Unimaginably, despite the correctly calculated equal basal circle-surface area, where r is smaller than $0.5a$ and also smaller than half of the basal triangle height? It directly indicates, without any further calculation effort, that the pseudo-cone must be sharper but not blunter than the pyramid with $\beta = 65.27^\circ$.

Surprisingly, the corresponding bias was repeated for cubecorner$_{-c}$ with $\beta_{-c} = 35.264^\circ$ and $h_{\text{pseudocone-c}}/h_{\text{pyr-c}} = 0.909378623/\tan\alpha$ where the divisor was falsely made to "tanα_{-c} and thus α_{-c} to 42.282713°". This bias is the commonly used false "value of 42.28°".

The four-sided Vickers indenter is more often used in industries. The biased published angle values for the "equivalent" pseudo-cone$_{-V}$ are 70.32° or

70.2996°: As above, the corresponding unbelievable trick was used for precisely obtaining the second of these values.

All these false pseudo-cone angles withstood for more than 30 years until the apparently first challenge started with [4]. Involved scientists, authors, reviewers, funding providers, textbook writers, academic teachers, and industrial users did not check and complain. But apparently, all of them liked a "same depth" for pyramids and their pseudo-cone heights at the same force. Any "equality" of these pseudo-cones and pyramids with the faulty biased angles is now strictly excluded.

Our error discovery clearly reveals the disastrous historical "deductions", more than about 30 years ago. Every hardness measurement (e.g. $H_{\mathrm{ISO}} \propto F_{\mathrm{N}}/h^2_{\mathrm{contact}}$ or $E_{\mathrm{r\text{-}ISO}}$) by simulations with iterating data-fitting that used this type of pseudo-cones (notwithstanding the unphysical exponent on h that should be 3/2 instead [8,9]) is also obsolete for that reason. Unfortunately, these very frequent unphysical simulations create severe risks with the technical materials' characterizations. An unbiased deduction of pseudo-cone geometries is thus very important for the quantification of the huge involved errors. It will become evident in Section 3.2.

16.3.2 Deduction Test for Unbiased *ψ*-Cones with Correct Volumes and Heights

We start with the equalized basal areas for the expression of radius r in units of the three-sided pyramidal side length a (Fig. 16.1). For the correct deduction of unbiased *ψ*-cones (now *ψ* for pseudo) with the equal volume (as required by the energy law) the unequal heights of the pyramids and *ψ*-cones ensue. The requirement of $A_{\mathrm{triangle\text{-}pyr}} = A_{\mathrm{circle\text{-}cone}}$ gives Equation (16.1).

$$a^2 3^{0.5}/4 = \pi r^2 \text{ and } r^2 = a^2 3^{0.5}/4\pi \text{ with } r = a3^{0.25}/2\pi^{0.5} \tag{16.1}$$

With $V_{\mathrm{pyr}} = Ah_{\mathrm{pyr}}/3$ and $V_{\mathrm{cone}} = Ah_{\mathrm{cone}}/3$ the respective heights are $h_{\mathrm{pyr}} = 3^{0.5}a/6\tan\beta$ and $h_{\mathrm{cone}} = r/\tan\alpha = 3^{0.25}a/2\pi^{0.5}\tan\alpha$. The respective volumes are $V_{\mathrm{pyr}} = a^3/24\tan\beta_{\mathrm{pyr}}$ and $V_{\psi\text{-cone}} = a^3 3^{0.125}/24\pi^{0.5}\tan\alpha_{\mathrm{cone}}$ after substitutions and simplifications. For Berkovich ($\beta_{\text{-B}} = 65.27°$) we calculate $V_{\mathrm{pyr\text{-}B}} = 0.019190963a^3$ at $h_{\mathrm{pyr\text{-}B}} = .132958897a$ and for its *ψ*-cone $V_{\psi\text{-cone-B}} = 0.019190963a^3$ at $h_{\psi\text{-cone-B}} = 0.264191103a$. For cubecorner ($\beta_{\text{-c}} = 35.264°$) we calculate $V_{\mathrm{pyr\text{-}c}} = 0.058926415a^3$ at $h_{\mathrm{pyr\text{-}c}} = 0.408254180a$ and for $V_{\psi\text{-cone-c}} = 0.058926415a^3$ at $h_{\psi\text{-cone-c}} = 0.811206506a$. The height values calculate unequal for pyramid and its *ψ*-cone. We use the energy law that requires equalizing the volumes at equal force to obtain Equation (16.2), and there from Equation (16.3). This allows for the calculation of $\tan\alpha_{\psi\text{-cone}}$.

$$a^3/24\tan\beta_{\mathrm{pyr}} = a^3 3^{0.125}/24\pi^{0.5}\tan\alpha_{\psi\text{-cone}} \tag{16.2}$$

$$\tan\alpha_{\psi\text{-cone}} = 3^{0.125}\tan\beta_{\mathrm{pyr}}/\pi^{0.5} = 0.647239808\tan\beta_{\mathrm{pyr}} \tag{16.3}$$

The angles α_{cone} are thus 54.563917° for the Berkovich-ψ-cone (as compared with commonly 70.2996°) and 24.591634 for the cubecorner-ψ-cone (as compared with commonly 42.28°).
For four-sided Vickers (β_{-v} = 68°) is $r = a/\pi^{0.5}$ larger than $a/2$ for the ψ-cone$_{-v}$. Thus, $h_{pyr\text{-}v}$ = 0.20201a is now larger than $h_{\psi\text{-cone-v}}$ = 0.19741a and also the angle $\alpha_{cone\text{-}v}$ = 70.71521° (here larger than β_{-v}) for the Vickers-ψ-cone (as compared with commonly 70.32° or 70.2996°). Mimicry is also here excluded.

The different bracketed values from Section 16.3.1 compare the still stubbornly used common pseudo-cone angle values. These huge angle faults of the biased common values of Section 16.3.1 are enormous for the biased simulations of (nano)indentations. They make them completely worthless.

Our results with so many decimals demonstrate the precision of the used arithmetic. They have to be rounded to the precision of the β-angles. We must stress that they represent the height of the indenters. The penetration depths are only equal to the heights in the absence of pile-up and internal migrations upon indentation. These cases require corrections for their depth decreases, as reported in [4]. The sideward influences had been exhaustively exemplified in [10].

We do not encourage using the non-biased ψ-cones for simulations. On the contrary: Pyramids and their ψ-cones are also not equivalent due to their different sloping angles. The unbiased Berkovich- and cubecorner-ψ-cones would penetrate about two times deeper (49.67%) than the pyramids. The now completed challenge of [4] was therein already evident but required this final quantifying deduction. When the unbiased ψ-cones would be used for simulations, their outputs would also be incorrect for the unequal directions. Such simulations with whatever mimicking cones must never be tried again; the existing ones must be deleted. Phase-transition onsets under load must be experimentally detected and for technical objects strictly avoided upon operation, because polymorph-interfaces promote disastrous cracking (e.g. at airliners) [4] [10,11]. Phase-transitions play also their important role in pharmaceutical solids (e. g. two polymorphs of crystallized *cis*-platinum [12]).

16.3.3 The Depth Directions for the Forces in Pyramids as Compared with Their ψ-Cones

It is our duty now to calculate the differences between the pyramids and their unbiased ψ-cones without data-fitting. The calculated sideward force component angles vertical to the indenter slopes of the pyramid are 90° − 65.27° = 24.73° for Berkovich and 90° − 54.564° = 35.436° for its ψ-cone. In the case of cube corner we have correspondingly 90° − 35.264° = 54.736° and 90° − 24.5916° = 65.4084°. These directional angles with respect to the central vertical axis are now 15.73° and 18.03° respectively steeper than in [4] where the biased false common pseudo-cone α_{cone}-angles had been used. Fig. 16.2 exemplifies it with the cube corner angles. It depicts the enlarged pyramidal cross-section of one from the flat triangular force-fields and for its ψ-cone the enlarged cross-section of the circular

force-field all around (cf Fig. 16.1). They are set close to each other for immediately observing the enormous differences, e.g. their depth differences. The geometric questions (including off-angle and length of the diameter in the parallelograms) are trigonometrically evident.

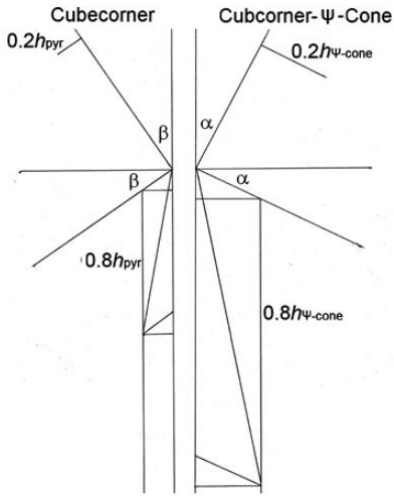

Fig. 16.2. The depth directions diagram with the angles of the cube corner (left side) in relation to its vertical axis and of its *ψ*-cone (right side) in relation to its vertical axis

The sidewise angles (lesser down) with respect to the horizontal axis are equal to the *β*-angles of the pyramids and also the *α*-angles of the *ψ*-cones (cf Fig. 16.1). They indicate the flatness of the sidewise force component. It is much flatter for cubecorner than for Berkovich and it had already been told in [4] that this qualifies the cubecorner for fracture toughness determinations. Here, the *ψ*-cone models with the unbiased *α*-angles would be flatter than the pyramids. But that excludes their mimicry power completely. Also the simulations with the new mimickry model could again not take care of the slope-angle influence in relation to materials' cleavage planes or channels. There is no pass by 1) at the use of pyramidal geometry and 2) at the prior experimental detection of the phase-transition onset with depth and force [8,9].

For the calculation of the resulting downward direction we distinguish the downward and sideward depths with their long known undeniable 80:20 ratio [9] to obtain the directional parallelogram from the pyramidal apex at both sides of Fig. 16.2. It is calculated with the respective sine, tangent, and cosine functions. The parallelograms are characterized by their smaller angle ($90 - \beta_{pyr}$) for the pyramid or ($90 - \alpha_{\psi\text{-cone}}$) for the *ψ*-cone. Their sides are the respective fractions of h_{pyr} or $h_{\psi\text{-cone}}$: 0.2 times for sideward and 0.8 times for downward direction. For the calculation of the resulting diameter length and off-angle we

add the small top triangles to the bottom of the parallelogram. The so obtained right angle triangle gives the resulting downward depth direction and its off-angle with the vertical axis. Table 16.1 compares the pyramidal and *ψ*-conical angle and lengths to show how much they differ from each other. From there we can calculate the forces by using the experimental indentation of individual materials with $F_N = kh^{3/2}$ [8] in their calculated directions up to the (by simulations unavailable) phase-transition onset. From such onset force we start with a physically and chemically different polymorph. We can also calculate the different directions of the not mimicking *ψ*-cone for comparison to see how much the error of *ψ*-cones would further increase when using these.

Table 16.1. Depth direction angles, heights and lengths for Berkovich and cube corner indentations and for the respective *ψ*-cone models

Indenter with *β*-Angle or *ψ*-cone[a)]	Sideward[b)] DeepAngle	Sideward[c)] Flat Angle	Vertical off-Angle	0.8 Indenter Height[d)]	Diagonal Length
Berkovich (65.27˚)	24.73˚	65.27˚	4.8894˚	0.106367*a*	0.130997*a*
Berkovich-*ψ*-Cone	35.436˚	54.564˚	6.9163˚	0.211353*a*[a)]	0.256268*a*
Cube corner (35.264˚	54.754˚	35.246˚	10.2979˚	0.326603*a*	0.379948*a*
Cube corner-*ψ*-Cone	65.4083˚	24.5917˚	11.8992˚	0.648965*a*[a)]	0.731194*a*

[a)]Instead of r the a-fractions from the pyramid is used for the equal basal area calculation; [b)]in relation to the center axis; [c)]in relation to the horizontal axis; [d)]the height and length values represent the mathematical 8/2 ratio of the force distribution directions downward and sideward [9] in the absence of pile-up and hidden internal migration apart from the created half volume diameter [4]

Table 16.1 shows the calculated slightly rounded depth directions and angles of the more sideward and the resulting downward directions. The forces at these directions are obtained by using the physically deduced [8] formula $F_N = kh^{3/2}$ after determination of the physical hardness k ($mN/\mu m^{3/2}$) (F_N is the normal indentation force) from the slope of the indented material's loading curve. All values in Table 16.1 are larger for the sharper *ψ*-cones that do not mimic.

We must stress, that the resulting vertical force direction departs significantly from the vertical applied axis of the indentation.

The commonly disregarded differences between the pyramids and their biased pseudo-cones (with equal heights) or unbiased *ψ*-cones (with enormous height differences) are very large. But both are in fact not mimicking the pyramids.

Our quantification of the huge differences between pyramids and their *ψ*-cones makes obsolete any use for simulations of (nano)indentations. Their false claimed results are extremely dangerous for the use of technical including solid pharmaceutical materials [12], the mechanical properties of which must be very precisely known.

16.4 CONCLUSIONS

The purpose of this paper is to discourage any use of simulations by using faster calculated cones. Physically sound undeniable mathematic calculations are

reliable and much easier. The false common angles of the widely used pseudo-cones are severely biased. Their use for simulations to save computer time is strongly falsifying. All such simulations are obsolete and dangerous. They cannot simulate phase-transition onsets and they violate the energy law by excluding the 20% loss of normal force for not-penetrating events [9]. These simulations try to help themselves with a multitude of further iterative "work-hardening" simulations. Such published "results" cannot be repaired and must be fully extinguished. Also our tentatively deducted unbiased ψ-cones are not mimicking the pyramids. Three-sided pyramid-pseudo-cones are sharper and would go deeper than the pyramids with unlike force directions. Advanced simulations with the new unbiased ψ-cones are also impossible, because the force direction influences respond to specific materials properties. These must be experimentally determined (phase-transition onsets, cleavage planes' or channels' or holes' orientations and widths) [10].

Computer time is only saved by physical analysis using basic mathematical calculations, avoiding simulations and data-fittings. That requires characterization with properly analyzed pyramidal (or with real cones) indentations. Only these reveal the previously ignored sharp phase-transition onsets and energies under load. One needs crystallographic investigations for the pile-up questions in case of materials' anisotropy. Indentations are most important for the rapid optimization of materials' properties with respect to their safety, when exposed to unavoidable forces. It is important to always stay below any materials' phase-transition onset force to avoid the cracking-risk. Simulations and data-fitting iterations produce dangerous risks with false H_{ISO} or false $E_{r\text{-}ISO}$ and therefrom derived mechanical properties of technical materials and by denying phase-transitions. Beware of using simulated and fitted indentation data for artificial intelligence applications. They are on the Internet but they must be urgently disregarded and stopped.

COMPETING INTERESTS

Author has declared that no competing interests exist.

REFERENCES

1. Scordaris, G., Bouzakis, K. and Charalampous, C. (2018) A Critical Review of FEM Models to Simulate the Nano-Impact Test on PVD Coatings. MATEC Web of Conferences, 188, Article ID: 04017. https://doi.org/10.1051/matecconf/201818804017
2. Huang, S. and Zhou, C. (2017) Modeling and Simulation of Nanoindentation. JOM, 69, 2256-2263. https://doi.org/10.1007/s11837-017-2541-1
3. Oliver, W.C. and Pharr, G.M. (1992) An Improved Technique for Determining Hardness and Elastic Modulus Using Load and Displacement Sensing Indentation Experiments. Journal of Materials Research, 7, 1564-1583. https://doi.org/101557/JMR.1992.1564

4. Kaupp, G. (2021) Volume, Side-Area, and Force Direction of Berkovich and Cubecorner Indenters, Novel Important Insights. Advances in Materials Physics and Chemistry, 11, 212-241. https://doi.org/10.4236/ampc.2021.1111019
5. Yan X, Zhao H, Shen Y, Ding H. Material removal mechanism and penetration depth modeling of CF/PEEK composites under nano-scratching. Composites Science and Technology. 2022 Jun 3:109566.
6. Fu X, Ghauri P, Ogbonna N, Xing X. Platform-based business model and entrepreneurs from Base of the Pyramid. Technovation. 2022 Jan 5:102451.
7. Tomić Z, Jukić K, Jarak T, Fabijanić TA, Tonković Z. Phase-Field Modeling of Fused Silica Cone-Crack Vickers Indentation. Nanomaterials. 2022 Jul 9;12(14):2356.
8. Kaupp, G. (2016) The Physical Foundation of $F_N = k\ h^{3/2}$ for Conical/Pyramidal Indentation Loading Curves. Scanning, 38, 177-179. https://doi.org/10.1002/sca.21223
9. Kaupp, G. (2013) Penetration Resistance: A New Approach to the Energetics of Indentations. Scanning, 35, 392-401. https://doi.org/10.1002/sca.21080
10. Kaupp, G. (2019) Physical Nanoindentation: From Penetration Resistance to Phase-Transition Energies. Advances in Materials Physics and Chemistry, 9, 103-122. https://doi.org/10.4236/ampc.2019.96009.
11. Kaupp, G. (2018) Six Polymorphs of Sodium Chloride upon Depth-Sensing Macroindentation with Unusual Longrange Cracks Requiring 30 N Load. Journal of Material Sciences and Engineering, 7, 473-483. https://doi.org/10.4172/2169-0022.1000473
12. Wang, Y., Zhang, H., Chen, Y. and Wang, L. (2019) New Insights into the Discovery of Novel Drugs to Treat Human Pulmonary Adenocarcinoma. Journal of Cancer Therapy, 10, 178-187. https://doi.org/10.4236/jct.2019.102014

DISCLAIMER
This chapter is an extended version of the article published by the same author(s) in the following journal.
Journal of Applied Mathematics and Physics, 10, 1158-1166, 2022.

Biography of author(s)

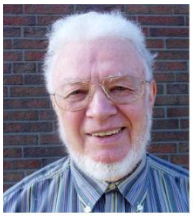

Prof. Dr. Gerd Kaupp
Carl Von Ossietzky University of Oldenburg, Germany.

He was born 1940 in Nagold Germany, he studied Chemistry at the University of Würzburg Germany and received my PhD from there. He served as a postdoc at the Universities of Ames Iowa USA, Lausanne Switzerland, and Freiburg Germany, where he received habilitation. The full-professorship at the University of Oldenburg Germany followed in 1981. His research interests started with organic syntheses, kinetic studies, and preparative Excimerlaser Photosynthesis. He developed the unprecedented solventless gas-solid and solid-solid reactions wasteless with 100% yields, which is environmentally friendly, with more than thousand reactions all along chemistry. The reasons for the unexpected success were found by application of AFM (atomic force microscopy) on rough surfaces. It proved the (strongly attacked) molecular migrations along cleavage planes or channels within crystals. He used crystal analyses and developed the first SNOM (scanning near-field optical microscopy) for rough surfaces excluding surface artefacts. It proved that the characteristic surface features are the emerging reaction products. Additional proof required nanoindentation and nanoscratching on organic and inorganic crystals. Surprisingly, already the first and more than 100 measurements always showed linearity of force F_N versus $h^{3/2}$ relations for conical and pyramidal indentations. Thus, exponent 2 on the depth h from 1882, as enforced by ISO-ASTM after 1992, is experimentally unsupported. Only our correct plots exhibit phase-transition unsteadiness onsets under load. So detected polymorph interfaces create risks for catastrophic mechanical disasters with technical materials at forces above such transition onsets. Unfortunately, these occur too often. His mathematical founded proofs revealed: the enforcing ISO-ASTM standards violate the first energy law, and $h^{3/2}$ is physical. These proofs were nevertheless strongly fought against with cheating and quackish offences, but elementary calculation rules cannot be disproved. Unfortunately, false ISO-ASTM standards are still (2022) obligatory for industry. He must therefore collect the opposing mathematical proofs in this E-Book for liability reasons.

London Tarakeswar

Registered offices
India: Guest House Road, Street no - 1/6, Hooghly, West Bengal, PIN-712410, India, Corp. Firm Registration Number: L77527, Tel: +91 7439016438 | +91 9748770553, Email: director@bookpi.org, (Headquarters)
UK: 27 Old Gloucester Street London WC1N 3AX, UK
Fax: +44 20-3031-1429 Email: director@bookpi.org, (Branch office)